HAL
archives-ouvertes.fr

Hot workability of duplex stainless steels

Guilhem Martin

▶ **To cite this version:**

Guilhem Martin. Hot workability of duplex stainless steels. Autre. Université Grenoble Alpes, 2011. Français. <NNT : 2011GRENI078>. <tel-00721764>

HAL Id: tel-00721764

https://tel.archives-ouvertes.fr/tel-00721764

Submitted on 30 Jul 2012

HAL is a multi-disciplinary open access archive for the deposit and dissemination of scientific research documents, whether they are published or not. The documents may come from teaching and research institutions in France or abroad, or from public or private research centers.

L'archive ouverte pluridisciplinaire **HAL**, est destinée au dépôt et à la diffusion de documents scientifiques de niveau recherche, publiés ou non, émanant des établissements d'enseignement et de recherche français ou étrangers, des laboratoires publics ou privés.

UNIVERSITÉ DE GRENOBLE

THÈSE

Pour obtenir le grade de

DOCTEUR DE L'UNIVERSITÉ DE GRENOBLE

Spécialité : « **Matériaux, Mécanique, Génie civil, Electrochimie** »

Arrêté ministériel : 7 août 2006

Présentée par

Guilhem MARTIN

Thèse dirigée par **Yves BRECHET** et
codirigée par **Muriel VERON**

préparée au sein du **Laboratoire SIMaP**
dans **l'École Doctorale I-MEP2**

Hot workability of duplex stainless steels

Thèse soutenue publiquement le **4 novembre 2011**,
devant le jury composé de :

Mr. Javier GIL SEVILLANO
Professeur à l'Université de Navarre, Président
Mme. Anne-Françoise GOURGUES-LORENZON
Professeur à l'Ecole des Mines de Paris, Rapporteur
Mr. Jacques GIOVANOLA
Professeur à l'Ecole Polytechnique Fédérale de Lausanne, Rapporteur
Mr. Yves BRECHET
Professeur à Grenoble-INP, Directeur de thèse
Mme. Muriel VERON
Professeur à Grenoble-INP, Directeur de thèse
Mr. Thomas PARDOEN
Professeur à l'Université Catholique de Louvain, Examinateur
Mr. Jean-Denis MITHIEUX
Ingénieur de recherche chez APERAM à Isbergues, Examinateur
Mr. Christophe PINNA
Professeur à l'Université de Sheffield, Invité
Mr. Michel BORNERT
Professeur à l'Ecole Polytechnique, Invité

Remerciements

Préambule :

Ces remerciements s'inspirent du discours prononcé le 4 novembre 2011 à l'issue de la délibération du jury, ils se veulent plus exhaustifs et personnalisés. J'ai également souhaité y ajouter quelques anecdotes vécues lors de ces trois dernières années passées au sein du laboratoire SIMaP à Grenoble.

♠ ♣ ♥ ♦

« Dans une équipe de rugby, il n'y a pas de passagers, il n'y a qu'un équipage ».
Pierre Villepreux

M'ayant régulièrement vu le lundi matin, le visage marqué par le match de la veille, quoi de plus naturel que d'ouvrir ce manuscrit en parlant de rugby mais aussi de cette expérience unique que représente une thèse. Bref, vous l'aurez compris, je vais filer la métaphore rugbystique… En effet, tout au long de ces trois années, j'ai pu remarquer d'étranges similitudes entre un match de rugby et un travail de thèse, l'objectif que je me suis fixé à travers ces remerciements est de mettre en exergue ces similitudes.

Les instances dirigeantes

Tout sport est régi par des instances, qui sont à l'origine des règles du jeu, mais aussi de l'organisation et du financement des matchs. Il en va de même pour une thèse puisqu'un travail de recherche, surtout lorsqu'il s'agit d'un travail expérimental nécessite un cadre et des fonds. Je vais donc commencer en remerciant les deux organismes qui ont fixé le cadre de ce travail et qui l'ont cofinancé à travers une bourse de docteur-ingénieur (BDI). Merci au CNRS et à la société ARCELORMITTAL, devenue aujourd'hui APERAM, pour le financement de ces travaux de thèse. Une fois les règles établies, il faut ensuite s'entourer d'un staff technique aux compétences multiples afin de se trouver dans le meilleur « bouillon scientifique » possible !

Le staff technique

Le coup d'envoi est donné, je me retrouve en réunion avec l'ensemble du staff technique afin de définir le projet et les ambitions de la saison à venir. J'aimerais remercier mes encadrants, ou mes « coachs », si je m'exprime dans un jargon rugbystique. Comme une thèse ne se fait pas sans mentors, je voudrais saluer les deux personnes qui méritent pleinement cette appellation et qui m'ont accompagné au cours de ces trois ans : merci à toi Yves, véritable encyclopédie métallurgique, et merci également à toi Thomas l'amoureux des fissures pour votre investissement et vos encouragements. Merci aussi à toi, Muriel, pour ta bonne humeur et tes conseils avisés que tu as su distiller au bon moment, notamment lorsque j'ai été amené à présenter mes travaux en réunion, en conférence et aussi à l'occasion de cette soutenance.

Je me dois d'adresser ici mes plus sincères remerciements à mes conseillers techniques, au nombre de 4.

Jean-Denis, que de chemin parcouru depuis mon premier séjour à Isbergues lors de mon stage de deuxième année en compagnie de Jean-Christophe ! Austénite en lattes ? Austénite vermiculaire ? Cinétique de réversion de la ferrite ? C'est sans doute à ce moment précis qu'a germé dans mon esprit l'idée de poursuivre l'aventure dans la recherche et plus particulièrement dans la métallurgie. Merci d'avoir gardé le contact jusqu'à notre accord final pour se lancer dans cette formidable aventure au cours de laquelle je me suis passionné pour un morceau de métal !

Laurent, je tiens à te remercier pour ta disponibilité et ta gentillesse que j'ai eu l'occasion d'apprécier lors de mes visites à Louvain. Quelle chance j'ai eu d'écouter attentivement tes cours particuliers d'introduction à la plasticité cristalline ! Les travaux entrepris ensemble à ce sujet se sont révélés précieux, surtout pendant la défense de mon travail.

Je suis également très reconnaissant envers Christophe Pinna. L'histoire de notre collaboration remonte à la simple lecture d'une publication… Il s'en est suivi un échange d'emails qui m'ont finalement conduit du côté de l'Université de Sheffield afin d'y mener quelques expérimentations.

J'exprime ma gratitude à Michel Bornert qui n'a pas hésité un seul instant lorsqu'il s'est agit de mettre ses compétences au service de mes travaux. Notre collaboration vient cette fois-ci d'un simple coup de téléphone. « Allo…Oui, bonjour, Guilhem Martin, doctorant au laboratoire SIMaP à Grenoble. Je travaille avec Yves Bréchet et j'aimerais discuter avec vous de champs de déformation...». Quelques semaines plus tard, me voilà dans les locaux du LMS à Palaiseau pour goûter aux joies de la micro-lithographie et des méthodes de mesure des champs de déformation…

Je tiens également à remercier Béchir, mon prédécesseur, pour les nombreuses discussions scientifiques qui ont participé à faire mûrir mes réflexions. J'en ai terminé avec l'encadrement de l'équipe mais je tenais à souligner qu'en plus de leur culture scientifique, musicale et historique, n'est-ce pas Yves ? sans égale, l'ensemble des personnes qui ont encadré ce travail ont aussi largement contribué à la réussite de cette thèse par leur côté humain ; valeur qui contrairement aux clichés du savant fou, autiste, enfermé dans son laboratoire est d'après moi cruciale et représente même une condition sine qua non de la réussite d'un travail de recherche. Je suis également très reconnaissant de la liberté que le staff technique m'a accordée pour mener à bien ce travail et pour avoir pris le temps d'écouter mes nombreuses idées et questions. Et pour ne rien gâcher, c'est un véritable match au sommet européen que j'ai disputé : Belgique (Université Catholique de Louvain), Angleterre (Université de Sheffield) et bien évidemment France (Laboratoire SIMaP à Grenoble, LMS à Palaiseau, et enfin, Centre de recherche d'APERAM à Isbergues).

Le staff administratif

Je n'oublierai pas non plus de remercier le staff administratif. Merci d'abord au directeur du laboratoire SIMaP, Mr. Michel PONS pour son accueil et l'intérêt qu'il porte à la qualité de vie des doctorants, notamment en finançant des activités qui favorisent l'intégration des nouveaux et renforcent les liens entre doctorants : journée d'accueil, week-end ski, tournoi de foot, barbecue... La notion de « cohésion » empruntée au rugby et si souvent évoquée pour expliquer la réussite d'un groupe trouve alors ici tout son sens. J'adresse également de sincères remerciements à toutes les secrétaires, assistantes et gestionnaires qui m'ont aidé de près ou de loin, régulièrement ou occasionnellement dans les tâches administratives : merci donc à Sanie, Virginie, Nathalie, Bruno, Fabienne, Augustine, Jacqueline et Nadine.

Les joueurs et le terrain

La charnière

Passons maintenant au terrain, je me retrouve à la baguette de l'équipe au sein du projet « CrackHot », accompagné de mon compère de la charnière, Sampath, qui a œuvré du côté de Louvain-la-Neuve et qui a aussi sa part dans la réussite de ces recherches. Merci à toi Sam pour ta joie de vivre et m'avoir fait partager tes compétences en modélisation micromécanique.

Le paquet d'avant

Mes remerciements s'adressent aussi aux travailleurs de l'ombre, j'ai nommé le paquet d'avant, avec ses piliers indéboulonnables sans qui rien ne serait possible : merci à l'ensemble du personnel technique avec lequel j'ai eu l'occasion de travailler pendant ces trois années lors de mes recherches ou lors des quelques heures d'enseignements que j'ai eu l'opportunité de dispenser à PHELMA. Je pense notamment à :

Daniel, l'as des micro-grilles et véritable plaque tournante de la micro-mécanique expérimentale.

L'équipe du CMTC, les experts en microscopie.

La « Gleeble team », Patrice le photographe et Stéphane le marathonien, un travail efficace agrémenté d'une bonne dose d'humour à votre sauce qui, il faut bien l'avouer, peut s'avérer un soupçon pimentée…

Alain Lemoulec, roi de la soudure et mécanicien hors pair.

Alain Domeyne, technicien multi-services, toujours prêt à aider et détenteur de délicieuses recettes comme le génépi à la cocotte minute ou le jambon à la moutarde.

Merci au duo Karine & Muriel, techniciennes responsables des travaux pratiques de chimie à PHELMA que j'ai connu lors de ma scolarité d'ingénieur et avec qui j'ai conservé des liens d'amitiés. Ce fut toujours un plaisir de venir partager un café ou un gâteau en votre compagnie.

Merci à Bernard, le technicien des travaux pratiques matériaux à PHELMA, très froid au premier abord, mais tellement généreux et sympathique après quelques heures passées en sa compagnie dans son bureau enfumé .

La ligne de 3/4

Je souhaiterais aussi remercier la ligne de ¾, c'est-à-dire l'ensemble des personnes qui m'ont aidé à concrétiser ce travail de thèse au travers de discussions scientifiques ou amicales. A ce titre, j'adresse mes remerciements à l'ensemble de l'équipe PM et à ses personnalités incontournables : Jean-Louis, le support technique du groupe ; Patricia et Alexis, les deux personnes qui ont eu en

charge la responsabilité de l'équipe, tâche pas toujours évidente compte tenu des fortes personnalités en présence, et qui ont toujours veillé à ce que les activités de chacun soient connues de tous; Frédéric L., personne dotée d'un sens de la provocation très développé et avec qui il est toujours agréable de débattre de sujet sensibles comme le nucléaire ou la corrida… ; Bruno, le « geek » de la bande ; Marie, l'instinct maternelle de l'équipe ; Guillaume B., celui qui m'a accompagné dans ma traversée du désert quand arrivait le mois d'août ; Sinh, le photographe; Sandrine, un modèle de pédagogie mais aussi Frédéric D.G., Guillaume P., Mireille, Marc V., Marc D.B., et Françoise. Dans le même ordre d'idée je suis reconnaissant envers les chercheurs permanents appartenant aux autres groupes du laboratoire avec qui j'ai pu collaborer ou discuter ponctuellement de choses et d'autres, je pense notamment à: Jean-Marc, Sabine, Raphael, Edgar, Catherine, et Ricardo (merci pour tous les contacts et adresses lors de mon séjour dans la « cita marvilhosa »).

Les supporters

Tous les ingrédients étaient donc présents pour réaliser un match plein, à non j'oubliais une chose très importante, les supporters !

Je remercie toute ma famille, mes grands-parents pour les valeurs qu'ils m'ont inculquées : travail, persévérance, générosité, trois mots sans lesquels tout travail de recherche serait impossible. Merci aussi à mes parents, mon frère Nils et ma sœur Laurie pour leur soutien, leurs encouragements, ils ont toujours cru en mes capacités et pour cela je les en remercie du fond du cœur. Merci aussi aux cousins-cousines, oncles et tantes avec qui j'ai partagé de sympathiques moments !

Merci à tous les doctorants et post-doctorants que j'ai pu côtoyer au cours de ces trois ans et qui ont largement contribué à la bonne ambiance qui régnait, qui règne et qui je l'espère régnera pour les générations de futurs thésards. Il existait une réelle entraide et solidarité entre nous. J'aimerais m'attarder ici sur quelques personnes ou anecdotes, qui je l'espère, feront sourire certains à la lecture des ces lignes… Je vais d'abord commencer par le bureau 217. A mon arrivée, je me retrouve en face de Coraline et Valérie, Oussama se trouvant à ma gauche, tous diplômés plus ou moins fraichement de notre bonne vieille ENSEEG. Coraline, si je devais t'attribuer un surnom ce serait sans hésitation « la tornade de bonne humeur », jamais au cours de ces années tu n'es rentrée dans ce bureau en étant de mauvais poil ! Ta recette s'il te plait ? Cette bonne humeur quotidienne et permanente a largement contribué à mon intégration et à l'atmosphère si particulière du bureau 217. Oussama, homme au caractère discret teinté d'une pointe de timidité mais d'une gentillesse inégalable, merci pour tout mais surtout pour tes comptes-rendus footballistiques du lundi matin, digne d'un Thierry Gilardi des grands soirs. Et j'oubliais une chose…longue vie aux « blaugranas » qui redorent un peu le blason du football grâce à un certain Messi(e) venu d'Argentine… Valérie est partie très vite poursuivre son aventure en Allemagne, je ne l'ai côtoyée que quelques semaines mais je retiendrai son dynamisme et sa volonté d'aller de l'avant. Valérie partie, la place était vacante mais elle ne le resta pas longtemps. En effet, de nombreux stagiaires, venus du pays des caribous et plus particulièrement du Grenoble canadien : Hamilton, pôle universitaire avec la célèbre « Mc Master University », ont occupé cette place dans le bureau 217. Une petite polytechnicienne branchée sur du 200 000 Volts, Fanny, a également partagée pendant quelques mois ce bureau devenu si chaleureux sous l'influence de ses divers occupants. Dès mon arrivée, j'ai tout de suite compris que la deuxième place forte des doctorants au bâtiment THERMO se trouvait au bureau 109. J'ai ainsi fait la connaissance de Sylvain et de son humour voltairien rempli d'ironie, de « Jean-Jo » qui venait me rendre visite en pleine séance de polissage pour un petit « battle » sur le « dancefloor » au son de l'émission radiophonique « Party Fun », d'Aurélie et de son caractère bien trempé alliant susceptibilité et franchise, de Céline et Emre, éléments discrets mais forts sympathiques. A cette même époque, d'autres doctorants, un peu éparpillé dans les divers bureaux du bâtiment étaient présents et m'ont permis de m'intégrer facile-

ment : je pense ici à Ian et Nicolas deux passionnés de l'acier, Malika l'ultra-sportive, et Benjamin alias Dom Juan. Trois ans, c'est long, j'en ai tout juste terminé avec la première génération de doctorants que j'ai côtoyé, qu'il me faut déjà saluer la deuxième génération. Je ne peux m'empêcher de commencer ici par notre nationaliste breton Jean-Marie, premier fournisseur de pièces pour les projets d'expertise d'avarie grâce à ses talents de cycliste, non pardon, d'acrobate... Je me dois aussi de le remercier, car avec lui j'ai appris la patience… 1 h la partie de tarot ça fait long non ? Après une ou deux fausses donnes, 20 minutes pour trier ses cartes avec sa dextérité légendaire, et encore 20 minutes de réflexion pour faire son chien, la partie pouvait enfin commencer ! Heureusement, il y avait ta bonne humeur associée à tes délicieuses tartes aux pommes ! Je poursuivrais avec la colloc' de choc Coraly & Clairette, je me suis toujours demandé si elles étaient doctorantes ou patronnes d'un bouchon lyonnais tellement leurs conversations tournaient inévitablement autour de la gastronomie…un canon de rouge avec le fromage ? Je n'oublierais pas non plus Thomas, le bon vivant du groupe que j'ai eu l'occasion de mieux connaitre car il fut mon co-équipier de Feria ; Quentin, toujours prêt à partager une entrecôte quand l'aube pointait son nez ; Thiago, mon guide touristique à Rio de Janeiro ; et enfin Christophe, membre à part entière de la famille « duplex ». Enfin, quelques semaines avant l'échéance, j'ai vu arriver la troisième génération de thésards : Laurent, un de mes ex-étudiants ; Nicolas, notre socialo-Montebourgeois, quelle franche rigolade lorsque quelques jours seulement après avoir fait ta connaissance j'ai lu une de tes interviews politicienne ! Merci également à tous les autres doctorants avec qui j'ai échangé quelques mots pendant ces trois ans : Laurent, Jennifer, Audrey, Souad, Mathilde…j'espère que je n'en oublie pas… J'ai remercié l'ensemble des thésards, mais quand la thèse touche à sa fin, c'est pour un bon nombre, l'heure du post-doc ! Merci aussi aux post-docs : à Benoit, c'est toujours un plaisir de discuter avec toi, ta franchise est pour moi une grande qualité ; à J-P pour son humour noir, à Seb pour les fou-rires en tout genre et enfin à Jean pour m'avoir fait part de ses expériences de fin de thèse. J'ajouterai juste qu'une étude statistique menée sur les trois années de ma thèse a montré que la consommation de café était proportionnelle au nombre d'années d'expériences dans la recherche. La preuve en chiffre…première année de thèse : 1 tasse par jour, deuxième année de thèse 2, troisième 3 ; post-doc : 7-8 tasses quotidiennes ; et chercheur permanent, l'unité de mesure « nombre de tasses » ne convenant plus, il faut ensuite évaluer cette consommation en litres !

Merci également à tous les amis de l'extérieur, ceux qui m'ont permis de m'évader au détour d'une soirée ambiancée, d'un tournoi de beach rugby ou encore d'une petite virée à la feria de Nîmes ou de Dax. Merci à vous amis, copains, copines de longues dates !

Merci à Patrick et toute son équipe du restaurant l'Epicéa pour leur humour décalé et pour les petites faveurs qui nous étaient accordées : tartes et gâteaux en tout genre.

Merci aux étudiants que j'ai pu encadrer en travaux pratiques de métallurgie, en projet, ou même en stage pour certains. Mon bêtisier s'est diversifié grâce à vous ! Je tiens à remercier particulièrement la dernière génération d'étudiants venus de Mc Master avec une immense soif de découverte de l'Europe. J'ai, grâce à vous, fait d'énormes progrès dans la langue de Shakespeare alors que, je dois bien le concéder, je n'étais initialement pas très doué pour « speaker english » si je peux me permettre de m'exprimer dans un « franglais » propre à notre cher Docteur Renaud, Mister Renard.

Sur un plan plus personnel, je voudrais en terminer avec les supporters en accordant quelques mots à Marie. Merci à elle qui a supporté mes humeurs métallurgiques pendant presque trois ans et qui m'a souvent permis de me sortir du cercle infernal labo-rugby / rugby-labo au travers de week-ends toujours très agréables ou de voyages exotiques dont je garderai des souvenirs inoubliables.

L’arbitre

Je suis aussi profondément reconnaissant envers l’arbitre de cette rencontre, qui a accepté de venir présider cette soutenance malgré un emploi du temps surchargé, merci à vous, Professeur Javier GIL SEVILLANO.

Les journalistes

Merci également aux deux rapporteurs, les professeurs Jacques GIOVANOLA et Anne-Françoise GOURGUES que j’assimilerai aux journalistes, juge, critique de ma prestation écrite et orale.

La 3eme mi-temps

Il est tant pour moi d’en finir et d’évoquer comme à la fin de tout match de rugby qui se respecte, la 3eme mi-temps, c'est-à-dire le pot qui a suivi la défense. Je me suis senti obligé à la suite de nombreuses remarques de rappeler ici que le moment partagé ensemble lors de ce pot fut incroyablement sympathique et au combien convivial avec une touche bien franchouillarde amené par le fameux civet de sanglier avec lequel j’avais fais saliver plusieurs collègues pendant les trois années précédentes

Abstract

The Duplex Stainless Steels (DSS) are defined as a family of stainless steels consisting of a two-phase microstructure involving δ-ferrite and γ-austenite. Exceptional combinations of strength and toughness together with good corrosion resistance under critical working conditions designate DSS a suitable alternative to conventional austenitic stainless steels. Unfortunately, the relatively poor hot workability of these alloys makes the industrial processing of flat products particularly critical. Cracking of the coils during hot rolling along the edges is frequently reported. As a consequence, additional operations like grinding, discontinuous processing or scraping are often required, leading to a dramatic increase of the manufacturing costs. The different parameters affecting the hot working of duplex stainless steels have been reviewed in order to identify which are the missing pieces of the "puzzle". The bibliographical review reveals that two pieces are missing in the "hot workability puzzle". On the one hand, it is necessary to develop a new hot ductility test which allows discriminating microstructures in terms of high temperature tearing resistance, and on the other hand, quantitative data about the strain partitioning between ferrite and austenite during the hot working operations are needed. The Essential Work of Fracture (EWF) concept has been applied at high temperature. It has been demonstrated that this method is a reliable and discriminating tool for quantifying the high temperature tearing resistance and to generate a physically relevant index to guide the optimization of microstructures towards successful forming operations. A modified microgrid technique has been developed to experimentally simulate the local state of deformation of different duplex microstructures at high temperature. This technique provides qualitative results about the deformation features as well as quantitative data about the strain partitioning between ferrite and austenite. The micro-scale strain distributions measured can be used to validate the models predicting the hot deformation of duplex stainless steels during the roughing-mill operations. The two tools developed in this investigation allow suggesting possible remedies for the edge cracking phenomenon.

Key words: Duplex stainless steels; Hot workability; Essential Work of Fracture; Hot tearing resistance; Microgrid technique; Local strain distribution

Table of contents

Remerciements i
Abstract vii
Table of contents 1
List of symbols 7
Chapter I. Introduction: scientific and industrial motivations 11
I.1 Industrial motivations 12
I.2 Materials and microstructures 14
I.2.1 Materials investigated 14
I.2.2 Microstructures after continuous casting 15
I.2.3 Microstructures during hot rolling 16
I.2.3.1 The hot rolling process 16
I.2.3.2 Microstructures after the roughing-mill operations 17
I.2.3.3 Microstructures in the vicinity of the edges 18
I.3 Guideline 18
Chapter II. State of the art regarding the hot working of duplex stainless steels 21
II.1 Microstructural evolution during hot working 22
II.1.1 As-cast microstructure 22
II.1.2 Changes in morphology and distribution of the dispersed γ-austenite 23
II.1.2.1 Interphase boundary sliding 24
II.1.2.2 Rotation 25
II.1.2.3 Shear banding 26
II.1.3 Plastic deformation 27
II.2 Mechanical behaviour during hot working 28
II.2.1 Viscoplastic hardening laws: influence of temperature and strain rate 28
II.2.2 Influence of the chemical composition 30
II.2.2.1 Volume fraction of phases 30
II.2.2.2 Influence of alloying elements and element partitioning 32

II.2.3 Strain partitioning 33
II.2.4 Influence of the deformation mode 35
II.2.5 Influence of the phase morphology 36
II.3 Damage during hot working 37
II.3.1 Influence of the chemical composition 37
II.3.1.1 Influence of the major elements 38
II.3.1.2 Influence of the minor elements 39
II.3.2 As-cast microstructures 40
II.3.3 Influence of temperature and strain rate 41
II.3.4 Origin of damage 42
II.4 Conclusions 43
Chapter III. Hot cracking resistance 45
III.1 Literature review about the Essential Work of Fracture concept 45
III.2 Experimental procedure 49
III.2.1 High temperature testing 49
III.2.2 Dimensions of the DENT specimens 50
III.2.3 Characterization tools 51
III.2.3.1 Observation of the fracture surfaces 51
III.2.3.2 Microstructural characterizations 52
III.2.3.3 Damage characterization 52
III.2.3.4 Inclusion content 53
III.2.3.5 Micro-hardness 54
III.3 Comparison between as-cast D1 and D2 54
III.3.1 Results 54
III.3.1.1 EWF results 55
III.3.1.2 Fracture observations 56
III.3.1.3 Damage 58
III.3.2 Discussion 60
III.3.2.1 Origin of the differences between D1 and D2 in the as-cast conditions 60
III.3.2.2 Origin of the dispersion of the results 63
III.3.3 Conclusions 65
III.4 Generation of model microstructures 65
III.4.1 Materials and characterizations 66
III.4.2 γ-Widmanstätten microstructure 66
III.4.2.1 Understanding of the as-cast slab microstructure 66
III.4.2.2 Generation of a γ-Widmanstätten microstructure 68
III.4.3 γ-Equiaxed microstructure 69
III.4.4 Conclusions 71
III.5 Comparison between D1 and D2 γ-Widmanstätten microstructures 72
III.5.1 Results 72
III.5.1.1 EWF results 72
III.5.1.2 Fracture and damage observations 74
III.5.2 Discussion 76

III.5.2.1 Origin of the difference between D1_W and D2_W 76
III.5.2.2 As-cast vs. model Widmanstätten microstructures 77
III.5.3 Conclusions 78
III.6 Influence of the phase morphology: γ-Widmanstätten vs. γ-equiaxed 78
III.6.1 Results 78
III.6.1.1 EWF results 78
III.6.1.2 Fracture and damage observations 80
III.6.2 Discussion: D2_E vs. D2_W 81
III.6.2.1 Rheology 81
III.6.2.2 Nature of the interphase boundaries 82
III.6.2.3 Effect of the morphology on the crack path 82
III.6.3 To go further…necking vs. damage 85
III.6.3.1 Question 85
III.6.3.2 How to answer this question? 86
III.6.4 Conclusions 87
III.7 Influence of the inclusion content 88
III.7.1 Materials 88
III.7.2 Results 89
III.7.3 Discussion about the nature, size and density of the inclusions 91
III.7.3.1 Nature of the inclusions 91
III.7.3.2 Density of inclusions 92
III.7.3.3 Size of the inclusions 93
III.7.4 Conclusions 94
III.8 Conclusions 96
Chapter IV. Strain partitioning 97
IV.1 Techniques to measure strain distribution 97
IV.1.1 Grid techniques 98
IV.1.2 Image correlation techniques 99
IV.1.3 Microgrid vs. correlation 100
IV.2 Measurement of micro-scale deformation at high temperature 100
IV.3 Selection of the experimental technique for measuring the micro-scale strain distribution 102
IV.4 Experimental Procedure 104
IV.4.1 Processing high-temperature resistant microgrids 104
IV.4.1.1 Sample preparation 104
IV.4.1.2 Modified microgrid technique 104
IV.4.2 Plane strain compression testing 108
IV.4.2.1 The plane strain compression test 108
IV.4.2.2 Modifying the plane strain compression test 109
IV.4.2.3 Plane strain compression machine 110
IV.4.2.4 Testing conditions 112
IV.4.2.5 Extraction of the deformed microgrids 113
IV.4.3 Strain distribution mapping 114

IV.4.3.1 Procedure ... 114
IV.4.3.2 Calculation of the local strain components ... 115
IV.4.3.3 Computation of the in-plane components of the logarithmic strain tensor ... 117
IV.4.3.4 Per-phase average strains ... 118
IV.4.3.5 Errors on the computation of the strains ... 118
IV.5 Comparison between D1 and D2 Widmanstätten microstructures 119
IV.5.1 Results ... 119
IV.5.1.1 Macroscopic stress-strain curves ... 119
IV.5.1.2 Micro-scale strain analysis ... 120
IV.5.2 Discussion ... 129
IV.5.2.1 What is the origin of the difference between D2_W and D1_W in terms of strain partitioning? ... 129
IV.5.2.2 Why is the overall strain different from the macroscopic strain? ... 132
IV.5.3 Conclusions ... 135
IV.6 Factors potentially impacting strain localization ... 135
IV.6.1 Influence of the temperature ... 135
IV.6.1.1 Equiaxed morphology ... 135
IV.6.1.2 Widmanstätten morphology ... 140
IV.6.1.3 Conclusion ... 143
IV.6.2 Influence of the phase morphology ... 143
IV.6.3 Conclusions ... 145
IV.7 Limits of the technique ... 146
IV.7.1 A time consuming technique ... 146
IV.7.2 Effect of sliding at the δ/γ boundaries and consequence on the strain calculation ... 147
IV.7.3 A 2-dimensional measurement ... 147
IV.7.4 Limitations due to experimental conditions ... 150
IV.8 Perspective: derivation of per-phase flow properties ... 151
IV.8.1 Introduction ... 151
IV.8.2 Microstructure modelling ... 151
IV.8.2.1 Image processing of the SEM micrograph ... 152
IV.8.2.2 Discretization of the microstructure ... 153
IV.8.2.3 Optimization of flow properties ... 153
IV.9 Conclusions ... 160
Chapter V. Conclusions and perspectives ... 161
V.1 Summary of the chapters III and IV ... 162
V.1.1 Chapter III ... 162
V.1.2 Chapter IV ... 163
V.2 Recommendations for an optimized microstructure ... 164
V.3 Perspectives ... 164
V.3.1 Essential work of fracture concept ... 164
V.3.2 Modified microgrid technique ... 165
Bibliography ... 167

Appendices 175
Appendix A : Post processing-analysis of the raw data of the plane strain compression tests 177
A.1 Specimens measurements 177
A.2 Breadth spread, origin and machine compliance corrections 177
A.3 Calculation of pressure and equivalent strain ε_{eq} 180
A.4 Determination of equivalent flow stress σ_{eq} 180
Appendix B : Strain computations 183
B.1 Definition of the local strain 183
B.2 Average strain over a domain 183
B.3 Computation of local strains 184
B.4 Computation of average strains 188
Appendix C : Illustration of the microgrids 191
C.1 Undeformed configuration 191
C.2 Deformed configuration 207
Résumé étendu 221

List of symbols

Symbol	Description
SIMaP	Sciences et Ingénierie des Matériaux et Procédés
LMS	Laboratoire de Mécanique des Solides
UCL	Université Catholique de Louvain
δ	ferrite
γ	austenite
DSS	Duplex Stainless Steel
PREN	Pitting Resistance Equivalent Number
E	Young modulus
σ_m	Ultimate tensile strength
σ_0	Yield strength
A	Elongation to fracture
ND	Normal Direction
RD	Rolling Direction
TD	Transverse Direction
K-S	Kurdjumov-Sachs
N-W	Nishiyama-Wassermann
SEM	Scanning Electron Microscope
TEM	Transmission Electron Microscope
$\dot{\varepsilon}$	Strain rate
Q	Activation energy

σ_{ss}	Steady state stress
R	Universal gas constant
T	Temperature
$\%\delta$	Volume fraction of ferrite
$\%\gamma$	Volume fraction of austenite
σ_{eq}	Von Mises equivalent strain
ε_{eq}	Von Mises equivalent strain
CSI	Crack Sensitivity Index
EWF	Essential Work of Fracture
DPZ	Diffuse Plastic Zone
FPZ	Fracture Process Zone
DENT	Double Edge Notch Tension
l_0	Ligament length of a DENT specimen
W_{tot}	Total work of fracture
W_e	Essential work of fracture
W_p	Plastic work
w_{tot}	Specific total work of fracture
w_e	Specific essential work of fracture
w_p	Specific plastic work
t_0	Initial thickness of the DENT specimens
L	Width of the DENT specimens
α	Shape factor
F	Force
U	Displacement
r_p	Radius of the plastic zone
$\varepsilon^{eq}_{fracture}$	Von Mises equivalent strain to fracture
t_f	Thickness of the DENT specimens at the fracture
ε^{eq}_i	Von Mises equivalent strain at a position i
t_i	Thickness at a position i
EDS	Energy Dispersive Spectroscopy

WDS	Wavelength Dispersive Spectroscopy
EBSD	Electron Back Scattered Diffraction
HV	Hardness Vickers
s	Standard deviation
σ	Variance
$\varepsilon_{damage}^{eq}$	Strain at which the number of voids increases significantly
e_γ	Average thickness of the austenite laths
$Ø_\gamma$	Average diameter of the austenite equiaxed grains
'E'	Equiaxed austenite
'W'	Widmanstätten austenite
HTE	Heat Treatment to generate an equiaxed austenite
HTW	Heat Treatment to generate a Widmanstätten austenite
D_i^j	Diffusion coefficient of the element i in the phase j
D_0	Pre-exponential constant
l_i^j	Diffusion length of the element i in the phase j
t	time
R^2	Regression linear coefficient
W_0	Work spent for growing voids to final material separation
W_n	Work spent in crack tip necking specimen thickness
w_0	Average work spent per unit area for growing voids to final fracture
w_n	Average work per unit volume dissipated in the neck in front of the crack tip
β	Shape factor
CCD	Charge-Couple Device
DIC	Digital Image Correlation
PMMA	Poly-methyl methacrylate
PSC	Plane Strain Compression
l	Length of the PSC specimens
h_0	Initial height of the PSC specimens
b_0	Initial width of the PSC specimens
TTT	Time Temperature Transformation

ε_{ij}	Strain components, i = 1,2,3 and j = 1,2,3
F_{ij}	Gradient components, i = 1,2,3 and j = 1,2,3
$\overline{\overline{F}}$	Gradient tensor of the transformation
$\overline{\overline{R}}$	Rotation tensor
$\overline{\overline{U}}$	Distortion tensor
$\overline{\overline{Q}}$	Tensor giving the orientation of the principal directions of the distortion
$\overline{\overline{\varepsilon^{\log}}}$	Logarithmic strain tensor
$\overline{\overline{D}}$	Diagonal tensor
θ	Polar angle of the principal distortion
$<.>$	Average over a domain
β	Parameter of the Kocks-Mecking hardening law
θ_0	Parameter of the Kocks-Mecking hardening law
FE	Finite Element
$\bar{\varepsilon}_{ij}$	Average strain component
$'\varepsilon_{ij}$	Dispersion in the strain component
v^k	Volume of an element k in the finite element mesh
K	Total number of finite elements in a given phase
R	Residual
W	Weight factor
h_h	Deformed cold thickness of the PSC specimens
h_f	Deformed hot thickness of the PSC specimens
α	Thermal expansion coefficient
T_0	Room temperature
C_b	Spread coefficient
b_f	Average breadth post deformation of the PSC specimens
p	Average pressure
w	Platen width
b	Instantaneous breadth of the PSC specimens
h	Instantaneous height of the PSC specimens
μ	Friction coefficient
k	Maximum shear stress
f	Correction factor

Chapter I. Introduction: scientific and industrial motivations

Chapter I. Introduction: scientific and industrial motivations

Worldwide demand for stainless steel is increasing at a rate of 5-6% per year. Annual consumption is now well over twenty million tons and is rising in areas such as the building industry and household appliances in addition to the chemical applications in energy production and chemical industry. New markets are continuously found for the attractive appearance, corrosion resistance, low maintenance cost and strength of stainless steel. Stainless steel is more expensive than standard grades of carbon steels but it exhibits greater corrosion resistance and requires less maintenance operations and does not need painting or other protective coatings. As a consequence, stainless steels can be more economically viable when service life and life-cycle are considered.

The major elements entering the composition of stainless steel are: iron (Fe), chromium (Cr), nickel (Ni), molybdenum (Mo) and manganese (Mn) and small amounts of others metals. On the basis of their crystalline structure, stainless steels can be broadly divided into four families. Iron is always the main constituent and the rest of the chemical elements are present in varying proportions in each family of stainless steel. However, in any of them, the chromium content should not be below 11% otherwise the material loses its high corrosion resistance. The main families of stainless steels are:

- Austenitic stainless steels;
- Ferritic stainless steels;
- Duplex stainless steels;
- Martensitic stainless steels.

Duplex stainless steels (DSS) are defined as a family of stainless steels consisting of two phases: δ-ferrite and γ-austenite with a proportion of each phase around 50%.
First, the industrial motivations of this work are briefly described. Then, the materials and the microstructures at different steps of the industrial process are presented. Finally, the scientific strategy to solve the industrial problem is explained.

I.1 Industrial motivations

Austenitic stainless steels represent more than 70% of the stainless steel market. For the last decade, the price of nickel and molybdenum (raw material) fluctuates widely and, as a general trend, tends to increase, see Figure I.1.

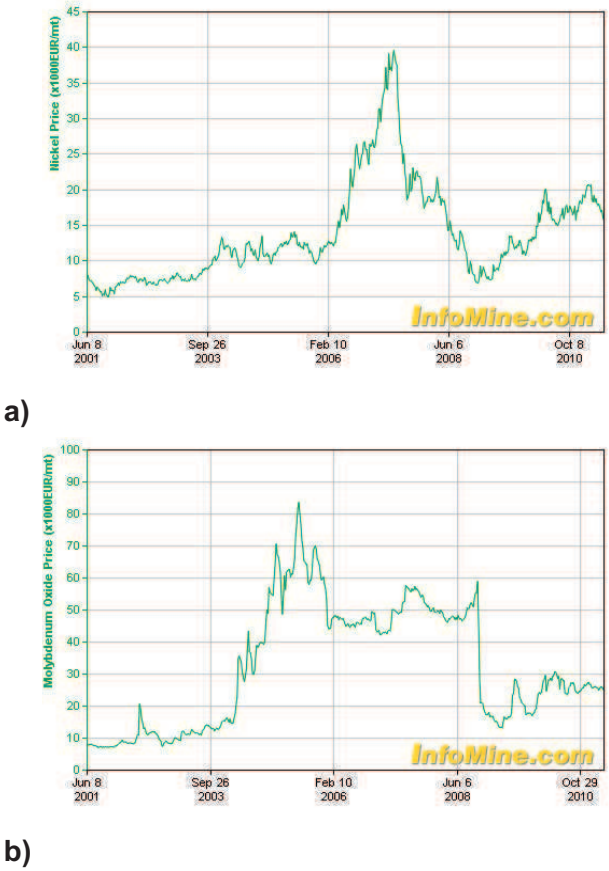


Figure I.1. Evolution of the raw material cost during the last ten years; a) Nickel price evolution and b) Molybdenum oxide price evolution [1].

Thus, with nickel content between 8 and 11%, the austenitic grades show a strong susceptibility to raw material cost fluctuation. As a consequence, to face the high volatility of nickel price, steel manufacturers have developed new alloys such as lean duplex in which the nickel and molybdenum contents are lower than in the conventional austenitic grades: 304 L and 316 L, see Table I.1. Even if the chromium content is slightly higher in duplex steels (4-5% more), as the chromium price (~2000 €/ ton in 2010) is significantly lower compared to the nickel (~15000 €/ ton in 2010) and molybdenum (~25000 €/ ton in 2010) prices, a 4%-increase of the amount of chromium does not represent a significant additional cost.

		%C	%Si	%Mn	%Cr	**%Ni**	**%Mo**	%N	%Cu
Ferritic	430	0.05	0.35	0.40	16.50	**-**	**-**	-	-
Austenitic	304 L	0.02	0.45	1.30	18.10	**10.10**	**-**	-	-
	316 L	< 0.02	0.40	1.20	16.70	**10.05**	**2.05**	-	-
Duplex	2205	0.02	0.30	1.80	22.80	**5.50**	**3.10**	0.17	-
	2304	0.02	-	1.30	23.00	**4.50**	**0.50**	0.10	0.40
	2202	0.02	-	1.30	23.00	**2.50**	**< 0.30**	0.20	-

Table I.1. Typical chemical composition in %wt of different grades belonging to different stainless steel families.

In addition, duplex stainless steels are very attractive because they exhibit outstanding mechanical properties (better than the austenitic grade, see Table I.2) combined with excellent corrosion resistance (Figure I.2). In others words, duplex stainless steels seem to be very good candidates for substituting the austenitic stainless steels.

Stainless Steel Family	Commercial Grade Designation	European Designation	ASTM	E Young Modulus (GPa)	σ_m Ultimate Tensile Strength (MPa)	σ_0 Yield Strength (MPa)	A (%)
Ferritic	K30	1.4016	430	220	510	340	26
Austenitic	18-10 L	1.4306	304 L	200	590	270	52
	18-11 L	1.4404	316 L	200	620	310	48
Duplex	DX2205	1.4462	2205	200	840	620	29
	DX2304	1.4362	2304	200	730	550	30
	DX2202	1.4062	2202	200	730	550	31

Table I.2. Mechanical properties of the different stainless steel families: ferritic, austenitic and duplex.

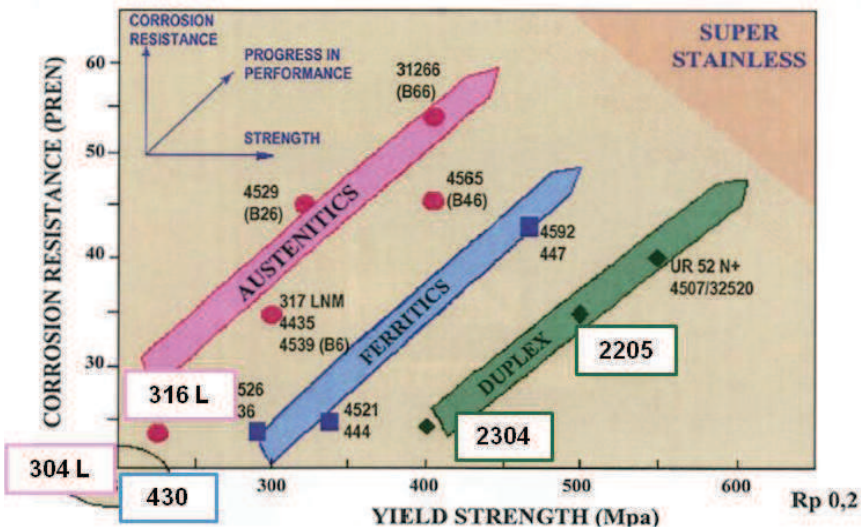


Figure I.2. Performance of the different stainless steel families, pitting corrosion resistance and yield strength [2].

Nevertheless, for a given application, a material has to fulfill technological criteria as well as economical requirements. From a technological point of view, duplex stainless steels are very suitable for many applications, especially for marine and petrochemical applications. From an economical point of view, the problem is more complicated. Indeed, the manufacturing cost has to take into account the raw material costs, the processing costs, and the maintenance costs. In duplex stainless steels, the raw material cost is significantly reduced because of a low nickel and molybdenum content. Unfortunately, the manufacturing cost remains very high due to a poor hot workability. This poor hot workability makes the industrial processing of flat products particularly critical. Indeed, cracking occurs along the edges during hot rolling, see Figure I.3. Consequently, additional operations like grinding or scraping are often required. All these additional operations lead to increase dramatically the manufacturing costs. Therefore, the poor hot workability of these alloys explains why the duplex stainless steels market is still limited.

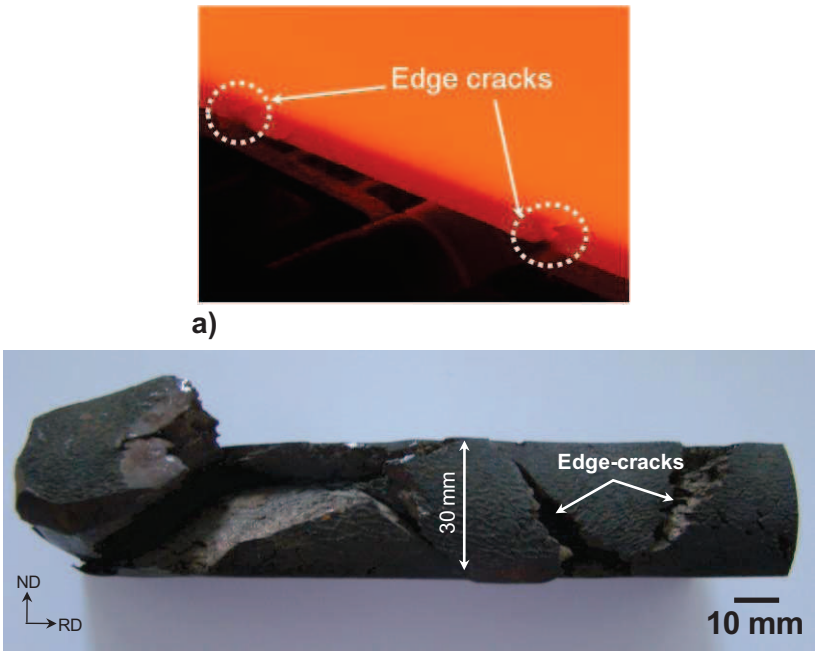


Figure I.3. Illustration of the poor hot workability of duplex stainless steels; a) occurrence of the first edge-cracks during the roughing mill operations; b) example of edge cracks after the roughing-mill operations.

To summarize, from an industrial point of view, investigating the hot ductility of duplex stainless steels must permit to answer to more general questions related to the damage of two-phase materials. The aim is to give some guidelines about the process (elaboration, casting, reheating, hot rolling), the chemical composition of the grades (volume fraction of the second phase, spatial distribution of the phases, and rheology of the two phases), and new characterization tools.

I.2 Materials and microstructures

I.2.1 Materials investigated

The two investigated grades are provided by APERAM. The first grade is named D1, corresponding to the commercial 2205-duplex stainless steel alloy (grade 1.4462 according the EN10088), and the second alloy is D2, an industrial experimental material (i.e. produced in order to carry out some tests). The chemical composition of both duplex grades is given in Table I.3.

	%Cr	%Ni	%Mo	%Mn	%Si	%Cu	%C	%N
D1	22.90	5.59	3.11	1.75	0.55	0.19	0.02	0.17
D2	21.96	2.99	0.91	2.88	0.39	0.67	0.03	0.18

Table I.3. Chemical composition in %wt of the two investigated grades.

These two grades were selected because of a known very different degree of hot workability. The grade D1 shows a reasonable level of hot workability: edge cracks length does not exceed 5mm on the hot rolled strip, see Figure I.4.a, whereas the D2 grade is affected by 50mm-edge crack lengths, see Figure I.4.b. Comparing these two grades should allow unravelling the key parameters involved in the hot workability of duplex stainless steels.

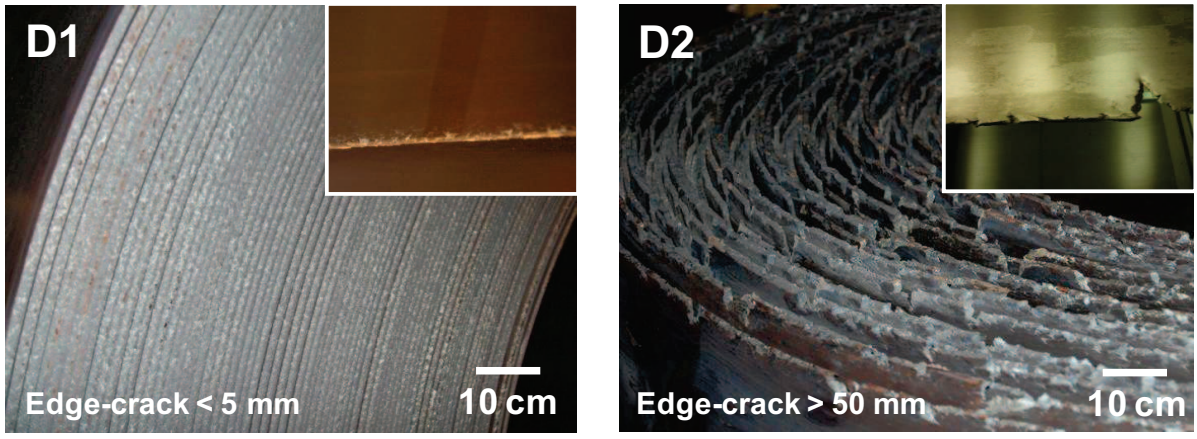


Figure I.4. Coils at the end of the hot rolling process showing different levels of edge-cracking depending on the grade; a) coil of the D1 grade with edge-cracks < 5mm; b) coil of the D2 grade with edge cracks > 50mm.

I.2.2 Microstructures after continuous casting

The schematic equilibrium phase diagram provides qualitative indications about the origin of the as-cast microstructures, see Figure I.5. From the liquid, the alloy solidifies into δ-ferrite (Figure I.5.a). During cooling, the austenite precipitates by a nucleation and growth mechanism. Allotriomorphic austenite (γ-allotriomorphic) nucleates at existing δ-ferrite grain boundaries (Figure I.5.b). Widmanstätten austenite laths nucleate from the allotriomorphic austenite with an orientation relationship with the ferrite close to that of Kurdjumov-Sachs.

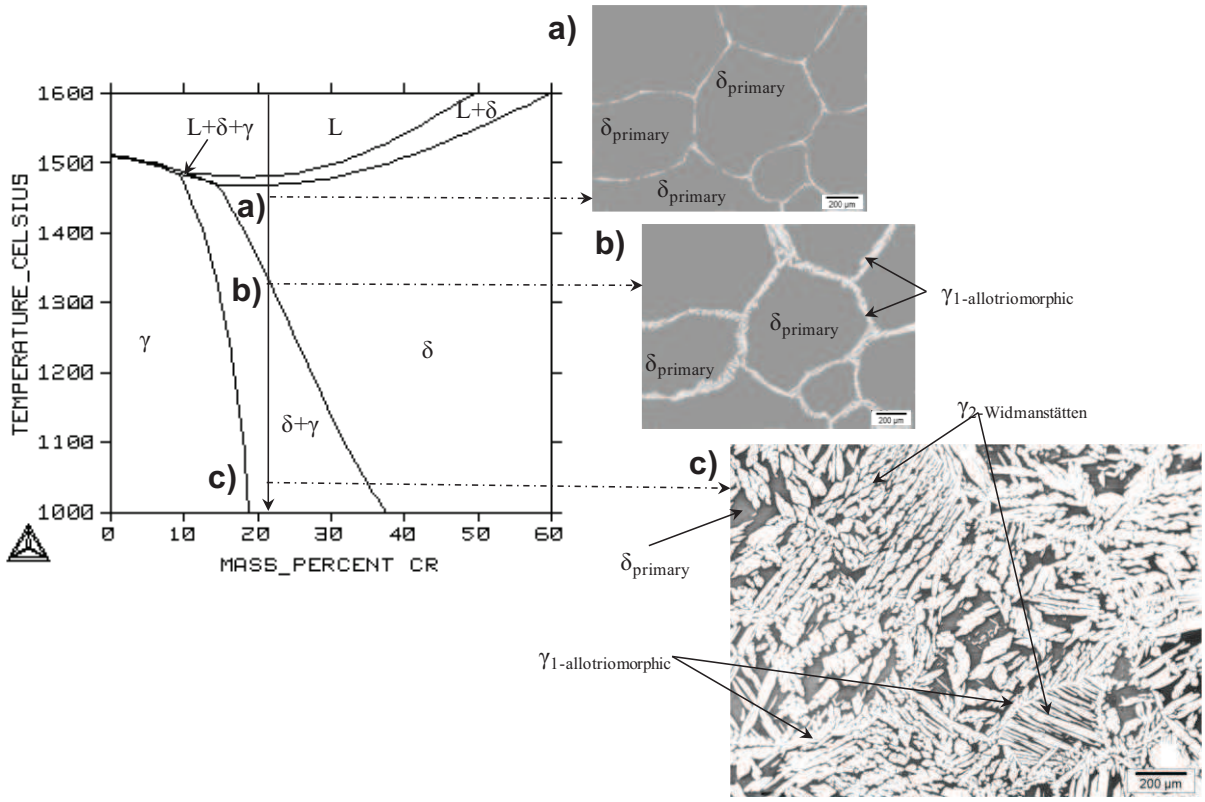


Figure I.5. Origin of the as-cast microstructure in duplex stainless steel; a) at high temperature duplex stainless steel is entirely ferritic; during cooling, the austenite precipitates b) at existing ferrite grain boundaries and c) inside the ferrite matrix with a lath morphology; thermal history explains the as-cast microstructure.

For both grades, the as-cast microstructure consists of a ferritic matrix with allotriomorphic austenite on the grain boundaries and Widmanstätten austenite (γ-Widmanstätten) laths inside the grains, see Figure I.6.

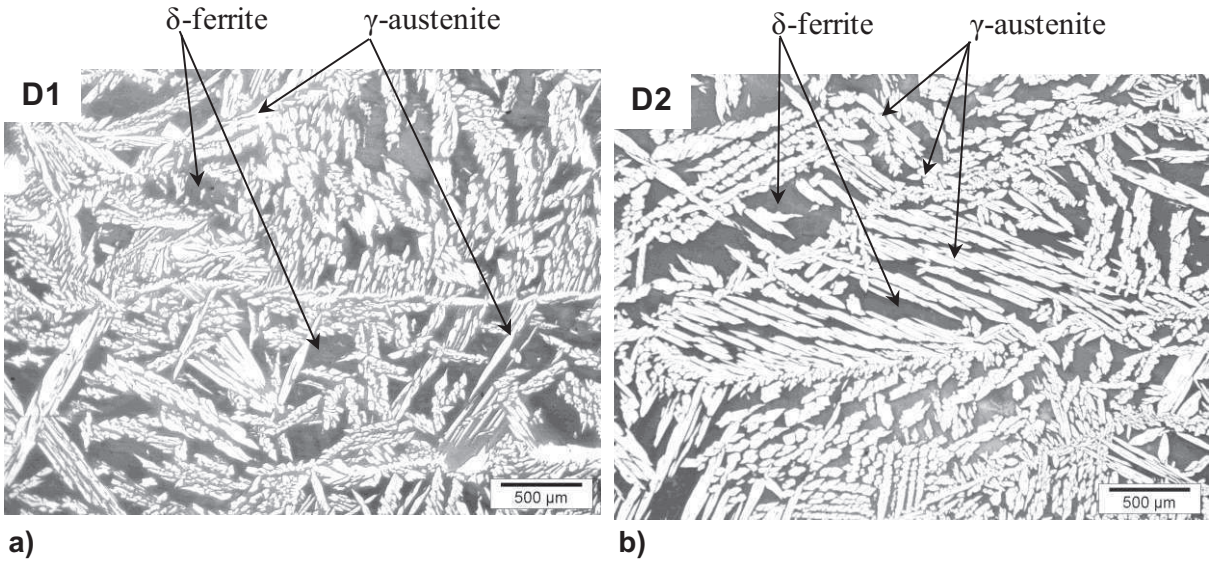


Figure I.6. Microstructures of the as-cast slabs; a) D1 grade; b) D2 grade; γ-austenite in white, δ-ferrite in grey.

I.2.3 Microstructures during hot rolling

I.2.3.1 The hot rolling process

An industrial hot rolling schedule used for standard duplex stainless steel sheets, i.e. type EN 1.4462 (D1) or 1.4362 is shown in Figure I.7.

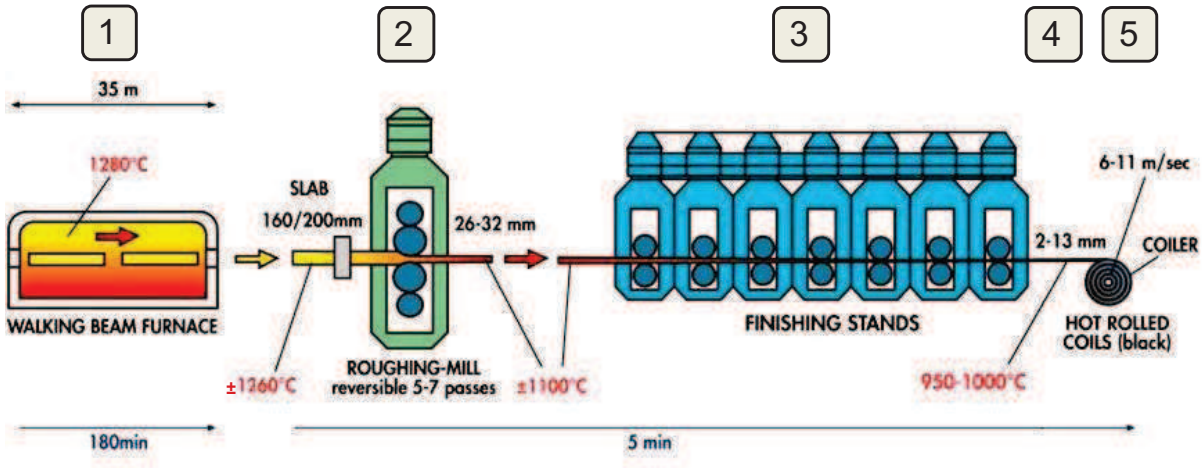


Figure I.7. Industrial hot rolling process; the number corresponds to the different steps and some details are given in the text below.

(1) Continuous cast slabs are first reheated to 1280°C and kept at this temperature. The duration of this stage is about 3h.

(2) The slabs are then rough rolled on a reversible mill in 5-7 rolling passes. With a very strong thickness reduction, i.e. from 200mm to 30mm thickness.

(3) The rough rolled sheets are then hot rolled on 7 consecutive finishing mills to the final thickness from 2 to 13mm. The temperature is around 800-1000°C at the end of the hot rolling process.

(4) Cooling of the sheet on a specific table.

(5) Coiling at a temperature between 500 and 800°C. The final length coil can measure more than 100m.

I.2.3.2 Microstructures after the roughing-mill operations

The as-cast slabs are then reheated before to be rolled at high temperature. The microstructures after the roughing-mill operations present an elongated austenite in the rolling direction, see Figure I.8.

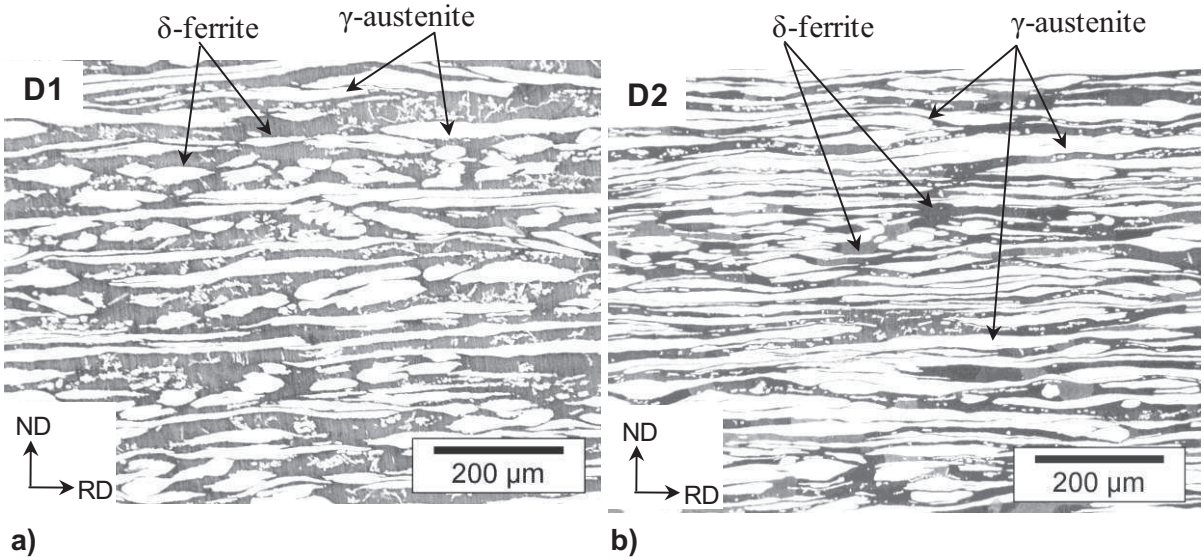


Figure I.8. Microstructures of the transfer bar, i.e. just after the roughing-mill operations; a) D1 grade; b) D2 grade; γ-austenite in white, δ-ferrite in grey.

I.2.3.3 Microstructures in the vicinity of the edges

As shown in Figure I.4 and in Figure I.9.a, the cracks are always observed along the edges of the hot rolled material hence the name “edge-cracks”. The first characterizations have revealed that damage nucleation always takes place at the δ/γ interphase boundaries, see Figure I.9.b. In addition, the cracks seem to always propagate within the ferrite. No damage nucleation site is visible in the austenite and the cracks never propagate through an austenite grain.

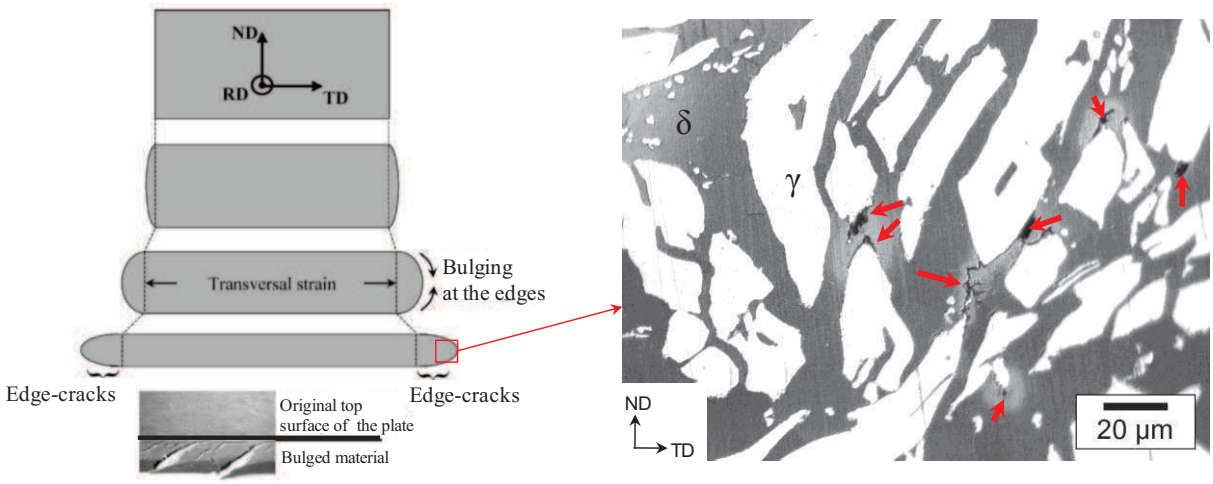


Figure I.9. a) Evolution of the transverse dimensions of the hot rolling blocks with increasing reduction; a clear transverse strain develops and cracks have been observed only in the bulged region; b) microstructure in the edge part illustrating the damage; red arrows emphasize the voids.

I.3 Guideline

The poor hot workability of duplex stainless steels increases dramatically the manufacturing cost and explains partly why the duplex stainless steel market is still limited. Thus, the purpose of this work is to understand the origin of the poor hot workability of these alloys and to suggest solutions to avoid or control the edge-cracking phenomenon.

First of all, the main factors affecting the hot workability of duplex stainless steels are reviewed in order to identify the key parameters and to point out what are the missing pieces of the “hot workability puzzle”. The review reveals that two “pieces” are missing in the “puzzle”. On the one hand, it is necessary to develop a new hot ductility test which allows discriminating microstructures in terms of high temperature tearing resistance, and on the other hand, quantitative data about the strain partitioning between ferrite and austenite during the hot working operations are needed. These two parts must allow suggesting possible remedies for the edge cracking phenomenon. Figure I.10 gives a summary of the approach followed throughout this work.

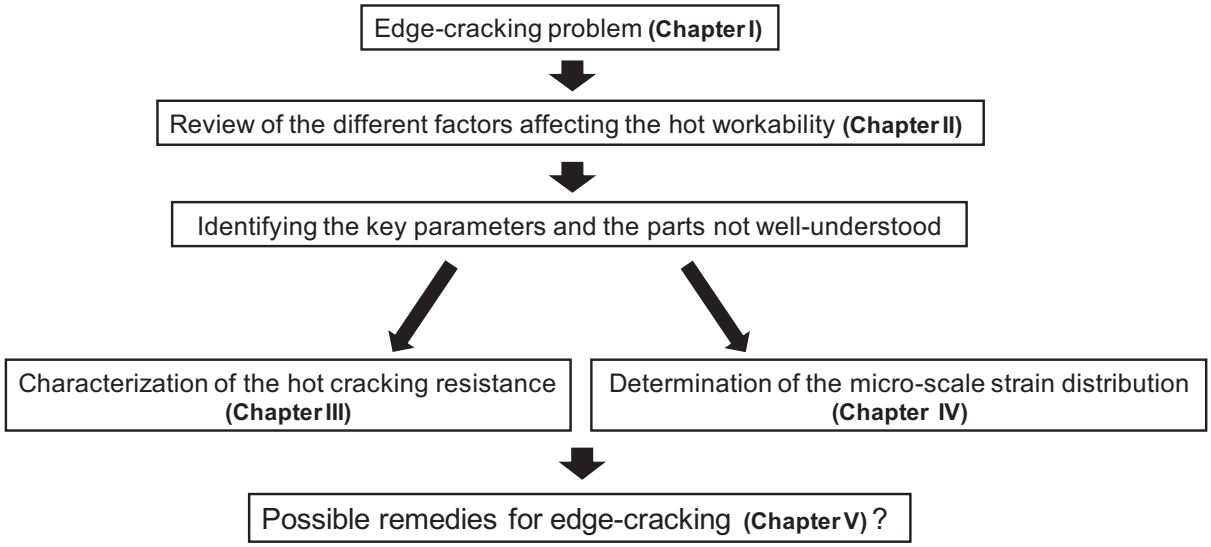


Figure I.10. Outline of the thesis. The bibliographical review permits to identify the missing pieces of the puzzle required to understand the hot workability problem. The first missing piece is the lack of a hot ductility test that quantifies the hot tearing resistance; as a consequence a new tool has been developed. The second missing piece deals with the quantification of the high temperature strain partitioning. This approach should permit to suggest some remedies for the edge-cracking problem.

Chapter II. State of the art regarding the hot working of duplex stainless steels

Chapter II. State of the art regarding the hot working of duplex stainless steels

Portevin [3] defined the hot workability as the ability of a metal to be shaped by plastic deformation at high temperature without appearance of defects like slivers[1] or edge cracks. It turns out that the hot workability depends in a complex manner on the material properties, and on the hot forming processes. Therefore, it is not fully relevant to separate the two contributions as suggested in [4]:

$$Hot\ \ workability = f_1(material) \times f_2(working\ \ process), \qquad \textbf{eq II-1}$$

where f_1 is a function of the intrinsic hot ductility of the material, and f_2 is a function of the external factors such as the state of stress and strain.

In the present chapter, the different metallurgical factors influencing the hot workability of duplex stainless steels are reviewed. In order to properly account for the interplay of factors depending on the material and on the process, respectively, the review is divided into three sections. The first section deals with microstructure evolutions occurring during the hot forming process. Mechanical aspects are treated next, starting with the plastic behaviour, followed by the analysis of damage. The review is based on the chapter entitled “Hot Workability” in Ref. [5], but it is adapted, completed and updated according to the specific topic of the present work. The purpose is to identify the key parameters affecting the hot deformation of duplex stainless steels and to point out the missing pieces of the puzzle in order to better understand the origin of damage during hot forming operations.

[1] Sliver: defect which can appear during hot working operations.

II.1 Microstructural evolution during hot working

II.1.1 As-cast microstructure

At the millimeter scale, the typical solidification macrostructure consists of three different zones through the slab thickness: a refined equiaxed grain region close to the chill surface, a columnar zone and a coarse equiaxed grain zone in the centre [6]. In general, DSS solidify to δ-ferrite. The as-cast microstructure consists of a ferritic matrix with two types of austenite inclusions: allotriomorphic austenite on the grain boundaries and Widmanstätten austenite laths inside the grains, see Figure II.1. This kind of solid-state phase transformation leads to a Kurdjumov-Sachs (K-S) or a Nishiyama-Wasserman (N-W) crystallographic orientation relationship between the new austenite and the parent ferrite [7-10]. These orientation relationships lead to semi-coherent interphase boundaries due to lattice plane correspondences:

- K-S: $\{110\}_\delta$ // $\{111\}_\gamma$ and $<1\text{-}11>_\delta$ // $<0\text{-}11>_\gamma$;
- N-W: $\{110\}_\delta$ // $\{111\}_\gamma$ and $<001>_\delta$ // $<\text{-}101>_\gamma$.

The allotriomorphic austenite at the ferrite grain boundaries corresponds to one of these orientation relationships with one of the adjacent ferrite grains, whereas the other interphase boundaries are incoherent [7].
The amount, morphology and size of the austenite depend on the thermal history: initial temperature and cooling rate. For instance, the thickness of Widmanstätten austenite laths depends on the cooling rate, the higher the cooling rate is, the thinner the austenite laths.

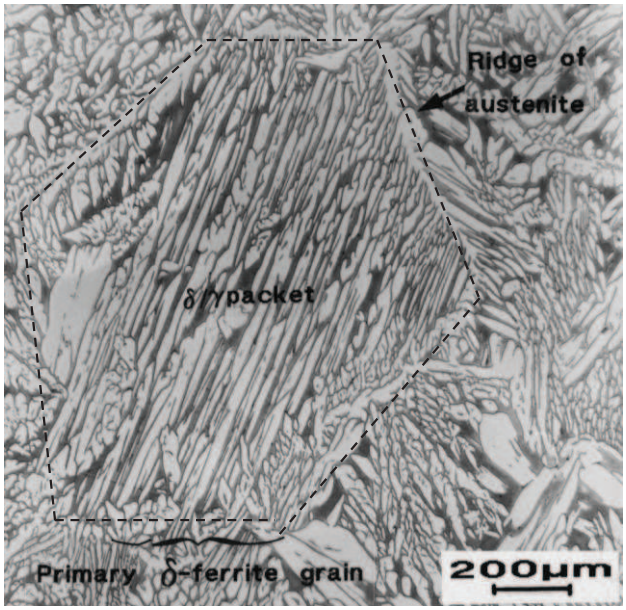


Figure II.1. As-cast microstructure in a conventional 2304 duplex stainless steel; the dotted lines indicate the primary δ-ferrite grain, allotriomorphic austenite decorates the primary δ-ferrite grain boundaries and Widmanstätten austenite appears inside the primary δ-ferrite grain [12].

When the as-cast material is reheated at high temperature before hot working, it is the as-cast microstructure which is relevant for the analysis of damage. This as-cast microstructure will evolve throughout the process (Figure II.2). For instance, as the rolling reduction increases, the austenite grains become more and more elongated in the rolling direction.

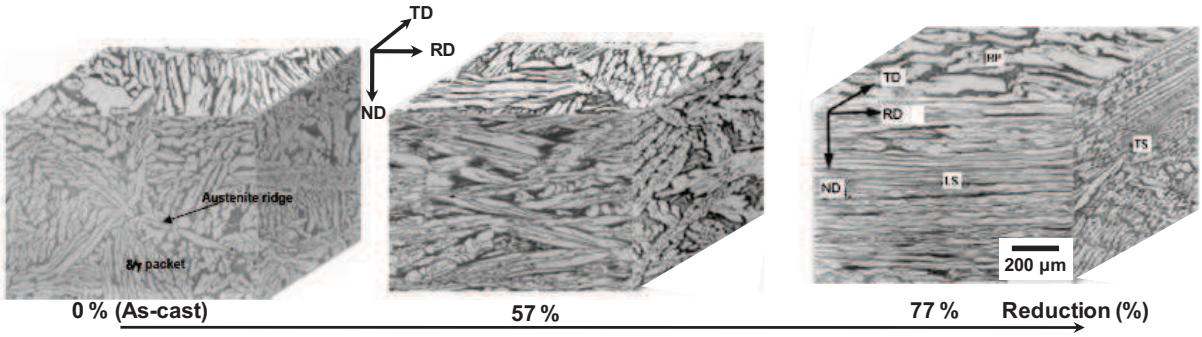


Figure II.2. Evolution in 3D of the as-cast microstructure with the applied rolling reduction of the duplex microstructure; as the deformation proceeds, austenite becomes more and more elongated in the rolling direction (RD) [11].

In the following sections, a particular attention is paid to the microstructural evolution throughout the hot working process.

II.1.2 Changes in morphology and distribution of the dispersed γ-austenite

Pinol-Juez et al. [12, 13] drew markers on specimens and then performed thermo-mechanical treatments. The microstructural observations of these specimens revealed several mechanisms which change the shape and distribution of the austenite. These mechanisms are listed in Figure II.3, some of them account for plastic deformation, whereas others are the result of strain partitioning among the phases, strain localization and thermally-induced microstructural evolution towards equilibrium.

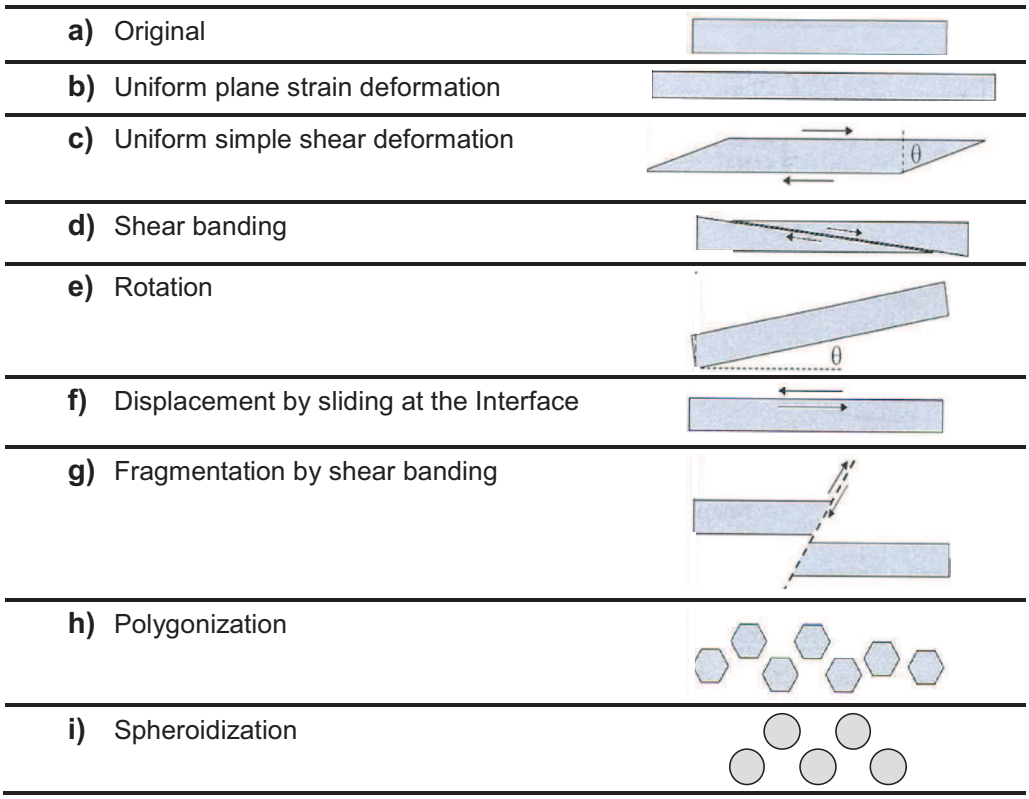


Figure II.3. Mechanisms acting on the dispersed phase that are responsible for the morphological and distribution changes undergone by the austenite during hot-working of austeno-ferritic stainless steels [5].

II.1.2.1 Interphase boundary sliding

Sliding involves the translation of a grain with respect to another parallel to a common boundary. Sliding has been identified in hot-worked, as-cast and hot rolled specimens by characterization after deformation of polished and marked specimens [12-14].

The SEM picture in Figure II.4 is a good illustration of this phenomenon. It shows that the microgrid lines are discontinuous along an austenite-ferrite interphase.

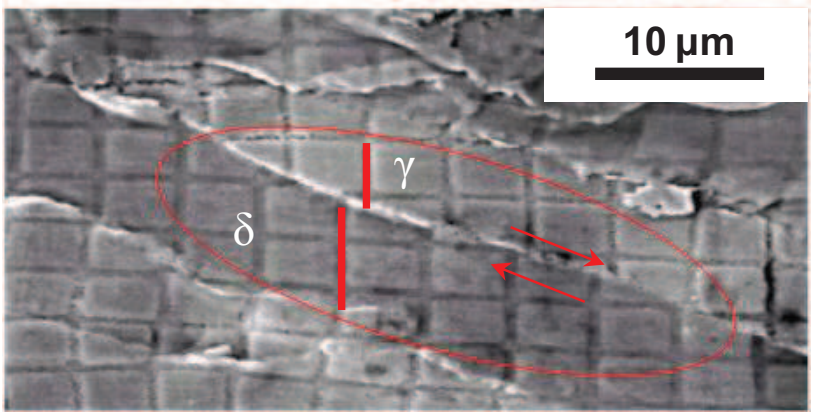


Figure II.4. A clear example of interphase boundary sliding in a 2205 duplex stainless steel deformed to 0.15 at 1050°C and $1s^{-1}$ [14].

The ability to slide depends on the character of the boundary: coherent and semi-coherent interfaces being less prone to sliding than incoherent interfaces. This applies also to hot-worked duplex stainless steels for which the crystallographic nature of the interface is a key parameter controlling the sliding ability [12]. Indeed, deformation applied to marked, as-cast and wrought specimens showed that sliding at the austenite-ferrite interface is not possible as long as the two phase orientations are related by a Kurdjumov-Sachs orientation relationship. In a Widmanstätten microstructure, the scratch markers are slightly deflected at each interphase boundary but do not lose continuity (Figure II.5.a). On the contrary, in a hot-rolled microstructure, such as the one seen in Figure II.5.b, the scratch markers reflect the occurrence of sliding: relative displacements of the markers may reach several micrometers at the interphase boundaries.

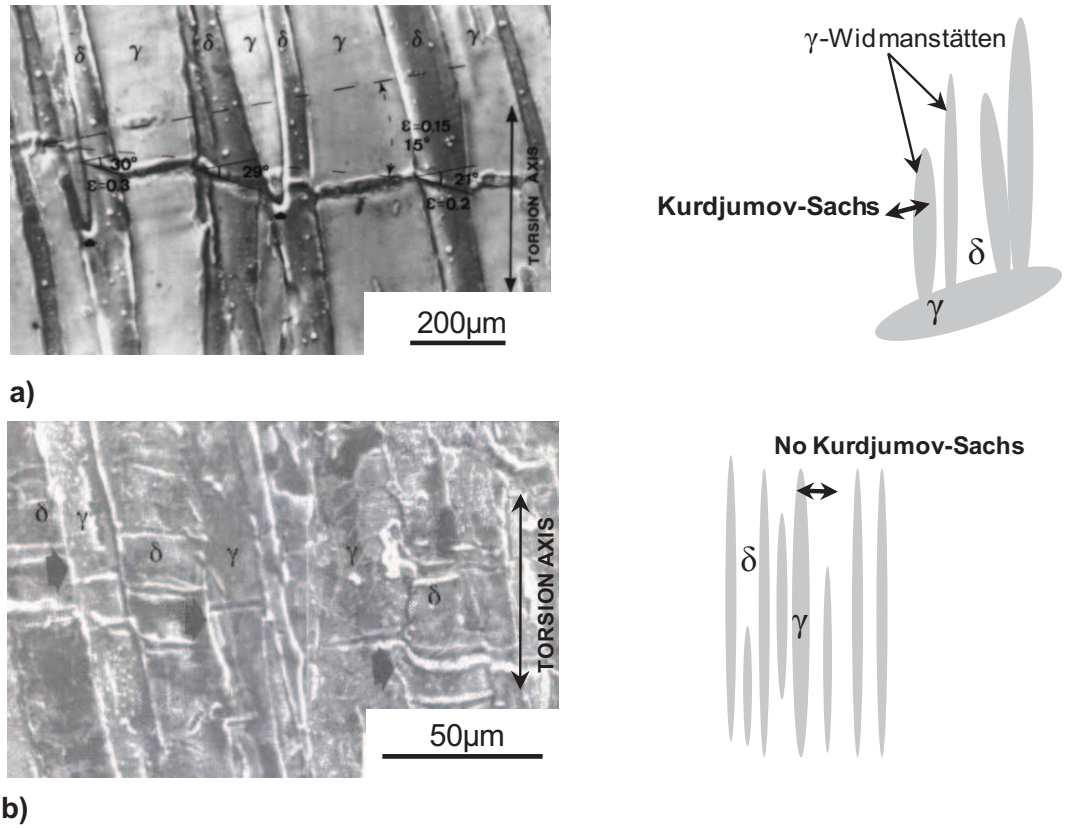


Figure II.5. SEM micrographs showing the surface of two marked specimens of a 2304 duplex stainless steel deformed to 0.17 under torsion at 1000°C and $1s^{-1}$; a) in the as-cast condition, δ is related to γ by a Kurdjumov-Sachs orientation relationship; b) in the hot-rolled condition (reduction 77%), no lattice correspondence between δ and γ [12].

II.1.2.2 Rotation

Independently from the lattice rotations occurring at the substructural scale due to constrained dislocation slip, marked specimens reveal rotations of the second-phase inclusions. The scratch markers in Figure II.6 clearly illustrate that the austenite in the middle of the picture has rotated within the ferrite matrix, which accommodates this through intense local shearing [13]. The mechanism of rotation appears when deforming an as-cast microstructure but is not very frequently observed.

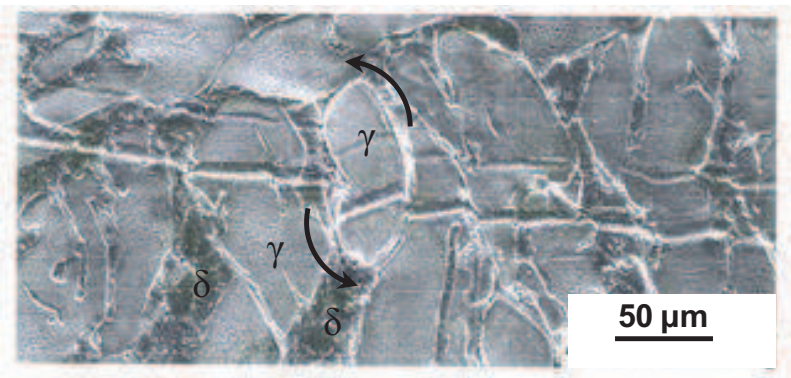


Figure II.6. SEM picture showing the rotation of an austenite grain highlighted by the displacement of the scratch markers at the specimen surface; as-cast 2304 duplex stainless steel deformed under torsion to 1.6 at 1000°C and $1s^{-1}$ [13].

II.1.2.3 Shear banding

Laboratory testing, modeling, and observation of industrially deformed duplex stainless steels have shown that these materials have a strong tendency to localize plastic deformation and that they develop shear bands. Finite element modeling applied to austenite-ferrite microstructures deformed under plane strain compression predicts the development of shear bands [15, 16]. Finite element simulations are in agreement with experimental observations (Figure II.7).

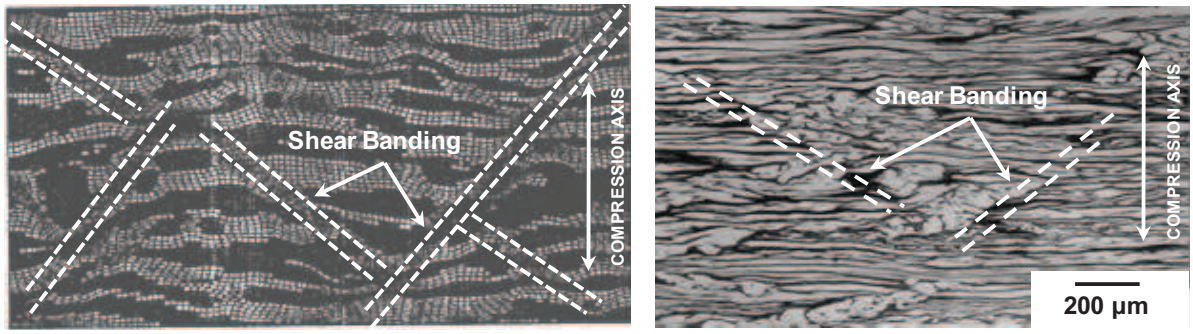


Figure II.7. Shear banding development in duplex stainless steel; a) deformed mesh obtained via finite element modeling after simulation of a specimen deformed at 1050°C under plane strain compression [16]; b) optical micrograph of a hot-rolled 2304 specimen (77% reduction) [9].

The application of the microgrid technique also revealed that shear banding takes place during plane strain compression at 850°C (see Figure II.8) of a duplex microstructure with an equiaxed austenite morphology [17-19]. The presence of two phases with highly contrasted mechanical strengths should be considered as the one of the main reasons for shear bands development. In addition, shear banding phenomenon is not limited to laboratory tests but it is also observed in industrial hot rolled materials [20].

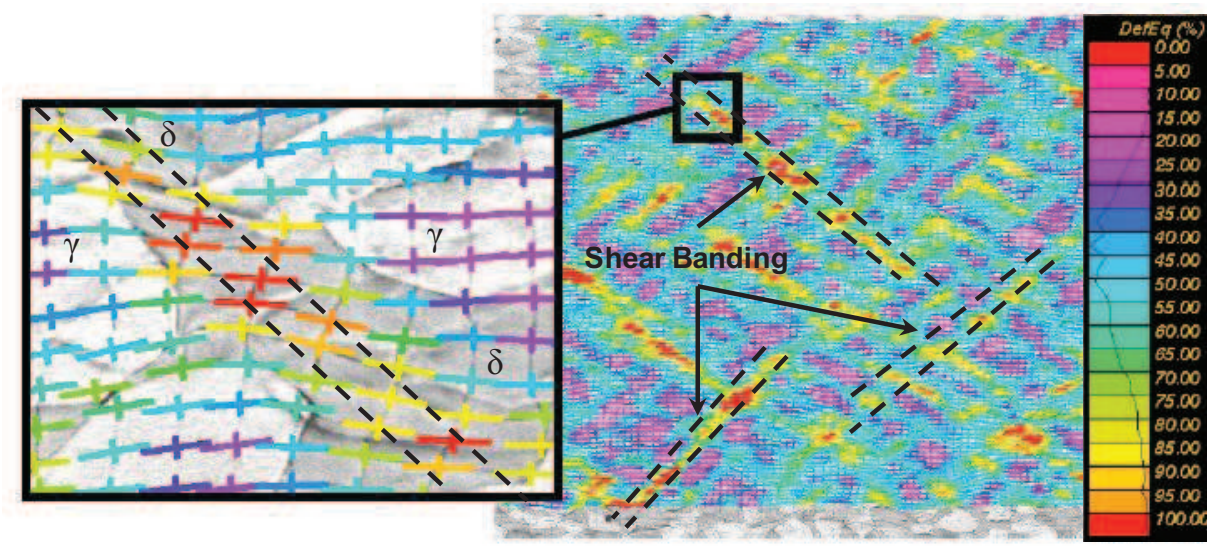


Figure II.8. Map of the Von Mises equivalent strain superimposed with the deformed microstructure revealing the development of localization bands under plane strain compression at 850°C and $1s^{-1}$ of a 29%Cr-11%Ni duplex stainless steel [17].

II.1.3 Plastic deformation

The microstructural evolution taking place during hot deformation within both phases in a duplex microstructure can significantly differ from the evolution observed in single-phase materials. This is because, in addition to their respective high (ferrite) and low (austenite) stacking fault energies, others factors, such as relative strength and morphology play a crucial role on strain partitioning.

Ferritic stainless steels undergo dynamic recovery, hence developing a well-defined subgrain microstructure that remains equiaxed and with a constant size once steady state is reached. In duplex microstructures, dynamic recovery is the primary softening mechanism in ferrite, see subgrains in Figure II.9. The ferrite substructure becomes more polygonized at higher deformations and low strain rates. However, the interphase boundary imposes some restrictions. As the strain increases, ferrite becomes partially enclosed between austenite stringers. The thickness of ferrite subregions decreases with increasing strain, until it becomes comparable with the ferrite subgrain size. This is quite an heterogeneous process that leads to a bamboo-type structure. Narrow bands of ferrite are limited laterally by the interphase boundaries and are subdivided by a succession of mixed low and high-angle ferrite-ferrite boundaries. The mechanism responsible for the formation of high-angle boundaries in the ferrite has been attributed to continuous dynamic recrystallization or extended recovery [21-24].

Due to their low stacking fault energy, austenitic stainless steels undergo significant work hardening before the onset of dynamic recrystallization at hot working temperatures. In duplex stainless steels, microstructural observations have shown that, even at high strains and after very long annealing, recrystallization is rarely observed. In addition, when it is observed, it involves negligible volume fractions [5, 23, 24]. In fact, when deforming a duplex microstructure around 1000°C, the austenite remains structureless.

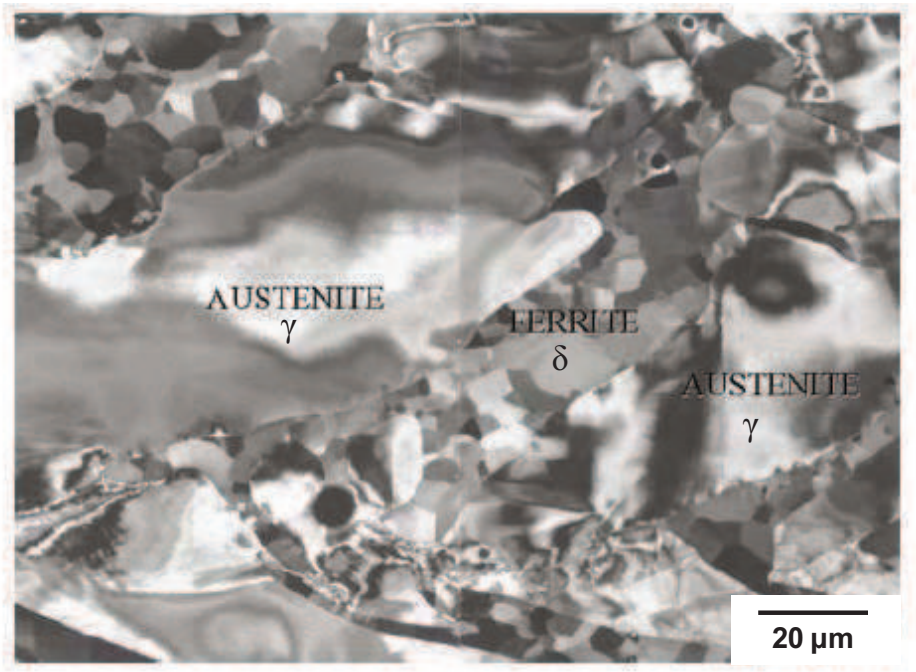


Figure II.9. SEM backscattered electron picture; as-cast 2304 duplex stainless steel deformed to 0.4 at 1000°C and $1s^{-1}$ [9].

The development of high-angle boundaries in the ferrite implies lattice rotations that significantly change the character of the ferrite-austenite interphase boundaries, as illustrated in Figure II.10. The channeling contrast image shows a ferrite unit located between two austenite grains. The central part of the ferrite region maintains the K-S orientation relationship within a deviation of 3-6° with respect to the austenite at each side. Other subgrains in the ferrite have lost their semi-coherent character and random interphase boundaries have developed.

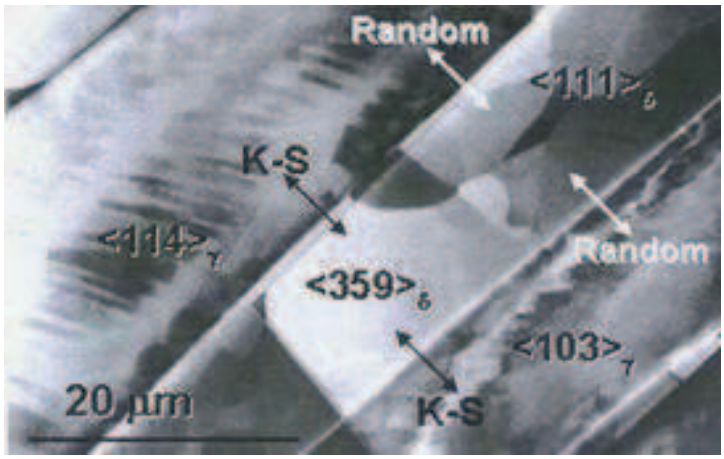


Figure II.10. STEM channeling picture and crystallographic orientation analysis; as-cast duplex stainless steel deformed to 1.6 at 1000°C and $1s^{-1}$ [5].

II.2 Mechanical behaviour during hot working

II.2.1 Viscoplastic hardening laws: influence of temperature and strain rate

Any attempt aimed at producing models applicable to hot working requires constitutive equations relating the flow stress to deformation conditions (temperature, strain and strain rate) and taking account of the chemical composition and the microstructure evolution too. Very often only the steady state flow stress is expressed as a function of the strain rate and temperature. Investigation and modeling efforts devoted to stainless steels have mainly concentrated on austenitic grades. Quantitative data concerning ferritic and duplex steels are much scarcer. In addition, the usual difficulties involved with single-phase materials, the case of austenite-ferrite microstructures introduces supplementary complications. New problems arise due to the presence of two phases with different mechanical behaviours and with a wide range of possible microstructural arrangements (see the previous section II.1 entitled Microstructural evolution during hot-working). The effect of temperature and strain rate on the stress required to deform the material may be estimated based on the following equation:

$$\dot{\varepsilon}\exp\left(\frac{Q_{HW}}{RT}\right) = A[\sinh(\alpha\sigma_{ss})]^n, \qquad \text{eq II-2}$$

where $\dot{\varepsilon}$ is the strain rate, σ_{ss} is the steady stress, Q_{HW} is the hot working activation energy and, α, A and n are constant parameters obtained from hot deformation tests.

The values reported by different authors for the coefficients in this equation are summarized in Table II.1.

The influence of both variables (temperature and strain rate) is very important because, under any deformation mode, they are the two factors which can be modified in order to improve the hot ductility.

Ref	n	α	A (s)	Q_{HW} (kJ/mol)	Material	Deformation Mode
[25]	4.2	0.0139	$7.12\ 10^{16}$	450	2304, 77% hot rolled	Plane Strain Compression
	4	0.0143	$6.2\ 10^{21}$	578		Torsion
[26]	3.85	0.008	$3.54\ 10^{14}$	380	2205, as-cast	Plane Strain Compression
[27]	6.9	0.009	$1.5\ 10^{22}$	569	2205, bar	Uni-axial Compression
	4	0.007	$2.3\ 10^{16}$	438	2507, bar	
[28]	3.75			425	2205, 80% hot rolled	Torsion
[29]	5.63	0.012	$1.0\ 10^{20}$	525	2304, hot rolled	Torsion
	3.8	0.012	$1.0\ 10^{15}$	394	2205, hot rolled	
[30]	4.18	0.01	$3.95\ 10^{15}$	400	27.6Cr-4.25Ni-1.3Mo-0.14N, bar	Torsion
[31]	3.77	0.0115	$2.68\ 10^{16}$	447	2507, bar	Torsion
[32]				380	2205, hot rolled	Torsion
				360		Tension
[33]	4.07	0.015	$2.04\ 10^{19}$	488	26.5Cr-4.9Ni-1.63Mo-0.04N	Torsion
[34]	4.9	0.014	$8.1\ 10^{14}$	430	2205, bar	Tension
[35]	4.2	0.012	$2.0\ 10^{16}$	432	2205, hot rolled	Uni-axial Compression
	3.64	0.0103	$6.32\ 10^{12}$	310	Ferritic with duplex ferrite composition	
	4.57	0.0066	$1.44\ 10^{15}$	454	Austenitic with duplex austenite composition	
[36]	5.1	0.012	$2.14\ 10^{21}$	479	2205, hot rolled	Uni-axial Compression
[37]	2.6	0.012	$2.7\ 10^{10}$	263	2304, hot rolled	Uni-axial Compression
[38]	4	0.012		474	2205, hot rolled	Torsion
[39]*	5.8	0.0091	$3.19\ 10^{15}$	450	Austenitic 304	Plane Strain Compression
[40]*	3.1	0.0115		261	Ferritic	Plane Strain Compression

Table II.1. Values reported by different authors for the parameters of the constitutive equations. *More data in [41].

II.2.2 Influence of the chemical composition

Changes in composition impact the hot mechanical behaviour of duplex stainless steels:

- Volume fraction of the two phases depends on the amount of austenite stabilizers (C, N, Ni, Mn) and ferritic stabilizers (Cr, Mo, Si).
- The hot strength of both austenitic and ferritic stainless steels is modified through solute strengthening. In case of duplex steels, chemical composition also contributes to the high temperature strength of austenite-ferrite microstructures in a more complex way because of element partitioning.

In this section, the influence of the phase balance and the influence of the composition in the main alloying elements on the hot mechanical behaviour of duplex stainless steels are successively addressed. The influence of the minor elements will be discussed later in section II.3.

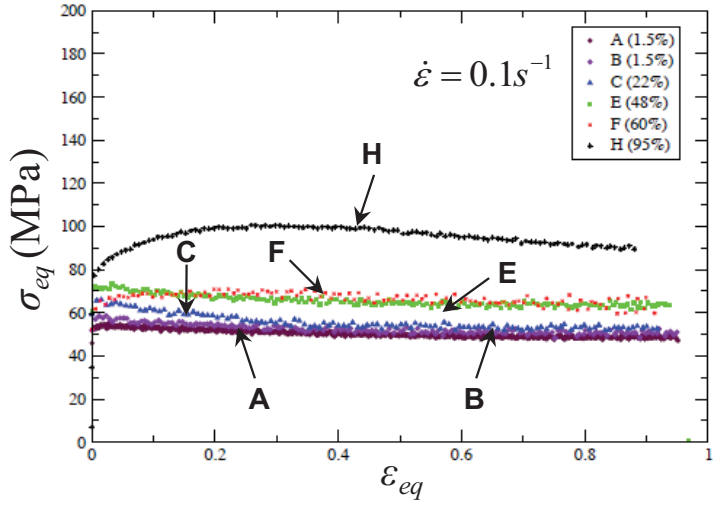
II.2.2.1 Volume fraction of phases

Rupin et al. [42] have investigated the influence of the δ/γ-phase ratio on the flow properties of duplex stainless steels. Duplex steels were cast with various chemical compositions (Table II.2) leading to different phase balances. The different duplex alloys were hot rolled and then hot deformed under plane strain compression at 1050°C at different strain rates (0.1, 1 and 10 s^{-1}).

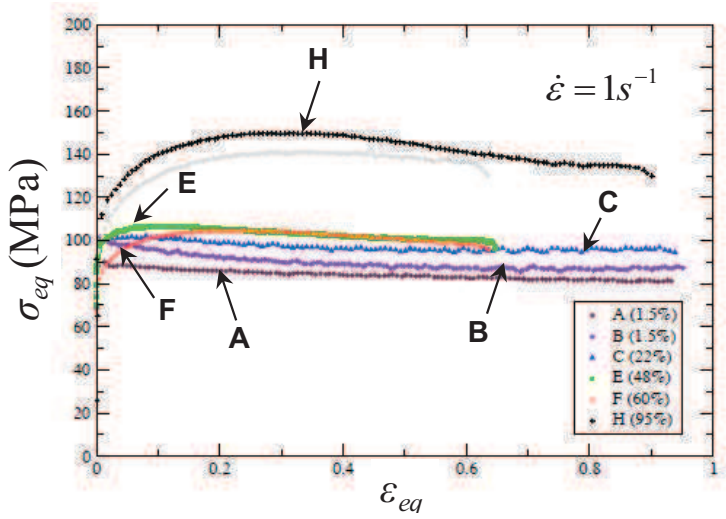
Designation	%γ	Ni (wt%)	Cr (wt%)	Fe (wt%)
A	1.5	7.5	33.5	59
B	1.5	8.3	33.2	58.5
C	22	9.6	30.4	60
E	48	10.8	27	62.2
F	60	11.8	25.4	62.8
H	95	13.6	25.1	61.3

Table II.2. Chemical composition of the different duplex stainless steels alloys elaborated and characterized in [42].

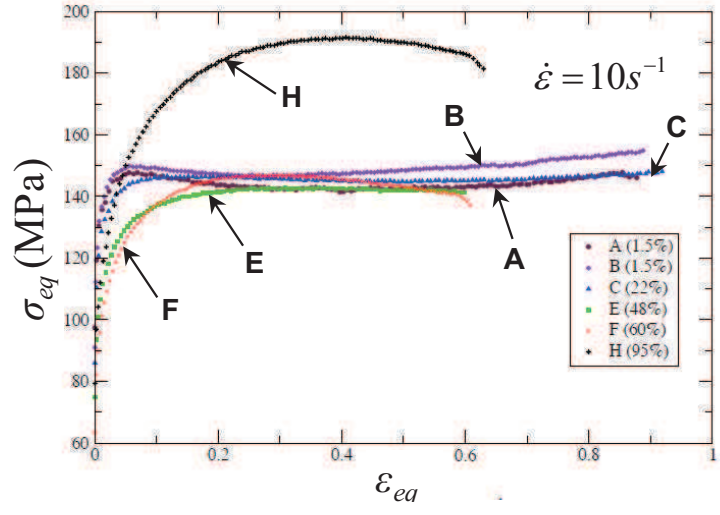
At high strain rate, pure austenite exhibits a lower yield stress compared to pure ferrite, see Figure II.11.c. Nevertheless, in the testing conditions presented in Figure II.11, the flow stress of the austenitic alloy becomes higher than the flow stress of the ferritic alloy after a few percents of plastic deformation due to a pronounced work-hardening stage. Furthermore, it must be highlighted that the steady state stress of the duplex materials converge towards the steady state stress of the pure ferritic alloy, thus confirming the significant influence of the ferritic phase on the hot mechanical behaviour of the duplex alloys.



a)



b)



c)

Figure II.11. Equivalent flow stress strain curves of different duplex stainless steels deformed under plane strain compression at 1050°C and at different strain rates; a) $0.1s^{-1}$; b) $1s^{-1}$; $10s^{-1}$. The value between the parenthesis gives the austenite content [42].

II.2.2.2 Influence of alloying elements and element partitioning

II.2.2.2.1 Influence of N

Tendo et al. [43] analyzed the effect of nitrogen (N) on the hot strength of austenitic stainless steels, concluding that N contributes to the high temperature strength by about 25 MPa by 0.1% of N in a 18% Cr 9% Ni alloy. Other investigations at the laboratory scale confirmed this effect on AISI 304 and 316 steels, the solid solution hardening at hot working temperatures is between 16 and 20 MPa per 0.1%N [44].

The influence of N on the hot strength of duplex stainless steels was evaluated at 27 MPa for each addition of 0.1%N [45]. This effect can be attributed, on the one hand, to the increasing volume fraction of austenite (N is a strong austenite stabilizer) and, on the other hand, to the strong solution strengthening effect of N.

II.2.2.2.2 Influence of Mo

The solid solution hardening is about 10MPa per 1% Mo for a 18Cr 14Ni 0-3%Mo [4]. According to [4], other authors obtained the same value by comparing the austenitic alloy 316 with the alloy 304.

In ferritic stainless steels, the addition of about 0.9% of Mo increases the strength between 10 and 20 MPa [41].

II.2.2.2.3 Element partitioning

In duplex steels, partitioning of elements between ferrite and austenite takes place and contributes to the difference of hot strength between ferrite and austenite. This means that some alloying elements can dissolve preferentially in one phase compared to the other, depending on the nature of the considered chemical element: austenite or ferrite stabilizer. The partitioning coefficient (X^i_δ/X^i_γ) between ferrite and austenite of several alloying elements is shown in Figure II.12 as a function of the temperature. Equilibrium conditions are assumed for a 2205 duplex stainless steel. At both extremes, Mo is the element that segregates most to ferrite, whereas C and N tend to leave ferrite. The high N content in the austenite and its important solute strengthening effect tends to increase the hot strength of austenite. The partitioning changes with temperature. As a consequence the hot deformation behaviour of duplex steels can be different at the beginning and at the end of the hot rolling process. The higher the temperature, the more uniform the element partitioning is between ferrite and austenite.

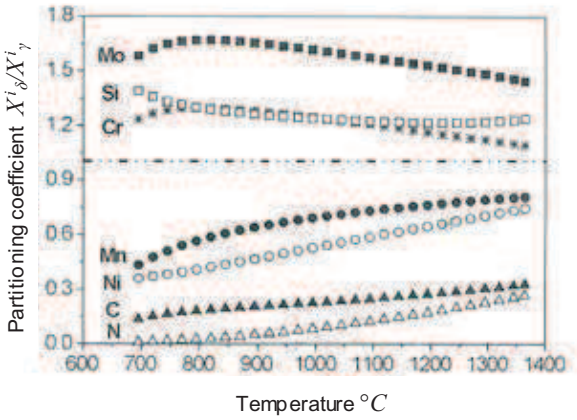
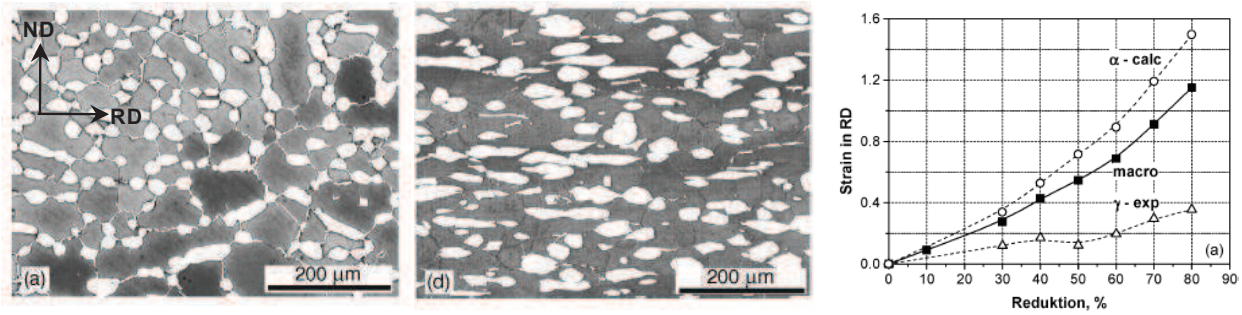


Figure II.12. The partitioning coefficient of the alloying elements between δ-ferrite and γ-austenite as a function of temperature; the compositional changes will influence the strength and the deformation behaviour of the material [46].

II.2.3 Strain partitioning

Some examples taken from different authors suggest the occurrence of strain partitioning in the hot-worked duplex microstructures. Evidence of strain partitioning can be found in the micrograph in Figure II.9, which represents as-cast steel after hot deformation [9]. Ferrite shows a well-developed sub-grain microstructure whereas austenite seems to be structureless. In others words, it means that the ferrite softens quickly while the austenite becomes harder. The difficulty is to quantify the high temperature strain partitioning in duplex stainless steels. Several authors have already attempted to estimate the high-temperature strain distribution in duplex stainless steels.

Al-Jouni and Sellars [47], and more recently Duprez et al. [48] have used the Unckel method [49] to estimate the strain partitioning. The Unckel method consists in estimating the strain differences between the constituent phases by measuring the dimensions of the phases before and after deformation. The partitioning is deduced from the assumption that the total strain is achieved collectively. The results reveal that the strain partitioning increases with deformation. For example, for a 80% reduction, the ratio between the average strain of the ferrite over the average strain of the austenite, $\bar{\varepsilon}_\delta / \bar{\varepsilon}_\gamma$ can increase to a value larger than 3 (Figure II.13.c).



a) **b)** **c)**

Figure II.13. Microstructure evolution during hot rolling at 1250°C for reduction a) 0% and b) 80%. Initially austenite equiaxed islands are embedded in a ferrite matrix. During hot rolling, these islands become more elongated in the rolling direction. c) Strain partitioning in the rolling direction, austenite seems to accommodate only a fraction of the applied strain [48].

Although the Unckel method provides quantitative information about the strain partitioning between ferrite and austenite in a duplex stainless steel, this method turns out to be rather inaccurate as it cannot account for shear strains. In addition, the results give only an average strain value per phase and do not detect possible localization of the deformation.

Important experimental progresses have been made by Pinna et al. [14] in order to perform accurate measurement of the high temperature micro-scale strain distribution in duplex stainless steels. Pinna et al. [14] adapted the microgrids technique to simulate experimentally the local state of deformation and to map the strain in a 2205 industrial grade duplex stainless steel. Hernandez-Castillo [19, 50] and Boldetti [18] have applied this method to laboratory austenite-ferrite microstructure. The analysis permits on the one hand to map the deformation and on the other hand to quantify the average strain per phase at high temperature.

An example [19] of a strain map obtained at 950°C with the modified microgrid method is given Figure II.14. The strain map showed that deformation is localized at the vicinity of the δ/γ interfaces.

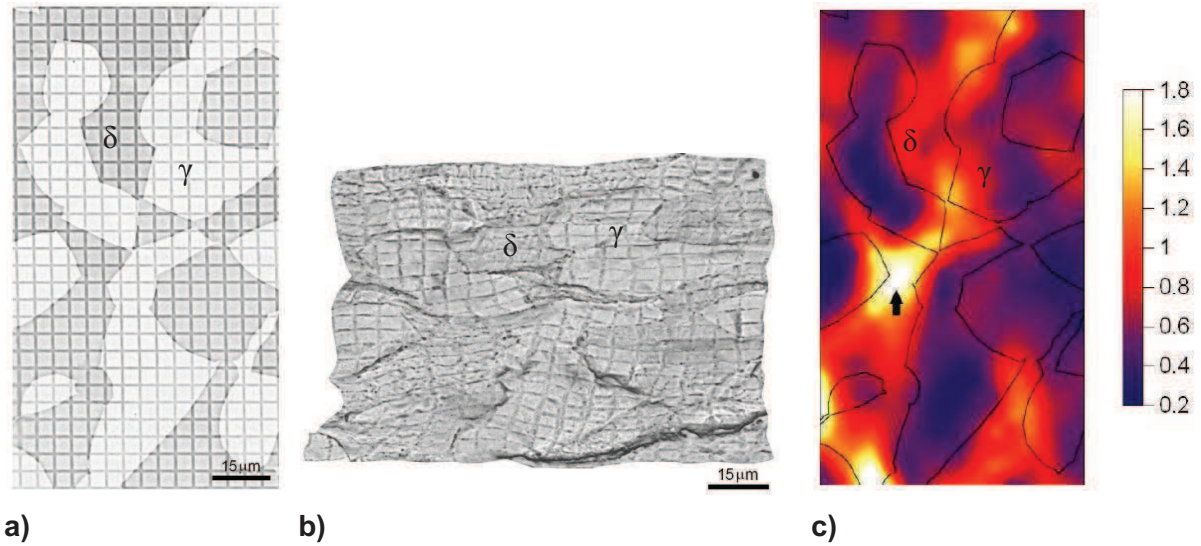


Figure II.14. Highlighting of strain partitioning via the microgrid technique in a laboratory 29.6%Cr-11.6%Ni-0.27%Mn duplex steel deformed at 950°C and $1s^{-1}$; a) undeformed state of a relatively small area; b) deformed configuration of the same area; c) distribution of the Green-Lagrange equivalent Von Mises strain [19].

The development of the modified microgrid technique could be a good way to provide quantitative data about strain partitioning at high temperature. However, up to now, only a few results are available and only small areas were analyzed (3-4 grains). In addition, the available results were most of the time obtained on model ferrite-austenite microstructures. The lack of quantitative data concerning more realistic alloys and the influence of different parameters on the strain partitioning (temperature, phase morphology…) is clear.

In order to fully understand the mechanical behaviour of duplex stainless steels, an essential piece of the puzzle is missing: the rheology of both ferrite and austenite, i.e. the stress-strain behaviour of the single phases. Duprez et al. [48] have intended to determine the rheology of each phase in a duplex steel. The authors have measured accurately the composition of the ferrite and the austenite in a commercial 2205 duplex stainless steel. Then, they have elaborated single-phase alloys with, respectively, the composition of the austenite and the ferrite. Finally, specimens from each alloy were deformed under hot torsion at 1200°C. The stress strain curve revealed a large difference of yield stress and flow stress between the ferrite and the austenite, which resulted in an austenite-ferrite steady stress ratio $(\sigma^{\gamma}/\sigma^{\delta})_{steady\ state} \approx 3.5$ (Figure II.15). Nevertheless, this method presents a few disadvantages. First of all, this method is very time consuming. Indeed, as the composition and the phase ratio evolve with temperature, a different casting is required for each temperature and for each phase. In addition, such method gives the rheology of each phase at different temperatures but it does not take into account the possible interaction between both phases.

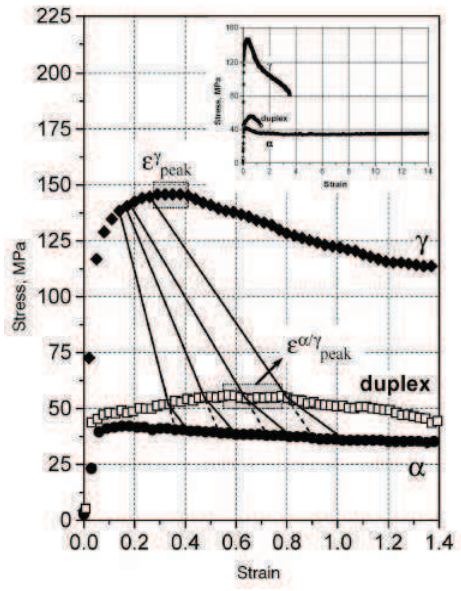


Figure II.15. Results of the hot torsion test performed at 1200°C and $1s^{-1}$ for a single ferritic, a single austenitic and a duplex stainless steel [48].

II.2.4 Influence of the deformation mode

Estimating the influence of the deformation mode consists in comparing, for a given microstructure, the Von Mises flow stress strain curves under two different mechanical solicitations. The equivalent stress strain curves of duplex microstructures fall between those corresponding to ferritic and austenitic stainless steels, but their shape and the stress levels depend on the deformation mode, as shown in Figure II.16. The flow curves of two different microstructures (as-cast and hot-rolled) belonging to the same 2304 duplex stainless steel obtained under plane strain compression and pure shear at 1000°C and $1s^{-1}$ are presented in Figure II.16 [25]. The stress strain curves of the as-cast and of the hot rolled microstructures are quite similar when obtained under plane strain compression. On the contrary, the shape of the flow stress strain curves and the stress levels of as-cast and hot rolled material are significantly different in the case of pure shear and differ from plane strain compression curves. This is attributed to the orientation of the austenite grains in relation with the loading direction.

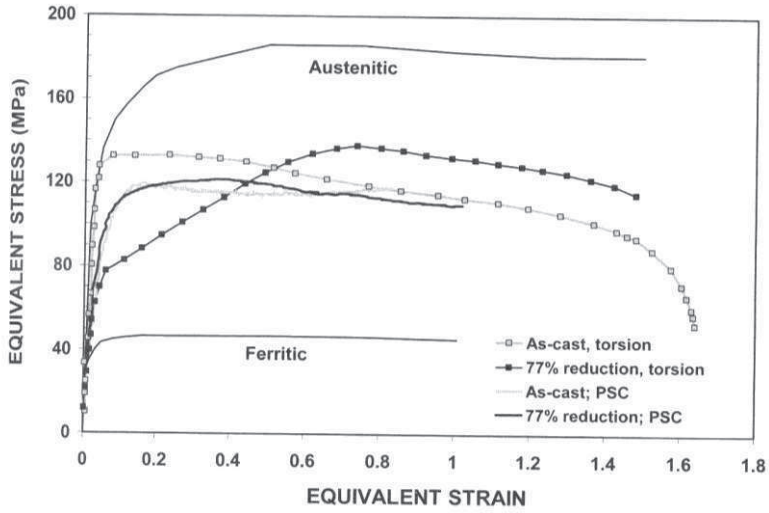


Figure II.16. Effect on the equivalent stress strain curves of the deformation mode for a 2304 duplex stainless steel deformed at 1000°C and $1s^{-1}$ under torsion and plane strain compression [25].

II.2.5 Influence of the phase morphology

The influence of the phase morphology on the hot mechanical behaviour has been studied by different authors. However, contradictory results are reported.

Vernusse et al. [51] performed hot uni-axial compression tests on the same duplex grade with different microstructures. The authors have taken care that the different microstructures presented the same volume fraction at the temperature of the hot mechanical test. The results showed that there is no significant influence of the phase morphology, and the similarity between the curves increases with increasing temperature, see Figure II.17.

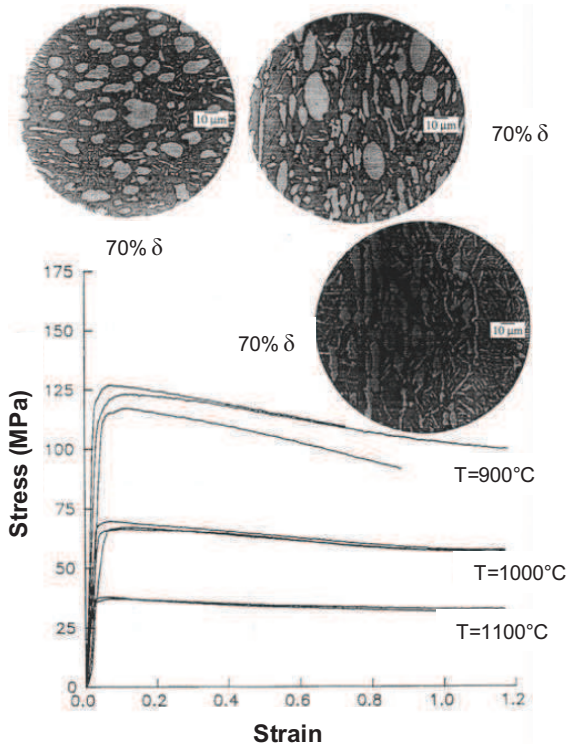


Figure II.17. Influence of the phase morphology on the flow stress of duplex stainless steel with 70% δ deformed under uniaxial compression at different temperature at a strain rate of 0.03s^{-1} [51].

Contradictory results were obtained by Pinol-Juez et al. [11]. Indeed, in order to investigate more deeply the possible effect of the phase morphology on the hot mechanical behaviour of duplex stainless steels, the authors tested various microstructures with different austenite morphologies under hot torsion conditions. Some samples involved an elongated austenite in a ferrite matrix, microstructure resulting from the hot rolling of an as-cast microstructure. Microstructures with elongated austenite aligned parallel and perpendicular to the torsion axis, and microstructures showing a Widmanstätten austenite (as-cast material, see Figure II.1) or an equiaxed austenite were tested at 1000°C. The results are summarized in Figure II.18. The main differences are observed on the stress strain curve shape and the stress levels reached. The curves of the differently oriented austenite (parallel and perpendicularly) with respect to the torsion axis and the samples with an equiaxed austenite have the first part of the curve which overlap. After this, the curve corresponding to the sample with the elongated grains oriented parallel to the torsion axis exhibits a strong work-hardening stage compared to the sample with the grains oriented perpendicular to the torsion axis.

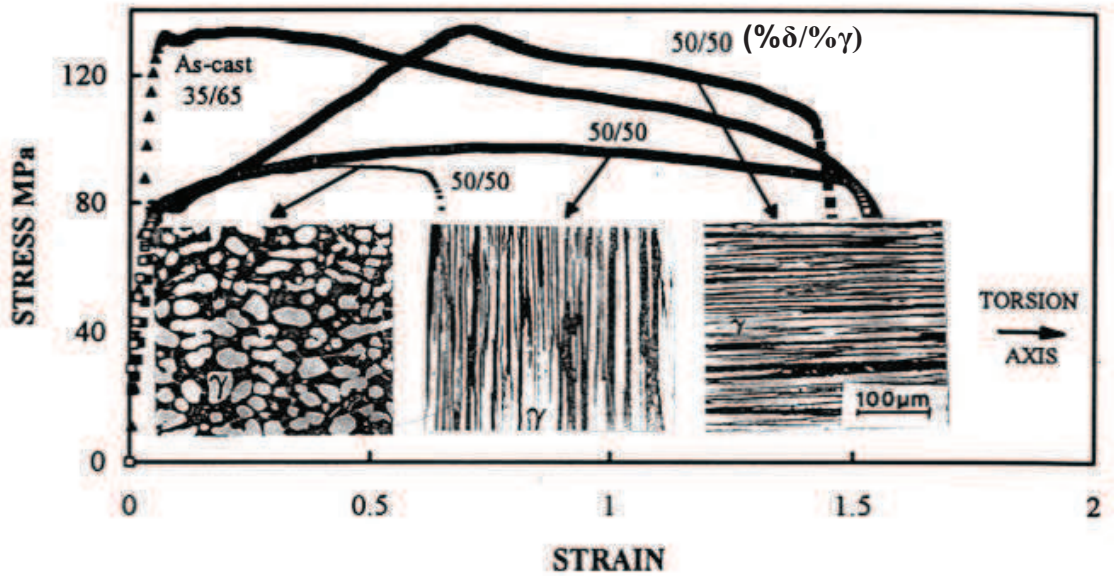


Figure II.18. Influence of the phase morphology and phase orientation on the flow stress of a 2304 duplex stainless steel deformed under torsion at 1000°C at a strain rate of $1s^{-1}$ [11].

II.3 Damage during hot working

The ability of a material to be hot-worked without cracking phenomena depends on both the intrinsic ductility and the process itself. The strain to fracture or the reduction in area, respectively from torsion or tension laboratory tests are approximately equivalent parameters that quantify the material ductility. Such analysis allows systematic studies that are relatively easy to perform in the laboratory and provide valuable information although purely macroscopic. However, this only partially addresses the complexity of the hot workability problem.

In addition to heterogeneities in microstructure and in composition inherited from the casting, local conditions during industrial hot working can have a dramatic effect on the hot workability.

In this section, only the factors directly related to crack formation during hot forming process will be addressed.

II.3.1 Influence of the chemical composition

In the chemical composition of duplex steel, it is possible to distinguish the major elements (Cr, Ni, Mo, Mn, N), i.e. those which control the phase balance as well as the rheology of the phases from the minor elements which are responsible for inclusions or segregations (S, O, Al, Ca…). The effect of the major elements and minor elements are successively discussed in this section.

II.3.1.1 Influence of the major elements

II.3.1.1.1 Fraction of phases

Several authors showed that the ductility reaches a minimum for a certain fraction of ferrite at about 0.30-0.60. Muller [52] reviewed the strain to fracture of several stainless steels at different temperatures. These results were completed by Iza-Mendia et al. [20]. The data in Figure II.19 show that, for stainless steels deformed between 900 and 1200°C, the strain to fracture is affected by the presence of a second phase. The ductility of a duplex stainless steel is significantly lower than that of a pure ferritic steel and is slightly lower than that of a purely austenitic steel. The reduction in the volume fraction of ferrite has a higher negative effect on hot ductility than reducing the testing temperature, but given that the ferrite content runs parallel with temperature, the two contributions cannot be easily separated. As a result, alloying elements play a crucial role in the phase proportion following their ferritic (Cr, Mo, Si) or austenitic (C, N, Ni, Mn) stabilizing nature.

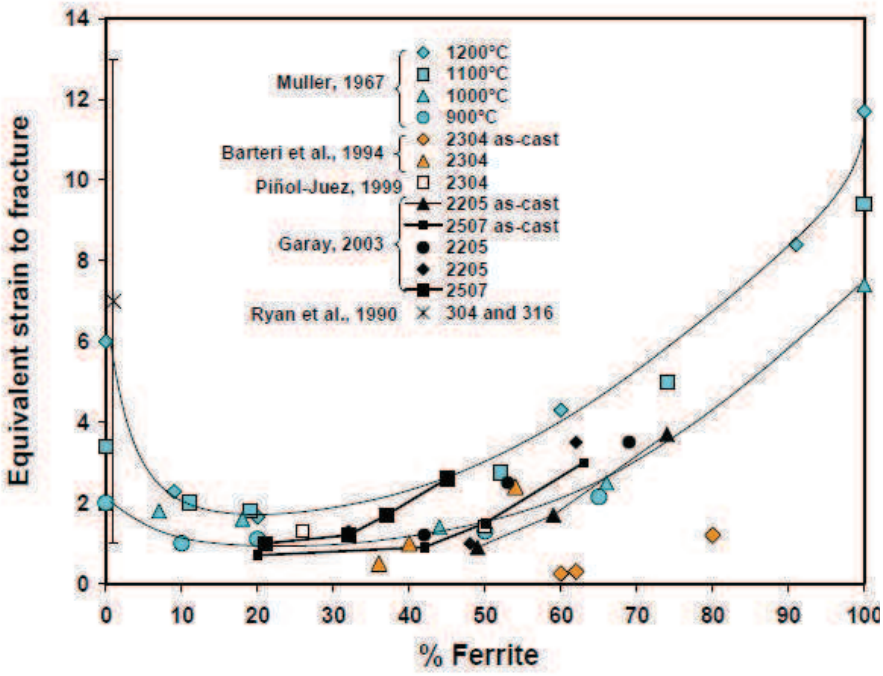


Figure II.19. Effect of the volume fraction of ferrite and temperature deformation on the strain to fracture for different duplex stainless steels [20].

To summarize, duplex stainless steels generally present a relatively poor hot ductility. Nevertheless, significant improvements in terms of hot ductility can be reached in the presence of micro-duplex microstructures which are known to exhibit super-plastic behaviour [53-58]. Unfortunately, the generation of a micro-duplex microstructure requires operations which are not suitable during the conventional hot processing of duplex stainless steels.

II.3.1.1.2 Influence of N

Liou et al. investigated the influence of N on the hot workability [59]. The results showed that the extent of edge cracking of DSS tends to increase with increasing N content (Figure II.20). In the same paper, the dependence of edge crack length (estimated by measuring the ten longest edge cracks) on the alloying elements in 2205 steel was expressed with the help of an empirical fracture index based on the alloy composition (CSI: Crack Sensitivity Index):

$$CSI = 45{,}2\%C + 18{,}3\%N + Mo + Cu + 0{,}65\%Ni - 297\%B - 0{,}14\%Cr - 0{,}7\%Mn \qquad \textbf{eq II-3}$$

with all the elements concentrations in weight percent. When the value of CSI is higher than 5.5, the steel is susceptible to develop edge cracks.

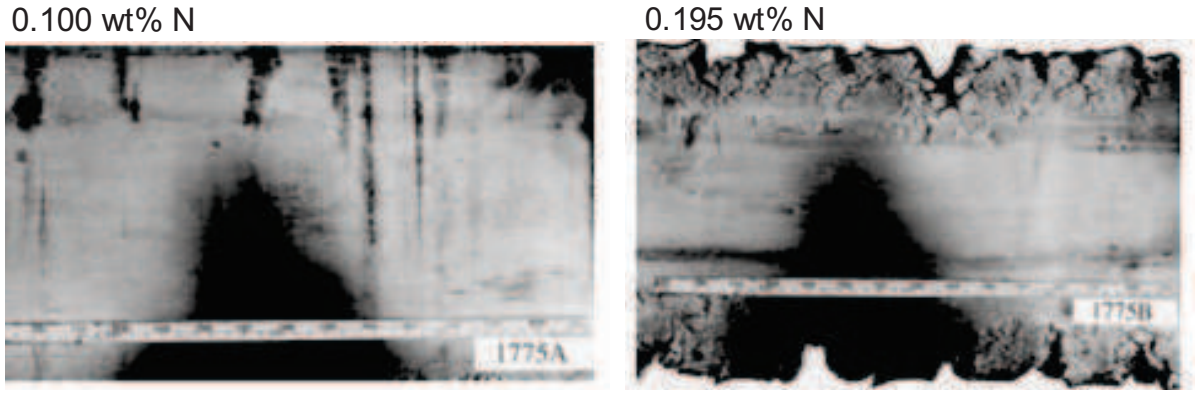


Figure II.20. Influence of N content on the hot workability of a 2205 duplex stainless steel; the level of edge cracking increases with the N content; a) 0.100 wt %N, CSI = 5.9; b) 0.195 wt %N, CSI = 7.7 [59].

II.3.1.2 Influence of the minor elements

Impurities and trace elements can seriously deteriorate the hot workability of duplex stainless steels. Segregations can produce compounds with a low melting point and possibly lead to liquid metal embrittlement fracture. Among these elements the most harmful is sulfur (S), but trace elements like lead (Pb), bismuth (Bi) and tin (Sn) can also have a detrimental effect [4]. Inclusions can be also mentioned when considering the hot workability problem in duplex steels.

II.3.1.2.1 Influence of S

Sulfur is well-known to strongly deteriorate hot ductility of steels through the precipitation of sulfides FeS at the grain boundaries which causes a higher intergranular brittleness. In general, the weakening of the grain boundary region is attributed to the effect of sulfur. Indeed, in addition to a low melting point (920°C), the sulfide inclusions impair grain boundary sliding and act as nucleation sites for voiding. This kind of brittleness can be reduced by the addition of Mn via the formation of MnS. The formation of MnS is beneficial because it allows lowering the sulfur solubility in the matrix. In addition, the precipitation of MnS, with a higher melting point, tends to take place uniformly in the matrix rather than exclusively at the grain boundaries. It is generally recommended to maintain sulfur as low as possible to obtain an acceptable hot workability. Calcium treatment and further reduction are usually used at steel factory to reduce the sulfur content. The work done by Komi et al. [60] reveals the detrimental effect of S, involving a minimum of ductility at around 1100°C leading to the formation of edge cracks

during hot rolling of the duplex stainless steels. Recent studies have confirmed the detrimental effect of S on the hot ductility of duplex stainless steels [59, 61, 62]. The combined effect of oxygen and sulfur on the hot workability of DSS was studied by Tsuge [63]. Tsuge presented a diagram on the effect of S and O content on edge crack length after hot rolling for a 2205 DSS (Figure II.21). According to this graph, sulfur is the key parameter in the formation of edge cracks, and this despite high contents in oxygen (up to 125ppm). However this graph does not seem very relevant due to difficulties in accurately measuring the sulfur content in a range only comprised between 0 and 10ppm.

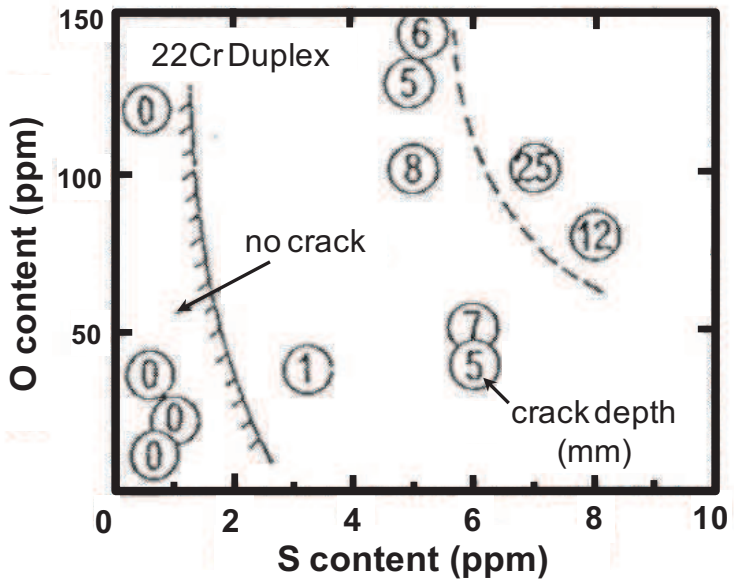


Figure II.21. Effect of S and O contents on the crack length of a 2205 hot-rolled duplex stainless steels (85% reduction) [63].

II.3.1.2.2 Influence of O

The oxygen content can also turn out to be a key parameter, as it is related to the inclusion cleanliness [63, 64]. Indeed, different kind of inclusions (alumina, silicate, globular oxide…) can also affect the hot-workability of duplex stainless steels depending on their volume fraction, shape and location. However, as the literature is not rich about the effect of the oxygen content, it is difficult to give more information.

II.3.2 As-cast microstructures

Plane strain compression tests performed showed that fine equiaxed grains at the surface of the as-cast material act as a protective layer against formation of severe edge cracks (Figure II.22) [20]. This contrasts with the easy propagation of cracks along the columnar grain boundaries when these appear at the surface or are close to it.

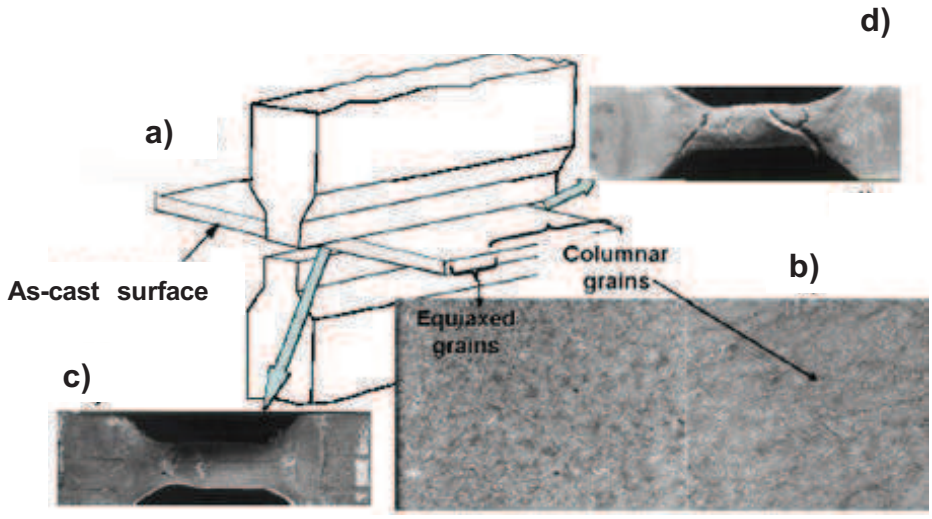


Figure II.22. Plane strain compression at 1000°C and $1s^{-1}$ in order to test the effect of the macrostructure on the crack formation; a) schematic view showing the position of the specimen on the machine; b) view of the as-cast microstructure seen on the transverse section of the specimen; c) level of defect on the equiaxed grain side; d) level of defect on the columnar grain side [20].

II.3.3 Influence of temperature and strain rate

In literature, there is a general agreement regarding the beneficial effect on the crack sensitivity of increasing the deformation temperature. An example of this beneficial effect is shown in Figure II.23, the higher the temperature the longer the uniform plastic regime in the stress strain curves. Increasing the temperature permits to improve the ductility and, as a consequence, reduces the number and the size of the cracks. For instance, the specimen deformed at 1000°C presents a lot of cracks whereas the specimen deformed at 1200°C is free of any cracks, see the pictures of the specimens after hot deformation in Figure II.23.

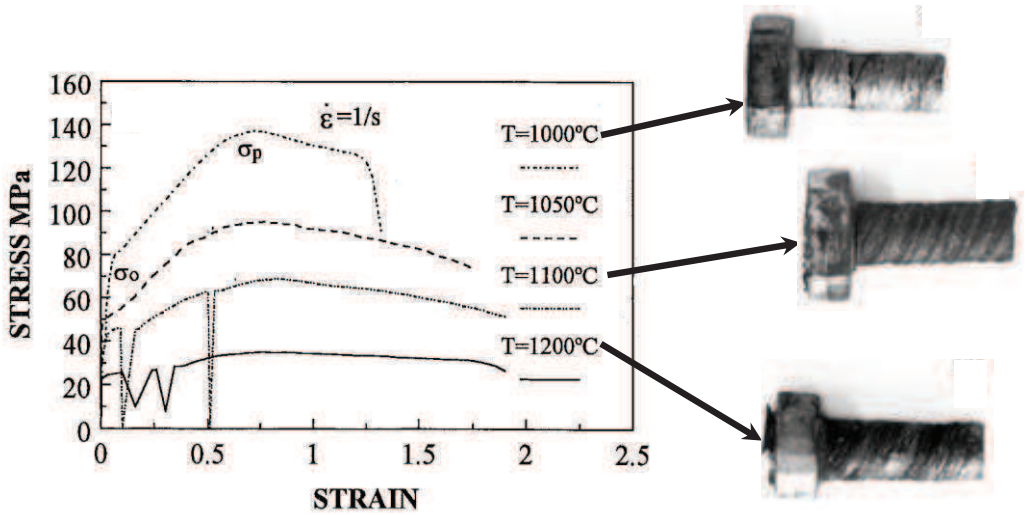


Figure II.23. Stress strain curves of a hot rolled 2304 grade deformed under torsion at different temperatures at $1s^{-1}$ and the corresponding deformed specimens showing different levels of damage [25].

The influence of the strain rate is temperature dependent. Indeed, at low deformation temperature (under 1050°C) the strain rate has a small effect, whereas at high deformation temperatures (above 1050°C), the effect of the strain rate on ductility becomes important [28, 29].

II.3.4 Origin of damage

Damage at the ferrite-austenite interphase boundaries has been identified as the main source of defects under hot working conditions in duplex stainless steels, see Figure II.24. Actually, in laboratory tests, damage is often observed well before the final fracture of the material.
Brittle intermetallic phases, such as the sigma phase, are suspected to play a role during hot working. In duplex stainless steels, the sigma phase precipitation takes place below 1000°C. However, it generally requires relatively long annealing or very slow cooling rates in the 1000-600°C temperature range [65-69]. In hot workability laboratory investigations, no trace of precipitation at the interphase boundaries has been observed. Consequently, most of the time, intermetallic precipitation can be easily ruled out as potential causes for hot working fracture.

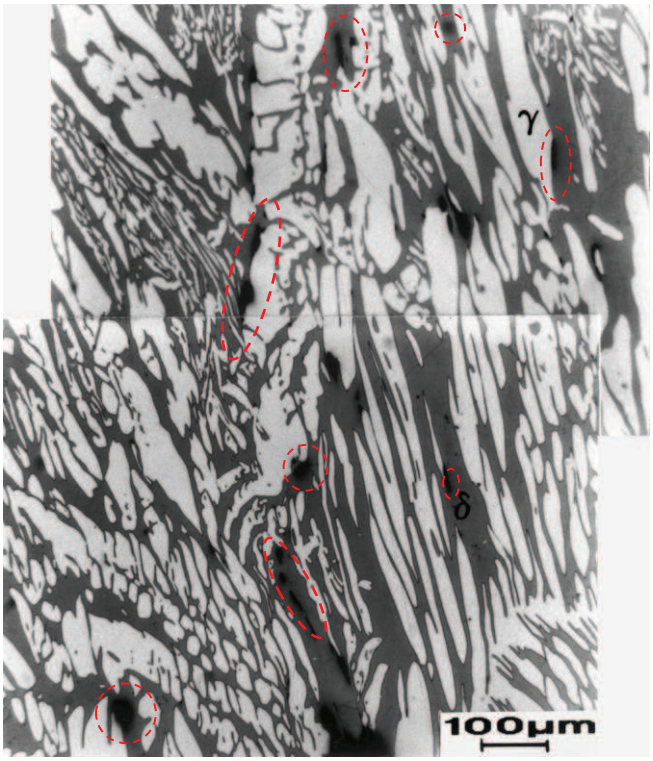


Figure II.24. Optical micrograph of an as-cast 2304 duplex steel deformed by hot torsion at 1000°C, showing cracks at the δ/γ interphase boundaries [25].

Sliding at the ferrite-austenite interfaces is an important source of damage. In duplex alloys, the dynamic recrystallization of the austenite is hindered and different degrees of sliding on the interphase boundaries have been observed [12, 14], depending on the material and the nature of the interphase boundaries. Sliding contributes to strain accommodation during the hot working of duplex stainless steels when strain is partitioned among the phases. Strain localization also induces some sliding. Figure II.7.a shows shear localization in hot-worked 2304 duplex steel. Normally shear stresses develop close to the surface in contact with the deformation tools, but in duplex microstructures shear stresses also appear as a consequence of the presence of two phases with different rheology.

In hot rolled microstructures, sliding affects most interphase boundaries, but it is not necessarily associated with damage nucleation at moderate strains under monotonic deformation conditions. In the as-cast conditions, most of the interphase boundaries share a K-S orientation relationship. As a result, strain accommodation is only possible through severe localized sliding at the incoherent interphases.

II.4 Conclusions

In this chapter, the main factors involved in the high temperature deformation of duplex stainless steels have been reviewed. The main conclusions emerging from the analysis of the literature are the followings.

- The presence of two ductile phases with different mechanical properties controls the complex behaviour of these materials during hot working.

- Composition and temperature define phase ratio and strength, and become key parameters for industrial processing, both for the constitutive behaviour, and for damage accumulation.

- Strain partitioning, rotation and interphase boundary sliding contribute to accommodate the applied deformation between ferrite and austenite, but can be at the origin of localization and crack nucleation.

- There is a significant effect of loading mode and microstructure evolution associated to it on the macroscopic mechanical response.

- The literature is relatively rich about the hot deformation of duplex stainless steels. However, the lack of quantitative data about strain partitioning as well as the lack of a method that properly characterizes the resistance to crack propagation at high temperature, remain the key issues preventing the hot workability problem.

Chapter III. Hot cracking resistance

Chapter III. Hot cracking resistance

The characterization of the high temperature fracture resistance of metallic materials and the understanding of the influence of microstructural parameters remain an experimental and theoretical challenge. The main difficulty is the definition of a relevant fracture parameter that properly quantifies the controlling fracture phenomenon, for example during high temperature roughing operations. In some applications, the resistance to damage initiation and growth is the main issue. In that case, the high temperature fracture strain measured on tensile specimens usually provides valuable information. In some other forming operations, the resistance to cracking initiation from a pre-existing defect is the main issue. Finally, the tearing resistance, i.e. the resistance to the propagation of a crack, is probably the key property in edge cracks issues during hot rolling.
The outline of this chapter is as follows. The main concepts of the Essential Work of Fracture are summarized in section III.1. The experimental procedures are described in section III.2. Then, the following materials will be discussed in this chapter:

- D1 versus D2 in the as-cast conditions (section III.3); these preliminary results obtained on as-cast materials will reveal the necessity of generating model microstructures in which the morphology, the volume fraction and the size of both phases will be well-controlled (section III.4).
- D1_W versus D2_W (section III.5), where 'W' means Widmanstätten and refers to the morphology of the austenite. This comparison will allow investigating the effect of the major alloying elements.
- D2_W versus D2_E (section III.6), where 'E' means equiaxed that corresponds to a different austenite morphology compared to the Widmanstätten one.
- D1_W versus D1bis_W (section III.7), where D1bis_W is the same material compared to D1_W, i.e. with the same chemical composition but arising from a different industrial casting. This will allow investigating the influence of the impurities.

III.1 Literature review about the Essential Work of Fracture concept

The essential work of fracture (EWF) concept was introduced by Cotterell and Reddel [70] as a mean of quantifying the fracture resistance of thin ductile metal sheets. The basic idea is simple. The EWF concept was introduced to handle ductile fracture from the point of view of complete fracture of a specimen and not from cracking initiation measurement such as in the traditional fracture mechanics approach. The purpose of the method consists in separating, based on dimensional considerations, the

work dissipated within the plastic zone from the total work of fracture in order to provide an estimate of the work spent per unit area within the fracture process zone (FPZ) to break the material [71].
For thin sheets, the double edge notch tension (DENT) geometry is particularly well suited owing to the symmetry and advantage of avoiding buckling problems (Figure III.1). If the ligament of a sheet specimen is, as shown in Figure III.1, completely yielded before initiation, and the plastic zone is confined to the ligament, then the plastic work dissipated for the complete fracture is proportional to the plastic volume at initiation and the work in the FPZ is proportional to the fracture area. That is, the plastic work and the EWF scale differently with specimen dimensions.

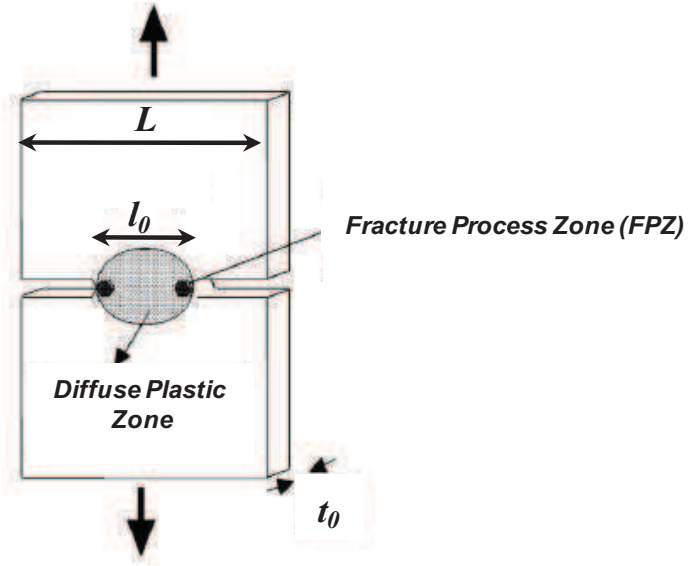


Figure III.1. DENT geometry showing the diffuse plastic zone as well as the localized necking zone in front of the crack tips.

The total work of plasticity dissipated during the test is proportional to the square of the ligament length, l_0^2 and thickness t_0. The work performed in the FPZ is proportional to l_0 time t_0. The total work of fracture, W_{tot}, can be written as the sum of the essential work, W_e, and the plastic work, W_p:

$$W_{tot} = W_e + W_p = t_0 l_0 w_e + \alpha t_0 l_0^2 w_p \,, \qquad \textbf{eq III-1}$$

where w_e is the specific essential work of fracture (work per unit area), w_p is an average plastic work density, t_0 is the initial sheet thickness and α is a shape factor ($\pi/4$ for a circular plastic zone). Normalizing the previous equation, the total specific work of fracture, $w_{tot} = W_{tot}/t_0 l_0$ is given by

$$w_{tot} = w_e + l_0 \alpha w_p \,. \qquad \textbf{eq III-2}$$

It means that if the term αw_p in eq III-2 does not depend on the ligament length, hence the variation of w_{tot} as a function of l_0 has to follow a linear relationship. Thus, if several DENT specimens with different ligament lengths l_0 are tested, the specific essential work of fracture, w_e is the constant term in the linear regression, i.e. the work obtained by extrapolating to a zero ligament length the linear evolution of the total specific work of fracture, w_{tot} against ligament length (Figure III.2). The total specific work of fracture was calculated from the areas under the load-displacement curves and depends on the specimen thickness [72].

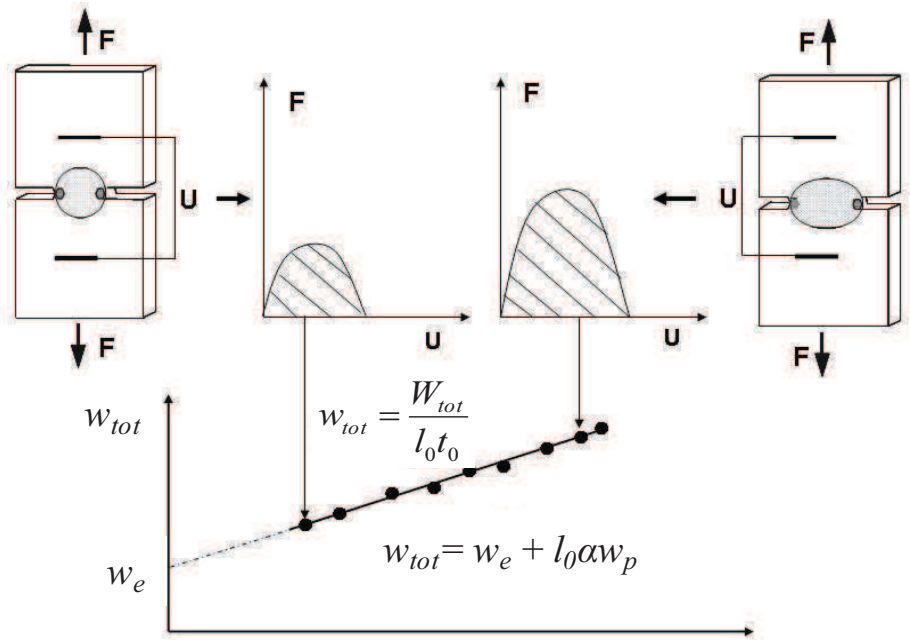


Figure III.2. Diagram illustrating the method to determine the specific Essential Work of Fracture.

According to Cotterell and Reddel [70], some restrictions on the ligament length are needed for this method to be valid. It requires imposing an upper and a lower bound to the ligament length.

The upper bound results from two restrictions:

- l_0 must be less than $L/3$ (where L is the width of the specimens) to warrant that yielding does not spread to the outer edges of the specimen.

- l_0 has to be smaller than the sum of the two plastic zone sizes in order for the plastic yielding to spread along the entire ligament before onset of cracking (Figure III.3).

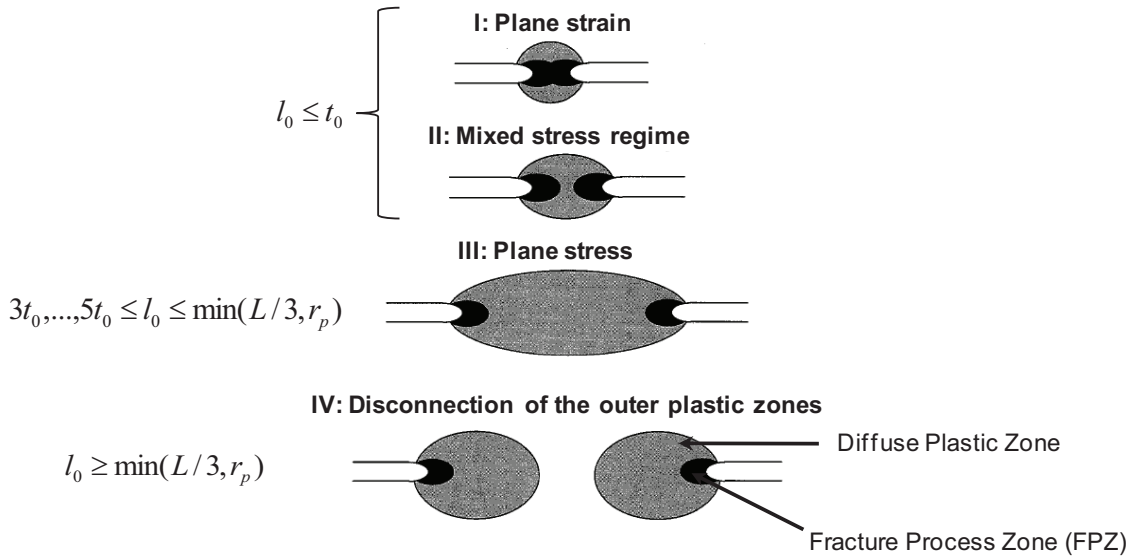


Figure III.3. Sketch of the plastic zones and fracture process zones in the ligament as a function of ligament length.

The lower limit is directly related to the specimen thickness: l_0 must be greater than 3 to 5 times the thickness of the specimens in order to allow necking to develop fully before cracking, in such a way that the same plane stress conditions prevail whatever the size of the ligament (Figure III.3).
To summarize, if eq III-2 is applied, this method should provide reliable values of the plane stress fracture toughness of a specimen plate on the condition that the ligament length lies between the limits given by eq III-3.

$$3t_0,...,5t_0 \le l_0 \le \min(L/3, r_p)\,, \qquad \textbf{eq III-3}$$

r_p is the size of the plastic zone, which can be estimated as

$$r_p = \frac{1}{\pi}\frac{Ew_e}{\sigma_0^2}\,, \qquad \textbf{eq III-4}$$

where E is the Young's modulus and σ_0 the yield stress [73].

The EWF concept was widely used to characterize the fracture toughness of several ductile metallic materials (brass, bronze, zinc alloys, aluminium alloys and steels) [72, 74-77] or polymer thin sheets or layers at room temperature [73, 77-82]. Barany et al. [83] have recently reviewed the results provided by the EWF concept applied to polymers and composites. When the conditions of validity of the method are fulfilled, it is relatively simple to determine the specific essential work of fracture which quantifies the tearing resistance. In previous investigations, concerning polymers, the EWF concept was used at intermediate temperatures (100-300°C) [84-91]. In this temperature range, the tensile tests on the DENT specimens were carried out inside a furnace.
For higher temperatures (>1000°C), performing EWF test is an experimental challenge. In addition to the difficulties related to the control of the microstructures at high-temperature in materials affected by phase transformations, carrying out the test in a homogeneous temperature furnace is difficult. Such challenge was recently taken up by Chehab et al. [92, 93] using a Gleeble-3500 thermo-mechanical simulator in order to characterize the high-temperature tearing resistance of dual-phase ferritic stainless steels. Chehab et al. [92] also pointed out that the application of the EWF concept at high temperature presents several advantages:

(i) The EWF method quantifies the resistance of the material to the propagation of a crack which is not true in usual hot ductility measurements (tensile or shear tests);

(ii) The conditions of validity of the method will almost always be fulfilled owing to the large ductility at high temperature;

(iii) The method does not require any crack detection systems which are complex to implement at high temperature;

(iv) The measurement of the overall displacement is accurate enough for calculating the energy spent during the test.

To summarize, the results from Chehab et al. [92, 93] have demonstrated the effectiveness of the essential work of fracture method to quantify the hot cracking resistance of metallic materials. As explained in the previous chapter, duplex stainless steels present in general a poor hot workability leading to edge cracks during the hot rolling process. This method is expected to be very useful to discriminate different grades or different parameters such as the microstructure: phase morphology, inclusion content.

III.2 Experimental procedure

III.2.1 High temperature testing

The high-temperature tensile tests using DENT specimens were carried out using a Gleeble-3500 thermo-mechanical simulator. This machine is equipped with a direct resistance heating system and a hydraulic mechanical device. The temperature is measured by a computer-controlled thermocouple welded to the DENT specimen, meaning that the temperature is imposed by the machine where the thermocouple is located. A cooling device allows quenching the surrounding ligament zone after the complete fracture of the specimen in order to retain the microstructure (Figure III.4). Thus, it is possible to observe the fracture profiles and to check the microstructure inside the heated zone.

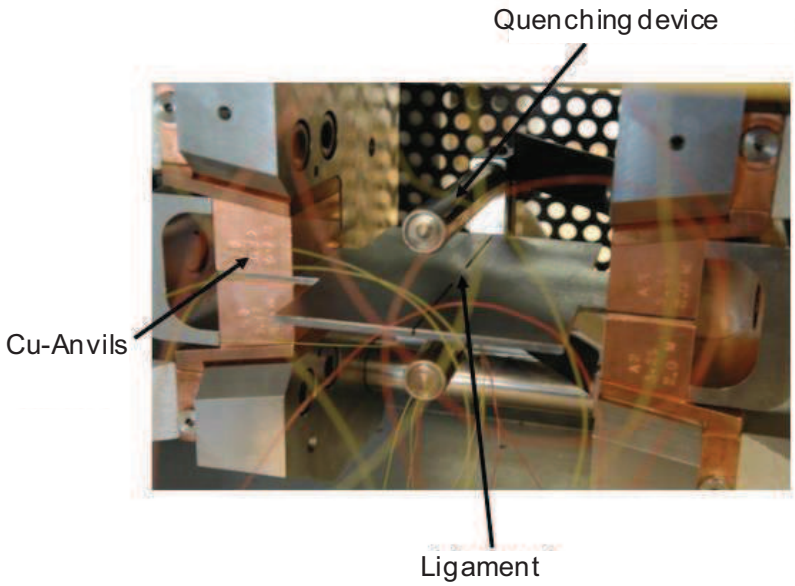


Figure III.4. Picture of the Gleeble chamber showing a DENT sample before testing. The specimen is heated by a current through the Cu-jaw and quenched with a special device permitting to spray with air or water.

The thermocouple controlling the temperature was welded next to the tip of the notch in order to provide a homogeneous zone of temperature throughout the ligament. This choice was made by Chehab et al. [93], who showed that locating the thermocouple in the centre of the ligament leads to strong temperature gradient between the middle of the ligament and the end of the notch. Estimated by Chehab et al. [93] around several hundred degrees, this gradient was leading to local microstructure modifications.

Nonetheless, a significant temperature gradient develops when moving from the ligament centre to the head of the specimens. This gradient helps confining the plastic deformation in the ligament while the rest of the sample remains purely elastic. In that manner, local plastic yielding is avoided at the gripping system, making the overall load-displacement results sufficiently accurate for data reduction (no need for a local extensometer to be used).

For the measurements of the EWF, DENT specimens with dimensions specified in Figure III.5 and with various ligament lengths ($15 \leq l_0 \leq 39$mm) were machined by electro-erosion in the metal blocks with the microstructure of interest. The pre-crack tip has an opening of ~ 0.5 mm, the smallest that can be obtained by machining. This initial opening is small enough compared to the critical crack tip opening displacement obtained at high temperature (~ 0.8 mm).

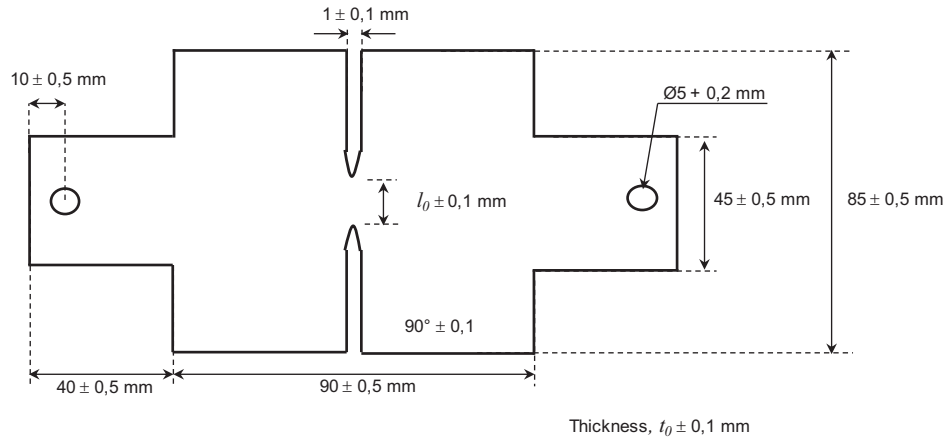


Figure III.5. Dimensions of the DENT (Double Edge Notch Tension) specimens used, t_0 = 3mm.

The complete thermo-mechanical path followed by the DENT specimens is presented in Figure III.6.a. The specimens were heated at the testing temperature (1050°C or 1200°C), annealed for 30s at this temperature, and deformed under uni-axial tension at a grip displacement rate of 10mm.s^{-1}. Heating was stopped just before starting the test in order to avoid a sudden increase of the temperature during necking. Indeed, the current is constant but the area crossed by the current decreases, as a consequence the temperature increases dramatically, possibly reaching a local fusion of the ligament deformed by necking before the final fracture. Figure III.6.b shows the shape of the heated zone around the ligament before deformation. A circular zone is observed around the ligament. The colour change emphasizes the development of a significant temperature gradient between the ligament and the head of the specimen.

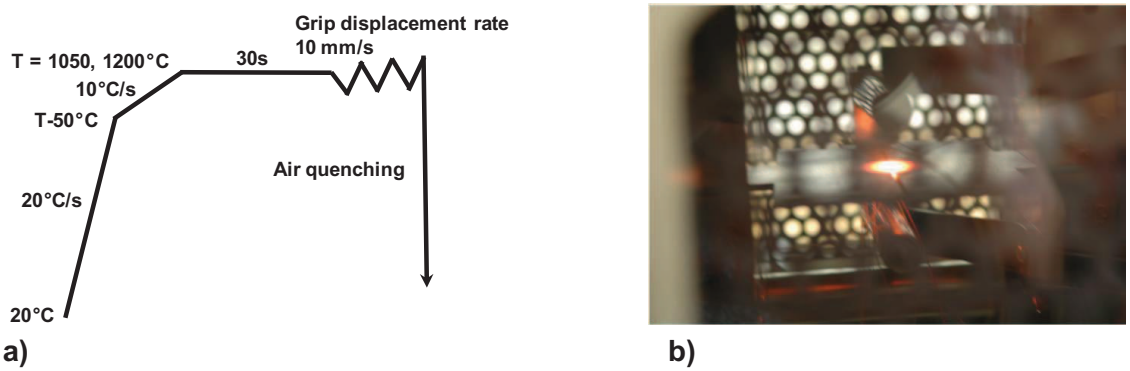


Figure III.6. a) The thermo-mechanical history path followed by the DENT specimens; b) picture showing the shape of the heated zone.

III.2.2 Dimensions of the DENT specimens

Edge-cracking occurs mainly during the high temperature roughing-mill operations. The microstructure is a key parameter, therefore the tests have to be carried out on specimens involving the microstructure of interest, i.e. an as-cast slab skin microstructure (fine columnar grains). Figure III.7 shows that

using specimens with the dimensions corresponding to the conditions of validity leads to a ligament located in the transition zone between the columnar zone and the slab heart equiaxed zone. It requires reducing the width of the DENT specimens in order to locate the ligament in the columnar zone. In addition, reducing the specimen width reduces the amount of material needed for the test.

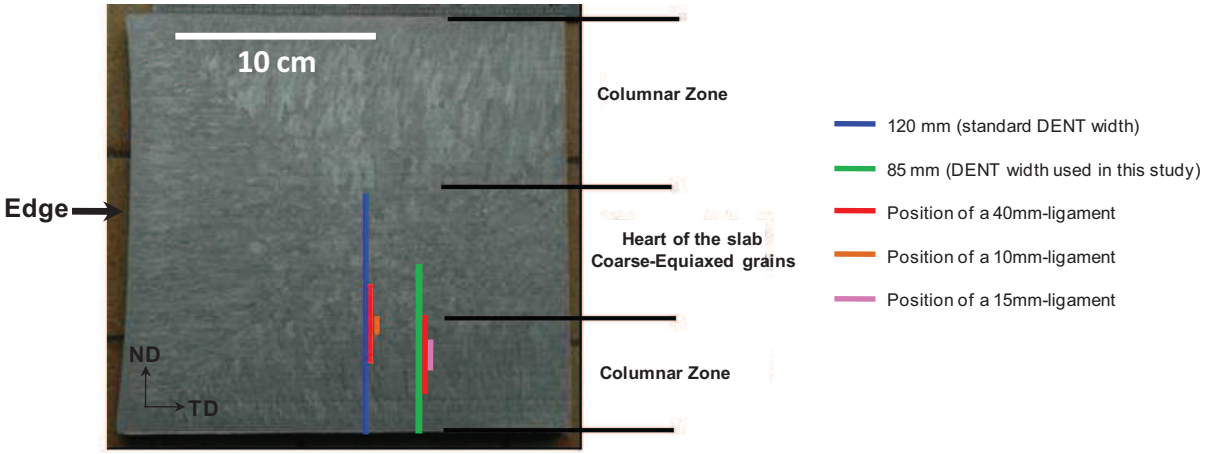


Figure III.7. Illustration of the specimen or ligament position as a function of the dimensions.

Chehab et al. [92] suggested that the restrictions concerning the validity conditions are less severe at high temperature than at room temperature. This difference was attributed to a better ductility and a strong temperature gradient between the centre of the ligament and the head of the specimen which helps for confining the plastic deformation in the ligament. As a result, it seems that the DENT width can be reduced. A feasibility study was carried out by the Aperam Research Center [94]. Several DENT specimens were tested with different width (44, 50, 60, 70, 80, 100, 120mm) and a constant ligament length (40mm). The results demonstrated that the force-displacement curves were unchanged, and consequently the area under the curves did not change when reducing the width of the DENT to 80mm. It means that the total specific work of fracture was unaffected as long as the DENT width exceeded 80mm. These results confirmed that it is possible to reduce the dimensions of the DENT specimens when the method was applied at high temperature. It explains why the DENT specimens used throughout this study, have a width of 85 mm instead of the 120 mm as recommended by the theory when tests are performed at room temperature.

III.2.3 Characterization tools

III.2.3.1 Observation of the fracture surfaces

After the high temperature tensile test, the specimens were systematically characterized by SEM to observe the fracture surfaces and to accurately measure the thickness of the DENT specimen at fracture, t_f. Neglecting the strain component in the direction of crack propagation and assuming plastic incompressibility, the average true equivalent fracture strain was estimated as:

$$\varepsilon_{fracture}^{eq} = \frac{2}{\sqrt{3}} \ln\left(\frac{t_f}{t_0}\right), \qquad \text{eq III-5}$$

where t_0 is the initial thickness of the DENT specimens and t_f the thickness at fracture.

III.2.3.2 Microstructural characterizations

The specimens were ground down on abrasive paper (silicon carbide) to 1200 grit, and polished with a diamond paste down to 3µm. The final polishing step was performed with a 1µm alumina powder.
The microstructure observations were carried out by optical and scanning electron microscopy (SEM, Zeiss Ultra 55) after etching. Two reagents were employed: the Beraha chemical selective etchant (100mL H_2O, 30mL HCl and 1-1,5g $K_2S_2O_5$) or a 40% aqueous sodium hydroxide electrolytic solution under a tension of 3V. Volume fractions of each phase, austenite lath thickness and grain size distributions were determined by image analysis using the Aphelion® software.
A few thin foils for TEM observations were also prepared from the DENT specimens with the following procedure: (1) samples were machined close to the fracture surface, (2) the samples were ground down on abrasive paper to 1200 grit up to reach a thickness of 70µm, (3) 3mm-diameter pellets were cut from the 70µm-thin metal sheet, (4) the 3mm-diameter pellets were electro-polished with a mixture of acetic and perchloric acids.

III.2.3.3 Damage characterization

Damage characterization consists in estimating the number of voids per unit area as a function of the strain. Sections cut perpendicularly to the ligament were polished. Then, the section was divided into different zones with a step of 500µm, see Figure III.8. Finally the cracks were manually counted in each region. The true effective strain in each region was estimated as:

$$\varepsilon_i^{eq} = \frac{2}{\sqrt{3}} \ln\left(\frac{t_i}{t_0}\right), \qquad \text{eq III-6}$$

where t_i is the thickness of the sample at a position i from the fracture, and t_0 (3mm) is the initial thickness of the DENT specimen. The thickness t_i was measured at the middle of each region. It has also to be noted that the plane strain assumption deteriorates when the distance from the ligament increases. The situation is then close to a simple tension.

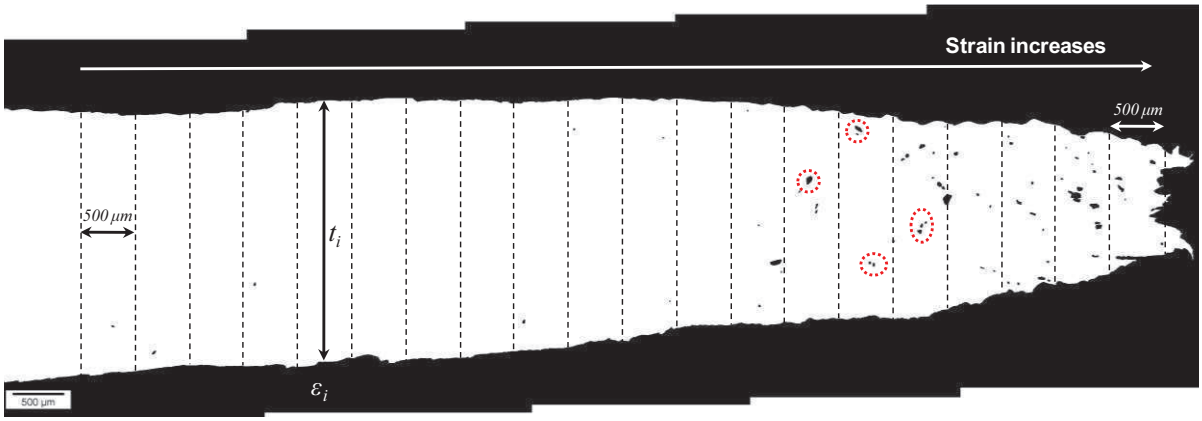


Figure III.8. Section perpendicular to the ligament in order to quantify the density of cracks per unit area (mm²) as a function of strain; the dotted lines correspond to the 500µm-step partition; the black arrow shows the position where the thickness was measured to estimate the strain; and the red circled zones highlight a few voids.

III.2.3.4 Inclusion content

First of all, the specimens were polished down to 1µm with a diamond paste. Then, the inclusion content was determined using two different methods.

III.2.3.4.1 Manual method

A set of 50 SEM micrographs was analyzed. In order to determine the nature of the inclusions, some of the particles were analyzed by EDS (Energy Dispersive Spectroscopy). Each micrograph was obtained using back scattered electron contrast in order to distinguish between austenite and ferrite with a magnification of 500x. The microscope settings, especially the brightness and contrast adjustments, allow producing micrograph such as the one presented in Figure III.9. The grey level of the inclusions, in black in Figure III.9 because of a lower atomic mass, permits the detection of the particles. Then, the number of inclusions per micrograph was determined by manual counting. The particles were classified according to their location, i.e. in the δ-ferrite, in the γ-austenite or at the δ/γ interfaces. Finally, the number of inclusions per unit area can be calculated.

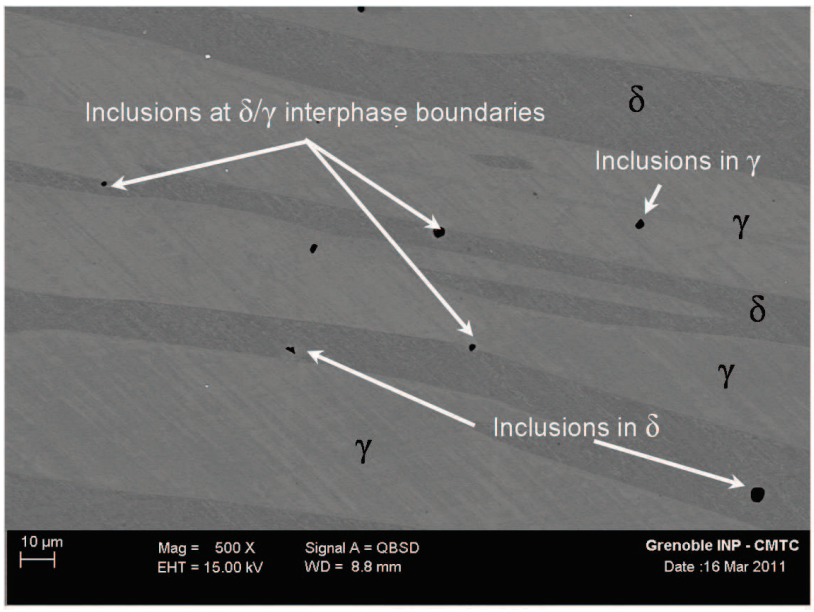


Figure III.9. SEM micrograph for the observation of the inclusion distribution in austenite-ferrite microstructures.

III.2.3.4.2 Automatic method

The second method was performed using the software “Feature” developed by Oxford®. The electron back-scattered contrast was used in order to detect automatically the particles thanks to a different grey level compared to the austenite-ferrite microstructure. This software must be programmed in order to move the stage and to count hundreds to thousands of particle per sample. The selected magnification was 700x that corresponds to a surface of 0.0215mm² per field. Several hundreds of fields are considered to analyze 20mm². Each particle detected is chemically analyzed by EDS (Energy Dispersive Spectroscopy).

The results must be analyzed with caution. Indeed, as the majority of the particles have a diameter between 1 and 3µm and the interaction volume is about 1µm^3, the chemical analysis can be affected by the matrix. In addition, the EDS technique does not permit to discriminate molybdenum and sulfur because the energy of the K-ray of the sulfur coincides with the energy of the L-Ray of the molybdenum.

III.2.3.4.3 Comparison between both methods

The two methods appear to be very complementary. The main advantages and disadvantages relative to each technique are summarized in Table III.1.

	Advantages	Disadvantages
Manual method	• Location of the inclusions	• Manual counting • Surface analyzed: 2mm² (50 pictures at a magnification of 500x) • No information about the nature and size of the particles
Automatic method	• Automatic counting • Surface analyzed: 20mm² (950 pictures at a magnification of 700x) • Information about the nature and size of the particles	• No location of the inclusions • Impossible to discriminate Mo and S

Table III.1. Summary of the advantages and disadvantages of both techniques used to determine the inclusion content.

III.2.3.5 Micro-hardness

Micro-hardness Vickers measurements were carried out on DENT specimens in both phases from the fracture surface down to the undeformed region. Then, it is possible to plot the evolution of the hardness as a function of the equivalent strain. These measurements provide information concerning the hardening/softening mechanisms involved in the investigated grades.

III.3 Comparison between as-cast D1 and D2

III.3.1 Results

D1 and D2 differ in chemical composition, especially in terms of nickel and molybdenum content (Table I.3). These two grades were selected because of a known very different degree of hot workability (section I.2.1). Comparing these two grades should allow unravelling the key parameters involved in the hot workability of duplex stainless steels.

The DENT specimens were machined in the as-cast slab of each duplex stainless steel with the ligament located in the columnar zone as shown schematically in Figure III.10.

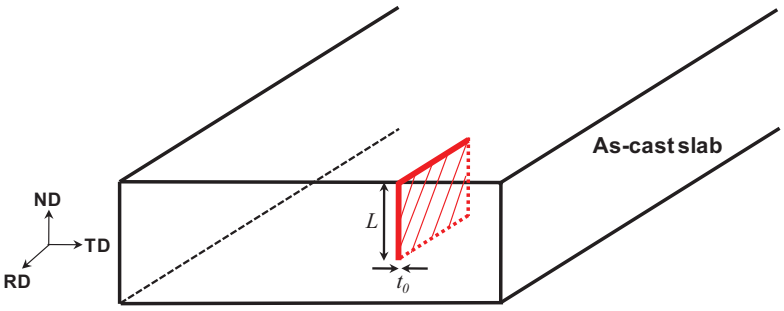


Figure III.10. Schematic the as-cast slab showing where the DENT specimens were machined.

The specimens were deformed in tension at 1050°C and 1200°C up to final fracture following the experimental procedure described in section III.2.1.

III.3.1.1 EWF results

The total specific work of fracture, w_{tot}, was calculated from the area under the load-displacement curves. A typical load-displacement curve for each grade corresponding to a ligament length l_0 = 25 mm is given Figure III.11 for a test performed at 1050°C. The area under the force-displacement curve and the maximum force are significantly different when comparing the two grades. The energy associated to the alloy D1 is larger than for the alloy D2. It means that, at 1050°C, more energy is required to break the specimen of D1 than to break the specimen D2.

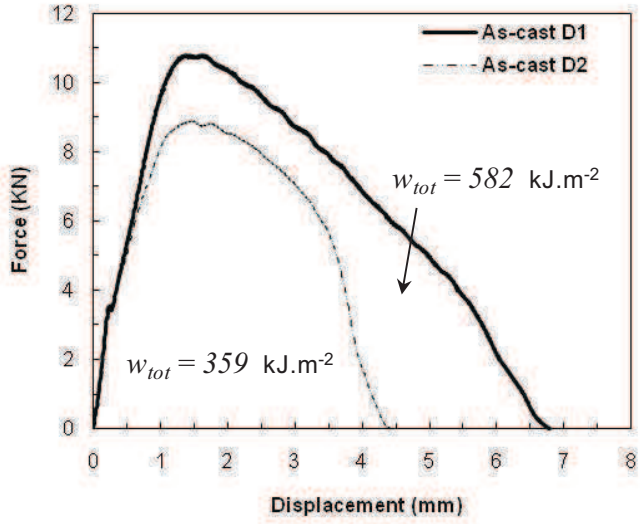


Figure III.11. Typical load-displacement curves at T= 1050°C for each duplex steel grade, for a DENT specimen with ligament length l_0 = 25mm.

The total specific work of fracture is plotted as a function of the ligament length l_0 in Figure III.12, giving the expected linear relationship.

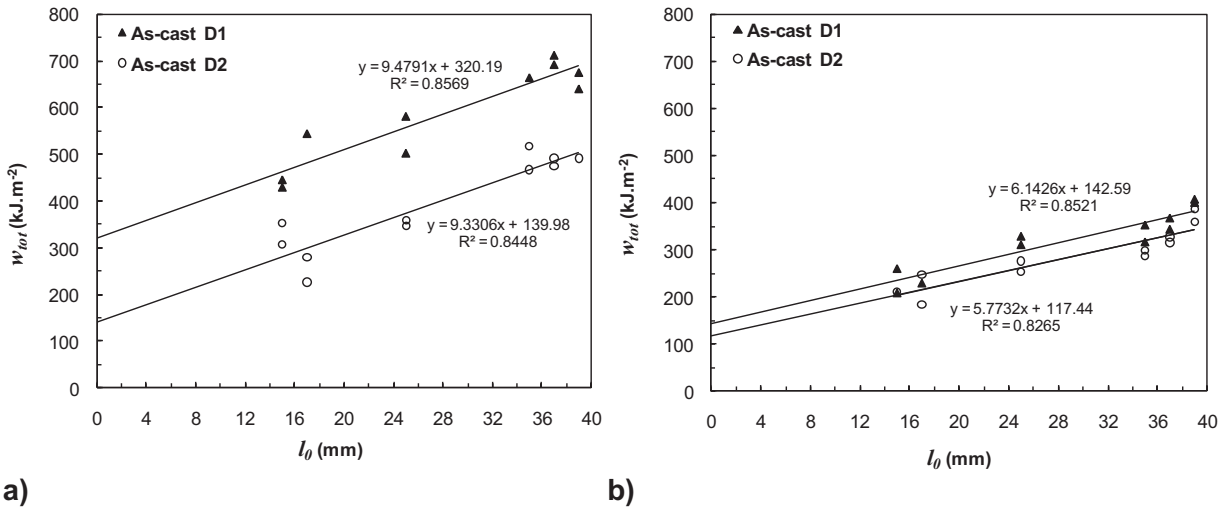


Figure III.12. Variation of the total specific work of fracture as a function of the ligament length for separation of the essential work of fracture; comparison between the two grades D1 and D2 in the as-cast conditions; a) T=1050°C; b) T=1200°C.

For the values of αw_p, the accuracy is also defined as plus or minus the standard deviations s_a of the slope, which, for a linear regression $y=ax + b$, is given by the following relation:

$$s_a = \left[\frac{\sum_{i=1}^{n} (y_i - \hat{y}_i)^2}{(n-2)\sum_{i=1}^{n} (x_i - \bar{x})^2} \right]^{1/2}, \qquad \text{eq III-7}$$

where n is the number of (x_i, y_i) data, $\bar{x}$ is the mean of the x_i values, and $\hat{y}_i$ are the values of y_i on the regression line at the corresponding value of x_i (i.e. fitted y_i values).

For the values of w_e, the accuracy is defined as plus or minus the standard deviation s_b of the intercept for $x = 0$, which, for a linear regression $y=ax + b$, is calculated from least-squares principle as:

$$s_b = \left[\frac{\sum_{i=1}^{n} (y_i - \hat{y}_i)^2 \cdot \sum_{i=1}^{n} x_i^2}{n(n-2) \cdot \sum_{i=1}^{n} (x_i - \bar{x})^2} \right]^{1/2}. \qquad \text{eq III-8}$$

Table III.2 summarizes the results obtained from Figure III.12.

		w_e (kJ.m^{-2})	αw_p (kJ.m^{-3})
As-cast D1	1050°C	320 ± 41	9.5 ± 1.4
	1200°C	143 ± 26	6.1 ± 0.9
As-cast D2	1050°C	140 ± 38	9.3 ± 1.3
	1200°C	117 ± 27	5.8 ± 0.9

Table III.2. Results of the EWF method applied to as-cast alloys D1 and D2 at 1050°C and 1200°C.

The specific work of fracture at 1050°C (also given by the intercept at the origin, see Figure III.12) is equal to 320 kJ.m-² and 140 kJ.m-² for alloys D1 and D2, respectively. At 1050°C, the alloy D1 is two times more resistant to ductile tearing than the alloy D2.

When increasing the temperature to 1200°C, both alloys D2 and D1 become more ductile and the difference in terms of the essential work of fracture decreases. The work performed in the plastic zone is similar for both alloys at 1050°C as well as at 1200°C.

III.3.1.2 Fracture observations

The fracture surfaces of broken specimens were characterized by scanning electron microscopy (SEM). An estimation of the nominal strain to fracture for each experimental condition is provided in Table III.3.

		$\varepsilon^{eq}_{fracture}$
As-cast D1	1050°C	2.6 ± 0.2
	1200°C	3.4 ± 0.2
As-cast D2	1050°C	1.1 ± 0.2
	1200°C	2.2 ± 0.2

Table III.3. Estimated values of the strain to fracture by measuring the thickness of the specimen at fracture

Figure III.13 presents typical fracture surfaces of DENT specimens for each grade investigated at different temperatures.

The fracture profile of grade D1 is predominantly flat along the whole ligament at 1050°C (Figure III.13.a). A classical ductile profile with dimples is observed at the micro-scale. The phenomenon responsible for cracking initiation is the growth and coalescence of voids ahead the blunted crack tip, see Figure III.14. The crack propagates under a constant thickness reduction, with a steady-state geometry of the fracture process zone (FPZ).

The fracture profile of the grade D2 at 1050°C is irregular and shows only a few ductile dimples (Figure III.13.b). The propagation occurs with varying thickness reduction.

Fracture profiles of both alloys D1 and D2 are flat along the whole ligament at 1200°C (Figure III.13.c & d). However, the fracture profile of the alloy D1 seems to be a little bit more regular than the fracture profile of the alloy D2. Examination of the fracture micrographs and profiles match very well with the EWF results.

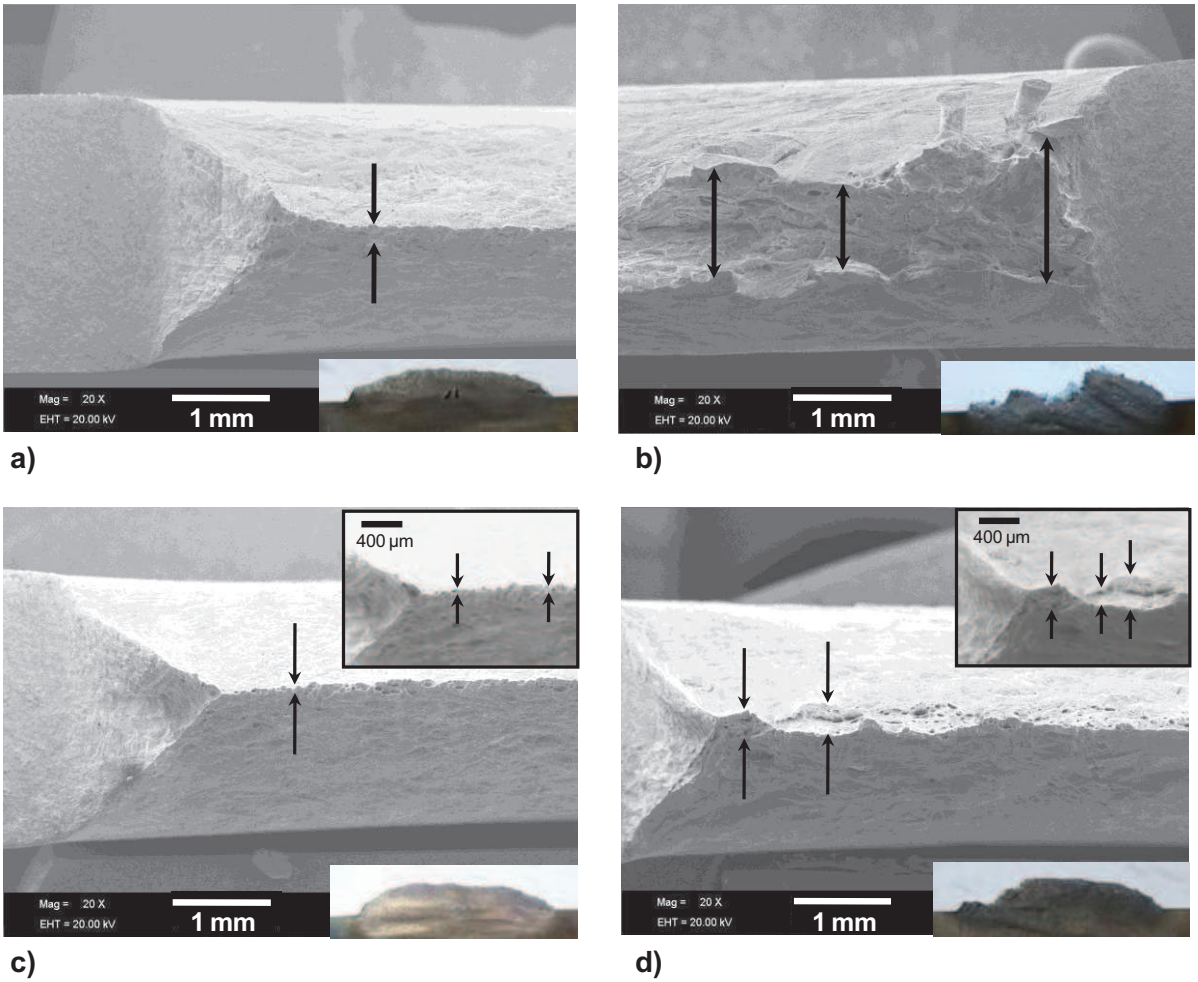


Figure III.13. Fracture micrographs and profiles of the broken DENT specimens (l_0 = 37mm); a) D1 at 1050°C; b) D2 at 1050°C; c) D1 at 1200°C. d) D2 at 1200°C. The arrows emphasize the thickness variation in the profile.

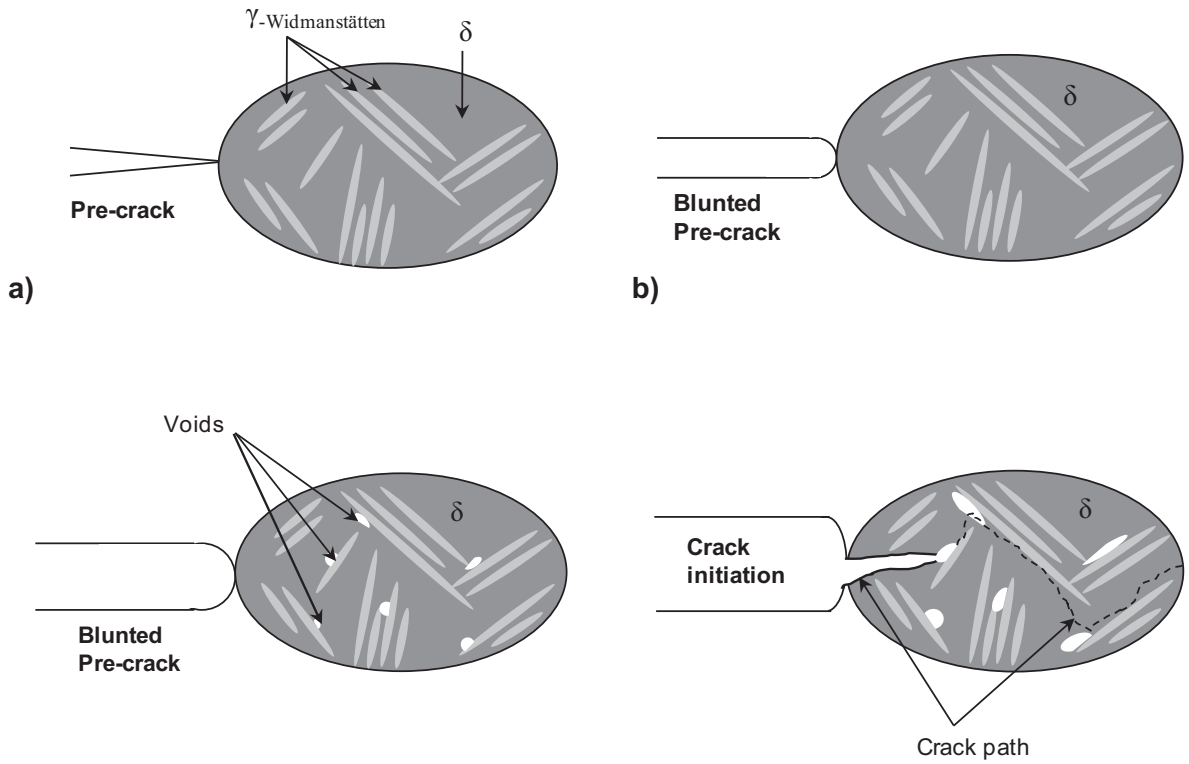


Figure III.14. Schematic illustration of the damage and fracture process taking place in the fracture process zone of duplex stainless steels ; a) initial state ; b) onset of the crack tip blunting ; c) damage nucleation ; d) void coalescence and crack initiation.

III.3.1.3 Damage

In all the characterized DENT specimens, the voids were always observed at the austenite-ferrite interfaces (Figure III.15) propagating along the interface or in the ferrite matrix. No crack was observed in the austenite. These observations are in perfect agreement with those carried out along the edge part of the hot rolled material (Figure I.9.b).

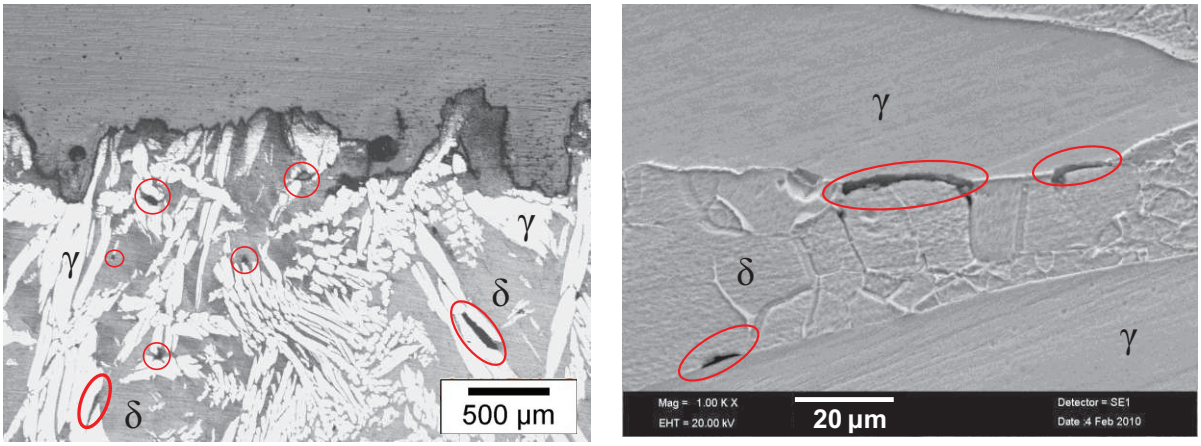


Figure III.15. a) Optical micrograph and b) SEM micrograph of a region close to the fracture of a DENT specimen deformed at 1050°C. Voids nucleate by a partial decohesion of the δ/γ interface, see circled red areas.

Damage characterizations using the method described in section III.2.3.3 were carried out on broken specimens from each grade deformed at 1050°C and 1200°C. The results are presented in Figure III.16. Due to experimental errors, it is difficult to accurately estimate the strain at which the first sign of void nucleation appears. Therefore, another criterion was selected. This criterion was based on the evolution of the crack density as a function of strain. The curves can be divided into two parts. During the first stage, the density of cracks is close to zero and does not significantly increase. During the second stage, the level of damage increases much more. As a result, the characteristic point on the damage evolution is the strain between the two regimes. This particular strain will be named $\varepsilon_{damage}^{eq}$, as shown by the arrows in Figure III.16.

Several elements must be highlighted.

- According to this new criterion, the strain at which damage begins to significantly increase, $\varepsilon_{damage}^{eq}$ is very different when comparing both grades. At 1050°C, the density of cracks starts increasing at $\varepsilon_{damage}^{eq} \approx 0.5$ for the alloy D2, whereas it requires reaching $\varepsilon_{damage}^{eq} \approx 1.4$ for the alloy D1. The slope of the curves after the critical strain can be considered as a "void nucleation rate" which is approximately the same between both grades at 1050°C. The same trend is observed at 1200°C since the first sign of a damage burst is observed around an approximate equivalent strain of 0.9 in the alloy D2 whereas damage nucleates only for larger equivalent strain in the alloy D1 (about 1.2). At 1200°C, the void nucleation rate seems to be different when comparing both grades.

- A high density of cracks seems to be reached at lower strain values for the alloy D2 whatever the temperature.

- The strain to fracture is always larger at 1200°C in comparison to that at 1050°C and the strain to fracture is also always larger for the alloy D1, confirming the fracture observations made by SEM.

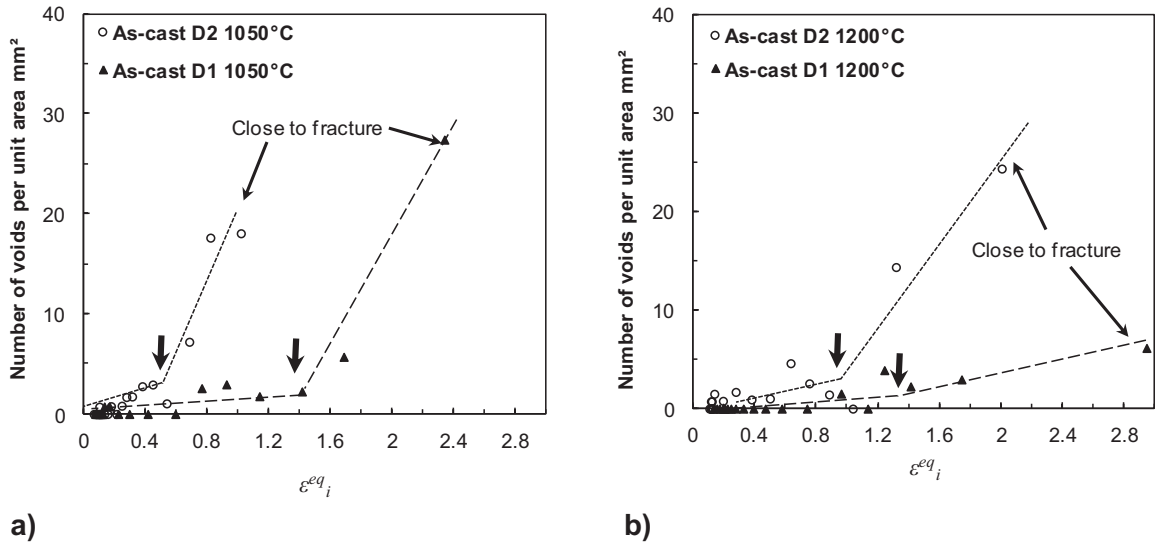


Figure III.16. Evolution of the damage as a function of strain for both grades in the as-cast conditions; a) T = 1050°C; b) T = 1200°C. The arrow indicates the strain at which damage starts increasing significantly, i.e. the approximate strain at which damage nucleation occurs.

III.3.2 Discussion

III.3.2.1 Origin of the differences between D1 and D2 in the as-cast conditions

According to the experimental results, at 1050°C, the alloy D1 is two times more resistant to hot cracking than the alloy D2 whereas at 1200°C even if the D1 is more resistant, the difference is not very significant. First of all, the factors which determine the difference between the hot tearing resistance of the alloys D1 and D2 have to be discussed.

This preliminary discussion focuses on two factors:

(1) on the difference in terms of microstructure between the two alloys;

(2) on the differences between the high-temperature rheology of the ferrite and austenite in each alloy.

The DENT specimens were machined in the as-cast slabs. As a consequence, microstructural observations were carried out along the thickness of the slab in order to investigate in more details the as-cast microstructures. Figure III.17 highlights the difference between both grades by comparing the as-cast microstructures at different positions along the thickness of the slab. In the as-cast conditions, strong disparities seem to exist between both grades (Table III.4):

- the austenite laths are thicker in the D2 grade compared to the D1 grade, see values of e_γ in Table III.4;
- the austenite content ($\%\gamma$) is higher in the alloy D2.

	D1			D2		
	e_γ (µm)	$\%\gamma$	$\%\delta$	e_γ (µm)	$\%\gamma$	$\%\delta$
Slab Skin (2mm)	7 ± 2	49 ± 1.4	51	20 ± 2	65 ± 3.5	35
Columnar zone (10mm)	23 ± 2	47 ± 2.3	53	45 ± 3	58 ± 2.4	42
Transition Zone (60mm)	24 ± 2	42 ± 3.1	58	45 ± 4	50 ± 3.2	50
Centre of the slab (100mm)	21 ± 3	37 ± 3.7	63	38 ± 3	50 ± 2.5	50

Table III.4. Comparison between the as-cast slab of the alloys D2 and D1.

Iza-Mendia et al. [20] have reviewed a wide range of reports about the hot ductility of duplex stainless steels as a function of the ferrite volume fraction. General trend is that the ductility of a duplex microstructure is significantly lower than the ductility of pure ferrite and is slightly lower than the ductility of pure austenite. The alloy D1 contains more ferrite than the alloy D2 which could partly explain the difference of ductility between the two alloys. The large lath size can be a reason for the poor hot workability of the alloy D2. Indeed, as the voids nucleate at the interface δ/γ, the Widmanstätten austenite forms a favorable percolating path to crack propagation. The longer the laths, the straighter are the cracks along the lath and the coarser is the mesoscopic tortuosity.

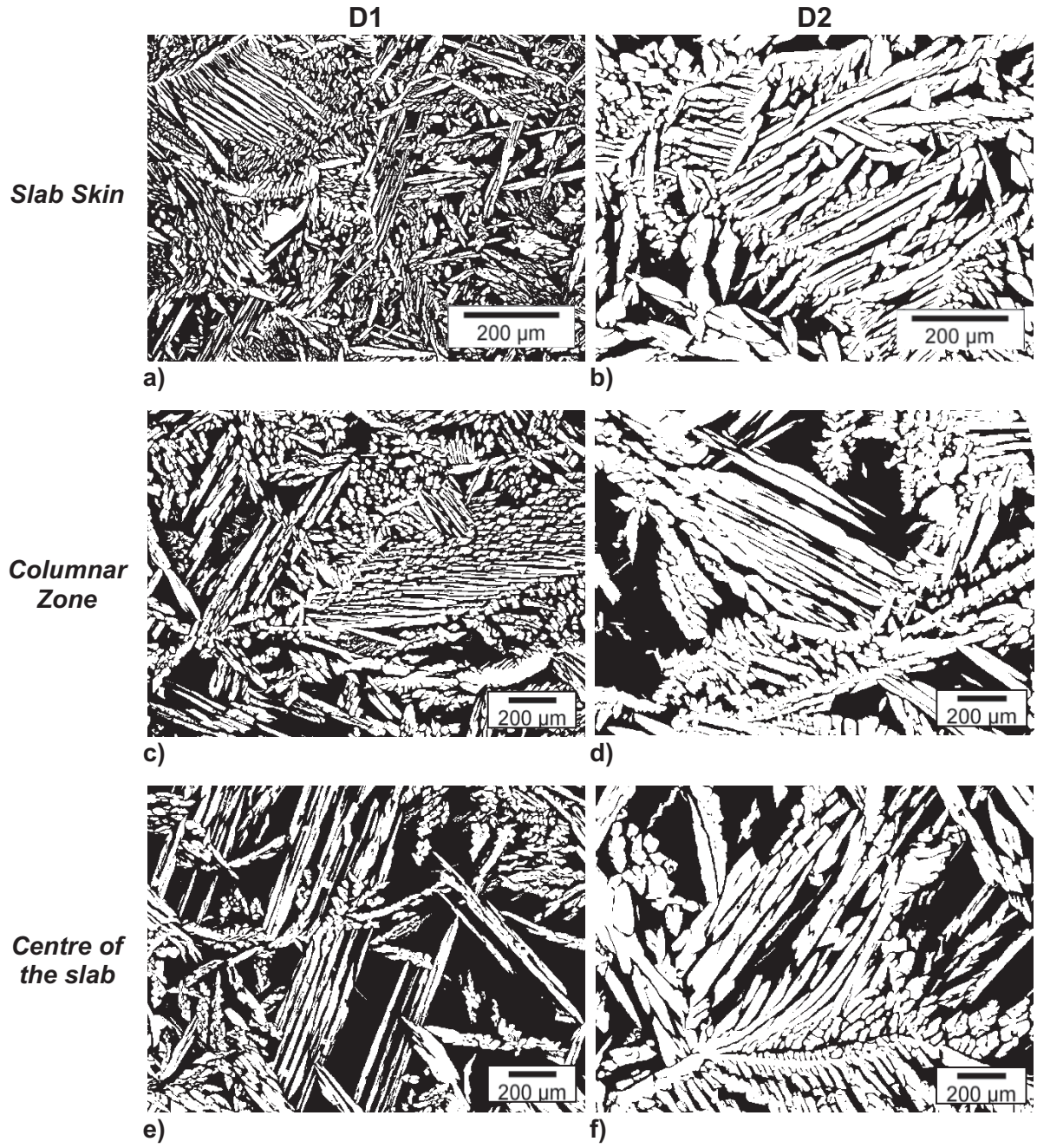


Figure III.17. Comparison between the as-cast slab of the alloys D1 and D2; a) & b) microstructures of the slab skin; c) & d) microstructures of the columnar zone; e) & f) microstructures at the centre of the slab. The austenite is in white and the ferrite in black.

Micro-hardness tests were also performed at room temperature giving micro-hardness profiles inside the ferrite and austenite, see Figure III.18. These profiles show the evolution of the hardness as a function of the distance from the fracture surface, therefore as a function of the accumulation of plasticity providing interesting information about hardening and possible softening mechanisms involved in each phase. Ferrite and austenite behave differently. The hardness of the ferrite changes by less than 5 HV showing the efficiency of dynamic recovery. On the contrary, the austenite hardness increases steadily up to the fracture region by typically 10 to 20%. In addition, there is no sign of austenite re-crystallization observed but a high dislocation density when analyzing the austenitic phase, using TEM for specimens tested at 1050°C and 1200°C, see Figure III.19. On the other hand, a well-recovered

microstructure with subgrains is observed in the ferrite while the austenite involves a high dislocation density. The only evolution noticed is the size of the subgrains which are coarser at 1200°C compared to 1050°C (Figure III.19). These results match with the observations performed previously by different authors [22-24, 29]: in duplex stainless steels, austenite recrystallization is rarely observed even after very long annealing. To summarize, ferrite and austenite are affected by similar hardening/softening mechanism independently of the grade.

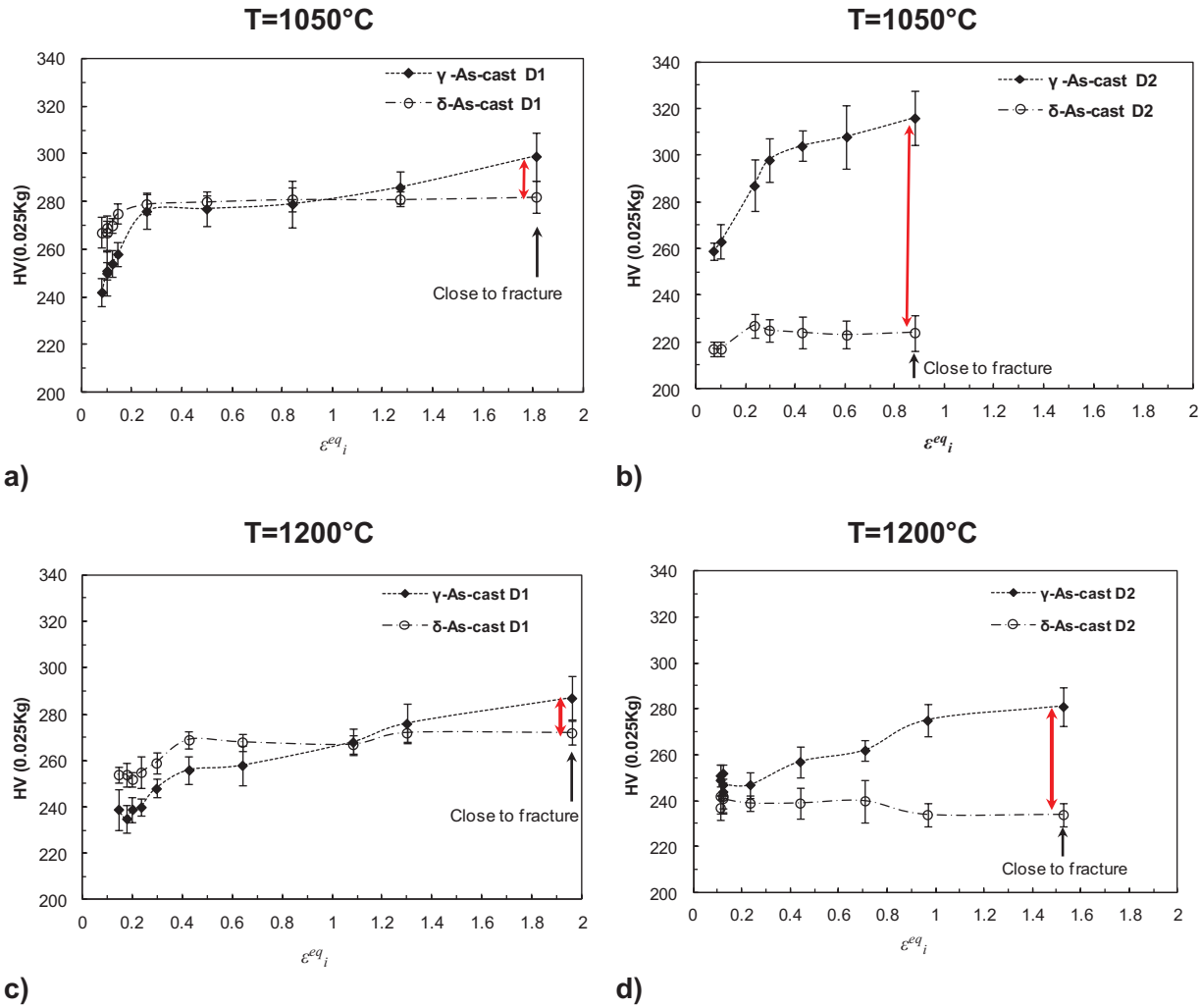


Figure III.18. Micro-hardness profiles along the homogeneous zone of DENT specimens in both phases; a) alloy D1, T=1050°C; b) alloy D2, T=1050°C; c) D1, T=1200°C; d) D2, T=1200°C. It is considered that there was no significant gradient of temperature along the region where the hardness tests were performed.

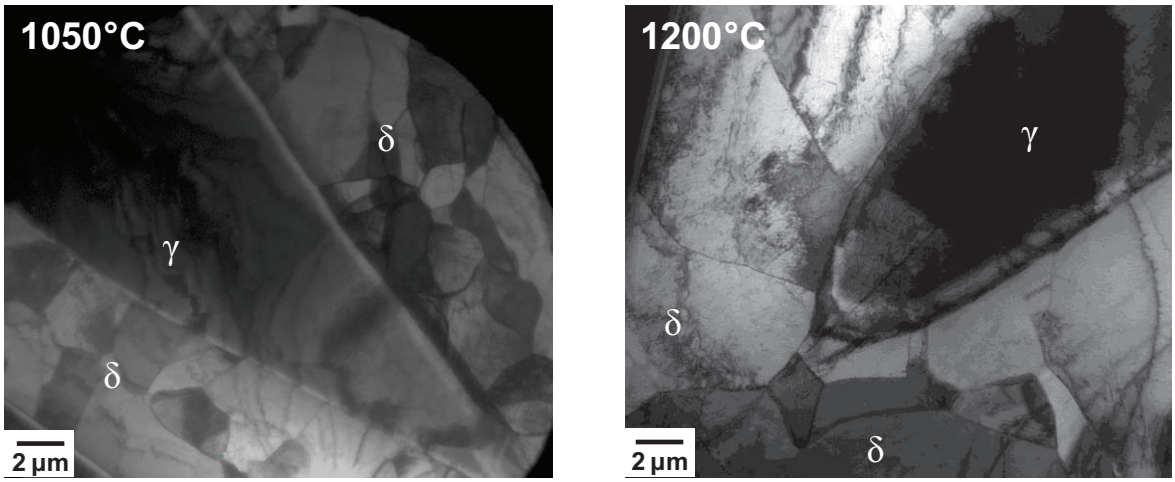


Figure III.19. TEM micrographs taken of the homogeneous zone of D2 broken DENT-specimens. A well-recovered microstructure in the ferrite with subgrains; and a high dislocation density with no sign of recrystallization in the austenite; a) T=1050°C; b) T=1200°C.

The austenite hardness is almost the same in each grade with the D1-austenite softer than the D2-austenite. However, differences in terms of the ferrite hardness values between the grade D2 and D1 can be pointed out. The hardness of the D2 ferrite fluctuates between 220 and 230 HV whereas the D1 ferrite exhibits higher values, around 280 HV. The harder ferrite of the D1 grade contributes to decrease the mismatch between the hardness of the austenite and the hardness of the ferrite. For instance, close to fracture, this mismatch is around 100 HV for the alloy D2 as it is only around 20 HV for the alloy D1 at 1050°C. At 1200°C, this mismatch tends to reduce. These preliminary results suggest the existence of differences in the stress and strain partitioning among the alloys and with temperature. Nevertheless, it is important to specify that these measurements have been performed at room temperature and as a consequence give only qualitative indications which must be confirmed at high temperature.

At this stage, it is difficult to state which of the factors is playing the dominant role: the microstructure (phase ratio and austenite lath size) or the difference in the rheology between ferrite and austenite. Chapter IV will be entirely dedicated to the second aspect through quantitative determination of the high temperature micro-scale strain distribution in both alloys.

III.3.2.2 Origin of the dispersion of the results

The application of the EWF concept at high temperature on duplex stainless steels gives interesting results but the dispersion of the results cannot be neglected, significantly affecting the essential work of fracture. This point requires more discussion.

Metallographic characterization of the as-cast slabs has revealed significant heterogeneity in the austenite content and in the lath mean thickness along the thickness of the slab, see Figure III.17 and Table III.4. This gradient of microstructure appears in the alloy D2 as-cast slab as well as in the alloy D1 as-cast slab (Figure III.17), see illustration of this gradient in the alloy D2 in Figure III.20.

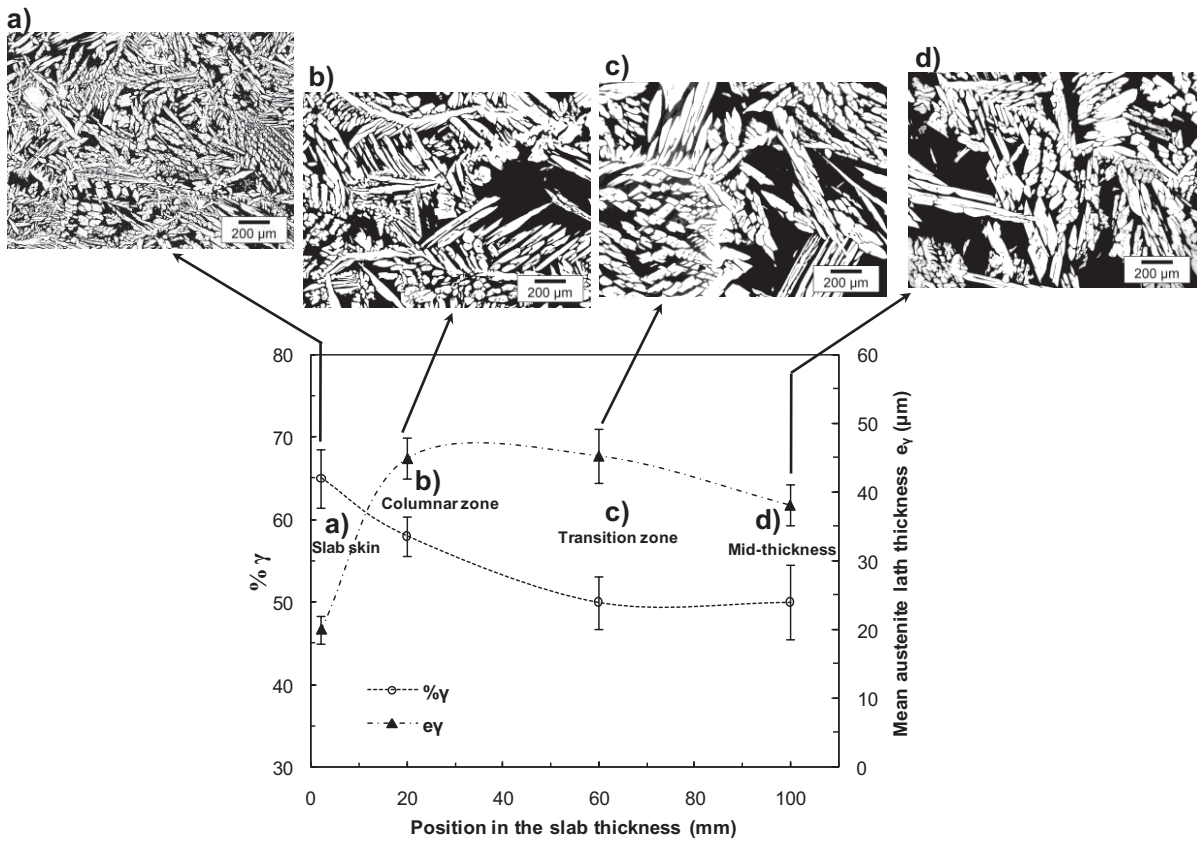


Figure III.20. Illustration of the alloy D2 as-cast slab heterogeneity through thickness; a) slab skin; b) columnar zone; c) transition zone; d) centre of the slab. The austenite is in white and the ferrite is in black.

The microstructural heterogeneity through the slab thickness can be explained by the process conditions and, more specifically, by the difference of cooling rate between the skin and the interior of the slab: the faster the cooling rate, the thinner the austenite laths. The microstructural differences between the two alloys can stem from differences in terms of chemical composition heterogeneities as well as from the process conditions.

The dispersion of the results can be attributed to the microstructure heterogeneity of the as-cast slabs. An rough estimation of the dispersion can be obtained by performing several tests with a given ligament length. For instance, two DENT specimens with a ligament length of 25mm belonging to D1 were tested. The total specific work of fracture, w_{tot} was significantly different: 582 kJ.m^{-2} for one specimen and only 503 kJ.m^{-2} for the other one.

These microstructures turn out to be too heterogeneous for performing reproducible hot ductility investigations delivering clear non ambiguous conclusions about the different parameters playing a role, hence motivating the generation of more homogeneous microstructures.

III.3.3 Conclusions

- In this part, the EWF concept was applied at high temperature to different grades of duplex stainless steels in the as-cast conditions. The results have shown that this method is a discriminating tool to characterize the hot tearing resistance of such materials.

- At 1050°C, the grade D1 is two times more resistant to crack propagation than the grade D2.

- At 1200°C, the grade D1 remains more ductile than the grade D2 but the difference in term of essential specific work of fracture is not significant considering the dispersion of the results.

- Fracture observations and damage quantification match very well with the EWF results.

- Hardness characterizations have permitted to highlight the softening mechanisms involved or not in each phase: dynamic recovery in the ferrite and no sign of recrystallization but a high dislocation density in the austenite. This last comment suggests the occurrence of stress and strain partitioning between ferrite and austenite at high temperature with a more significant effect in the D2-grade.

- The dispersion of the results is significant, attributed to the microstructure heterogeneity through the slab thickness: phase ratio and austenite lath size. This last comment suggests that better results, i.e. with less scattered and more accurate values of the essential specific work of fracture, could be obtained if homogeneous microstructures are considered.

III.4 Generation of model microstructures

The goal is to develop homogeneous microstructures of either the lath (Widmanstätten microstructure: 'W') or the equiaxed γ-austenite (equiaxed microstructure: 'E') in a δ-ferrite matrix which is stable at 1050°C, which is thus the temperature selected to measure the hot ductility. This effort to engineer microstructures must result in (1) a reduction of the dispersion, hence improving the accuracy of the results and (2) a more accurate determination of the influence of phase morphology on the hot workability comparing two different austenite morphologies with the same phase ratio. This last point has to be emphasized because, as pointed out in the bibliographical review (Chapter II), the phase ratio can significantly affect the hot ductility of duplex stainless steels.

Particular attention is paid to microstructural evolutions leading to different austenite morphologies starting from the same metallurgical state. In depth understanding of the nucleation and growth during the $\delta \rightarrow \gamma$ phase transformation allows the identification of the appropriate heat treatments. Some details concerning the different heat treatments are given for the D2 grade. For the alloy D1, as the results are very close to those of the D2 grade, only the resulting microstructures obtained with the appropriate heat treatments are presented.

III.4.1 Materials and characterizations

As the purpose of this section consists in generating homogeneous microstructures, it has been decided to start from a different and homogeneous metallurgical state, i.e. with reduced chemical segregations and with a similar microstructure whatever the position in the thickness of the metal blocks . From now on, a more homogeneous initial state, i.e. the hot-rolled material (industrial transfer bar), was used instead of the as-cast material. The materials, i.e. the D1 and D2 grades, in the as-received conditions present an elongated austenite in the rolling direction, see Figure III.21.

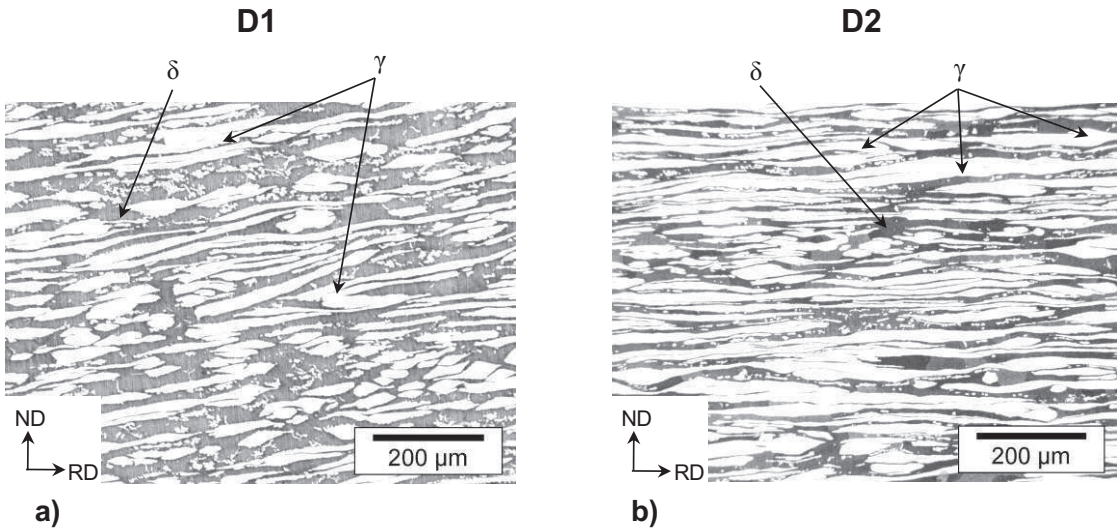


Figure III.21. Microstructures in the as-received conditions, i.e. after hot rolling; a) D1; b) D2.

Microstructural characterizations were carried out using the methods described in section III.2.3.2. Electron backscattered diffraction (EBSD) was used to determine crystallographic orientation relationships. Prior to the etching, the distribution of Cr, Ni and Mo in the austenite grains was analyzed by electron microprobe analysis. Specimen preparation for EBSD required additional steps. After the 1µm alumina polishing, samples were mechanically polished in colloidal silica with a 0.04µm particle size for 2min.

III.4.2 γ-Widmanstätten microstructure

III.4.2.1 Understanding of the as-cast slab microstructure

Generating a Widmanstätten microstructure requires a good understanding of the as-cast slab microstructure. The as-cast microstructure consists of a ferritic matrix with allotriomorphic austenite on the grain boundaries and a Widmanstätten austenite (γ-Widmanstätten) laths inside the grains. The schematic equilibrium phase diagram provides qualitative indications about the origin of the microstructure (Figure I.5): from the liquid, the alloy solidifies into δ-ferrite (Figure I.5.a). During cooling, the austenite precipitates by a mechanism of nucleation and growth. Allotriomorphic austenite (γ-allotriomorphic) nucleates at existing δ-ferrite grain boundaries (Figure I.5.b). Widmanstätten austenite laths nucleate from the allotriomorphic austenite with a Kurdjumov-Sachs orientation relationship Figure I.5.c (the Kurdjumov-Sachs orientation relationship was checked, see Figure III.22).

The composition profile obtained by WDS (Wavelength Dispersion spectroscopy) across an austenite lath shows that the austenite growth is diffusion-controlled with Cr partition between γ and δ (Figure III.23).

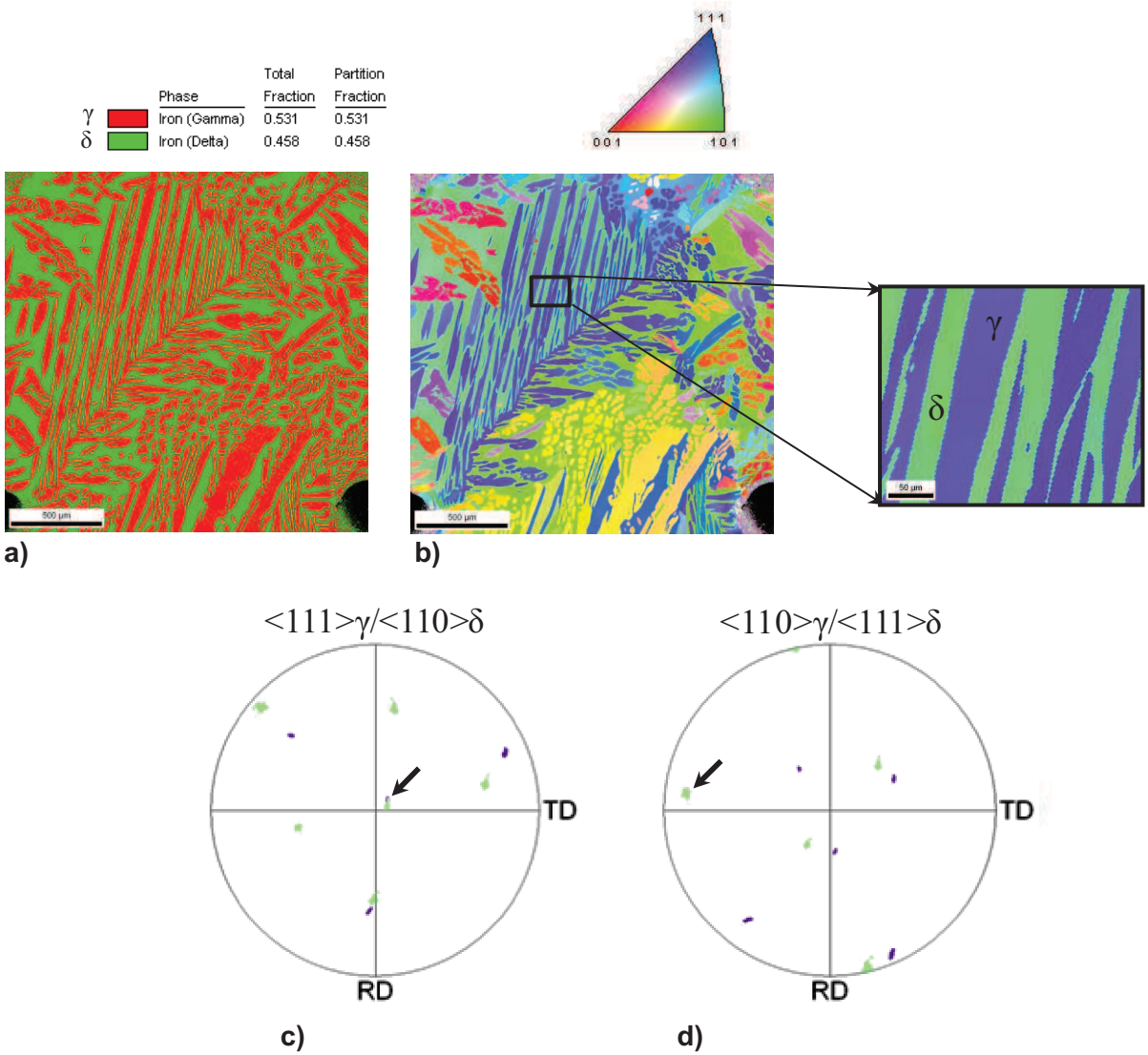


Figure III.22. EBSD analysis of the D2 as-cast microstructure; a) phase map; b) inverse Pole Figure orientation map; overlaying of c) <111>γ and <110>δ and of d) <110>γ <111>δ poles figures, showing the existence of Kurdjumov-Sachs orientation relationship between δ and γ.

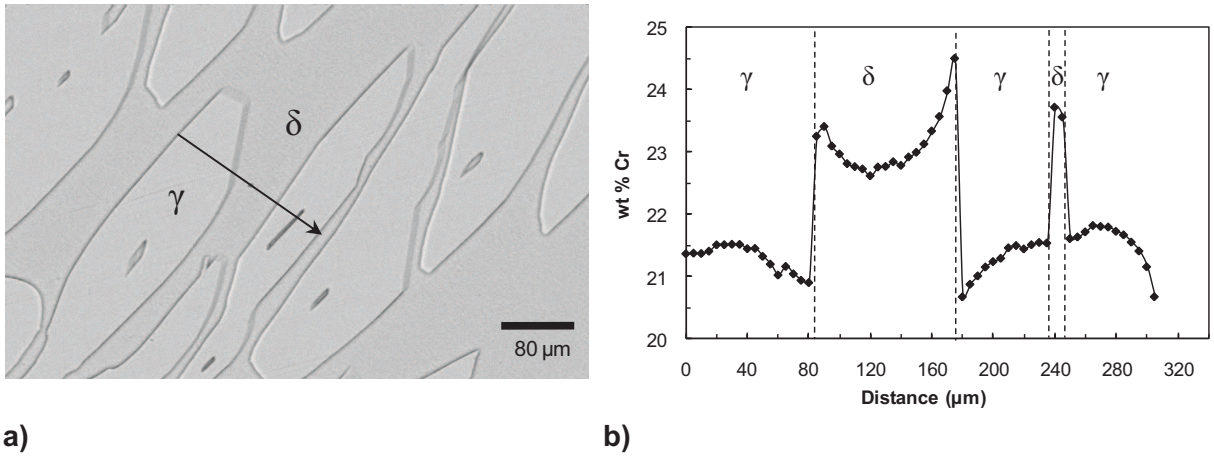


Figure III.23. Composition profile in wt% Cr from a D2 specimen obtained by WDS.

III.4.2.2 Generation of a γ-Widmanstätten microstructure

In order to produce a homogeneous Widmanstätten microstructure stable at 1050°C, the following heat treatment was used (HTW.1): solution-treatment at 1380°C for 15min in δ single-phase region, cooling to 1050°C in the δ+γ two-phase region, i.e. the temperature of the future mechanical test, holding for 8h at 1050°C, and finally water quenching (WQ) to room temperature, see Figure III.24.a. The thermal stability of the lath microstructure was assessed by annealing at 1050°C for 20min showing no evolution of the austenite volume fraction ($\%\gamma$), nor of the lath size (e_γ), see Figure III.24.b. If a specimen follows a similar thermal history with a shorter annealing time at 1050°C (HTW.2, see Figure III.24.c), a homogeneous microstructure is obtained but the stability test reveals that the microstructure is not stable: a fine secondary austenite (γ_2) has nucleated in the δ-ferrite matrix (see encircled regions in Figure III.24.d).

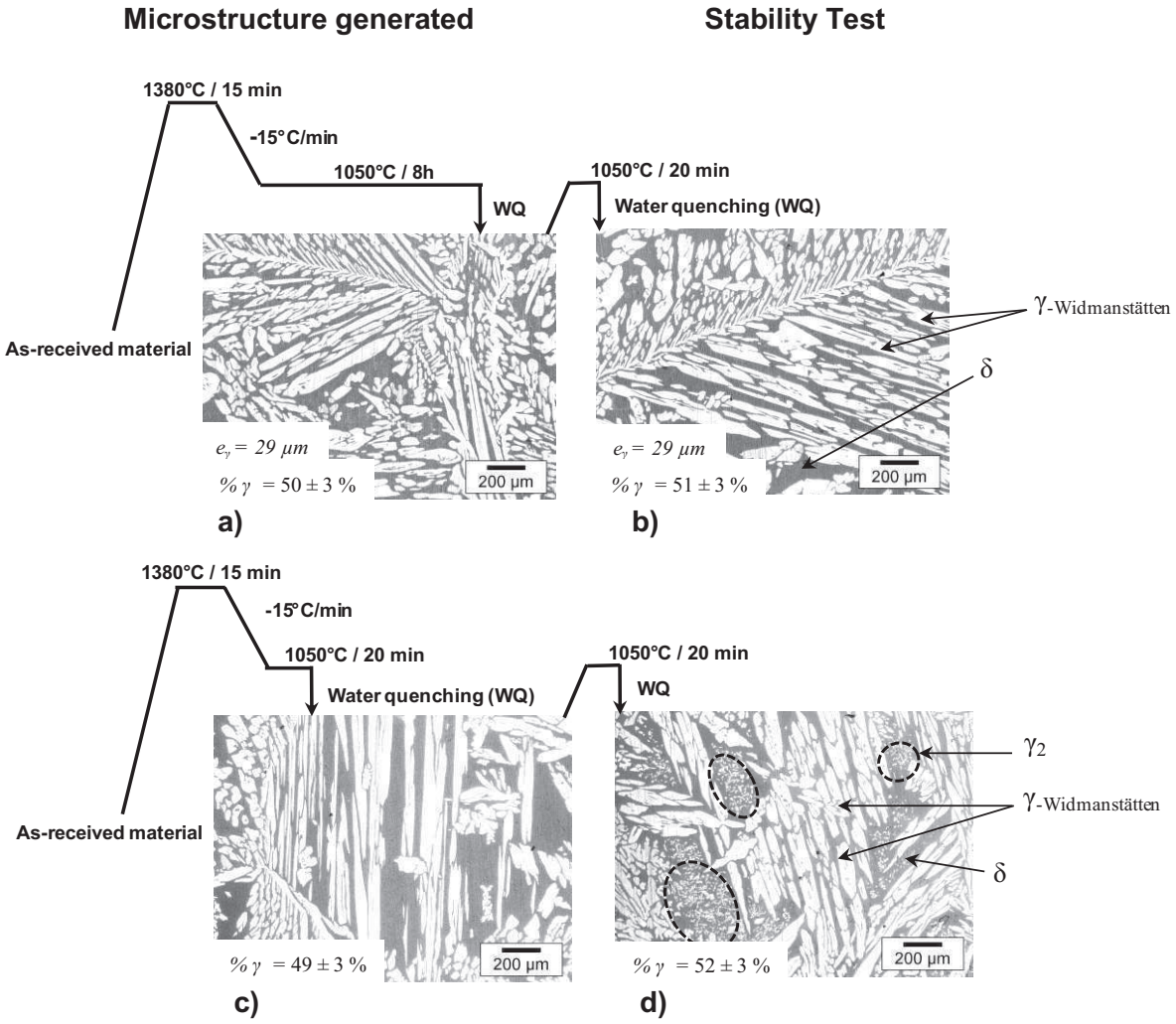


Figure III.24. Schematics of the HTW applied to D2 and resulting microstructures; white = γ, grey = δ; a) HTW.1; b) stability test of HTW.1; c) HTW.2; d) stability test of HTW.2. The encircled zones indicate the precipitation of the secondary fine austenite.

The austenite lath size can be optimized by controlling the cooling rate since the faster the cooling rate, the thinner the austenite laths, see Figure III.25. Eventually, after a few attempts, we have successfully generated homogeneous Widmanstätten microstructures with a controlled lath thickness, reproducing the as-cast slab microstructure.

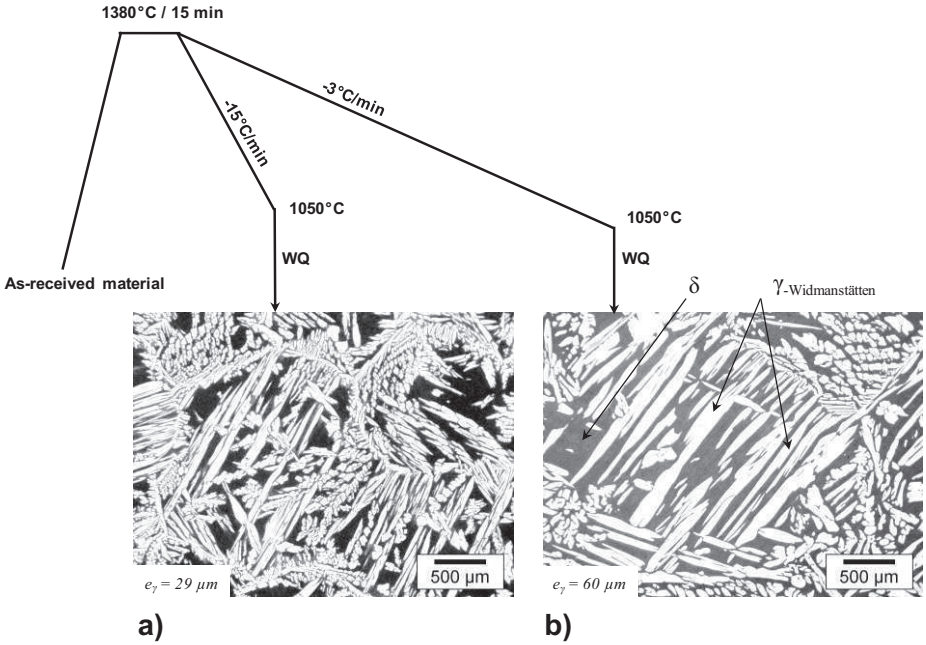


Figure III.25. Influence of the cooling rate on the austenite lath thickness in the D2 Widmanstätten microstructures.

III.4.3 γ-Equiaxed microstructure

In order to generate from the as-received material an equiaxed microstructure (E), that is thermally stable at 1050°C, an annealing at 1250°C (temperature required to dissolve quickly the fine secondary austenite, chromium nitrides, sigma or chi phase which could be present initially in the as-received condition) was followed by water quenching (WQ). An isotropic microstructure with a volume fraction of austenite close to the equilibrium fraction ($\%\gamma_{eq}$ = 35%) was obtained (Figure III.26.a).

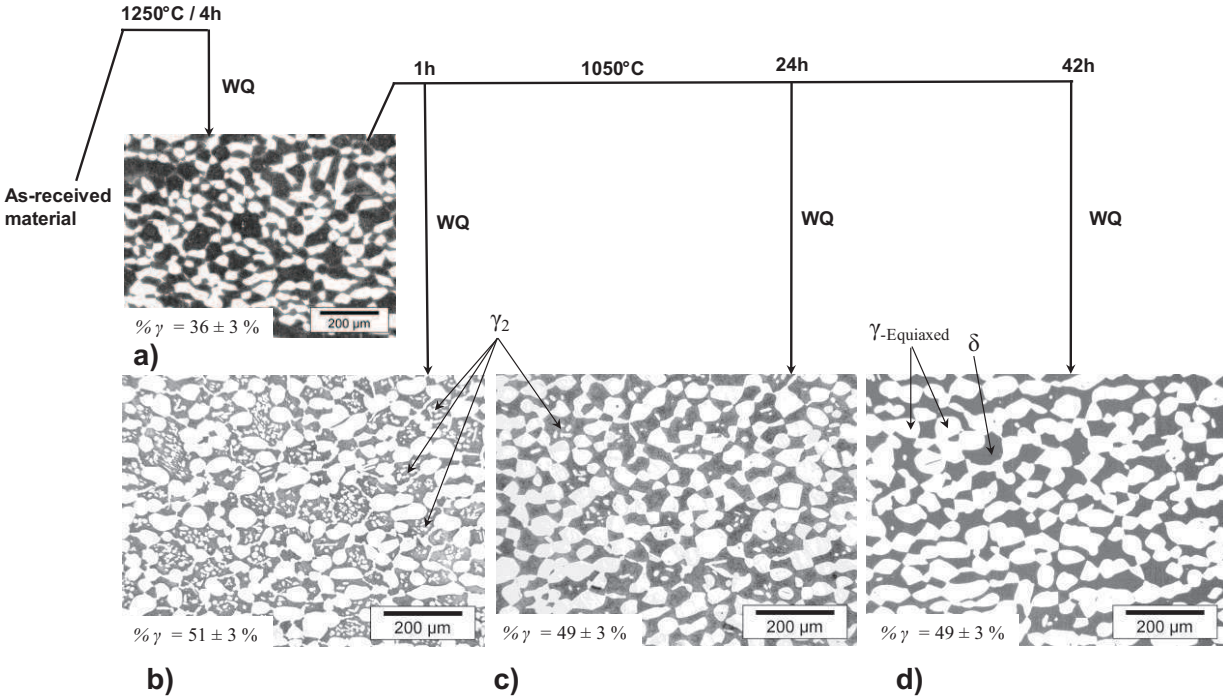


Figure III.26. Schematics of the HTE.1 applied to D2 and resulting microstructures; white = γ, grey = δ; a) 1250°C/4h + WQ; b) 1250°C/4h + WQ + 1050°C/1h + WQ; c) 1250°C/4h + WQ + 1050°C/24h +WQ; d) 1250°C/4h + WQ + 1050°C/42h + WQ.

As the hot ductility is characterized at 1050 °C, the aim is to generate the equiaxed austenite morphology at 1050°C. First, the HTE.1 (Heat Treatment for generating an equiaxed austenite) was performed (Figure III.26) leading to the expected microstructure only after a very long annealing at 1050°C (Figure III.26.d). When annealing at 1050°C was shorter (Figure III.26.b & .c), fine secondary austenite appears inside the δ-ferrite matrix. Increasing the duration of the annealing at 1050°C promotes coarsening which suppresses fine secondary austenite leading to the desired microstructure. However such a treatment is very long, i.e. 50h. In order to generate homogeneous equiaxed austenite morphology after only 5h of heat treatment, a slow cooling down from 1250°C down to 1050°C was performed promoting growth stage at the expense of nucleation (Figure III.27).
Finally, the stability of the microstructure generated by HTE.2 was assessed by performing an annealing at 1050°C for 20min.

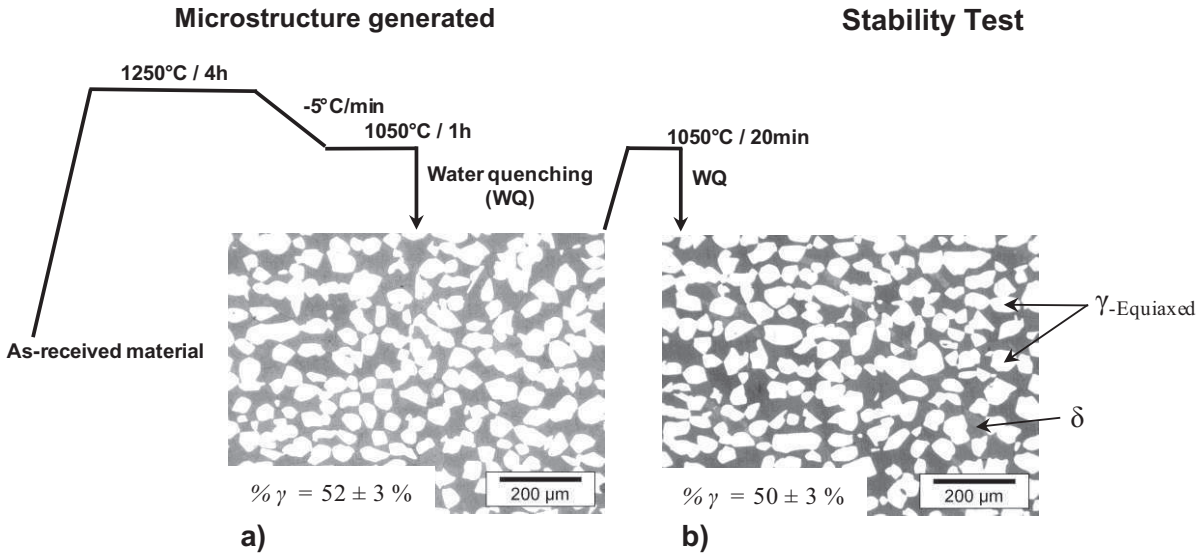


Figure III.27. Schematics of the HTE.2 applied to D2 and resulting microstructures; white = γ, grey = δ; a) HTE.2; b) Stability test of HTE.2.

The time required to eliminate the fine secondary austenite by coarsening can be directly related to the diffusion coefficient of Ni in the ferrite, D^{δ}_{Ni} by the relation:

$$D^{\delta}_{Ni}(T) = D_0 \cdot \exp(-Q/RT), \qquad \text{eq III-9}$$

where D_0 is the pre-exponential constant, Q is the activation energy, R the universal gas constant, and T is the temperature in Kelvin.

From the calculation of the diffusion coefficient of Ni in the ferrite (eq III-9), the diffusion length, l^{δ}_{Ni} can be estimated by eq III-10:

$$l^{\delta}_{Ni}(T) = \sqrt{D^{\delta}_{Ni}(T) \cdot t}, \qquad \text{eq III-10}$$

where $D^{\delta}_{Ni}(T)$ is the diffusion coefficient of the nickel in the ferrite at a temperature T, and t is the time.

For instance, the fine secondary austenite tends to disappear as soon as the diffusion length l^{δ}_{Ni} is larger than the distance between fine secondary austenite and a coarser equiaxed austenite grain.

Figure III.28 gives an estimation of the Ni-diffusion length in the ferrite for different duration of annealing at 1050°C.

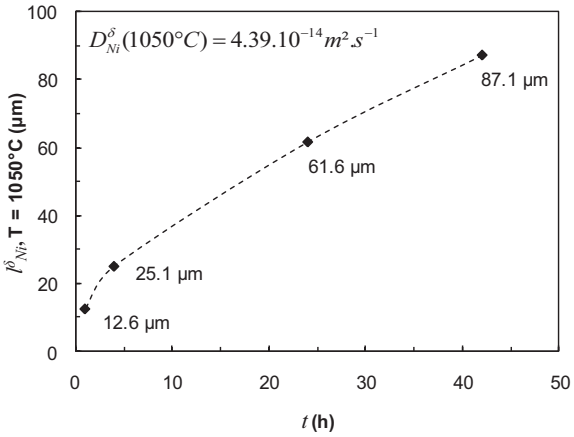


Figure III.28. Evolution of the Ni-diffusion length in the ferrite as a function of time at T = 1050°C.

III.4.4 Conclusions

Proper control of phase transformation mechanisms has allowed the generation of a variety of microstructures with different phase morphologies. By controlling the temperature, the duration of annealing sequences and the cooling rate, alloys with a desired phase proportion, and desired size and shape of the microstructure constituents have been produced. Figure III.29 summarizes, for both grades, the resulting microstructures generated with appropriate heat treatments.

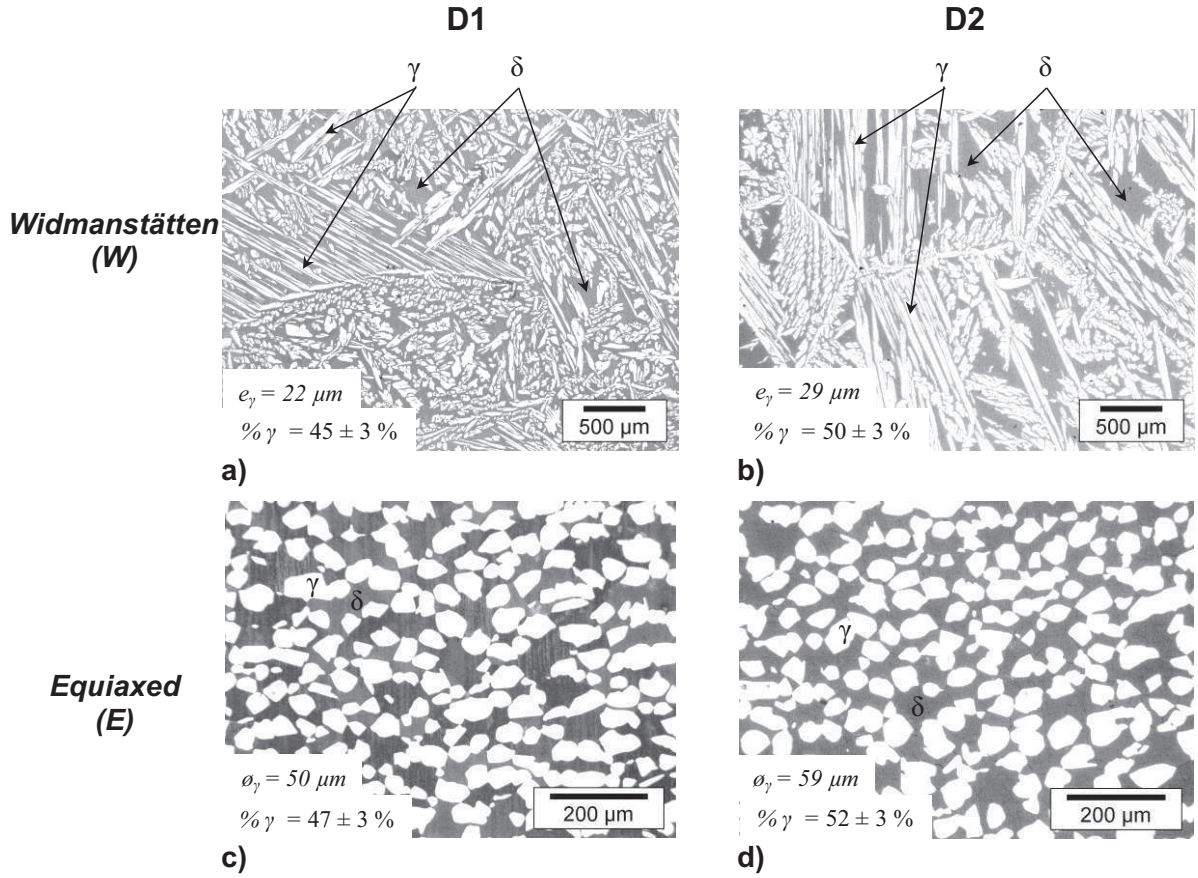


Figure III.29. Summary of the model microstructures obtained with the appropriate heat treatments; a) D1 Widmanstätten microstructure after HTW.1; b) D2 Widmanstätten microstructure after HTW.1; c) D1 equiaxed microstructure after HTE.2; d) D2 equiaxed microstructure after HTE.2.

As the stable model microstructures required a long time to be generated, i.e. about 5h for an equiaxed microstructure (HTE.2) and more than 8h for a Widmanstätten one (HTW.1), the generation of these microstructures in the Gleeble machine was inconceivable, especially when several DENT specimens with different ligament lengths had to be tested. In addition, the time spent at high temperature lead to a considerable oxidation and can also induce decarburization or denitriding, thus affecting the microstructure. Here, this problem has to be taken into account since the two heat treatments leading to the model microstructures include annealing at high temperature (1380°C for HTW and 1250°C for HTE).
This problem was solved by generating the microstructures on 3cm-thick metal blocks. Then, the DENT specimens were machined in the heat treated blocks. Finally, the DENT specimens followed regardless of the microstructure, the thermo-mechanical path history indicated in Figure III.6.a.

III.5 Comparison between D1 and D2 γ-Widmanstätten microstructures

III.5.1 Results

III.5.1.1 EWF results

The heat treatment HTW.1 has been performed on 3cm-thick blocks of alloys D2 and D1 in order to generate the Widmanstätten model microstructures D2_W and D1_W. The resulting microstructures are presented in Figure III.30. The average austenite lath thickness is larger than expected because the furnace could not reach the cooling rate of 15°C.min^{-1}.

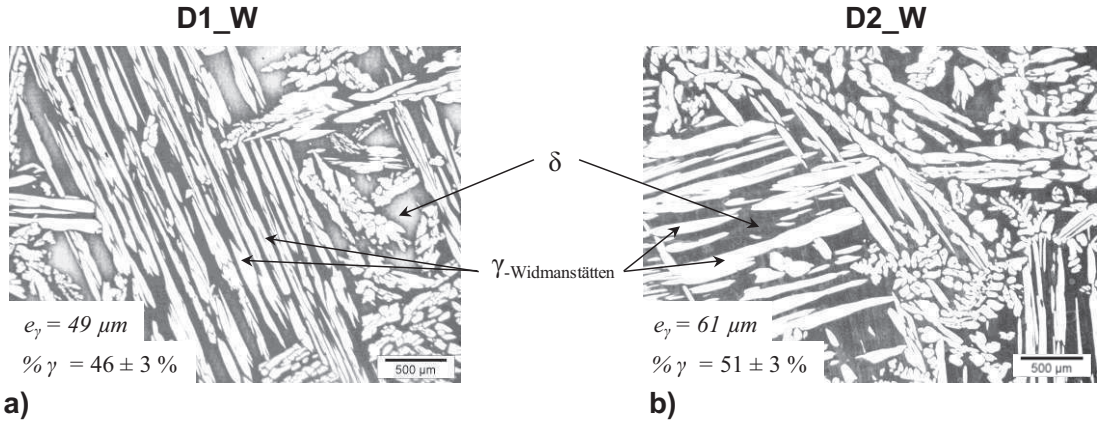


Figure III.30. Widmanstätten model microstructures after HTW.1; a) D2_W; b) D1_W.

The DENT specimens were deformed at 1050°C. A comparison between typical load-displacement curves of both grades is given in Figure III.31.a & b for two different ligament lengths. The displacement corresponding to the maximum of the load is approximately the same for both grades whatever the ligament length. However, for a given ligament length, the maximum load is significantly different, always higher in the alloy D1_W.

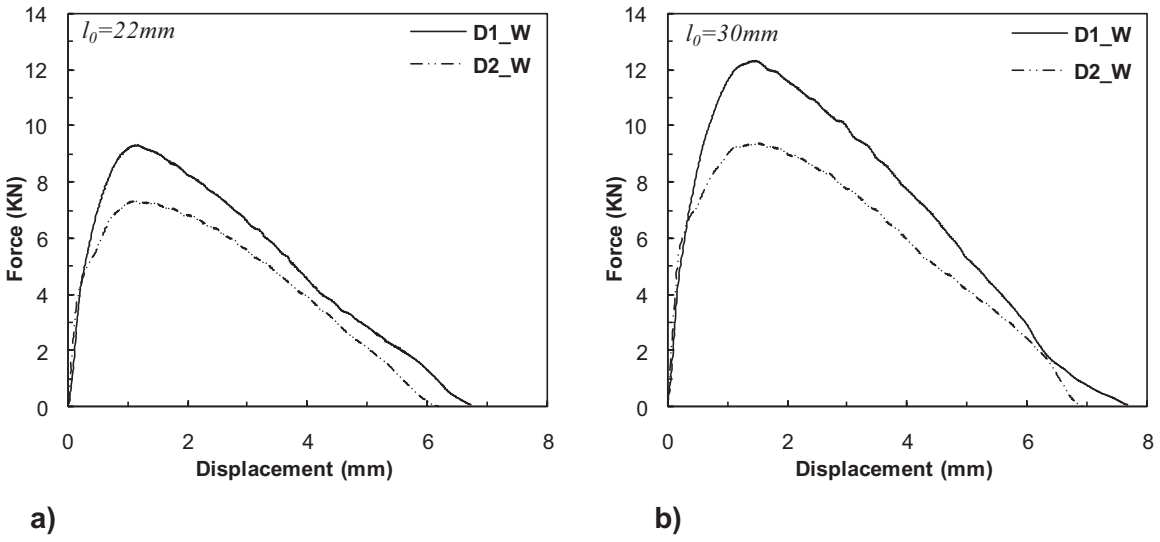


Figure III.31. Comparison between typical force-displacement curves of DENT specimens with the same ligament length l_0 for both grades, D1_W and D2_W with a Widmanstätten microstructure; a) l_0= 22mm; b) l_0 =30mm.

As in the previous section, the total specific work of fracture is plotted as a function of the ligament length l_0. Compared to Figure III.12.a, the scatter is much smaller as a result of the more homogeneous microstructure of the model material. The results, shown in Figure III.32, obey, as expected, a linear relationship for both grades.

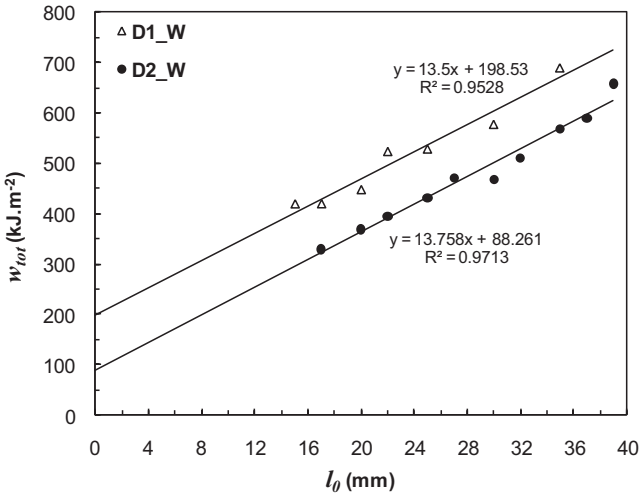


Figure III.32. Variation of the specific work of fracture versus ligament length for separation of the essential work of fracture. Comparison between two Widmanstätten microstructures at 1050°C: D1_W and D2_W.

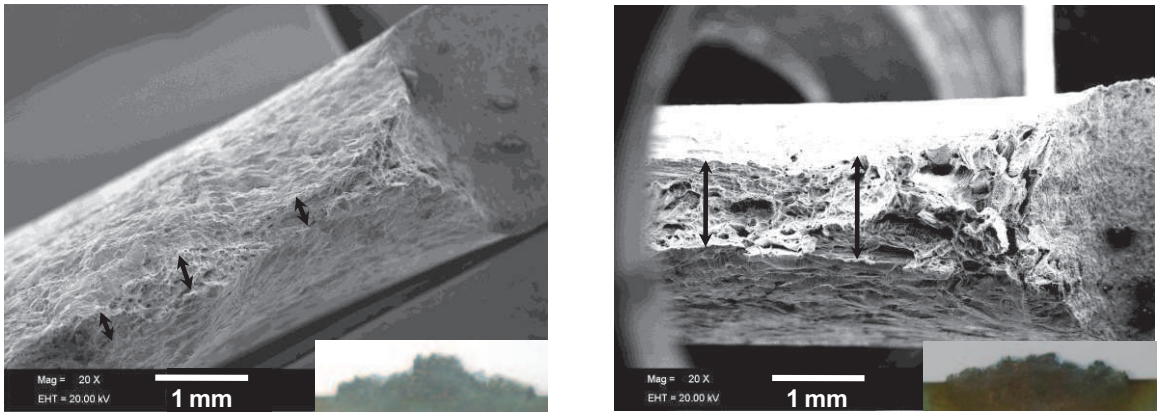
Table III.5 summarizes the results obtained from Figure III.32. The specific work of fracture at 1050°C is equal to 199 kJ.m^{-2} and 88 kJ.m^{-2} for microstructures D1_W and D2_W, respectively. It means that at 1050°C, the alloy D1_W is two times more resistant to ductile tearing than the alloy D2_W. This variation is consistent with the variation measured on the as-cast D1 and D2 although the absolute values are lower. This point will be discussed later.

		w_e (kJ.m^{-2})	αw_p (kJ.m^{-3})
D1_W	1050°C	199 ± 33	13.5 ± 1.3
D2_W	1050°C	88 ± 24	13.8 ± 0.8

Table III.5. Results of the EWF method applied at 1050°C to the model Widmanstätten microstructures: D1_W and D2_W.

III.5.1.2 Fracture and damage observations

The fracture surfaces of broken samples were observed by scanning electron microscopy (SEM). Typical fracture surfaces of DENT specimens are shown in Figure III.33. There are no major differences in term of fracture profiles, both microstructures D1_W and D2_W exhibit an irregular fracture profile. The main difference between the two microstructures is the fracture strain (Table III.6). The arrows in Figure III.33 indicate this difference when comparing Figure III.33.a and Figure III.33.b.



a) **b)**

Figure III.33. Fracture micrographs of the broken DENT at 1050°C; a) D1_W (l_0=35mm); b) D2_W (l_0=37mm).

		$\varepsilon^{eq}_{fracture}$
D1_W	1050°C	2.8 ± 0.1
D2_W	1050°C	1.3 ± 0.1

Table III.6. Estimated values of the equivalent strain to fracture by measuring the thickness of the specimen at fracture.

The damage evolution has been characterized on transverse sections of broken specimens for each microstructure, D1_W and D2_W, respectively as in the previous section. Voids nucleate always at the δ/γ interfaces for both grades. From a qualitative point of view, in Figure III.34, the number of damage sites seems to be higher in the D2_W microstructure compared to the D1_W microstructure. The density of damage site was plotted as a function of strain, see Figure III.35. The strain at which the density of cracks significantly changes is different. The crack density becomes considerable for strains around 0.5 for the D2_W microstructure, whereas it requires reaching a strain around 1.2 to start developing a large crack density in D1_W.

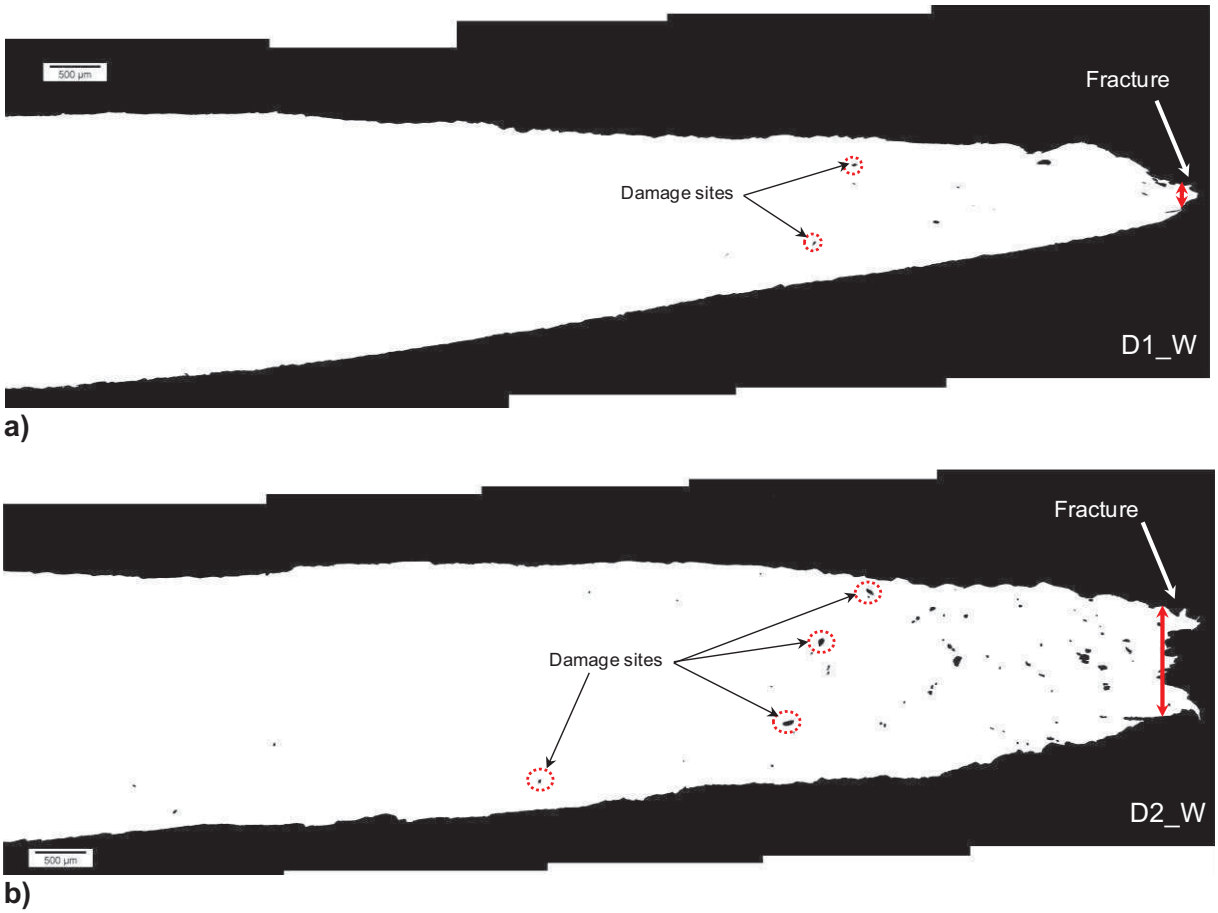


Figure III.34. Polished sections perpendicular to the ligament of broken DENT specimens; a) D1_W; b) D2_W.

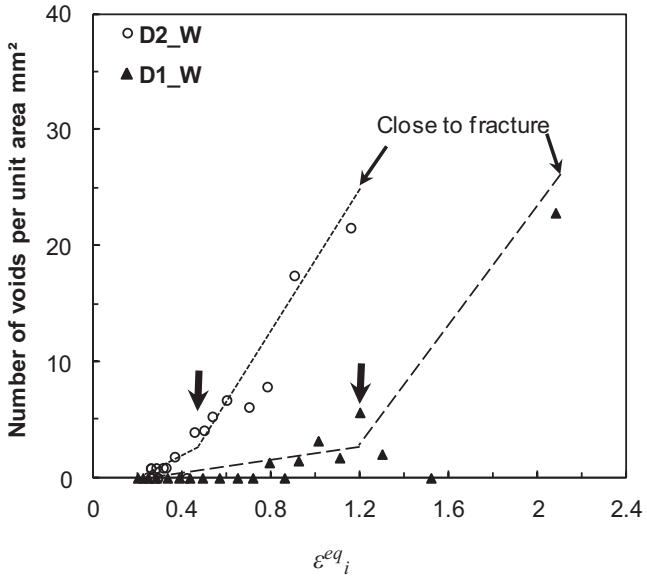


Figure III.35. Evolution of the damage as a function of equivalent strain for both grades. The arrows emphasize the approximate strain at which the damage evolution starts rising significantly.

III.5.2 Discussion

III.5.2.1 Origin of the difference between D1_W and D2_W

According to the experimental results (Table III.5), D1_W is two times more resistant to hot cracking than D2_W. As for the as-cast materials, the origin of this difference has to be discussed in more details regarding microstructural and rheological aspects.

The difference in terms of phase ratio and austenite lath size between D2_W and D1_W was significantly reduced thanks to the production of model microstructures in which austenite content and austenite lath size were well-controlled (Table III.7), but still the difference persists between the two alloys.

	$\%\,\gamma$	$\%\delta$	e_γ (µm)
D1_W	46 ± 3	54	49
D2_W	51 ± 3	49	61

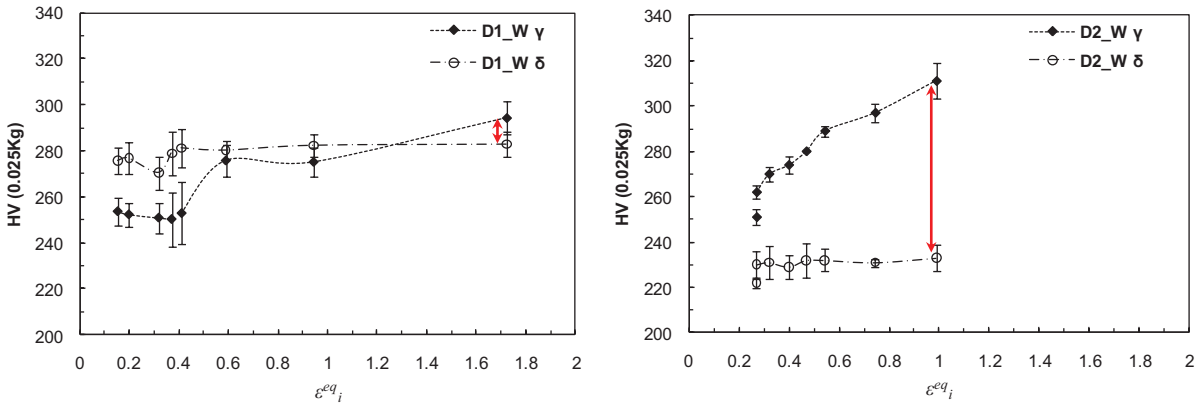
Table III.7. Comparison between D1_W and D2_W.

The micro-hardness profiles corroborate the results obtained in the as-cast conditions at 1050°C, see Figure III.36:

(i) Ferrite undergoes dynamic recovery (no evolution of the ferrite hardness with strain) and no sign of recrystallization is visible in the austenite (only work-hardening).

(ii) The D1_W austenite is slightly softer than the corresponding D2_W austenite and, the D1_W ferrite was significantly harder compared to the D2_W.

(iii) As the deformation progresses, the hardness difference between ferrite and austenite in the alloy D2_W increased dramatically to reach around 100 HV close to fracture. This hardness difference was only about 10-15 HV in the D1_W.



a) **b)**

Figure III.36. Micro-hardness profiles along the homogeneous zone of DENT specimens in both phases; a) D1_W, T=1050°C; b) D2_W, T=1050°C.

The microstructural difference between both Widmanstätten microstructures can be neglected. The difference in term of hot tearing resistance is unchanged compared to the industrial product (a factor two between the essential specific work of fracture of D1 and that of D2_W). As a result, it can be suggested that the rheology factor is predominant in comparison to the microstructure (phase ratio and lath size) factor.

As explained in Chapter IV and shown by S.K.Yerra [in preparation], an increasing mismatch leads to earlier voids nucleation at inclusions sitting at the δ/γ interphase boundaries and faster void growth.

III.5.2.2 As-cast vs. model Widmanstätten microstructures

Applying the EWF concept using homogeneous microstructures improves the quality of the results by reducing the dispersion, see Figure III.37, as indicated by a linear regression coefficient much closer to unity, see Table III.8. The main conclusions are similar comparing the as-cast results with the model microstructure results, see Table III.8:

(1) D1 is two times more resistant to crack propagation at 1050°C than the D2 grade whatever the microstructure: as–cast or model.

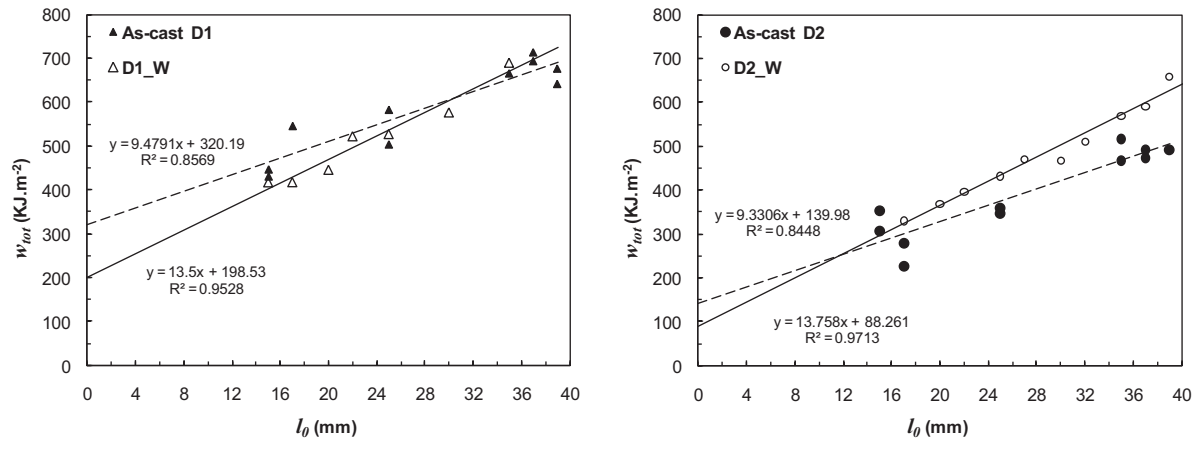
(2) All the characterizations showed that the results (fracture surfaces and profiles, strain to fracture, damage...) obtained on as-cast specimens were very close to those obtained using the model Widmanstätten microstructures.

However an interesting point has to be discussed in more details: the intrinsic values given by the EWF, w_e and the work dissipated in the plastic zone, w_p. The intrinsic values of w_e are much larger in the as-cast microstructures, see Table III.8.

	T (°C)	Fracture Profile Flat vs. Irregular	$\varepsilon^{eq}_{fracture}$	$\varepsilon^{eq}_{damage}$	w_e (kJ.m^{-2})	w_p (kJ.m^{-3})	R² Linear regression coefficient
D1 As-cast	1050	*Irregular*	2.6 ± 0.2	1.3 ± 0.2	320 ± 41	9.5 ± 1.4	0.86
D1_W	1050	*Irregular*	2.8 ± 0.1	1.2 ± 0.2	199 ± 33	13.5 ± 1.3	0.95
D2 As-cast	1050	*Irregular*	1.1 ± 0.2	0.5 ± 0.2	140 ± 38	9.3 ± 1.3	0.84
D2_W	1050	*Irregular*	1.3 ± 0.1	0.5 ± 0.2	88 ± 24	13.8 ± 0.8	0.97

Table III.8. Comparison between the results obtained for as-cast microstructures and model Widmanstätten microstructures.

The heterogeneity of the as-cast microstructures can partly account for these differences increasing the dispersion, reducing the linear regression coefficient and as a consequence affecting the accuracy of the estimated specific essential work of fracture. Actually, applying the EWF concept to as-cast microstructures gives only a qualitative result, it means that only comparisons can be established. On the contrary if accurate and quantitative results are required, model microstructures have to be used. A solution to improve the as-cast microstructure results would consist in breaking several DENT specimens for each ligament length in order to obtain better statistical results [73].



a) **b)**

Figure III.37. Comparison of the EWF results obtained in the as-cast conditions with those obtained starting from model Widmanstätten microstructures at T=1050°C; a) Alloy D1; b) Alloy D2.

III.5.3 Conclusions

- The EWF concept has been applied at high temperature to model Widmanstätten microstructures generated with an appropriate heat treatment permitting to control microstructural parameters such as phase ratio or austenite lath size. The results have shown that at 1050°C, D1_W was two times more resistant to crack propagation than D2_W.

- Characterization of the fracture surfaces and of the damage mechanisms match very well with the EWF results. In addition the results are in agreement with those obtained in the as-cast conditions.

- Hardness characterizations have confirmed the occurrence of stress and strain partitioning between ferrite and austenite: at room temperature $HV_\delta < HV_\gamma$ with a more significant effect in the D2_W microstructure. These results have to be checked and validated at high temperature.

- Using model microstructures significantly improves the accuracy of the results by reducing the dispersion.

III.6 Influence of the phase morphology: γ-Widmanstätten vs. γ-equiaxed

Model microstructures with different austenite morphologies can be generated with an equal balance of phase. In addition, the EWF concept at high temperature can be applied successfully and gives accurate results of the essential specific work of fracture. To summarize, all the required tools are available to investigate the influence of phase morphology on the hot cracking resistance.

III.6.1 Results

III.6.1.1 EWF results

3cm-thick blocks of alloys D2 have been heat treated (HTE.2) in order to generate an equiaxed model microstructure: D2_E. Then, the DENT specimens were machined from the heat treated blocks and deformed under tension at 1050°C. Figure III.38 shows the microstructures corresponding to each austenite morphology: Widmanstätten (D2_W) or equiaxed (D2_E).

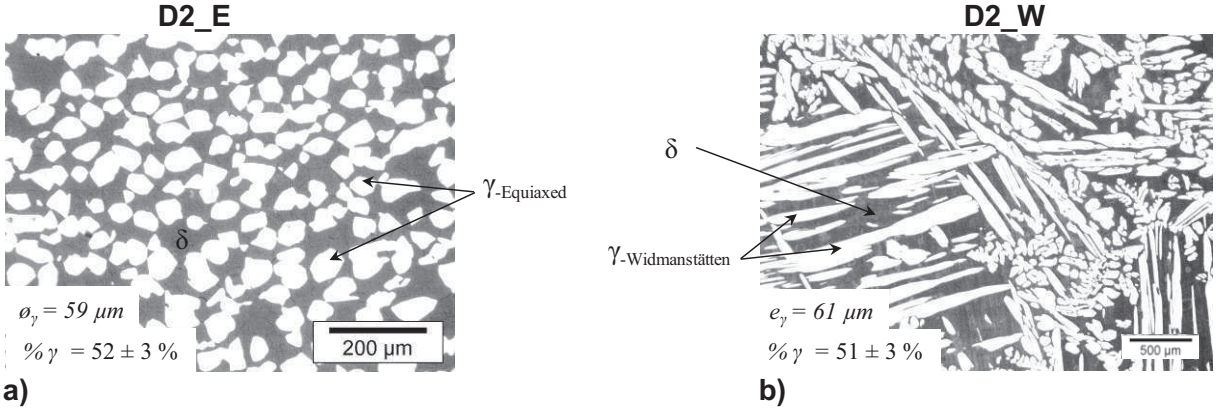


Figure III.38. Generated microstructures with a constant phase ratio but a different austenite morphology; a) Widmanstatten austenite (D2_W); b) equiaxed austenite (D2_E).

The total specific work of fracture, w_{tot}, was calculated from the areas under the load-displacement curves. Typical load-displacement curves obtained are presented for both morphologies in Figure III.39. Up to the maximum force, the curves corresponding to the two morphologies overlap. However, after the maximum, the D2_E microstructure shows more elongation.

As in the previous section, the total specific work of fracture is plotted as a function of the ligament length l_0. The results obtained with a model Widmanstätten microstructure D2_W are reported on the same graph (Figure III.40) in order to provide a comparison between the two austenite morphologies.

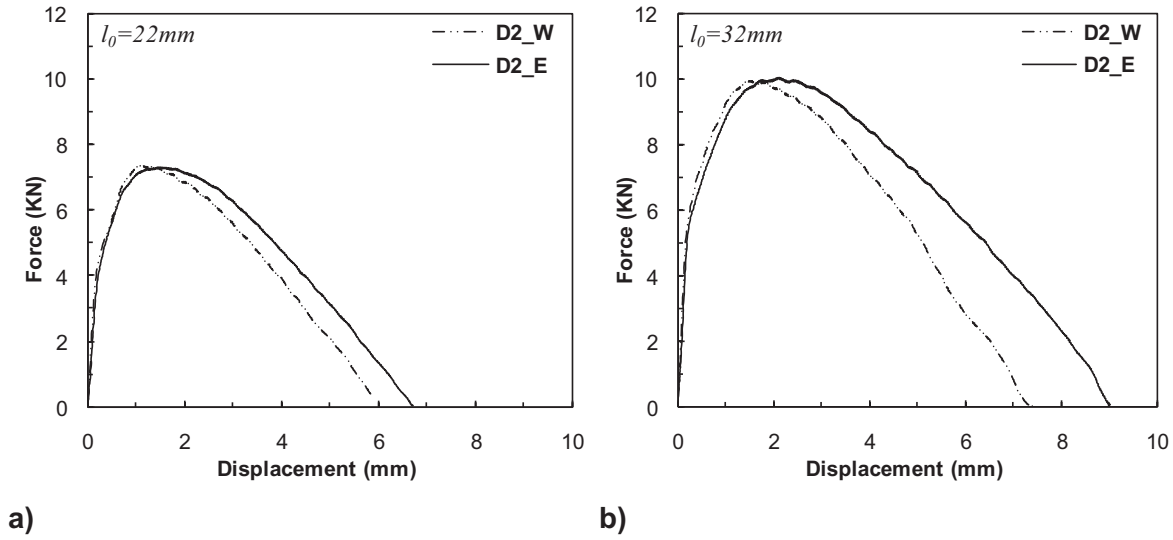


Figure III.39. Comparison between typical force-displacement curves (alloy D2) for both austenite morphologies; a) l_0=22mm; b) l_0=32mm.

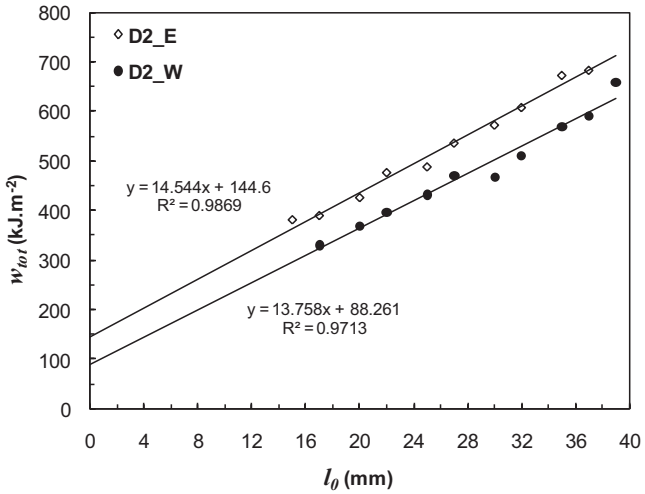


Figure III.40. Variation of the specific work of fracture as a function of the ligament length for separation of the essential work of fracture. Comparison between the two microstructures at 1050°C: D2_E and D2_W.

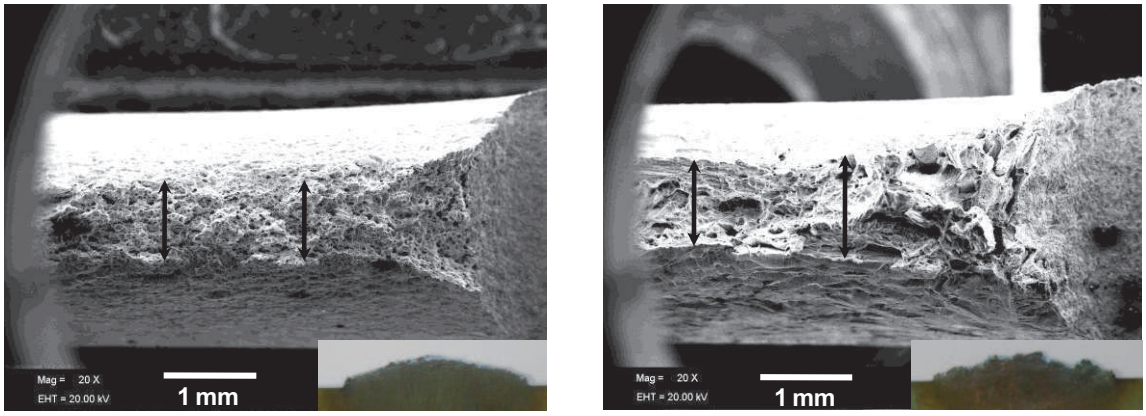
Table III.9 summarizes the results provided in Figure III.40. The plane stress specific work of fracture at 1050°C is equal to 145 kJ.m^{-2} and 88 kJ.m^{-2} for the microstructures D2_E and D2_W, respectively. It means that at 1050°C, the equiaxed austenite morphology is almost twice more resistant to ductile tearing than the Widmanstätten austenite morphology.

		w_e (kJ.m^{-2})	αw_p (kJ.m^{-3})
D2_E	1050°C	145 ± 16	14.5 ± 0.6
D2_W	1050°C	88 ± 24	13.8 ± 0.8

Table III.9. Results of the EWF method applied at 1050°C to model microstructures: equiaxed (D2_E) and Widmanstätten (D2_W).

III.6.1.2 Fracture and damage observations

Typical fracture surfaces of DENT specimens are shown in Figure III.41. There is no difference in term of equivalent strain to fracture, see Table III.10. A classical ductile profile with dimples is observed at the micro-scale in both cases. However, fracture profiles are significantly different: D2_E exhibits a flat profile along the whole ligament whereas D2_W exhibits an irregular fracture profile with much coarser dimples.



a) b)

Figure III.41. Fracture micrographs and profiles of the broken DENT at 1050°C; a) D2_E (l_0=35mm); b) D2_W (l_0=37mm).

		$\varepsilon^{eq}_{fracture}$
D2_W	1050°C	1.3 ± 0.1
D2_E	1050°C	1.2 ± 0.1

Table III.10. Estimated values of the equivalent strain to fracture by measuring the thickness of the specimen at the fracture.

The strain at which damage initiates is not very different when comparing both austenite morphologies, around 0.5 ± 0.2.

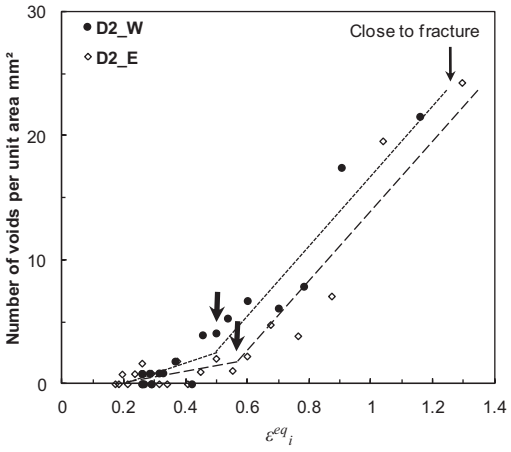


Figure III.42. Evolution of the damage as a function of equivalent strain for both austenite morphologies. The arrows indicate the approximate strain at which damage nucleation occurs.

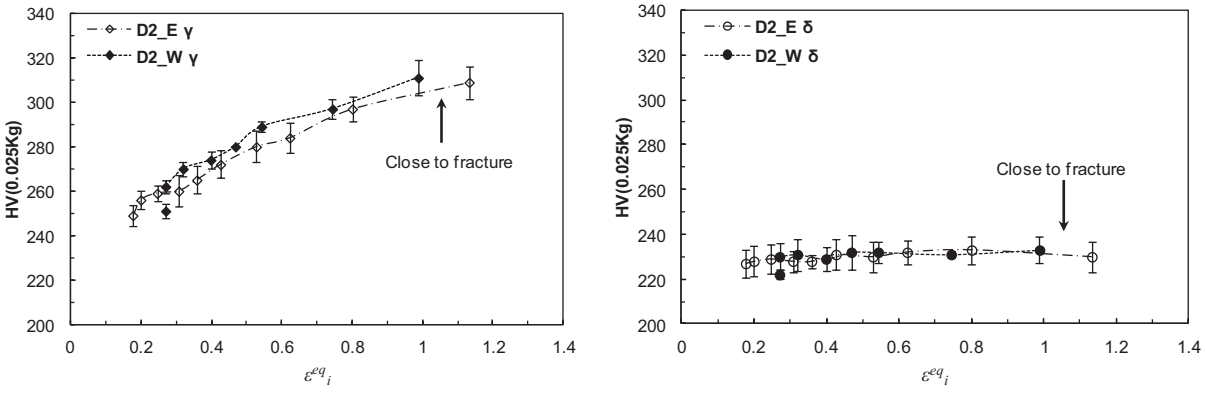
III.6.2 Discussion: D2_E vs. D2_W

As the equiaxed morphology and the Widmanstätten morphology were generated in order to obtain a similar phase ratio, this argument cannot be invoked to explain the difference of hot tearing resistance between D2_E and D2_W. The origin of the difference between D2_E and D2_W is not yet clearly identified. Some possible reasons of this difference are:

- ❖ The rheology;
- ❖ The nature of the interphase boundaries;
- ❖ The effect of the morphology on the crack path.

III.6.2.1 Rheology

Both morphologies have been generated using different heat treatments. The partitioning of the alloying elements between ferrite and austenite can be different from one morphology to another. Such difference can, on the one hand, change the rheology contrast between the two phases, and on the other hand affect the softening behaviour of the ferrite and austenite. The micro-hardness profiles performed on both phases for each morphology were exactly the same (Figure III.43). As a consequence, the argument of the difference of softening behaviour between both microstructures was not valid, see also further in section III.6.3.2.2.



a) **b)**

Figure III.43. Comparison between the micro-hardness profiles along the homogeneous zone of DENT specimens in both morphologies: D2_E and D2_W; a) Profile in the austenite, T=1050°C; b) Profile in the ferrite, T=1050°C.

III.6.2.2 Nature of the interphase boundaries

Pinol-Juez et al. [12, 95] have compared via a high temperature torsion test the ductility of a standard duplex stainless steel in the as-cast condition and after hot rolling. Both microstructures showed differences: stress strain curves did not have the same shape, the crack sensitivity was higher in the as-cast conditions than in the hot rolled material, and the deformation mechanisms were not similar. Pinol-Juez et al. [12] have essentially attributed these differences to the nature of the interfaces. Indeed, in the as-cast conditions, the interfaces mainly present a Kurdjumov-Sachs orientation relationship, giving them a semi-coherent character. This coherency of the interfaces does not allow them to accommodate the strain by sliding at the δ/γ boundaries. The authors explained that the predominant damage mechanism was the nucleation of voids at the δ/γ interfaces and crack propagation in the ferrite. On the contrary, in the microstructure after hot rolling, the δ/γ interfaces are incoherent due to the combined effect of strain and softening mechanisms. Sliding at the δ/γ boundaries was the predominant mechanism and allowed a better accommodation of the deformation.
In this work, it has been checked that in the Widmanstätten microstructure, the interphase boundaries showed a Kurdjumov-Sachs orientation relationship whereas in the equiaxed microstructure ferrite and austenite are not related by any orientation relationship. Therefore, it can be considered that the nature of the interphase boundaries can contribute to the difference of hot tearing resistance when comparing both morphologies. The microgrids experiments presented in Chapter IV will permit to check if sliding at the interphase boundaries takes place or not depending on the nature of the interfaces. In addition, an estimation of this deformation mechanism will be possible.

III.6.2.3 Effect of the morphology on the crack path

In the microstructure D2_E as well as in the microstructure D2_W, the mechanism responsible for cracking initiation is the growth and coalescence of voids ahead of the blunted crack tip (Figure III.14). The fracture and damage observations did not reveal strong differences between both morphologies. Neither the equivalent strain to fracture (approximately the same value for D2_E and D2_W, Table III.10), neither the damage nucleation equivalent strain showed significant difference (Figure III.42).
However, the fracture profiles corresponding to each morphology exhibit a different shape, see Figure III.44. This difference in terms of fracture profile is directly related to the morphology of the austenite. Indeed, as the voids nucleate at the interphase boundaries and propagate along these interfaces, the longer these interfaces are, the longer are the micro-cracks.

Despite the recurring change of crack path, the fracture profile of the equiaxed microstructure exhibits a relatively flat shape because the crack propagates only over short distances, see Figure III.44.a.

In the Widmanstätten microstructure, the length of the austenite laths can reach several millimeters, and such interfaces form favorable paths for crack propagation. The fracture profile irregularity was explained by the length of the interphase boundaries (several millimeters) and the change of crack propagation as a function of the austenite laths orientation, see Figure III.44.b.

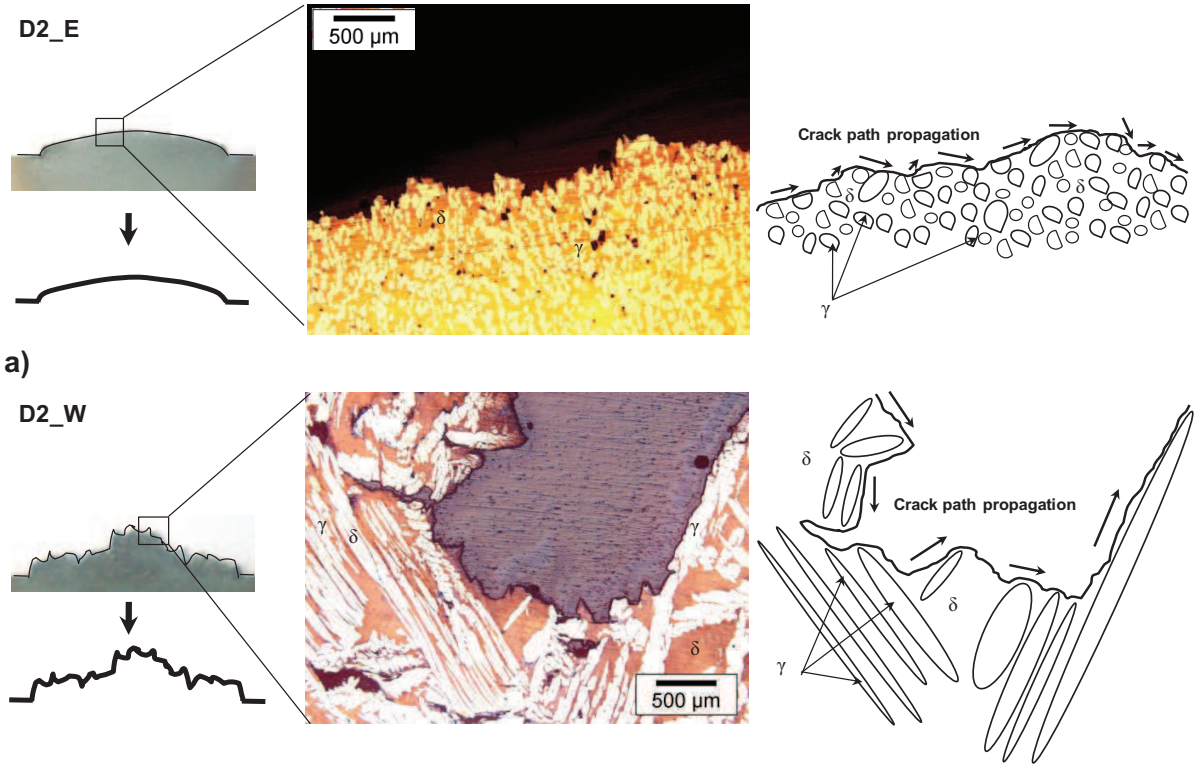


Figure III.44. Illustration of the difference of cracking propagation between two different morphologies; a) an equiaxed morphology D2_E; b) a Widmanstätten morphology D2_W.

Cotterell and Reddel [70] have also proposed the following relationship:

$$w_e = k\sigma_c\delta_c, \qquad \textbf{eq III-11}$$

where k is a factor depending on the shape of the load-displacement curve, σ_c is a critical stress which can be considered as the mean value of the maximum stress averaged over the ligament, and δ_c is a critical displacement which corresponds to the elongation that must be imposed on the elementary volume representative of the material at the blunted crack tip (fracture process zone) to completely break the material. This critical displacement can be written as,

$$\delta_c = X_c - X_0, \qquad \textbf{eq III-12}$$

where X_c is the height of the fracture process zone at fracture and X_0 is the initial height of the band of material in which, at some point in the deformation history, all the deformation and damage will localize. In the Widmanstätten microstructure, this zone is equal to the mean ferrite channel thickness, $X_0_W \approx 30\mu m$. The crack is forced to propagate between two austenite laths and then the crack path depends on the orientation of the austenite laths, see Figure III.45.a.
In the equiaxed microstructure, it is a bit more difficult to define, but it should approximately be equal to the spacing between austenite particles, i.e. $X_0_E \approx 65\mu m$.

In others words, it means that in the Widmanstätten morphology the crack can select a preferential path such that X_0 is smaller compared to the equiaxed morphology, see Figure III.45.

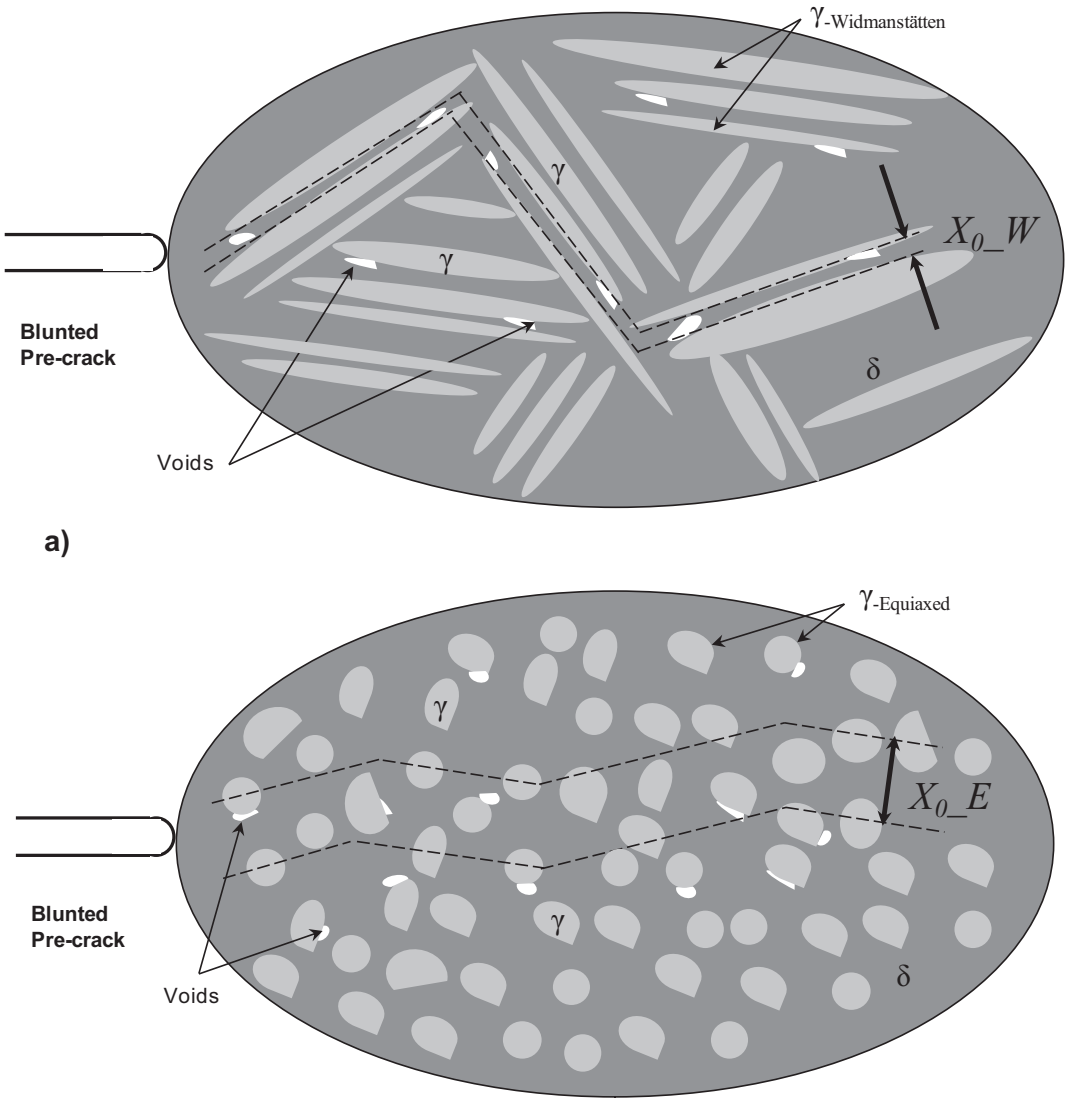


Figure III.45. Schematic definition of the characteristic length X_0 for each morphology: a) equiaxed morphology, and b) Widmanstätten morphology.

The corresponding critical strain can be defined as follows:

$$\varepsilon_c = \ln\left(\frac{X_c}{X_0}\right). \qquad \textbf{eq III-13}$$

From eq III-13, it can be deduced a relation for X_c:

$$X_c = X_0 \cdot \exp(\varepsilon_c), \qquad \textbf{eq III-14}$$

and by substituting X_c by this relation in eq III-12, the critical displacement can be written as

$$\delta_c = X_0 \cdot (\exp(\varepsilon_c) - 1). \qquad \textbf{eq III-15}$$

By applying eq III-11 to each morphology, gives respectively:

$$w_{e,D2_E} = k \cdot \sigma_{c,D2_E} \cdot X_{0,D2_E} \cdot (\exp(\varepsilon_{c,D2_E}) - 1), \text{ and} \quad \textbf{eq III-16}$$

$$w_{e,D2_W} = k \cdot \sigma_{c,D2_W} \cdot X_{0,D2_W} \cdot (\exp(\varepsilon_{c,D2_W}) - 1). \quad \textbf{eq III-17}$$

Considering that the critical strain is the equivalent strain to fracture: $\varepsilon_{c,D2_E} \approx \varepsilon_{c,D2_W}$, see Table III.10; and as the maximum of the load-displacement curves corresponds to the same point, i.e. $\sigma_{c,D2_E} \approx \sigma_{c,D2_W}$, see Figure III.39; the ratio between the specific essential work of fracture of the equiaxed morphology, $w_{e,D2_E}$ over that of the Widmanstätten one, $w_{e,D2_W}$ can be approximately estimated by:

$$\frac{w_{e,D2_E}}{w_{e,D2_W}} \approx \frac{X_{0,D2_E}}{X_{0,D2_W}}, \quad \textbf{eq III-18}$$

where X_0 is a characteristic length as defined in Figure III.45. Considering that X_0_E is approximately equal to 65µm and that X_0_W is about 30µm, the ratio X_0_E/X_0_W is about 2.2 and gives the correct order of magnitude. Indeed, the ratio $w_{e,D2_E} / w_{e,D2_W}$ is approximately equal to 2.

III.6.3 To go further…necking vs. damage

III.6.3.1 Question

As indicated in section III.1 “Literature review about the Essential Work of Fracture concept”, the total work of fracture of deep double edge notched specimens plates (DENT) can be expressed as the sum of an essential work of fracture, W_e spent in the end regions ahead of the crack tips, i.e. in the fracture process zone, and a non-essential plastic work, W_p dissipated in the outer region:

$$W_{tot} = W_e + W_p. \quad \textbf{eq III-19}$$

In the case of ductile materials where fracture occurs with constant thickness reduction, Pardoen et al. [76] showed that the essential work of fracture W_e can be separated into two contributions:

$$W_{tot} = W_0 + W_n + W_p, \quad \textbf{eq III-20}$$

where W_0 is the work spent for growing voids to final material separation and W_n is the plastic work spent in the localized neck which develops in front of the crack tip and which includes the region where material separation takes place.
This separation between the work of necking and the work spent for growing voids could help us answering the following questions.

- What is the origin of the difference between D2_E and D2_W?
- Does it originate from a difference in the necking contribution (W_n) or a difference of the damage contribution (W_0)?

III.6.3.2 How to answer this question?

III.6.3.2.1 Procedure

For dimensional reasons, the work of necking per unit area scales with the plate thickness while the work of diffuse plasticity scales with the ligament length. The total work, W_{tot} thus may be written

$$W_{tot} = t_0 l_0 w_0 + \beta t_0^2 l_0 w_n + \alpha t_0 l_0^2 w_p , \qquad \text{eq III-21}$$

where t_0 is the initial plate thickness, l_0 is the initial ligament length, α and β are shape factors, w_0 is the average work spent per unit area for growing voids to final fracture, w_n is the average work per unit volume dissipated in the neck in front of the crack tip and w_p is the average work per unit volume spent in plasticity in the diffuse plastic zone. By measuring the total energy for separating a DENT specimen, W_{tot}, for different thicknesses and ligament lengths and dividing this energy by the ligament area ($w_{tot} = W_{tot} / l_0 t_0$), it is thus possible to separate w_0, w_n and w_p (see Figure III.46):

$$w_{tot} = w_0 + \beta t_0 w_n + \alpha l_0 w_p . \qquad \text{eq III-22}$$

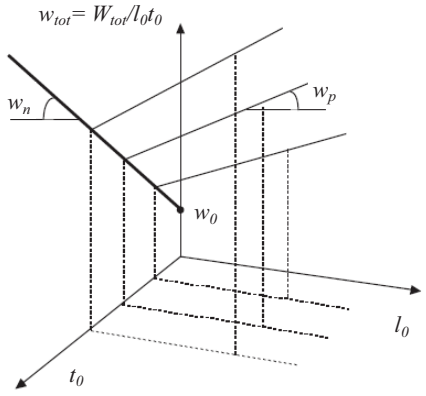


Figure III.46. Procedure followed to separate the three contributions to the total energy: the work of diffuse plasticity, w_p (per unit volume), the work of localized plasticity w_n (per unit volume), and the fracture work w_0 (per unit surface) [76].

III.6.3.2.2 Qualitative answer

In this work, the total energy for breaking a DENT specimen was not determined for different thicknesses, as a consequence it is not possible to separate the three contributions. However, Pardoen et al. [76] have demonstrated that the average work per unit volume spent in the neck, w_n is a function of the rheology of the investigated material and of the final fracture strain.

As the equivalent strain at fracture exhibit similar values when comparing the D2_E microstructure with the D2_W microstructure (Table III.10), it remains to check if both morphologies present a different rheology.

Normalizing the force-displacement curves by dividing the force by the area of the ligament and by dividing the displacement by the final displacement gives a good idea of the rheology (stress-strain curve) of the material. As shown in Figure III.47, the curves belonging respectively to D2_E and D2_W are superimposed. In others words, it means that there is no difference in terms of macroscopic rheological behaviour between D2_E and D2_W.

It can be concluded that the origin of the difference between D2_E and D2_W directly comes from to the work spent for growing voids to final fracture of the specimen.

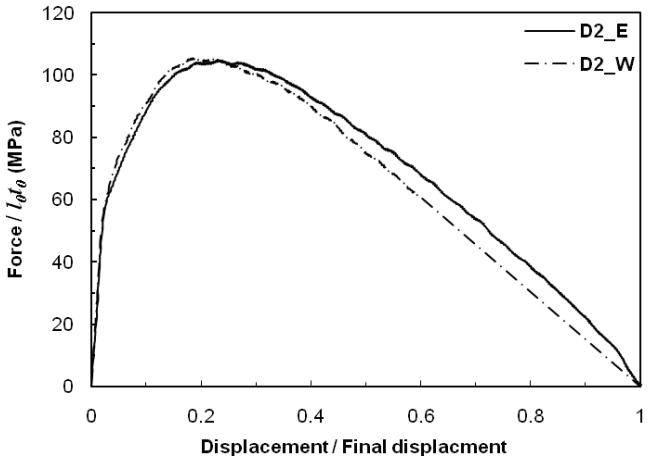


Figure III.47. Normalization of the force displacement curves for a ligament length of l_0 = 22mm for respectively, the D2_E and D2_W microstructures. The force is normalized by the area of the ligament that gives a stress and the displacement is divided by the final displacement.

III.6.4 Conclusions

- The EWF concept was applied at high temperature to model microstructures presenting a different austenite morphology (an equiaxed and a Widmanstätten), but with an equal and stable phase ratio. The results have shown that at 1050°C, an equiaxed morphology (D2_E) was two times more resistant to crack propagation than a Widmanstätten morphology (D2_W).

- Characterization of the fracture surface and damage match very well with the EWF results. No differences were pointed out in terms of damage nucleation strain or of crack density.

- Hardness characterizations have shown that there is no difference in term of rheology when comparing both morphologies.

- The higher hot tearing resistance of the equiaxed morphology compared to the Widmanstätten morphology is related to the path crack propagation and characteristic length X_0.

- Testing DENT specimens with different thicknesses would permit to separate the three contributions and thus estimate the high temperature toughness of the materials.

III.7 Influence of the inclusion content

III.7.1 Materials

In order to investigate the influence of the inclusion content on the hot cracking resistance, alloy D1 was considered and compared with alloy D1bis. D1 and D1bis are both 2205-conventional duplex steels. As a consequence, D1 exhibits the same chemical composition in terms of major elements (Cr, Ni, Mo, Mn, N…) compared to D1bis, see Table III.11.

	%Cr	%Ni	%Mo	%Mn	%Si	%Cu	%C	%N
D1	22.90	5.59	3.11	1.75	0.55	0.19	0.02	0.17
D1bis	22.67	5.57	3.21	1.76	0.68	0.20	0.02	0.17

Table III.11. Chemical composition of the D1 and D1bis alloys. Both alloys correspond to a conventional 2205 duplex stainless steel.

From the hot rolled material, model Widmanstätten microstructures of the alloy D1bis were generated using appropriate heat treatment (HTW.1). Figure III.48.b shows the resulting microstructure: D1bis_W and the Widmanstätten microstructure of the alloy D1_W is also reported in Figure III.48.a to compare both microstructures. Microstructure characterizations reveal that both microstructures: D1_W and D1bis_W were very similar in terms of austenite morphology, average austenite lath thickness, and volume fraction of phases.

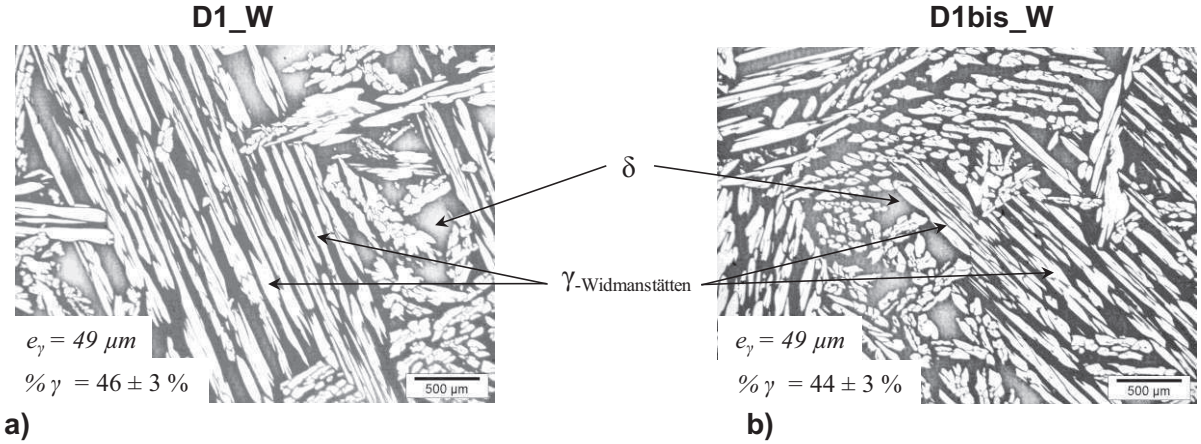


Figure III.48. Widmanstätten model microstructures after HTW.1; a) D1_W and b) D1bis_W.

Several DENT specimens with different ligament lengths were machined from the heat treated blocks of the alloy D1bis. Then, the specimens were tested under tension at 1050°C and the EWF method was applied.

III.7.2 Results

Figure III.49 gives the results obtained on the D1bis_W microstructure. The results from the D1_W microstructure are also reported in Figure III.49. The relationship between the total specific work of fracture and the ligament length follows the expected linear behaviour.

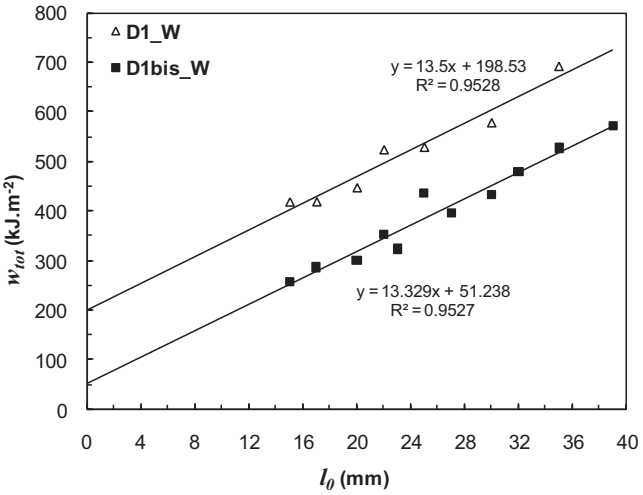
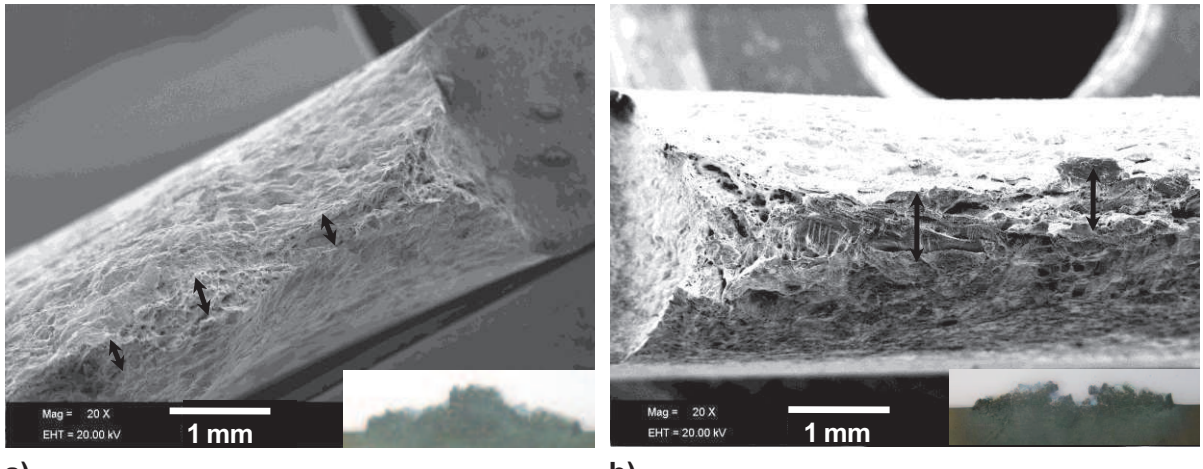


Figure III.49. Variation of the specific work of fracture as a function of the ligament length for separation of the essential work of fracture. Comparison between D1_W and D1bis_W microstructures at 1050°C.

The plane stress specific work of fracture at 1050°C is equal to 199 kJ.m^{-2} and 51 kJ.m^{-2} for the microstructures D1_W and D1bis_W, respectively. It means that at 1050°C, D1_W is almost four times more resistant to ductile tearing than D1bis_W.

Typical fracture profiles are shown in Figure III.50. Both microstructures, D1bis_W and D1_W exhibit an irregular profile along the ligament. D1bis_W and D1_W differ by their equivalent strain to fracture: the arrows in Figure III.50 emphasize this difference.



a) **b)**

Figure III.50. Fracture micrographs and profiles of the broken DENT at 1050°C; a) D1_W (l_0=35mm); b) D1bis_W (l_0=35mm).

Damage characterization were also carried out on D1bis_W broken DENT specimens to determine the strain at which the density of crack increases dramatically. The results for both D1_W and D1bis_W microstructures are reported in Figure III.51. The number of voids begins to significantly increase at a slightly lower strain in the D1bis_W microstructure, about 0.8 compared to the D1_W microstructure where, it is equal to about 1.2.

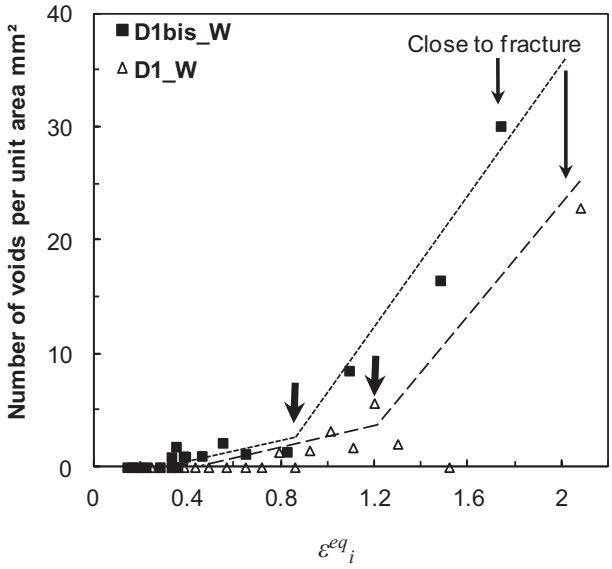


Figure III.51. Evolution of the damage as a function of equivalent strain for both D1_W and D1bis_W microstructures. The arrows indicate the approximate strain at which damage nucleation occurs.

Table III.12 summarizes the results provided by the several characterizations performed.

		w_e (kJ.m^{-2})	αw_p (kJ.m^{-3})	$\varepsilon^{eq}_{fracture}$	$\varepsilon^{eq}_{damage}$
D1_W	1050°C	199 ± 33	13.5 ± 1.3	2.8 ± 0.1	1.2 ± 0.2
D1bis_W	1050°C	51 ± 26	13.3 ± 0.9	1.9 ± 0.1	0.8 ± 0.2

Table III.12. Summary of the data: results from the application of the EWF method at 1050°C to D1_W and D1bis_W, equivalent strain to fracture, and equivalent strain at which the density of crack increases significantly.

As both microstructures exhibit a Widmanstätten austenite with a proportion of austenite of about 45% and a similar austenite lath size, these parameters cannot be invoked to explain such difference in terms of hot cracking resistance.

As pointed out in the literature review about the factors affecting the hot workability of duplex stainless steels (Chapter II), the sulfur content can be very detrimental.

As a result, the first idea was to measure the sulfur content. Several measurements for each microstructure were performed. The measured sulfur content in the different alloys was always under 5ppm (very low value) whatever the microstructure: D1_W or D1bis_W. Finally, the sulfur content cannot be responsible for the difference in terms of hot tearing resistance between D1_W and D1bis_W.

The second idea was to investigate the inclusion content. The purpose of the next section is to discuss the differences in terms of nature, density, and size of the particles.

III.7.3 Discussion about the nature, size and density of the inclusions

III.7.3.1 Nature of the inclusions

The chemical analysis performed by EDS (Electron Dispersive Spectroscopy) on polished samples has shown that the majority of the inclusions were oxides involving undesirable chemical elements such as aluminium, calcium, or magnesium. In Figure III.52, an example of a back scattered micrograph reveals the presence of several inclusions. Their chemical composition was determined using EDS maps. The nature of the inclusions does not differ between the D1_W microstructure and the D1bis_W microstructure.

These elements were present during the elaboration of the alloy at the steel factory. Therefore, it is not surprising to find these elements in the inclusions. Aluminium is added during the steel making in order to reduce the oxides. Calcium is used to trap the sulfur and hence to reduce its content in the matrix. Magnesium is one of the main constituents of the refractory ceramic materials used in the steel factory.

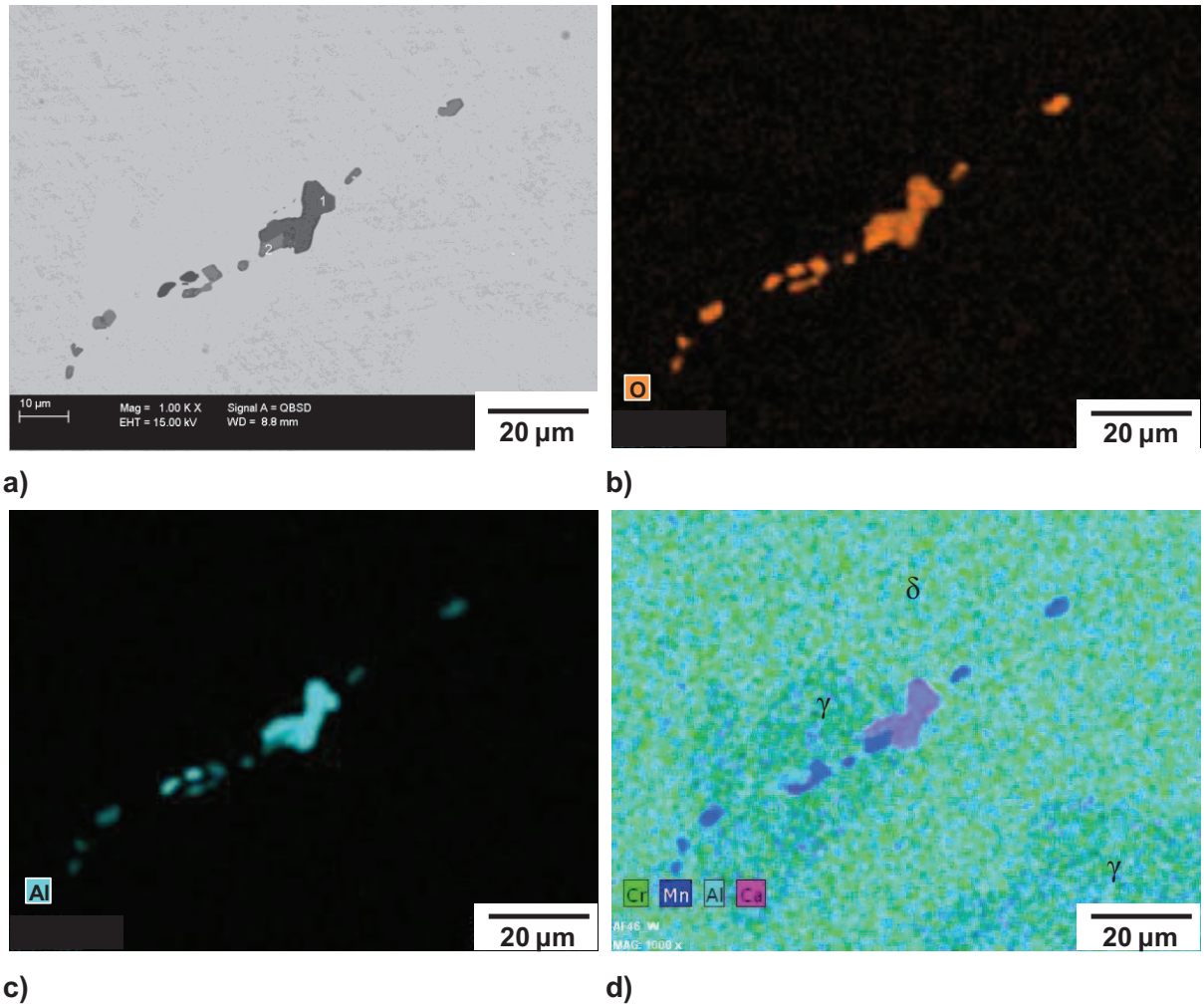
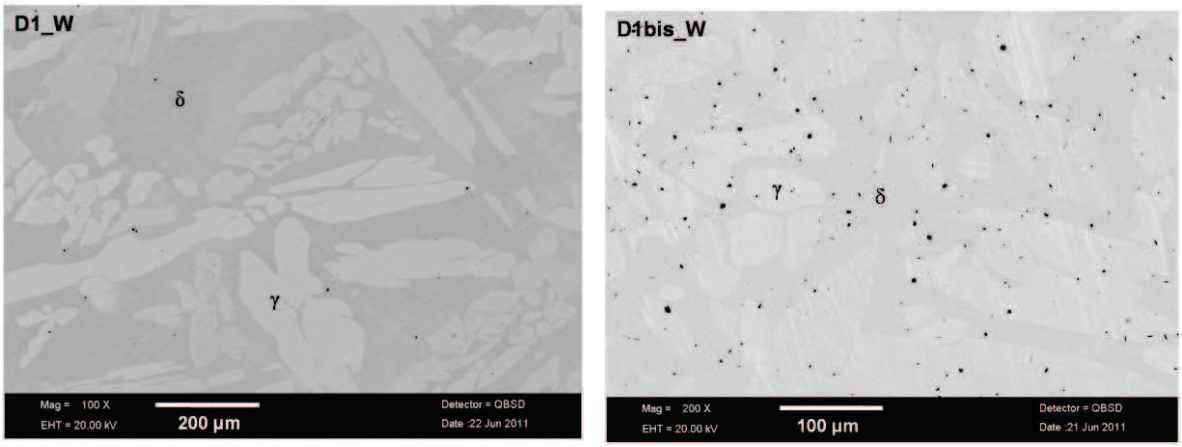


Figure III.52. Nature of the inclusions present in the D1_W and D1bis_W microstructures; a) SEM micrograph showing a string of particles; b) chemical composition map in oxygen; c) chemical composition map in aluminium; d) chemical composition map superimposing chromium, manganese, aluminium and calcium.

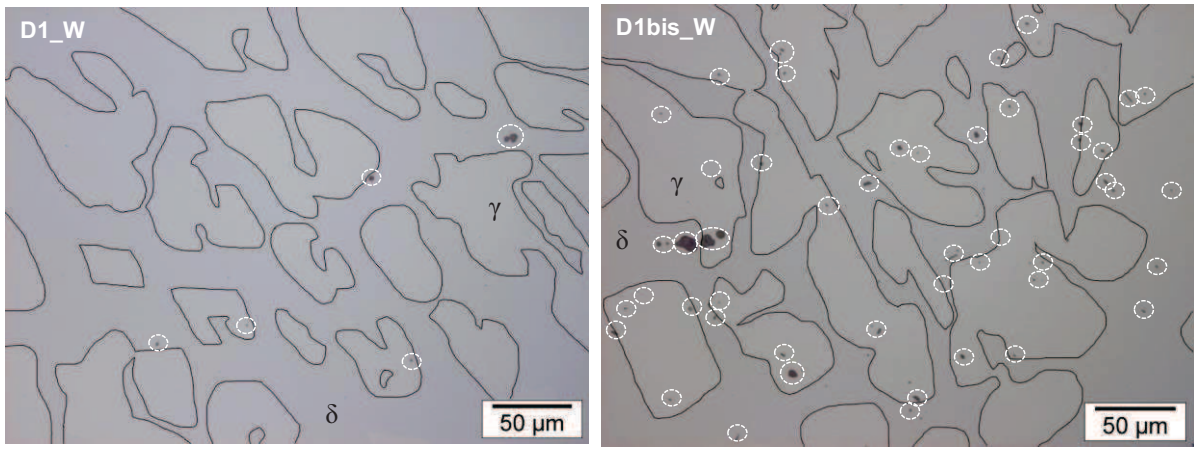
III.7.3.2 Density of inclusions

Typical SEM and optical micrographs at different magnifications are shown in Figure III.53 and Figure III.54, respectively. The micrographs reveal that the density of inclusions seems to be significantly lower in D1_W compared to D1bis_W.



a) b)

Figure III.53. SEM micrograph to illustrate the difference in terms of inclusion content between a) D1_W and b) D1bis_W. Austenite is the brightest phase, ferrite is the dark phase and the inclusions are in black due to a significant difference in terms of chemical composition.



a) b)

Figure III.54. Optical micrograph to illustrate the difference in terms of inclusion content between a) D1_W and b) D1bis_W. The inclusions are circled in white and the interfaces between ferrite and austenite are highlighted to determine the location of the particles.

Quantitative data obtained by the manual method and by the automatic method described in section III.2.3.4 are given in Table III.13 and Table III.14, respectively. Both methods give similar levels of inclusion content. These results confirm the microstructural observations of the inclusion cleanliness (Figure III.53 and Figure III.54). The density of inclusion is seven to ten times higher in the D1bis_W microstructure compared to in the D1_W microstructure. The manual method shows that the inclusions are randomly distributed in the austenite and in the ferrite with a significant number of inclusions at the interphase boundaries (between 15 and 20% of the particles are located in the vicinity of the δ/γ interfaces). In other words, it means that the larger the inclusion content is, the higher is the number of particles at the interphase boundaries.

Damage characterizations carried out on the hot rolled material or on the broken DENT specimens have demonstrated that the voids always nucleate by decohesion of the δ/γ interfaces and propagate in the ferrite or along the interphase boundaries. As a consequence, the inclusions located in the austenite are not so detrimental to the hot tearing resistance. On the contrary, it seems that there is a relationship between the number of inclusions located in the vicinity of the δ/γ interfaces and the hot cracking resistance.

The main conclusion of these results is that the lower the inclusion content, the higher the specific essential work of fracture and the better the hot cracking resistance.

Manual method	Density of inclusions (number of inclusions per mm²), f^i	
	D1_W	D1bis_W
γ-austenite	41	477
δ-ferrite	47	504
δ/γ interfaces	23	183
Total	112	1165

Table III.13. Densities of inclusions respectively in ferrite, austenite and interfaces determined with the optical method in both D1_W and D1bis_W microstructures.

Automatic method	Density of inclusions (number of inclusions per mm²), f^i	
	D1_W	D1bis_W
Total	150	1091

Table III.14. Densities of inclusions determined with the SEM method in both D1_W and D1bis_W microstructures.

III.7.3.3 Size of the inclusions

The automatic procedure provides information about the size of the particles. The average diameter of the particles is about 1.9µm in the D1_W microstructure and about 1.4µm in the D1bis_W microstructure, see Table III.15. These average values are very close to each other and cannot be invoked to account for the difference between D1_W and D1bis_W in terms of the hot tearing resistance.

	D1_W	D1bis_W
Average inclusion equivalent diameter (µm)	1.9	1.4

Table III.15. Average inclusion size in both microstructures D1_W and D1bis_W.

Another way to give information about the diameter of the inclusions is to plot the size distribution function corresponding to the D1_W and the D1bis_W microstructures, see Figure III.55. The size distribution function exhibit a similar shape with the majority of the particles with a diameter between 1 and 2µm. As a result the size criterion is not relevant to understand the origin of the difference in the hot cracking resistance between D1_W and D1bis_W.

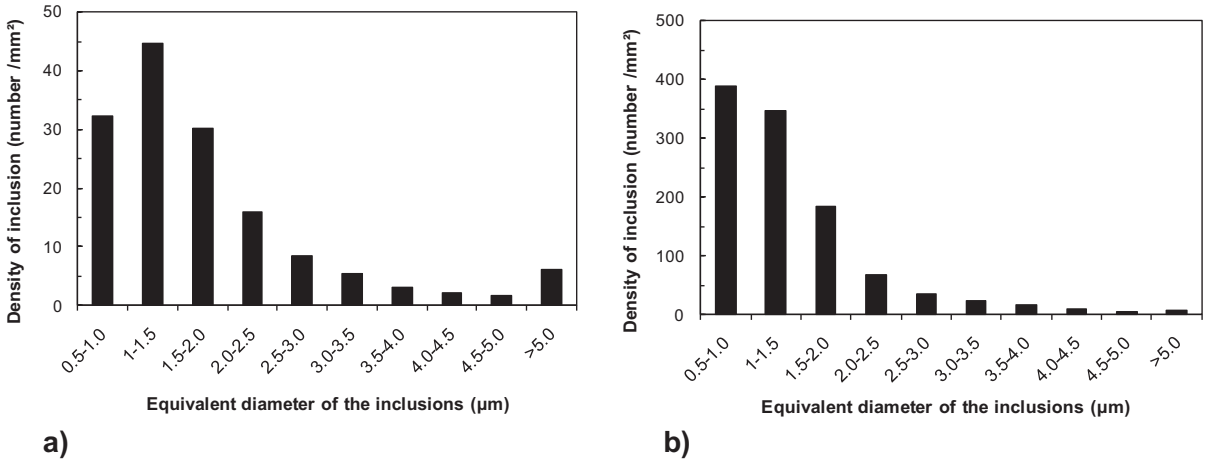


Figure III.55. Distribution of size of the inclusions for a) D1_W and b) D1bis_W.

III.7.4 Conclusions

The discussions lead to conclude that the key parameter which explains the difference in terms of hot cracking resistance between the microstructures D1_W and D1bis_W is the density of inclusions.

Again, the difference between D1_W and D1bis_W can be related to a different characteristic length as in section III.6.2.3. Indeed, the specific essential work of fracture relative to each microstructure, D1_W and D1bis_W, respectively, can be written as:

$$w_{e,D1_W} = k \cdot \sigma_{c,D1_W} \cdot X_{0,D1_W} \cdot (\exp(\varepsilon_{c,D1_W}) - 1),$$

eq III-23

and

$$w_{e,D1bis_W} = k \cdot \sigma_{c,D1bis_W} \cdot X_{0,D1bis_W} \cdot (\exp(\varepsilon_{c,D1bis_W}) - 1).$$

eq III-24

X_0 is always a characteristic length, not related to the crack path, but related to the spacing between the particles.

An estimation of the characteristic lengths are given by the following equations:

$$X_{0,D1_W} = \frac{1}{\sqrt{f^i_{D1_W}}},$$ **eq III-25**

and

$$X_{0,D1bis_W} = \frac{1}{\sqrt{f^i_{D1bis_W}}},$$ **eq III-26**

where $f^i_{D1_W}$ and $f^i_{D1bis_W}$ are the densities of particles per unit area, respectively for the microstructures D1_W and D1bis_W.

The ratio between $w_{e,D1_W}$ and $w_{e,D1bis_W}$ can then be estimated by:

$$\frac{w_{e,D1_W}}{w_{e,D1bis_W}} = \frac{k \cdot \sigma_{c,D1_W} \cdot X_{0,D1_W} \cdot (\exp(\varepsilon_{c,D1_W}) - 1)}{k \cdot \sigma_{c,D1bis_W} \cdot X_{0,D1bis_W} \cdot (\exp(\varepsilon_{c,D1bis_W}) - 1)}.$$ **eq III-27**

Assuming that the load-displacement curves exhibit the same shape and are superimposed for a given ligament length, then this ratio can be approximated by:

$$\frac{w_{e,D1_W}}{w_{e,D1bis_W}} = \frac{X_{0,D1_W} \cdot (\exp(\varepsilon_{c,D1_W}) - 1)}{X_{0,D1bis_W} \cdot (\exp(\varepsilon_{c,D1bis_W}) - 1)}.$$ **eq III-28**

Using the values of the equivalent strain to fracture indicated in Table III.12 for the critical strain and in Table III.13 and Table III.14 for the densities of particles, the ratio $w_{e,D1_W} / w_{e,D1bis_W}$ fluctuates between 7 and 10 that corresponds to the order of magnitude determined when estimating this ratio using the values determined via the linear regression ($w_{e,D1_W} / w_{e,D1bis_W}$ = 4).

III.8 Conclusions

- In the as-cast conditions, D1 was two times more resistant to hot tearing compared to D2. The effect of temperature was also pointed out: the larger the temperature is in the 1000-1250°C range, the better the hot workability is. However, the as-cast microstructures exhibit a high degree of heterogeneity. The direct consequence of these heterogeneities was a significant dispersion, making difficult to provide definitive conclusions regarding the separate effects of the dominant parameter.

- In order to improve the accuracy of the results and to investigate the influence of other parameters (phase morphology, inclusion content…), model microstructures were thus required. Proper control of the $\delta \rightarrow \gamma$ phase transformation mechanisms allowed the generation of a variety of microstructures with different phase morphologies. By controlling temperature, duration of annealing sequences and cooling rate, alloys with a desired phase proportion, and desired size and shape of the microstructural constituents were produced.

- The EWF applied to model microstructures confirmed that D1 was two times more resistant to hot tearing compared to D2 and the accuracy of the results was significantly improved.

- The hot mechanical behaviour contrast between the ferrite and the austenite when comparing D1 with D2 seems to reach significantly different levels and can partly account for the difference of hot cracking resistance. This idea will be investigated in details in Chapter IV.

- The austenite morphology impacts significantly on the high temperature fracture resistance: for a given alloy, to break a sample showing an equiaxed austenite required two times more energy than to break a sample presenting a Widmanstätten austenite.

- The inclusion content has to be very well-controlled because high densities of inclusions lead to a significant decrease of hot tearing resistance. In addition, they are clearly more damaging when they are located at the δ/γ interfaces.

Chapter IV. Strain partitioning

Chapter IV. Strain partitioning

One of the main objective of micro-mechanics of heterogeneous materials is the understanding of the influence of microstructural parameters, such as grain size, grain shape and crystallographic texture, on the mechanical behaviour at the scale of the grain and at the macroscopic scale (as proposed by Raabe et al. [96]). This approach requires to study local deformation mechanisms (slip systems, twinning systems, sliding at the interfaces etc.) in order to predict the overall mechanical behaviour. The local scale measurement of mechanical parameters (stress, strain…) has to be performed on surfaces or volumes that are small compared to the microstructural scale and large compared to the atomic scale in order to determine an "effective behaviour" of each phase. As it was highlighted, in micro-mechanics, there are two different scales: the microscopic scale and the macroscopic scale. These characteristic scales depend obviously on the materials considered and on the relevant mechanisms. In case of materials presenting an industrial interest, the relevant local scale is around several micrometers: for instance, in polycrystalline metallic materials this scale is the scale of the grain.
As it was stressed in the previous chapters, the poor hot workability of duplex stainless steels leads to severe edge cracking during the hot rolling process. The prediction of the high temperature mechanical behaviour of duplex stainless steels, and especially the hot ductility can be achieved through a physically based model, in which the hot deformation characteristics of both phases are input parameters. As a consequence, in order to understand this macroscopic phenomenon, characterization of the local state of deformation developed at the microscopic scale is therefore necessary. In the literature, several authors have suggested that the poor hot workability of duplex stainless steels was directly related to the high temperature strain partitioning between ferrite and austenite [25, 29, 97]. However, quantitative results for this strain partitioning are missing. After a presentation of the different techniques available to measure the strain partitioning between phases, the modified microgrid method will be presented in details. Then, the results obtained via this method will be discussed.

IV.1 Techniques to measure strain distribution

Several techniques have been developed to determine the micro-scale strain distribution. The purpose of this section consists in reviewing the main techniques which allow measuring the micro-scale strain distribution, and in pointing out the advantages and the disadvantages of each method. Many experiments have been devised to investigate the heterogeneous deformation in polycrystals. The most frequently applied methods are based on recognizing patterns whose distortion could be associated

with the deformation, which may later be observed and measured. It is possible to measure the in-plane strains at the surface of a specimen by taking images in the undeformed and in the deformed configuration, and by finding the homologous points in both configurations. Homologous points are the points in the images (undeformed and deformed) that belong to the same material point on the sample. The homologous points draw a displacement field, which can be differentiated to get the in-plane strain fields. The outcome of the procedure depends strongly on the accuracy of the matching procedure, on the density of the homologous points, and on the range of deformations. Several techniques for defining homologous points are available. Here, it has been chosen to introduce only the two main image analysis techniques.

IV.1.1 Grid techniques

Techniques commonly called “grid techniques” use markers arranged periodically on the surface of a specimen. In the literature different grid patterns have been used: fine array of dots [98], crosses [99] or lines (Figure IV.1).

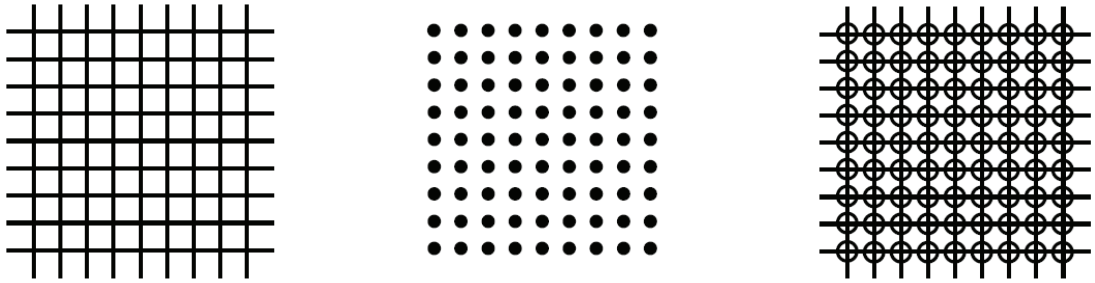
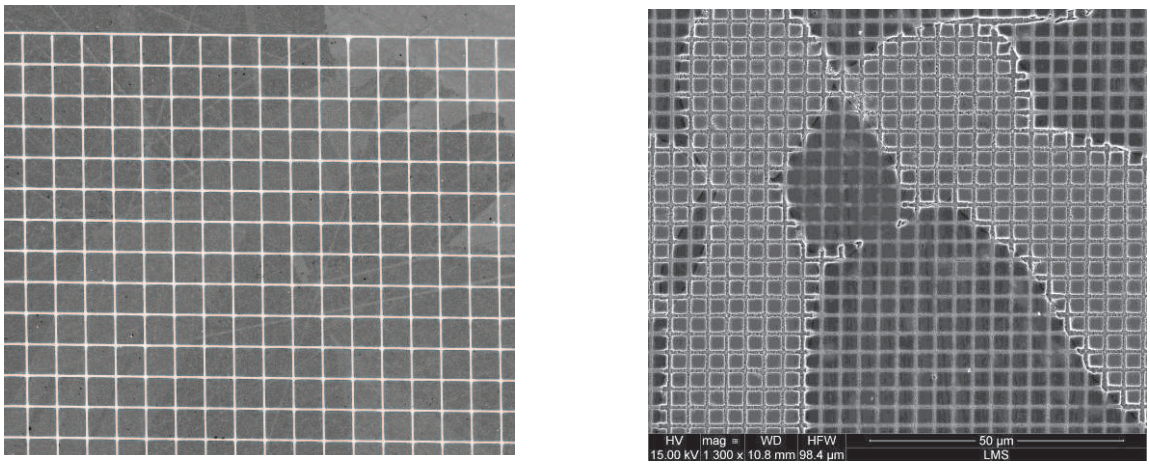


Figure IV.1. Illustration of different grid patterns; a) fiducial microgrids; b) fine array of dots; and c) fine array of lines encircled.

Different marking techniques have been developed in order to create the desired contrast on the surface of the specimen. Indeed, grids may be applied to the surface in a variety of ways: scribing [100, 101], printing, etching [14], embossing, embedding, reflection, depositing or lithography [98, 102-104]. Figure IV.2 shows respectively a grid processed by microlithography (Figure IV.2.a) and another one by engraving via chemical etching (Figure IV.2.b). The selection of the marking technique is closely related to the observation device. For instance, the painting techniques are not suited for with SEM observations because the paints are usually not electrical conductors. In addition, it requires adapting the marking technique to the conditions of mechanical loading applied to the specimen. In particular in thermo-mechanical applications, it is necessary to choose markers that are high-temperature resistant. This aspect will be discussed further (see section IV.2). The goal of the image acquisition procedure is to create high-contrast, high-resolution pictures for subsequent determination of grid points coordinates. These grid point coordinates are recorded numerically, after either manual determination, or after digital capture of the grid feature locations. Initially, grid point coordinates were determined with the help of a graduated ruler or micrometric tables. Now, thanks to numerical imaging, both pictures (undeformed and deformed) are digitized in grey levels and analyzed by image analysis: threshold or morphological operations (erosion, dilatation). Indeed, each marker showed a grey level different from the material. As a consequence, it is easy to find accurately their position. Then, the local strains are determined by calculations from the coordinates of the points in both undeformed and deformed configurations.



a) **b)**

Figure IV.2. 5µm-microgrid patterns [103]; a) processing by micro-lithography; b) engraving by chemical etching from this work.

IV.1.2 Image correlation techniques

Correlation techniques have been developed more recently than the grid techniques. Such techniques stem from investigations in optics and have been applied to the mechanics of materials. The range of applications is larger than for the grid techniques and their use is expanding rapidly. In the literature, correlation techniques have been used to determine the local strain field at the crack tip for several materials [105-110], to measure the strains at high-temperature [111-113], and to investigate the damage nucleation in composites materials like cellular aluminum alloys [114], polyurethane-foams [115, 116], fibrous composites… These techniques have reached a high level of development. Nowadays, the improvements consist essentially in estimating more directly the tridimensional strain components [117, 118].

Most of the studies deal with macroscopic investigations on tensile or compression specimens. The order of magnitude of the microscopic scale is the millimeter whereas the region of interest is in the order of a centimeter. The observation device is most of the time a CCD camera although more and more applications use optical microscopy or scanning electron microscopy to focus on mechanisms which take place at a lower scale. It means that these techniques are very powerful as they can be adapted to different scales. During the last decade, in several studies, correlation techniques have been even applied at a nanometric scale [119-121].

The purpose of the correlation technique consists in comparing two different pictures. This comparison suggests the presence of a lot of local details on the surface of the specimen. To do that, a random pattern, called speckle is used. The speckle provides the contrast required to perform the correlation. If the specimen does not naturally exhibits this contrast (such situations will be so scarce, especially for local applications), random patterns have to be applied by spraying black and/or white paints, or other techniques. It is also possible to use grids instead of speckle that present the advantage to not obscure the microstructure. This last detail turns out to be very important, in particular in cases where micro-mechanical investigations of heterogeneous materials are pursued. The speckle can also be obtained via an optical technique called photography speckle. This last kind of contrast can be applied only to optical applications. The comparison between both images consists in finding the homologous points by maximization of a cross-correlation function calculated in the vicinity of these points. The random pattern allows identifying each homologous point and therefore estimating the strain components.

IV.1.3 Microgrid vs. correlation

With both techniques, very wide fields can be examined. The limitation does not stem from the imaging equipment, but from the area of the surface covered by the microgrid. Furthermore, measurement of the deformation field is direct and unambiguous; qualitative assessment of the nature of the strain can be made with even casual examination. Set-up of the microgrid technique is relatively simple, requiring no specialized device, except for the manufacture of extremely fine submicrometer grids. The analysis of the deformed grid pattern does not require extensive computing or highly specialized software. In addition, because the grids are physically attached to the sample after deformation, the record of deformation is permanent.

Unfortunately, small strains cannot be accurately determined, as the deviation of the grid lines from their reference positions can be very small, compared with the width of the microgrid lines. Table IV.1, from Schroeter and McDowell [122], shows relative advantages and disadvantages between both strain-field measuring techniques discussed in this section.

Characteristics	Digital Image Correlation	Microgrid Technique
Physical basis	*Amplitude (image contrast figures)*	*Direct measurement*
Data collection method	*In-situ or post-mortem (for small strains)*	*Post-mortem*
Strain mapping	*Direct numerical differentiation of displacement data*	*Differentiation of grid lines or crossing points locations*
Imaging hardware/software	*Moderately demanding / Intensive*	*No specialized hardware / minimal software*
Displacement value	*Absolute*	*Absolute*
Surface quality requirement	*Diffusive, as-received*	*Smooth*
Surface decoration requirement	*Random or ordered intrinsic or artificial features*	*High-quality cross-line or speckle grid*
Surface decoration hardware	*Minimal or none*	*Minimal*
Deformation range	*Small or medium*	*Medium to large strains only*
Field of view	*Wide field, limited only by the specific image formation system*	*Wide field, limited only by the area of the grid*
Spatial resolution	*High, depending on the surface, and resolution of imaging equipment*	*Medium, depending on grid pitch*
Data storage requirement	*Large*	*Small*

Table IV.1. Comparison between two strain mapping techniques: digital image correlation and microgrid technique [122].

IV.2 Measurement of micro-scale deformation at high temperature

Ideally, during plastic deformation, all grains are strained homogeneously, following the polycrystalline body, but in real materials, strain is not homogeneous. As seen in section IV.1, several techniques are now available to measure the micro-scale strain distribution in polycrystals across a wide range of scales of observation, including resolutions fine enough to reveal intergranular deformation gradients. Marking samples with gold or platinum microgrids using electron lithography is now widely used to characterize the low to moderate temperature mechanical behaviour of heterogeneous materials. The temperature was so far restricted to a field ranging from 20 to 500°C because of the deterioration of the microgrids at high temperature.

However, investigations providing quantitative information about the local deformation at high temperature in polycrystalline metals are scarce in the literature. At high temperature, additionally to the difficulties related to the high-temperature microstructure control for materials affected by phase transformations, the determination of the micro-scale strain distribution remains an experimental challenge. Indeed, the speckle or grid material must exhibit an excellent resistance to thermal and environmental damage. In addition, solutions to avoid the excessive oxidation of the markers have to be found. Furthermore, the markers should exhibit a good high temperature deformability to reveal the material deformation without undesirable cracking or detachment of the markers. And, finally, the black-radiation of the sample is a barrier to collect data in-situ.
Carbonneau et al. [123] used $MoSi_2$ grids at 1200°C in air but even though microgrids survived the test, degradation of the coating material makes them unusable in an image analysis process (Figure IV.3).

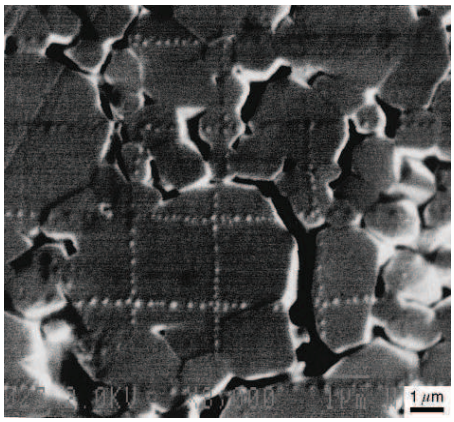
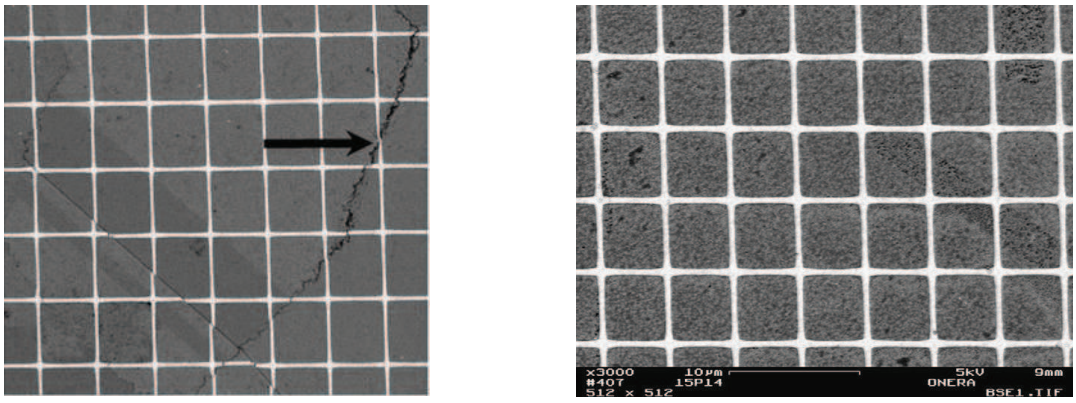


Figure IV.3. SEM micrograph (secondary electron mode) showing a $MoSi_2$ grid after 4h at 1200°C [123].

A micro-extensometry technique, using a microgrid made of hafnia (HfO_2) has been specifically developed by Soula et al. [103, 124] for analysis of grain boundary sliding during creep at high temperature (700–800°C) of a nickel-base superalloy for turbine disc applications (Figure IV.4.a). The hafnia microgrids turned out to be well-defined even after 1000h at 750°C under vacuum (Figure IV.4.b). In the same study, different grid materials: Au, Pt, W, $MoSi_2$, WSi_2 have been tested but all of them gave poor results due to a loss of contrast (Au, Pt) or a strong oxidation (WSi_2, $MoSi_2$).



a) **b)**

Figure IV.4. a) Illustration of the grain boundary sliding after creep at 750°C in nickel-based super alloy thanks to HfO_2 microgrids (step of 5µm); b) HfO_2 grid after 1000h at 750°C under vacuum (SEM, Back-scattered electron mode) [103].

In the paper published by Grant et al. [113], a method is presented for obtaining good images of sample surfaces at high temperature, suitable for strain measurement by digital image correlation (DIC) without the use of surface markers or speckles. This is accomplished by suppressing black-body radiation through the use of filters and blue illumination. Using only relatively low levels of illumination the method is demonstrated to be capable of providing accurate DIC measurements up to 1100 °C.

A novel modification of the classical microgrid technique has been proposed by Pinna et al. [14], allowing the measurement of deformation at the microstructural scale in laboratory hot-worked steels: austenitic and duplex stainless steels [50, 97, 125, 126]. Square microgrids were engraved by chemical etching on the surface of a small rectangular steel sample, see Figure IV.5.a and Figure IV.5.b. The sample was then inserted in a plane strain compression specimen to be deformed at high temperature (850-1050°C) and $1s^{-1}$ strain rate. After the hot compression, the sample was extracted from the plane strain compression specimen and analyzed in the SEM, see Figure IV.5.c and Figure IV.5.d. The distortion of the microgrid revealed deformation features such as sliding at the interphase boundaries in the case of duplex stainless steel. The displacement of the microgrid provided also the strain maps showing the heterogeneous strain distribution within the duplex microstructure as well as in the austenitic stainless steel microstructure, see Figure IV.5.e and Figure IV.5.f.

IV.3 Selection of the experimental technique for measuring the micro-scale strain distribution

The purpose of this section is to establish all the requirements for the technique which will be selected to measure the high temperature micro-scale strain distribution in duplex stainless steels.

(1) Deformation conditions have to be representative of the industrial hot rolling, i.e. large strain, temperature range (850°C-1250°C), strain rate between 0.1 and $100s^{-1}$ and plane strain compression.
(2) Markers must be high-temperature resistant.
(3) As the objectives are to determine the average deformation per phase and to map the strain, the markers must not hide the microstructure.
(4) The technique has to permit to avoid problems related to oxidation at the surface of samples which would destroy classical markers.

All these specifications lead to select the modified microgrid method developed by Pinna et al. [14].

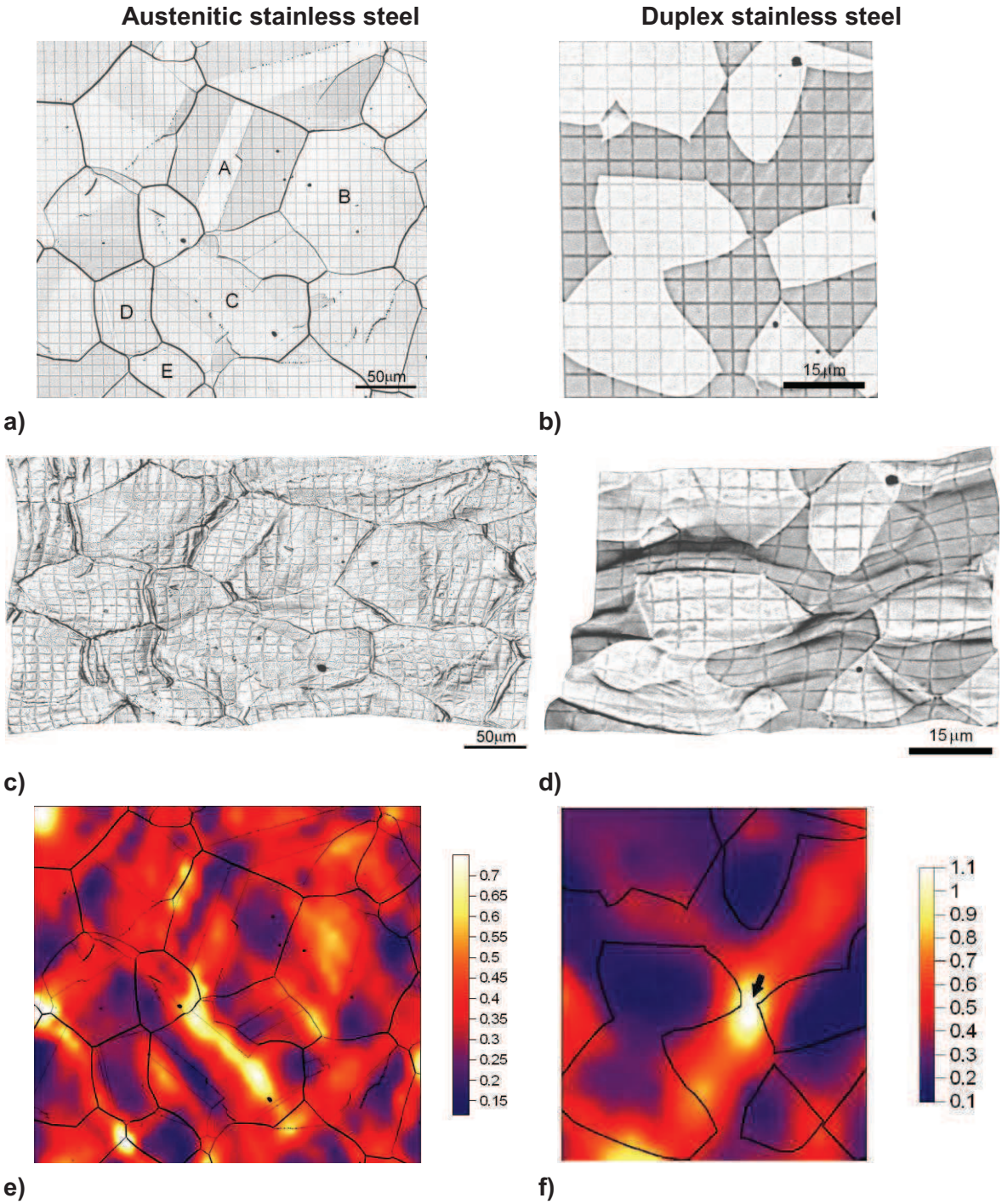


Figure IV.5. Results provided by the modified microgrid technique on model stainless steel alloys: austenitic (deformed at 900°C) and duplex (deformed at 850°C); a) & b) microgrids before deformation; c) & d) microgrids after deformation; e) & f) Green-Lagrange equivalent strain Maps [97].

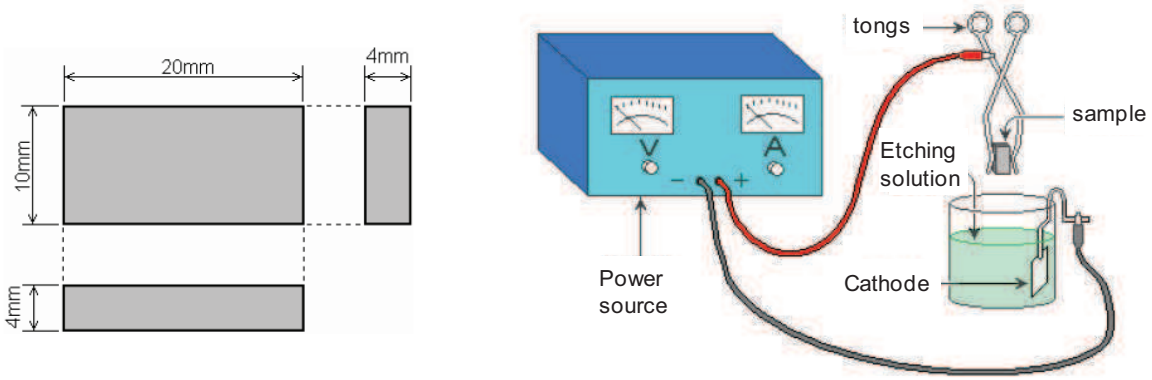
IV.4 Experimental Procedure

IV.4.1 Processing high-temperature resistant microgrids

IV.4.1.1 Sample preparation

Small rectangular samples, whose dimensions are given in Figure IV.6.a, were cut from the heat treated materials involving the microstructure of interest, i.e. with the targeted morphology (Widmanstätten or equiaxed), phase ratio, and austenite lath or grain size (see Chapter III, section III.4 dealing with the generation of model microstructures).

The samples were subjected to a sequence of grinding stages on successively finer silicon carbide abrasive papers (120, 320, 600, 800 and 1200 grit). Polishing was then carried out on a series of cloths impregnated with fine diamond pastes (9 and 3µm). The final polishing step was performed with a 1µm alumina powder.



a) **b)**

Figure IV.6. a) Dimensions of the small samples used to engrave the microgrids; b) schematic of the electro-etching circuit.

As the purpose was to map the strain field within each phase, the microstructure had to be preliminary revealed. The specimens were electro-etched using a solution of 20% aqueous sodium hydroxide electrolytic solution under a tension of 2.5V for 10s. As shown schematically in Figure IV.6.b, the sample, held by tongs, was connected to the positive pole of a Direct Current power source, and placed face to face with the cathode (a small plate of 316L-austenitic stainless steel). The cathode was connected to the negative pole of the power source and plunged into the etching solution, contained in a glass.

IV.4.1.2 Modified microgrid technique

The procedure used to engrave the microgrids is shown schematically in Figure IV.7, and some details are given by describing the main steps of the modified microgrid method.

(1) First of all, a thin film of an electro-sensitive resin was coated onto one faces of the microgrid sample, which had been already polished and electro-etched to reveal the microstructure. In order to create the resin film, the sample was held by screws on the top of a device used to spin the samples. Then, a drop of a polymer solution made of 5g of PMMA (Poly-methyl methacrylate) per every 100mL of 2-ethoxyethyl acetate was deposited at the middle of the pre-

pared surfaces and then spun at 1200rpm for 1min in order to obtain a uniform film thickness. Finally, the coated specimens were baked for 30min at 140°C, to promote the resin adhesion and to improve the mechanical resistance of the film.

(2) The coated samples were then irradiated with the electron beam of a SEM, following the pattern of a square grid. Conditions (magnification, current beam…) were selected to produce a grid step of 5µm. The austenite grain size was around 50-60µm in the equiaxed morphology, and the austenite lath thickness was around 30µm in the Widmanstätten morphology. A 5µm-grid step was chosen in order to introduce as many microgrid intersections as possible in every grain, and make further strain calculation more reliable.

(3) After the irradiation step, the irradiated polymer was dissolved using a specific solvent: 75%-propanol and 25%-butanol for 1min and 30s.

(4) The samples were electro-etched with a 40%-aqueous nitric acid solution applying 4.5V for about 1s, removing material only within the small areas without resin (the microgrid pattern). This step was undoubtedly the most critical step and will be discussed later.

(5) The final step consisted in dissolving the remaining resin in ethyl acetate by means of ultrasonic cleaning, resulting in engraved microgrids with a step of 5µm.

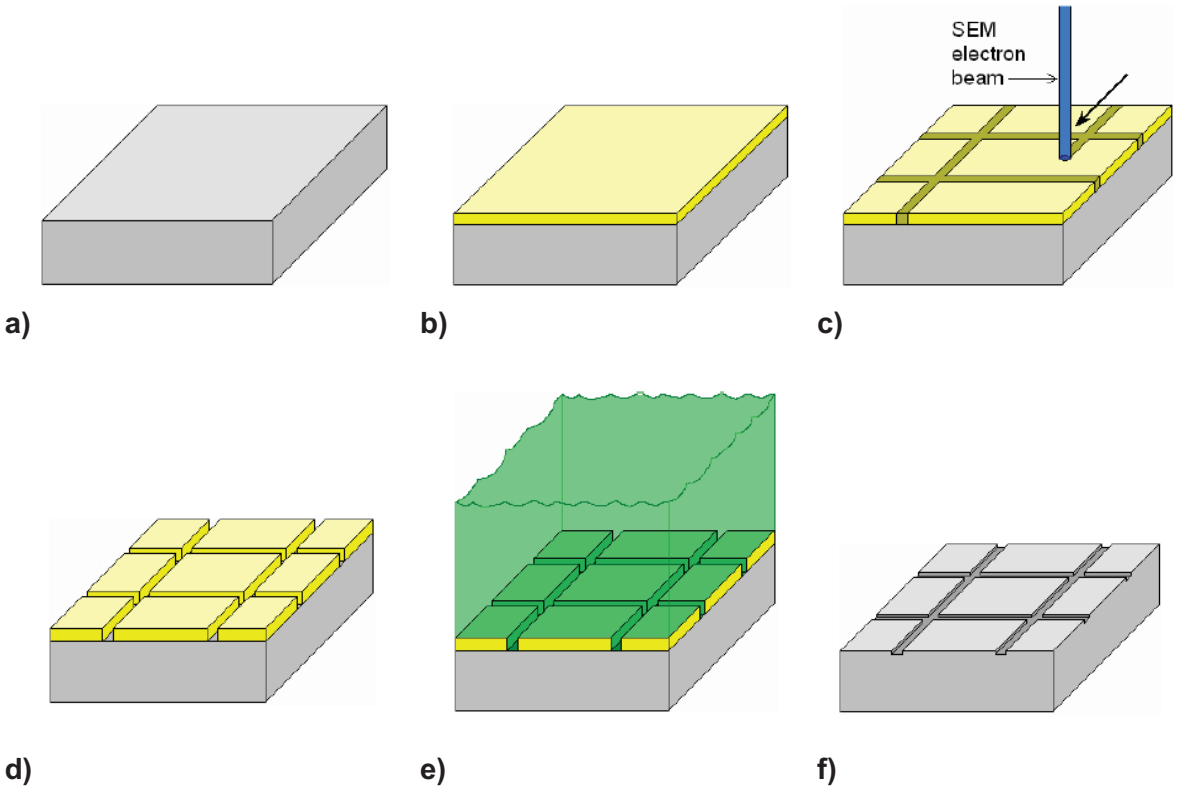


Figure IV.7. Steps of modified microgrid technique; a) polishing and electro-etching; b) coating with an electro-sensitive polymer; c) irradiation of the resin with the electron beam; d) dissolution of the irradiated polymer; e) engraving by electro-etching; f) dissolution of the remaining polymer [50].

After the fabrication of the microgrid, a low magnification-high resolution picture (4096x4096 pixels) was obtained by SEM, covering large areas before deformation (0.25mm²). Secondary electron contrast was used. The best matching of the homologous points by image correlation requires generating an optimal contrast on the SEM pictures. In other words, the picture must involve the entire 256-grey level histogram and must not be centered on a few grey levels. Furthermore, the grey values do not exceed the 0 and 255 boundaries in order to avoid saturation in the white or black field. A testing procedure consists in plotting the grey level histogram and to check its spreading. If the spreading is not acceptable, it will be changed by adjusting the brightness and contrast. Some examples of acceptable engraved microgrids are given in Figure IV.8.

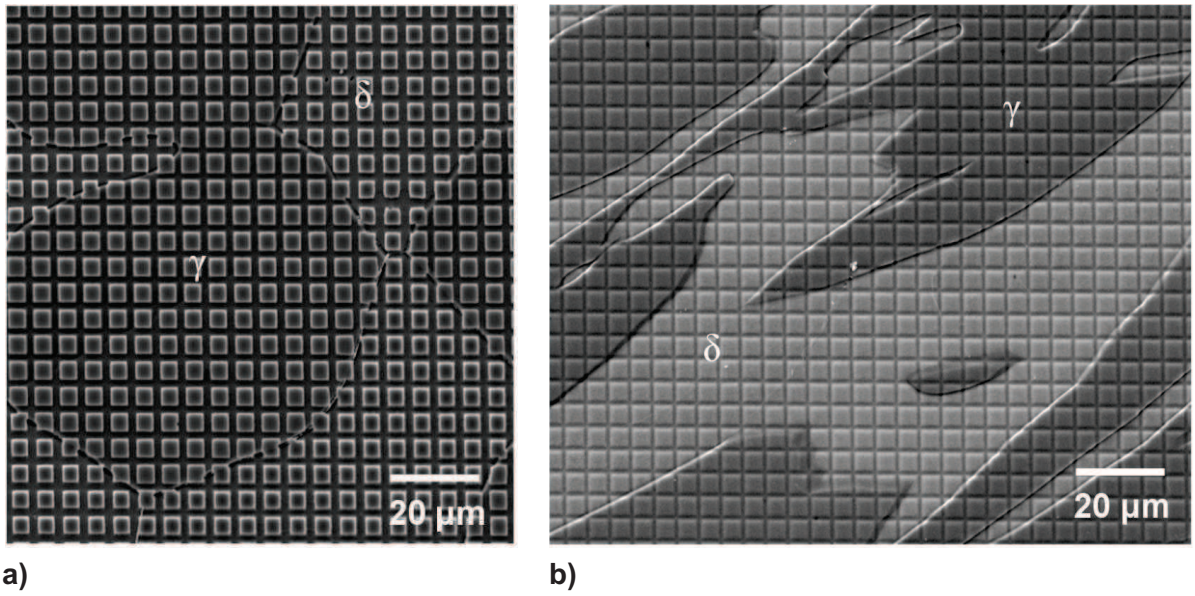


Figure IV.8. Examples of good microgrid high resolution pictures before deformation; a) equiaxed morphology; b) Widmanstätten morphology.

As highlighted previously, the most critical step in the modified microgrid method is the engraving step. The main difficulties are summarized below.

(i) Duplex stainless steels are two-phase material, and in general, the micro-etching principle consists in dissolving one phase and not the other one. To engrave microgrids in both phases requires finding a solution which could etch ferrite as well as austenite. The 40%-aqueous nitric acid electro-etching solution was that which gave the best results.

(ii) As can be seen in Figure IV.9.a, the microgrid appears to be more defined in the austenite compared to the ferrite. This was due to the etching used to reveal the phases prior the application of the modified microgrid technique. The etchant used for this purpose affects the ferrite and not the austenite. As a consequence when a uniform layer of resin was deposited on the surface, the resin on the top of the ferrite is thicker. Figure IV.9.b shows a schematic cross section of the material close to the surface and the layer of resin on it. When an electron beam of constant intensity and diameter scans the surface, the resin on top of the austenite is burnt all the way through

whereas the resin on top of the ferrite is not burnt up to the surface of the material. The resulting microgrid will be defective if a microgrid properly covers only one phase.

(iii) If the difference in heights due to the preliminary etching revealing the microstructure is considerable (long etching times or too high etching voltage) then a further problem arises. Indeed, as the electron beam will be focused on one phase (for example austenite), it will be out of focus on the other one (ferrite), making the spot size and the surface larger but less strong on the ferrite hence the beam will not allow burning the resin on the ferrite. If a more powerful beam is used to overcome the issue, the lines in the austenite will be too wide.

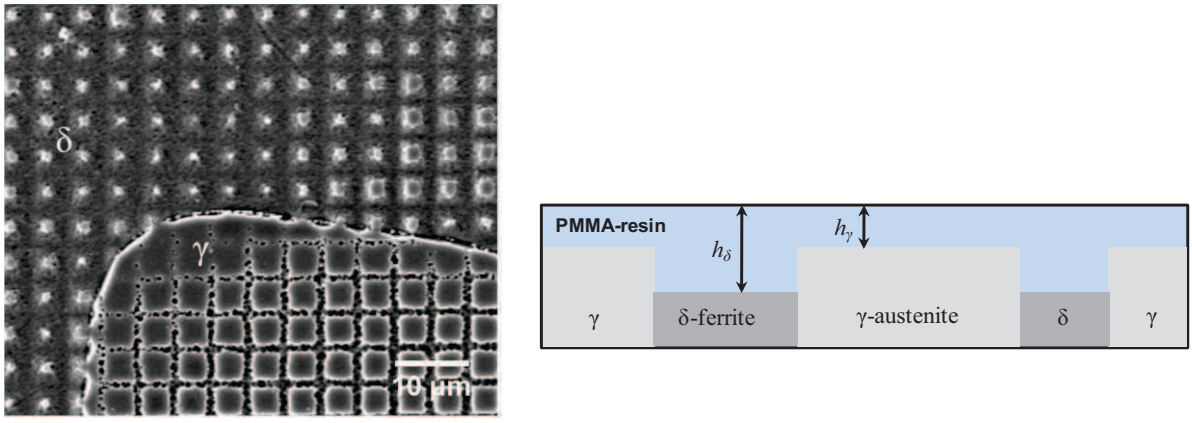


Figure IV.9. a) Microgrids before deformation (notice that the lines are more visible in the austenite); b) difference in terms of heights between austenite (light grey) and ferrite (dark grey) on the surface due to etching of ferrite.

(iv) If excessive engraving is performed, see Figure IV.10**,** the lines in both phases will be too wide, leading to less accurate strain calculations. On the contrary, if insufficient etching is used, the lines will not be visible, especially after high-temperature deformation.

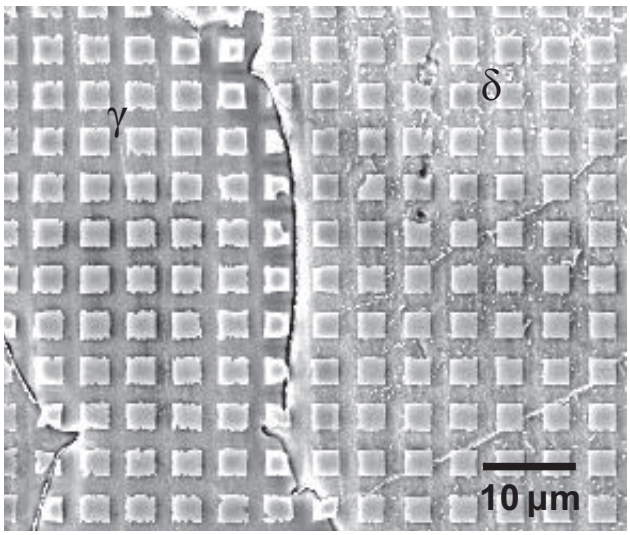


Figure IV.10. Illustration of an excessive engraving in both phase leading to wide lines and loss of accuracy in the strain estimation.

IV.4.2 Plane strain compression testing

IV.4.2.1 The plane strain compression test

The mechanical test used in this work is plane strain compression. Plane strain testing is a modified compression test which could simulate the material flow behaviour experienced during rolling. A schematic diagram of the plane strain compression test is given in Figure IV.11. When the dimensions w and h are significantly smaller than b, the strain can be considered as plane because of the constraint on the deformation in the direction of b due to friction. Here, direction 3 is the transverse direction (TD) parallel to the roller axis whereas directions 1 and 2 correspond, respectively, to the normal direction (ND) and, the rolling direction (RD). The stress system at a point can be represented by three principal stresses, σ_1, σ_2 and σ_3, which give rise to the associated principal strains, ε_1, ε_2, and ε_3. In the plane strain compression test, ε_1 is the thickness strain, ε_3 is the strain in the transverse direction, being in an ideal test equal to zero, and ε_2 is the strain in the rolling direction.

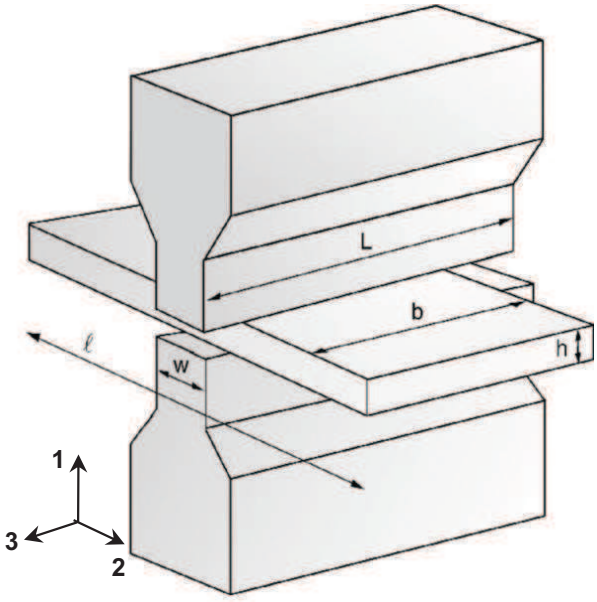


Figure IV.11. Schematic diagram of the plane strain compression test [127].

The purpose of this test is to characterize the mechanical macroscopic behaviour of the material. The test provides the force displacement data from which the equivalent flow stress strain curve can be derived based on a Von Mises material description. The data reduction requires taking into account the stiffness of the machine, the friction between the tool and the specimen, the thermal dilatation, and the imperfect planarity of the strain. Considerations about these corrections can be found in Appendix A. In addition, other problems related to the loss of the deformation symmetry are more difficult to take into account. For instance, an initial misalignment of the platens leads to a Z shape deformation of the specimen whereas a U shape is the consequence of different friction coefficients at the top and bottom tools. As shown in Figure IV.12, this phenomenon can be simulated by finite element modeling.

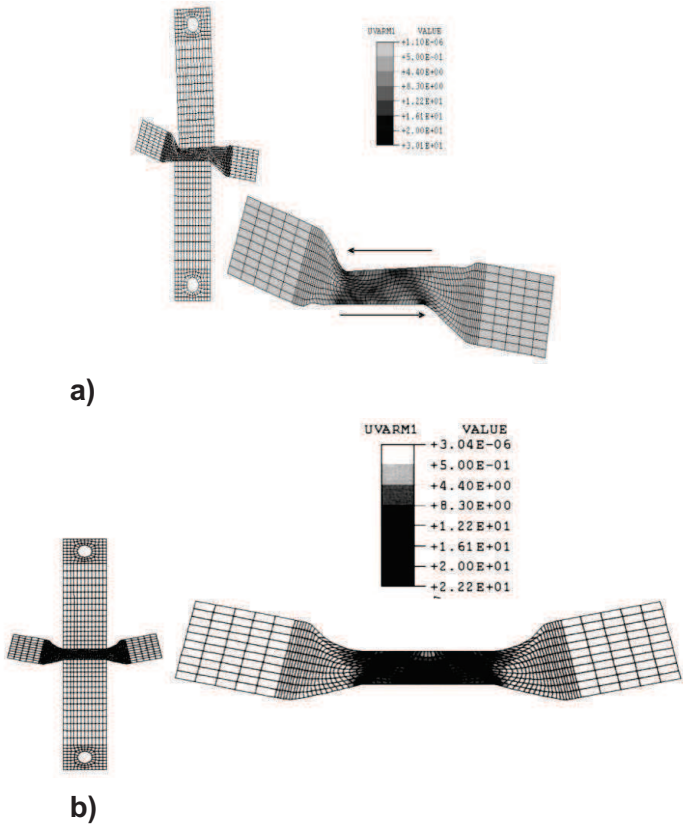


Figure IV.12. Possible problems encountered during plane strain compression; a) Z shape deformed specimen due to initial platen misalignment; b) U shape deformed specimen with different friction coefficients at the top and bottom tools [127].

IV.4.2.2 Modifying the plane strain compression test

Several microgrids engraved on different samples were prepared for plane strain compression testing at high temperature, following the procedure developed by Pinna et al. [14]. The standard geometry of the plane strain compression specimen is modified by machining a rectangular hole in the center in order to deform the samples with a surface-protection against oxidation, at a location of interest for the analysis of the deformation (Figure IV.13). A small circular hole was machined from the specimen side to insert a thermocouple to determine the temperature as close as possible to the microgrid.

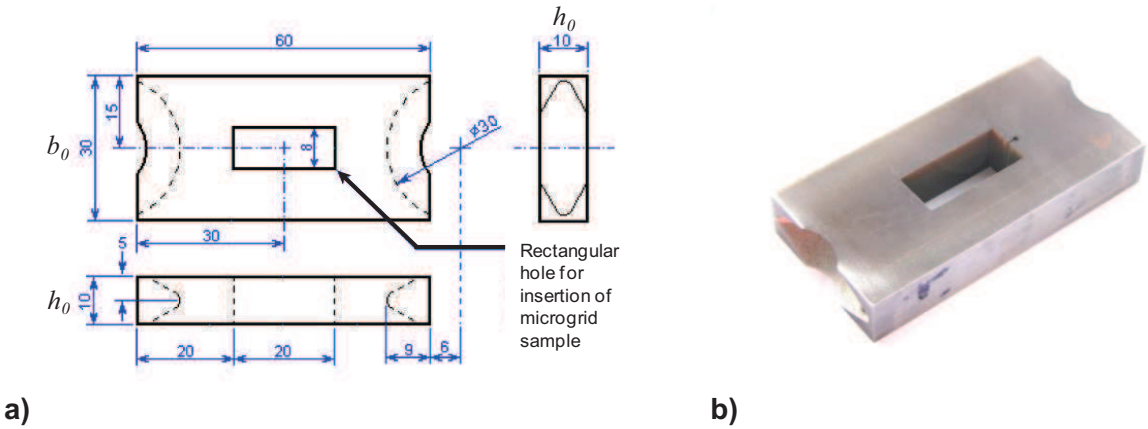


Figure IV.13. a) Technical drawing of the modified plane strain compression specimen, dimensions are in millimeters (mm); b) picture of a modified plane strain compression specimen.

Figure IV.14 summarizes schematically the procedure to assemble the modified plane strain compression specimen and a microgrid sample. This procedure follows three steps.

(i) The microgrid specimen is welded to a similar polished plate in order to protect the microgrid surface during the assembly within the plane strain compression specimen. The welding step has to be well-controlled so that the microgrid and the associated microstructure is not heat affected. In most of the cases, the thickness of the heat affected zone was about 2 mm.

(ii) The welded plates are inserted into the rectangular hole in the center of the plane strain compression specimen, with the microgrid surface parallel to the loading direction.

(iii) The inserts and the plane strain compression sample are welded together on top and bottom to protect the microgrid from oxidation during the high temperature test. The welding must be controlled to minimize the amount of melted material and to make sure that the welding affected area does not reach the microgrid.

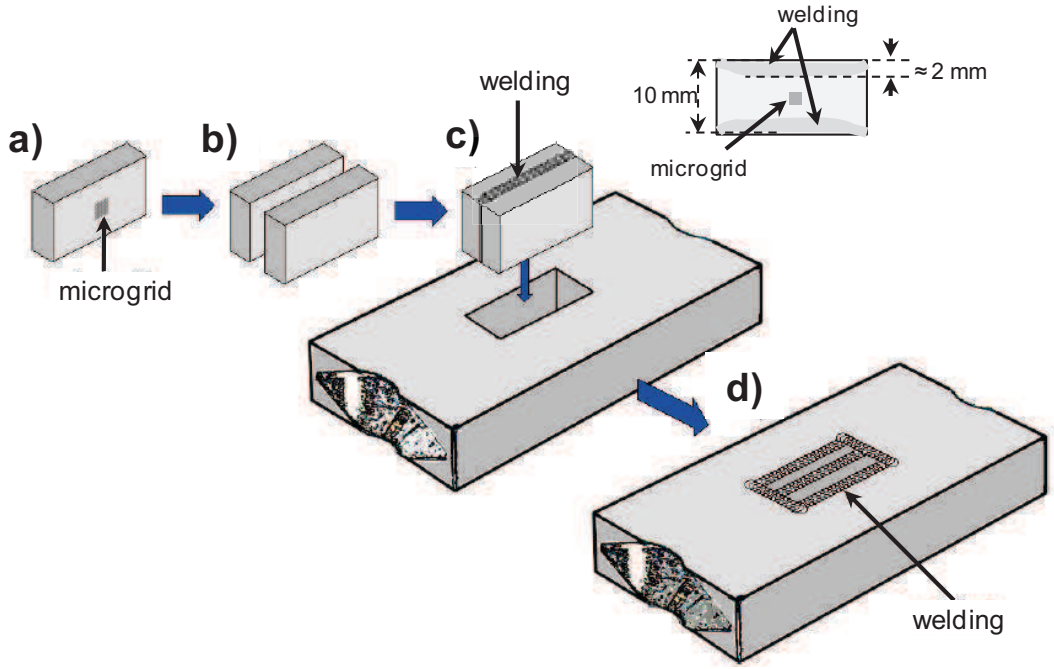


Figure IV.14. Preparation of the modified plane strain compression sample; a) microgrid sample; b) face to face with a similar polished plate; c) assembly with modified plane strain compression specimen; d) welding at top and bottom [97].

IV.4.2.3 Plane strain compression machine

The plane strain compression specimens were deformed with a thermo-mechanical compression machine (Figure IV.15). This device allows the simulation of multiple pass deformation schedules under isothermal conditions.

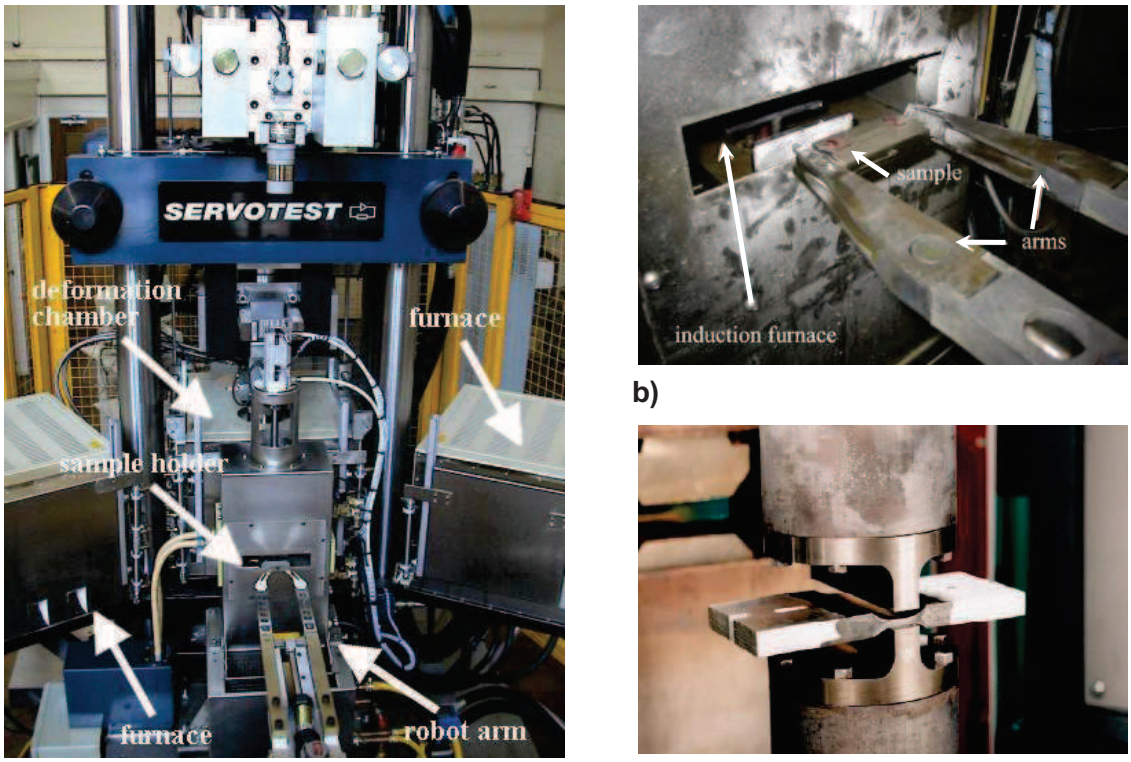


Figure IV.15. Different views of the thermo-mechanical compression machine; a) front view; b) view of the sample held by the two arms; c) view of the deformation chamber.

The testing machine involves a fast thermal treatment unit which provides high-controlled rates of heating and cooling in order to generate the required microstructure. The main use of such machine is to simulate hot and cold rolling, up to a strain rate of over $100s^{-1}$ and a temperature of 1200°C. In Figure IV.16, the directions 1, 2 and 3 correspond respectively to the normal direction (ND), rolling direction (RD) and transverse direction (TD). The microgrids inside the modified plane strain compression specimens were located at the middle of the deformation zone (aligned with the central line of the compression tools as shown in Figure IV.16, expecting pure compression conditions in the microgrid area).

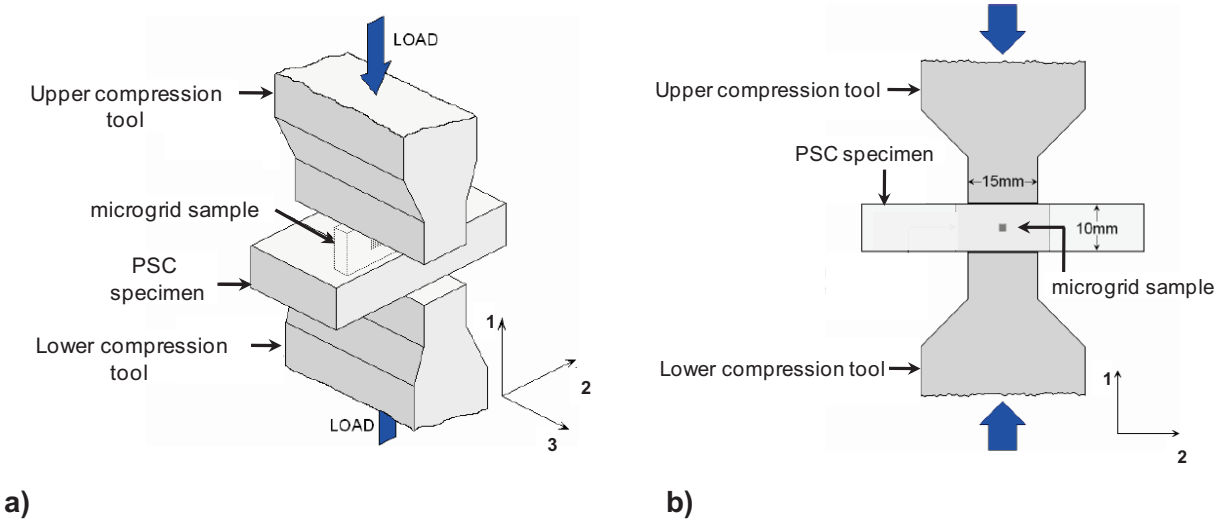


Figure IV.16. Schematic views of the microgrid sample inserted into the plane strain compression specimen and the compression tools during the tests; a) asymmetric view; b) plane view.

IV.4.2.4 Testing conditions

The complete thermo-mechanical path undergone by the plane strain compression specimens is presented in Figure IV.17. The specimens were quickly heated at the testing temperature, annealed for 30s at this temperature, and deformed under plane strain compression at a strain rate of $1s^{-1}$. Only four samples were deformed at a strain rate of $10s^{-1}$. The specimens were immediately quenched after deformation in order to limit microstructural modifications: phase transformation, grain growth or coarsening phenomena. Several temperatures (850, 950, and 1050°C), different nominal strains and two different austenite morphologies were used. The experimental conditions were chosen to compare both grades and to provide tendencies concerning the influence of the temperature, the macroscopic strain and also the morphology of the microstructure on the strain partitioning between ferrite and austenite at high temperature.

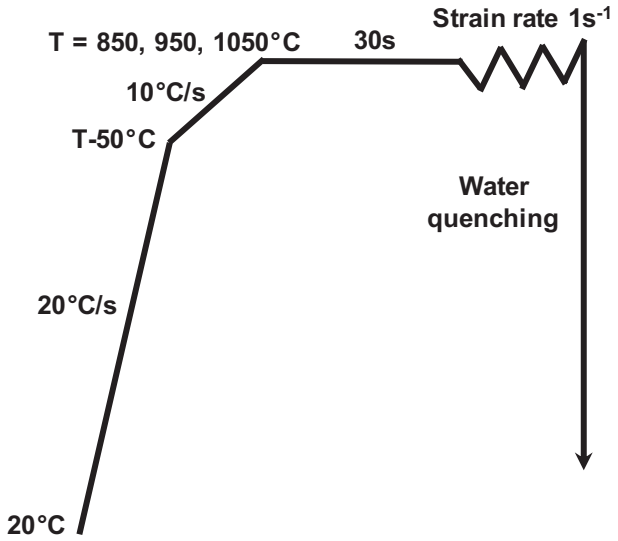


Figure IV.17. Thermo-mechanical path undergone by the plane strain compression specimens.

The tests must be performed as quickly as possible in order to avoid the precipitation of the brittle σ-phase, especially for the alloy D1 (2205). Indeed, considering a TTT-diagram (Figure IV.18) this brittle phase can precipitate rapidly in the D1 alloy. At 850°C, the σ-phase can nucleate just after 2min and 30s and after more than 3min thermal ageing at 950°C. At 1050°C, there is not any sign of the presence of the σ-phase. Indeed, 1050°C is the temperature at which the material is industrially annealed in order to make sure that the σ-phase is entirely dissolved and that the ferrite-austenite phase balance is close to 50-50%. Concerning, the alloy D2, a remote possibility exists to form the σ-phase because even at 850°C it would require long thermal ageing (more than 10min). It was checked for both grades, after a 1min 30s 850°C-ageing, that there was no sign of a σ-phase precipitation.

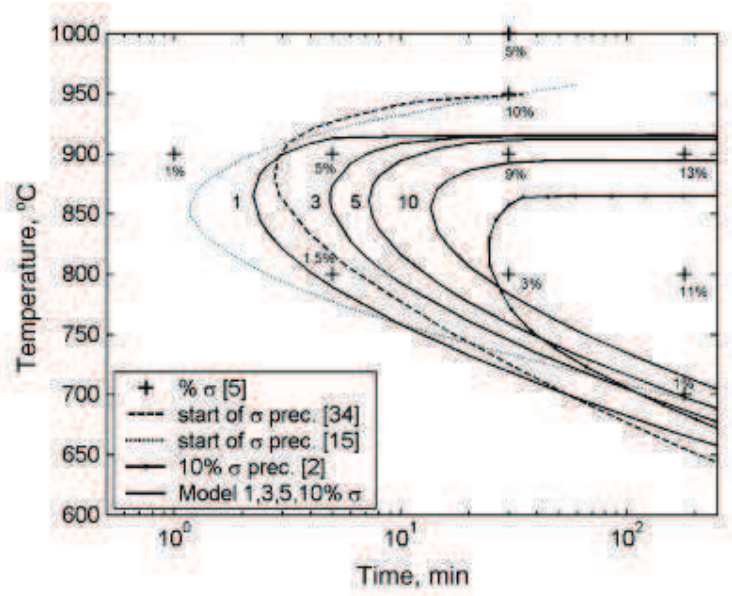


Figure IV.18. Time-Temperature-Transformation diagram of a 2205 duplex stainless steels. Illustration of the σ phase isothermal precipitation [69].

IV.4.2.5 Extraction of the deformed microgrids

Following the hot deformation and water quenching, the microgrid sample is extracted from the plane strain compression sample as shown schematically in Figure IV.19. The plane strain compression specimen is firstly cut into five pieces, and then the welding at the top and the bottom is polished down to the interface between the two inserts. Finally, one of the insert is tightened in a clamp and a wedge is delicately knocked along the interface in order to separate the two inserts.

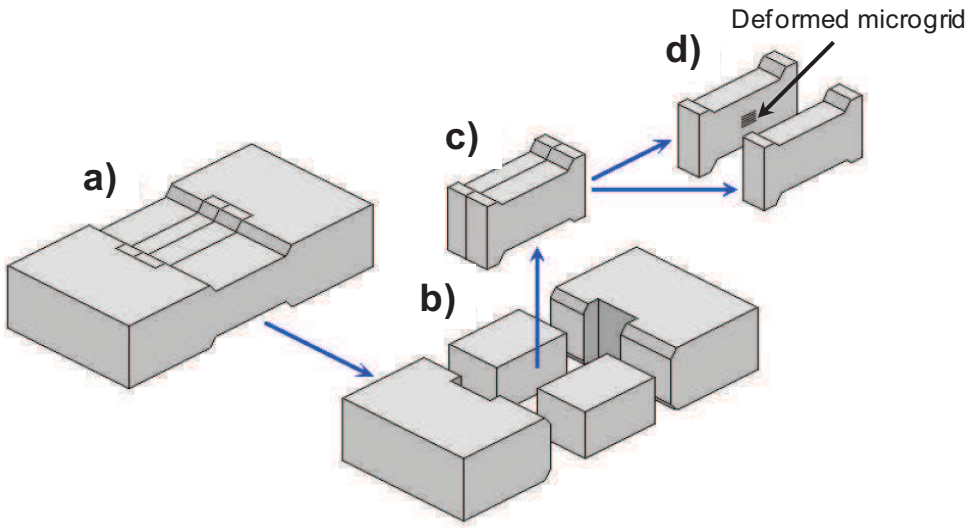


Figure IV.19. Schematic extraction of microgrid from deformed plane strain compression sample; a) deformed plane strain compression specimen; b) specimen cut in five pieces; c) inserts; d) separation of the two inserts, one of them being the microgrid sample.

All the microgrids which were still recognizable after deformation were analyzed in the SEM, the same way as before deformation. Table IV.2 summarizes the experimental conditions used for the different specimens.

Material	Sample	Temperature (°C)	Strain rate (s^{-1})	Reduction (%)	Thickness strain	Microgrid
D2_W	*II*	*850°C*	*1*	*20*	*-0.23*	- -
D2_W	*III*	*850°C*	*1*	*30*	*-0.37*	++
D2_W	*IV*	*950°C*	*1*	*20*	*-0.23*	- -
D2_E	*1*	*850°C*	*1*	*20*	*-0.22*	- -
D2_E	*2*	*1050°C*	*10*	*20*	*-0.22*	- -
D2_E	*3*	*1050°C*	*10*	*30*	*-0.37*	- -
D2_E	*4*	*1050°C*	*10*	*40*	*-0.51*	- -
D1_W	*ii*	*850°C*	*1*	*20*	*-0.22*	+
D1_W	*iii*	*850°C*	*1*	*20*	*-0.36*	++
D1_W	*iiii*	*950°C*	*1*	*30*	*-0.22*	++
D1_E	*A*	*950°C*	*1*	*20*	*-0.21*	+
D1_E	*B*	*850°C*	*1*	*20*	*-0.24*	++
D1_E	*C*	*850°C*	*1*	*20*	*-0.22*	- -
D1_E	*D*	*850°C*	*1*	*30*	*-0.35*	+

Table IV.2. Plane strain compression test conditions for all the specimens. In the column entitled microgrid, the symbol (- -) means that the microgrids were not sufficiently recognizable to perform strain calculations; (+) means that one of the microgrid was recognizable and (++) means that several microgrids were readable to carry out strain estimations.

IV.4.3 Strain distribution mapping

IV.4.3.1 Procedure

The micro-scale strain distributions within the microgrid area are calculated by comparing the undeformed and the deformed states. The calculation and plotting procedures of the micro-scale strain distribution can be summarized as follows. Some details about the strain computations are given in Appendix B.

(i) The largest areas possible where the microgrids were still recognizable were selected. From these areas, the coordinates of the microgrid intersections from the undeformed and deformed configurations were obtained by manual or automatic location depending on the quality of the microgrid pattern. Throughout this work, a fully automatic analysis was not possible because of the presence of small areas where the microgrid was damaged or exhibited too large variations of the local image contrast between the reference and deformed configurations. The local relief induced by the out-of-plane displacement as well as the slight oxidation which can occur during the thermo-mechanical were responsible for the variations of the local image contrast. In such areas, the grey level conservation principle on which correlation techniques rely is no longer valid. That is why the microgrid intersections were always manually located using *CorrelManuV* software developed by Bornert [128] and Doumalin [129].

(ii) Then, a database containing the intersections coordinates was processed using the same software, which provided the strain components ε_{11}, ε_{22}, ε_{33}, ε_{12} and the equivalent Von Mises strain, for every microgrid intersection following the procedure described in the next section. Note that according to the axes shown in Figure IV.16, ε_{11} and ε_{22} are the uniaxial strain components in the directions parallel and perpendicular, respectively, to the loading (vertical) direction, and ε_{12} is the shear strain component.

(iii) The distributions of the calculated strain components were then plotted using *CorrelManuV*, with different colours depending on the strain value.

(iv) Finally, the SEM micrographs of the undeformed microstructure were edited using the image software *Gimp* to generate the contour of the grain and interphase boundaries. These contours were then superimposed on the strain map in order to analyze how the strains were distributed in the microstructure.

IV.4.3.2 Calculation of the local strain components

The displacement gradient tensor can be written as indicated by eq IV-1:

$$\overline{\overline{F}} = \begin{bmatrix} F_{11} & F_{12} & F_{13} \\ F_{21} & F_{22} & F_{23} \\ F_{31} & F_{32} & F_{33} \end{bmatrix}. \qquad \textbf{eq IV-1}$$

The program developed by Bornert and Doumalin [129] provides the in-plane displacement components of each microgrid intersection, which leads to the in-plane components of the local transformation gradient tensor (F_{11}, F_{22}, F_{12}, and F_{21}). The procedure and equations required for calculating the local in-plane gradient components are described in details in the paper published by Allais et al. [98], in reference [128], and are also indicated in Appendix B.

Additional assumptions have to be formulated in order to estimate the unknown gradient components (F_{13}, F_{23}, F_{31}, F_{32} and F_{33}).

Traditionally, it is considered that the direction orthogonal to the image (direction 3 in Figure IV.16), is a principal direction for the transformation.

It is also assumed that there is no rotation outside the plane (ND, RD). Thus, only the F_{33} component is not equal to zero whereas $F_{i3}=F_{3i}=0$ for i = [1; 2] (eq IV-2), hence

$$\overline{\overline{F}} = \begin{bmatrix} F_{11} & F_{12} & 0 \\ F_{21} & F_{22} & 0 \\ 0 & 0 & F_{33} \end{bmatrix}. \qquad \textbf{eq IV-2}$$

Several assumptions are made to estimate F_{33}.

- The isochoric hypothesis (incompressibility, i.e. no volume variation during the deformation) consists in setting that the determinant of the gradient tensor is equal to unity (eq IV-3). The gradient tensor can be diagonalized and its eigenvalues are F_1, F_2 and F_3. It means that F_3 is equal to the inverse of the product of the two other gradient eigenvalues F_1 and F_2 as shown in eq IV-4.

$$\det \overline{\overline{F}} = F_1 F_2 F_3 = 1, \qquad \textbf{eq IV-3}$$

$$F_3 = \frac{1}{F_1 F_2}. \qquad \textbf{eq IV-4}$$

- The deformation is perfectly plane, it means that F_{33} =1.

Once the entire gradient components are estimated, the strain components (ε_{11}, ε_{22}, ε_{33}, ε_{12}) and the equivalent Von Mises strain ($\varepsilon_{eq}^{VonMises}$) can be calculated selecting a strain definition (Green-Lagrange, logarithmic or linear). The procedure for computing the strain components is summarized in Figure IV.20.

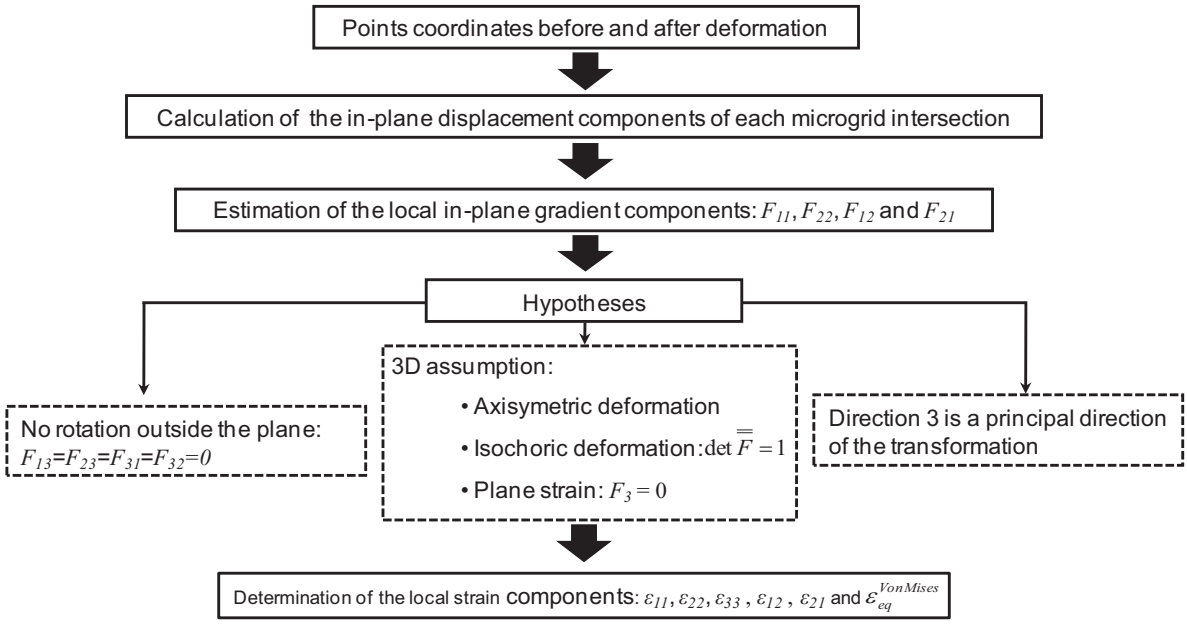


Figure IV.20. Procedure to calculate the strain components starting from the coordinates of the grid points.

In this study, the isochoric assumption will be suggested and it will be checked that F_{33} is close to unity as in a perfectly plane strain test. It has also been chosen to measure the strain components according to the logarithmic definition of the strain because it is the definition conventionally used by metallurgists.

IV.4.3.3 Computation of the in-plane components of the logarithmic strain tensor

Calculations of the strain components using the logarithmic definition are now clarified, details about the strain calculations according to the Green-Lagrange definition or the linear definition can be found in [128]. The gradient of the transformation can be written as the product of a rotation tensor, $\overline{\overline{R}}$ by a distortion tensor, $\overline{\overline{U}}$ (eq IV-5):

$$\overline{\overline{F}} = \overline{\overline{R}} \cdot \overline{\overline{U}} . \qquad \textbf{eq IV-5}$$

The distortion tensor $\overline{\overline{U}}$ can be diagonalized in an orthogonal base as in eq IV-6:

$$\overline{\overline{U}} = \overline{\overline{Q^t}} \cdot \overline{\overline{D}} \cdot \overline{\overline{Q}}, \qquad \textbf{eq IV-6}$$

where $\overline{\overline{D}}$ is the diagonal tensor, $\overline{\overline{Q}}$ a tensor giving the orientation of the principal directions of the distortion and $\overline{\overline{Q^t}}$ the transpose tensor of $\overline{\overline{Q}}$. The eigenvalues of the diagonalized tensor $\overline{\overline{D}}$ and of $\overline{\overline{F}}$ are the same. The logarithmic strain tensor is then computed from eq IV-7.

$$\overline{\overline{\varepsilon^{\log}}} = \overline{\overline{Q^t}} \cdot \ln \overline{\overline{D}} \cdot \overline{\overline{Q}} \qquad \textbf{eq IV-7}$$

where $\overline{\overline{\varepsilon^{\log}}} = \begin{bmatrix} \varepsilon_{11} & \varepsilon_{12} & \varepsilon_{13} \\ \varepsilon_{21} & \varepsilon_{22} & \varepsilon_{23} \\ \varepsilon_{31} & \varepsilon_{32} & \varepsilon_{33} \end{bmatrix}$, $\overline{\overline{Q}} = \begin{bmatrix} \cos\theta & \sin\theta & 0 \\ -\sin\theta & \cos\theta & 0 \\ 0 & 0 & 1 \end{bmatrix}$, and $\overline{\overline{D}} = \begin{bmatrix} F_1 & 0 & 0 \\ 0 & F_2 & 0 \\ 0 & 0 & F_3 \end{bmatrix}$;

θ is the polar angle of the principal distortion F_2, measured in the trigonometrical direction; actually it gives the tensile direction; F_1, F_2 and F_3 are the eigenvalues of the gradient tensor.

By developing eq IV-7, the logarithmic strain tensor is obtained (eq IV-8) as:

$$\overline{\overline{\varepsilon^{\log}}} = \begin{bmatrix} \ln F_1 \cos^2\theta + \ln F_2 \sin^2\theta & \sin\theta\cos\theta \ln(F_1/F_2) & 0 \\ \sin\theta\cos\theta \ln(F_1/F_2) & \ln F_1 \sin^2\theta + \ln F_2 \cos^2\theta & 0 \\ 0 & 0 & \ln F_3 \end{bmatrix}. \qquad \textbf{eq IV-8}$$

The equivalent Von Mises strain is calculated thanks to eq IV-9.

$$\varepsilon_{eq}^{VonMises} = \sqrt{\frac{2}{3} \cdot (\varepsilon_{11}^2 + \varepsilon_{22}^2 + \varepsilon_{33}^2 + 2\varepsilon_{12}^2)} \qquad \textbf{eq IV-9}$$

IV.4.3.4 Per-phase average strains

In Figure IV.21, two different polygonal lines joining microgrid intersections are drawn and represent two possible ways of defining the interface between ferrite and austenite, including or not part of the neighbour phase. The real interface is somewhere in between. Per-phase average deformation can be computed using the procedure described in section IV.4.3.2 applied to the two different polygonal lines mentioned previously and defined in Figure IV.21. Different results are obtained if the line “with or without interface” is used. The average of both values provides a good estimate of the exact values.

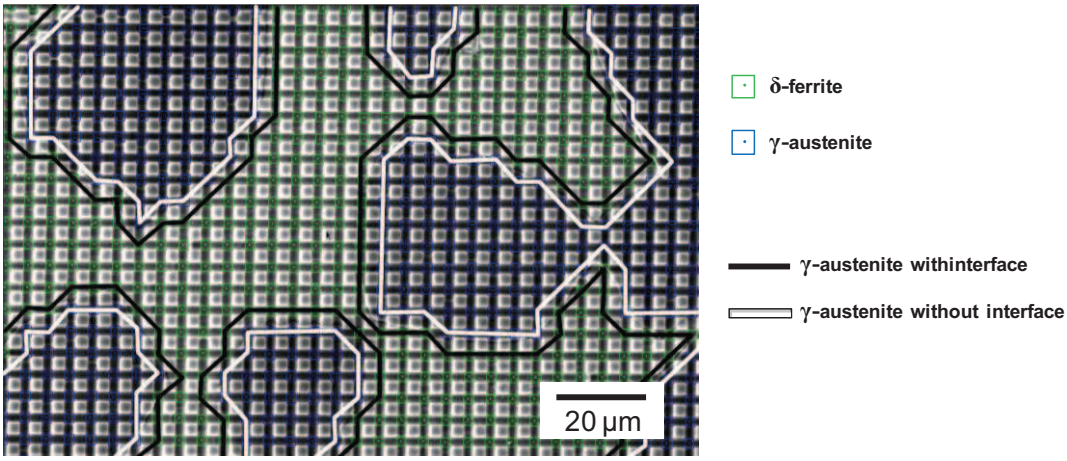


Figure IV.21. Integration scheme for the average gradient over a phase

IV.4.3.5 Errors on the computation of the strains

There are several elements that induce some errors on the strain calculation. In this section, only a few of these elements are considered, more details can be found in [98] and [128].

- To estimate the error related to the manual location of the microgrid intersections, the same region of interest has been analyzed two times and the results given in each case have been compared. The comparison of the results showed that the error related to the manual location of the microgrid intersections could be neglected.

- The main source of errors is due to the bad approximation of the interface, as shown by the difference in the area of the integration domains in each case, which generally is close to 15% of the area of the characterized area. In fact, the computations “with interface” for the harder phase (austenite) takes into account this phase plus some domain of the weaker phase (ferrite), more strained, and thus gives upper bounds for the average gradient components; it leads to lower bounds in case of the weaker phase. For a given phase, the error related to the bad location of the interface can be estimated by the half difference between the result “with interface” and without interface”. Note that the average of the result “with interface” of a given phase and the result “without interface” of the other phase, weighted with the corresponding areas, gives the overall value.

IV.5 Comparison between D1 and D2 Widmanstätten microstructures

As shown in Table IV.2, only a few satisfying results were obtained from the microgrid experiments for the alloy D2. As a consequence these results were used to compare both grades. In this section, the two investigated grades deformed at 850°C and $1s^{-1}$ up to a reduction of 30% and showing a Widmanstätten microstructure: D2_W (sample III) and D1_W (sample iii) are compared in terms of strain partitioning.

IV.5.1 Results

IV.5.1.1 Macroscopic stress-strain curves

The macroscopic equivalent stress-strain curves obtained from the plane strain compression tests were representative of the experimental material since the plane strain compression specimen and the inserts were machined from the same material. In previous studies [50, 97], only the insert was made of the investigated material and the rest of the sample was made of commercial steel. The macroscopic stress strain curves of both alloys deformed in the same conditions are presented in Figure IV.22.a. Although both curves show the same overall shape, the yield stress and the steady state stress reach significantly different levels, see Table IV.3. For instance the plastic deformation of the alloy D1 requires a higher stress when comparing with the stress required to deform plastically alloy D2. Figure IV.22.b shows the deformed D1_Wiii specimen with the deformation region at the middle of the specimen, involving a small amount of bulging.

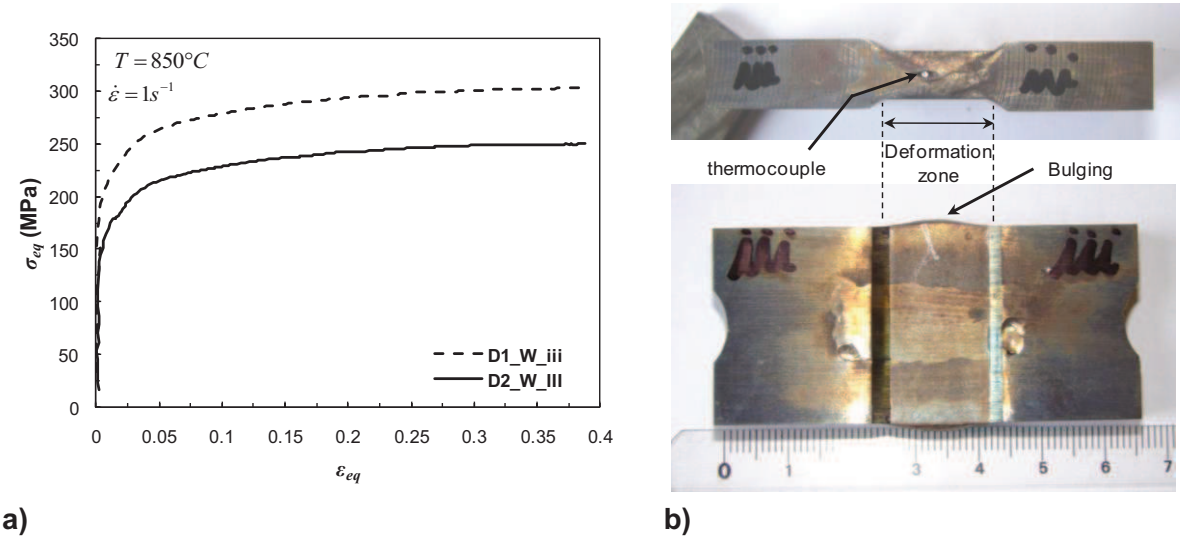


Figure IV.22. a) Comparison between the macroscopic stress strain curves of the D1_W and D2_W microstructures obtained under plane strain compression at 850°C and $1s^{-1}$ up to a reduction of 30%; b) pictures showing a top view and a front view of a deformed plane strain compression specimen.

	sample	T (°C)	$\dot{\varepsilon}$ (s^{-1})	σ_0 (MPa)	$\sigma_{steady\ state}$ (MPa)
D1_W	iii	850°C	1	175	300
D2_W	III	850°C	1	125	250

Table IV.3. Summary of the plane strain compression experimental conditions and typical stress values in both microstructures D1_W and D2_W.

IV.5.1.2 Micro-scale strain analysis

IV.5.1.2.1 Qualitative analysis

Relevant areas were selected from the large SEM pictures of the deformed microgrids, and the displacements of the grid intersections (with reference to their undeformed configurations) were used to calculate the distribution of the local strain components and of the equivalent strain using the procedure described in section IV.4.3. The calculated data were used to plot colour maps for different levels of strain. The corresponding microstructures, in their undeformed configuration, were edited to extract the interphase boundaries. The boundaries were then superimposed to the colour map in order to reveal clearly the link with the microstructure.
It has been chosen to plot the strain maps using the undeformed configuration because it was easier to extract the interphase boundaries from the initial microstructure compared to the deformed microstructure. Indeed, in the deformed configuration it is very difficult to see the interphase boundaries due to a slight oxidation, or in some areas large distortion of the microgrids.

The equivalent strain maps of the two microstructures D1_W and D2_W are respectively shown in Figure IV.23 and Figure IV.24. In each plane strain compression specimen, two different regions are analyzed, hence two strain maps are plotted (map1 and map2).

Some general qualitative considerations concerning the deformation features can be made by observing the strain maps and the deformed microgrids.

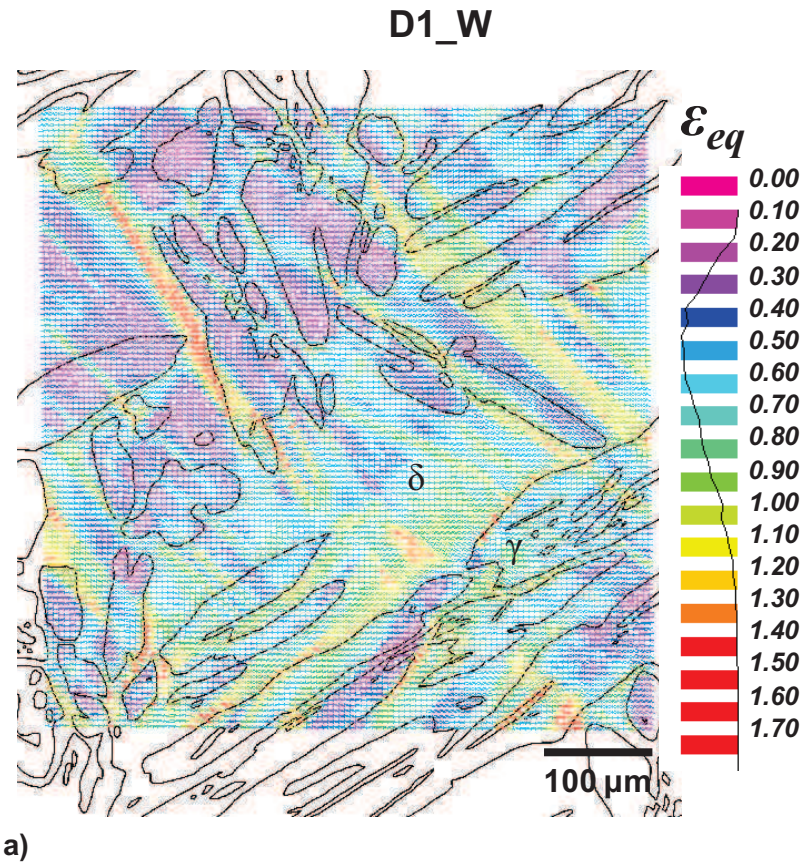


Figure IV.23. Equivalent strain distribution maps of the D1_W microstructure; a) map 1; b) map 2; the equivalent strain map is superimposed with the undeformed microstructure to clearly present where in the microstructure the strains are distributed; the compression axis corresponds to the vertical axis.

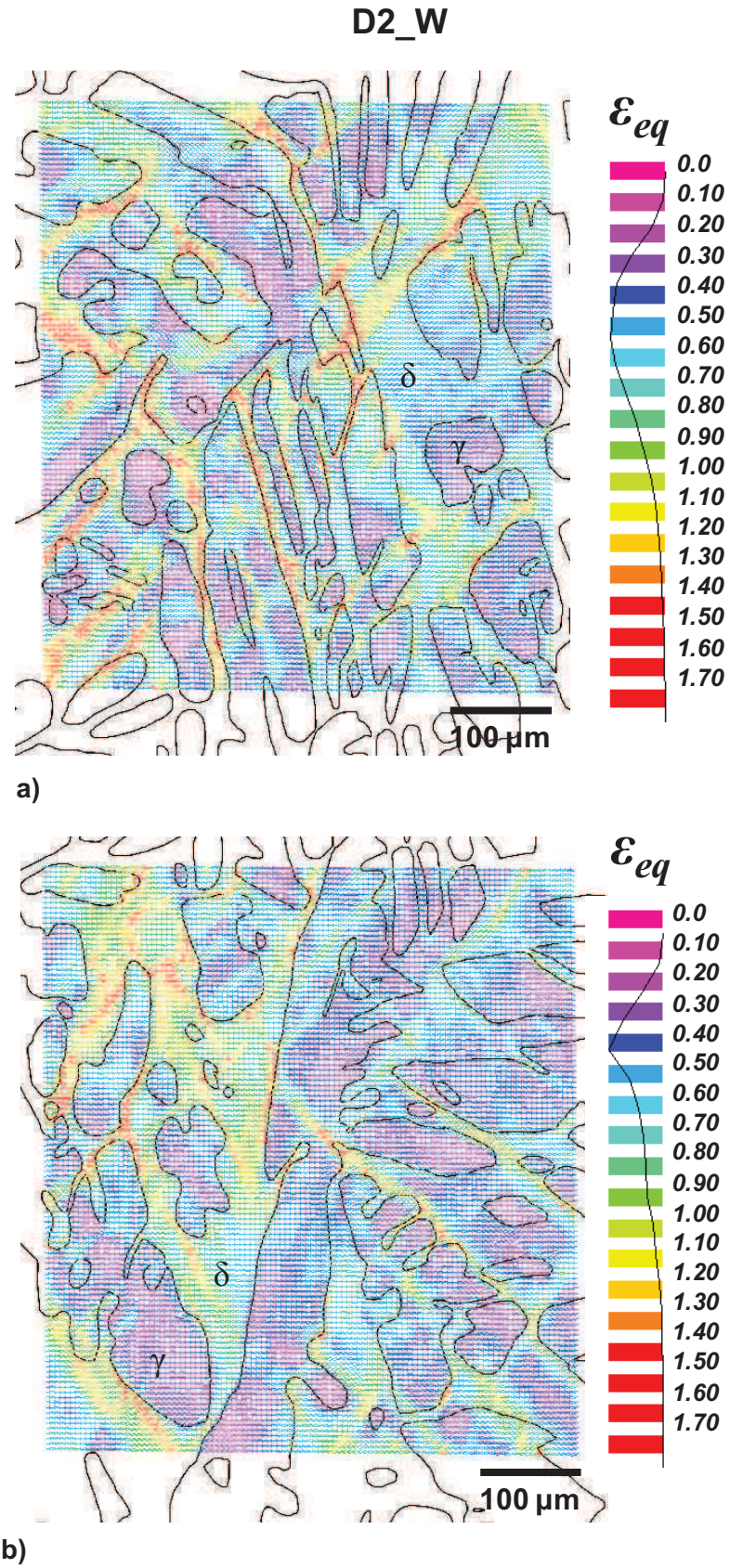
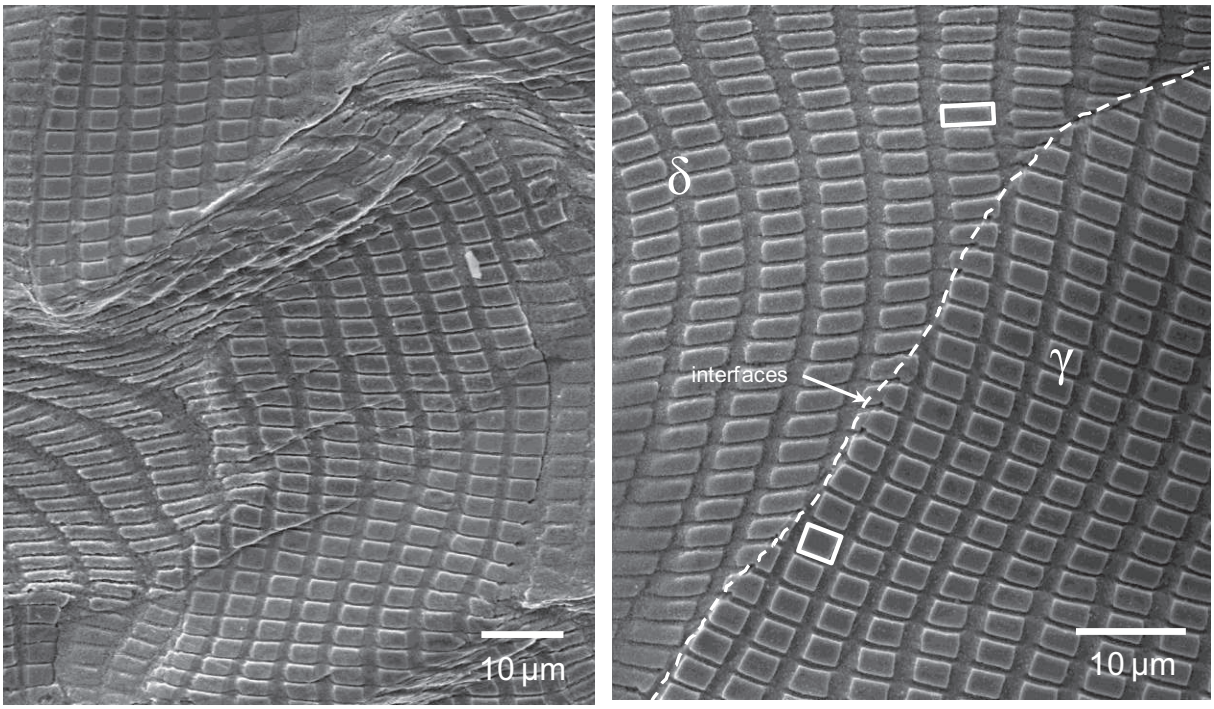


Figure IV.24. Equivalent strain distribution maps of the D2_W microstructure; a) map 1; b) map 2; the equivalent strain map is superimposed with the undeformed microstructure to clearly present where in the microstructure the strains are distributed; the compression axis corresponds to the vertical axis.

❖ **Heterogeneity of the deformation**

First of all, the strain maps show that the deformation is heterogeneously distributed in both grades; some areas are only slightly deformed whereas others are strongly deformed, see Figure IV.23 and Figure IV.24. SEM micrographs of the deformed microgrids corroborate these considerations; some examples are given in Figure IV.25. Furthermore, it seems that the deformation is more accommodated by the ferrite than the austenite because the more deformed regions (red colour in the strain maps) correspond to ferrite. A small area of the deformed D2_W microgrid is presented in Figure IV.25.b showing that the ferrite is more deformed than the austenite. Indeed, the initial microgrid squares were changed into rectangle in the ferrite whereas they kept their initial shape in the austenite.

Several SEM micrographs of the microgrids before and after deformation are also given in Appendix C and confirm that the deformation is heterogeneously distributed in the different microstructures.



a) **b)**

Figure IV.25. Illustration of the heterogeneity of the deformation in the D2_W microstructure after plane strain compression at 850°C and at a strain rate of $1s^{-1}$; a) SEM pictures showing strongly deformed areas and slightly distorted regions; b) SEM picture showing the strain partitioning between ferrite and austenite. The square in the austenite indicates a slight deformation in the austenite whereas the rectangle shape in the ferrite emphasizes a significant deformation in the ferrite. The compression axis is the vertical direction.

❖ **Out of plane displacement**

Another deformation feature which could be observed is the step developed at some grain or interphase boundaries, see Figure IV.26. This feature was presumably caused by the out-of-plane displacement of the microgrid surface during deformation. A few comments about this deformation feature will be formulated in section IV.7.3.

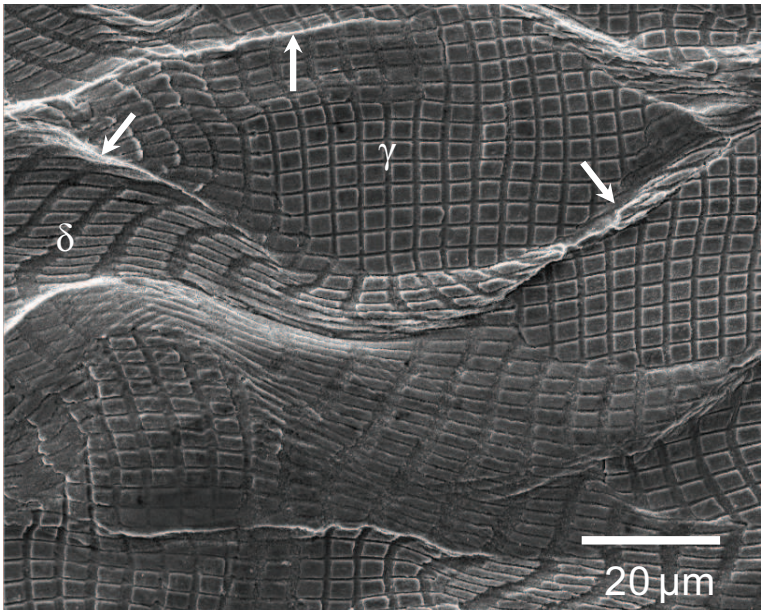


Figure IV.26. SEM micrograph of a deformed microgrid showing the out-of-plane displacement, the arrows point out the regions the most affected by this phenomenon.

❖ **Shear bands development**

The strain maps highlight an additional deformation feature: the development of shear bands. Their development seems to depend on the distribution of the austenite, see Figure IV.27.

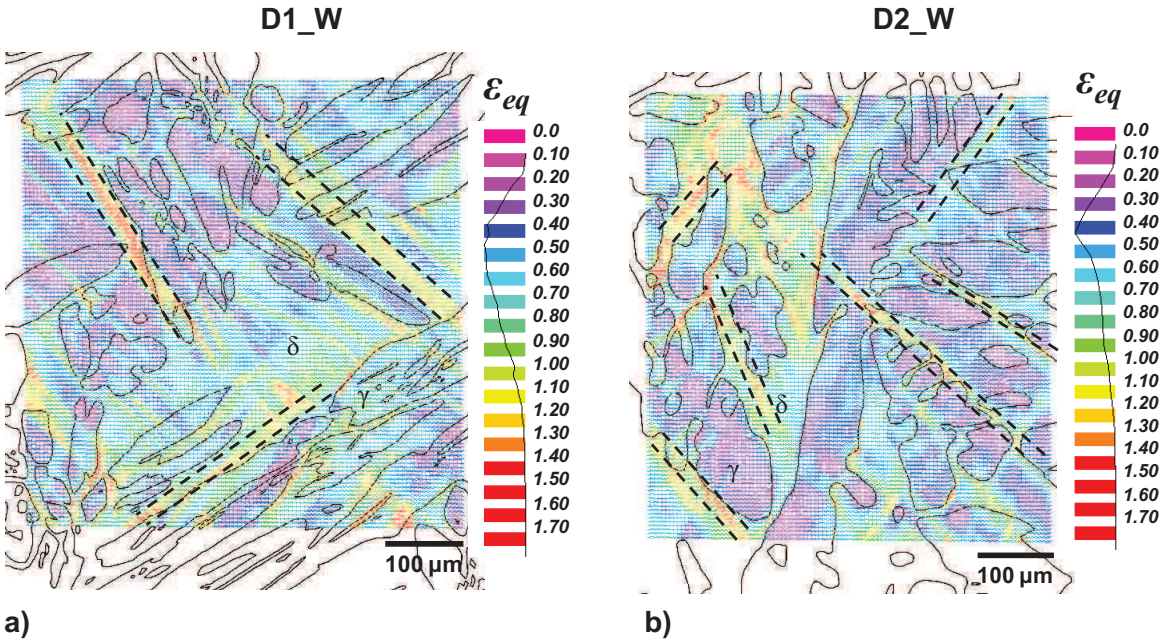


Figure IV.27. Strain maps superimposed with dotted lines which emphasize the development of shear bands; a) map 1 in D1_W; b) map 2 in D2_W.

❖ **More severely strained regions**

Finally, it has to be noticed that the more strained zones in the microstructures are almost always situated in the vicinity of the δ/γ interphase boundaries. Locally, the ratio $\varepsilon_{eq}^{\delta} / \varepsilon_{eq}^{\gamma}$ fluctuates between 2 and 3, and in a few areas, this ratio can reach 5. These results are in agreement with the observations carried out on the edge part of the hot rolled material or close to the fracture in the DENT specimens showing that damage always nucleates at the δ/γ interphase boundaries, see Figure I.9.b and Figure III.15.

All these deformation features can be observed in the D1_W microstructure as well as in the D2_W allowing a better understanding of the mechanisms involved in the high temperature deformation of duplex stainless steels. Nevertheless, these qualitative comments do not permit to establish accurate comparisons between both grades. Therefore, additional analysis is needed involving a more quantitative treatment of the strain partitioning in both microstructures.

IV.5.1.2.2 Quantitative analysis

Several options are available to provide quantitative results about the strain partitioning. An overview of these options is given in this section. The results are presented for each grade keeping in mind that two different regions were analyzed in the plane strain compression specimen providing two strain maps: map1 and map2.

❖ **Average deformation per phase.**

First of all, the average deformation per phase for both microstructures are computed, the results are summarized in Table IV.4 for the D1_W microstructure and in Table IV.5 for the D2_W microstructure.

D1_W		$<\varepsilon_{11}>$	$<\varepsilon_{22}>$	$<\varepsilon_{12}>$	$<\varepsilon_{33}>$	$<\varepsilon_{eq}>$
Overall	Map 1	-0.572	0.452	0.004	0.120	**0.603**
	Map 2	-0.753	0.633	-0.013	0.120	**0.809**
Austenite γ	Map 1	-0.495 ± 0.023	0.398 ± 0.015	0.003 ± 0.006	0.097 ± 0.008	**0.525**
	Map 2	-0.662 ± 0.025	0.589 ± 0.010	-0.001 ± 0.001	0.074 ± 0.016	**0.726**
Ferrite δ	Map 1	-0.642 ± 0.001	0.495 ± 0.002	0.004 ± 0.003	0.147 ± 0.001	**0.673**
	Map 2	-0.816 ± 0.002	0.661 ± 0.002	-0.020 ± 0.001	0.154 ± 0.003	**0.866**

Table IV.4. Average logarithmic deformation per phase in the two strain maps determined in the D1_W microstructure.

D2_W		$<\varepsilon_{11}>$	$<\varepsilon_{22}>$	$<\varepsilon_{12}>$	$<\varepsilon_{33}>$	$<\varepsilon_{eq}>$
Overall	Map 1	-0.540	0.463	0.177	0.077	**0.619**
	Map 2	-0.520	0.457	-0.061	0.064	**0.572**
Austenite γ	Map 1	-0.434 ± 0.028	0.364 ± 0.031	0.154 ± 0.009	0.070 ± 0.004	**0.499**
	Map 2	-0.416 ± 0.025	0.347 ± 0.026	-0.031 ± 0.007	0.070 ± 0.001	**0.447**
Ferrite δ	Map 1	-0.670 ± 0.010	0.559 ± 0.004	0.198 ± 0.001	0.111 ± 0.006	**0.754**
	Map 2	-0.646 ± 0.004	0.562 ± 0.007	-0.094 ± 0.003	0.084 ± 0.003	**0.711**

Table IV.5. Average logarithmic deformation per phase in the two strain maps determined in the D2_W microstructure.

A relevant parameter which allows quantifying the strain partitioning is the ratio between the average deformation in the ferrite divided by the average deformation in the austenite, see Table IV.6. The results show that in both microstructures, the ferrite accommodates more deformation compared to the austenite. However, the strain contrast between ferrite and austenite is significantly larger in the D2_W microstructure compared to the D1_W microstructure. In the D1_W microstructure, the ferrite can be deformed around 30% more than the austenite whereas in the D2_W the ferrite can be strained up to 60% more than the austenite on average.

		$< \varepsilon_{eq}^{overall} >$	$< \varepsilon_{eq}^{\delta} > / < \varepsilon_{eq}^{\gamma} >$
D1_W	Map 1	0.603	**1.28**
	Map 2	0.809	**1.20**
D2_W	Map 1	0.619	**1.51**
	Map 2	0.572	**1.60**

Table IV.6. Calculation of the ratio between the average deformation in the ferrite over the average deformation in the austenite, parameter that quantifies the strain partitioning between ferrite and austenite in duplex stainless steels.

❖ **Strain distribution functions**

Another way to characterize the strain heterogeneity is to plot the strain distribution functions. In Figure IV.28, the strain distribution functions of the ferrite and the overall strain distribution functions are superimposed for the large strain values whatever the considered microstructure. It means that the the most strained regions are always located in the ferrite. Focusing on low strain values, the strain distribution functions of the austenite and the overall strain distribution function are superimposed confirming that the less distorted regions are in the austenite.

The difference between D2_W and D1_W in terms of strain partitioning is also pointed out. The peak strain relative to each phase are closer in the D1_W microstructure compared to in D2_W microstructure, the arrows in grey in Figure IV.28 emphasize this idea.

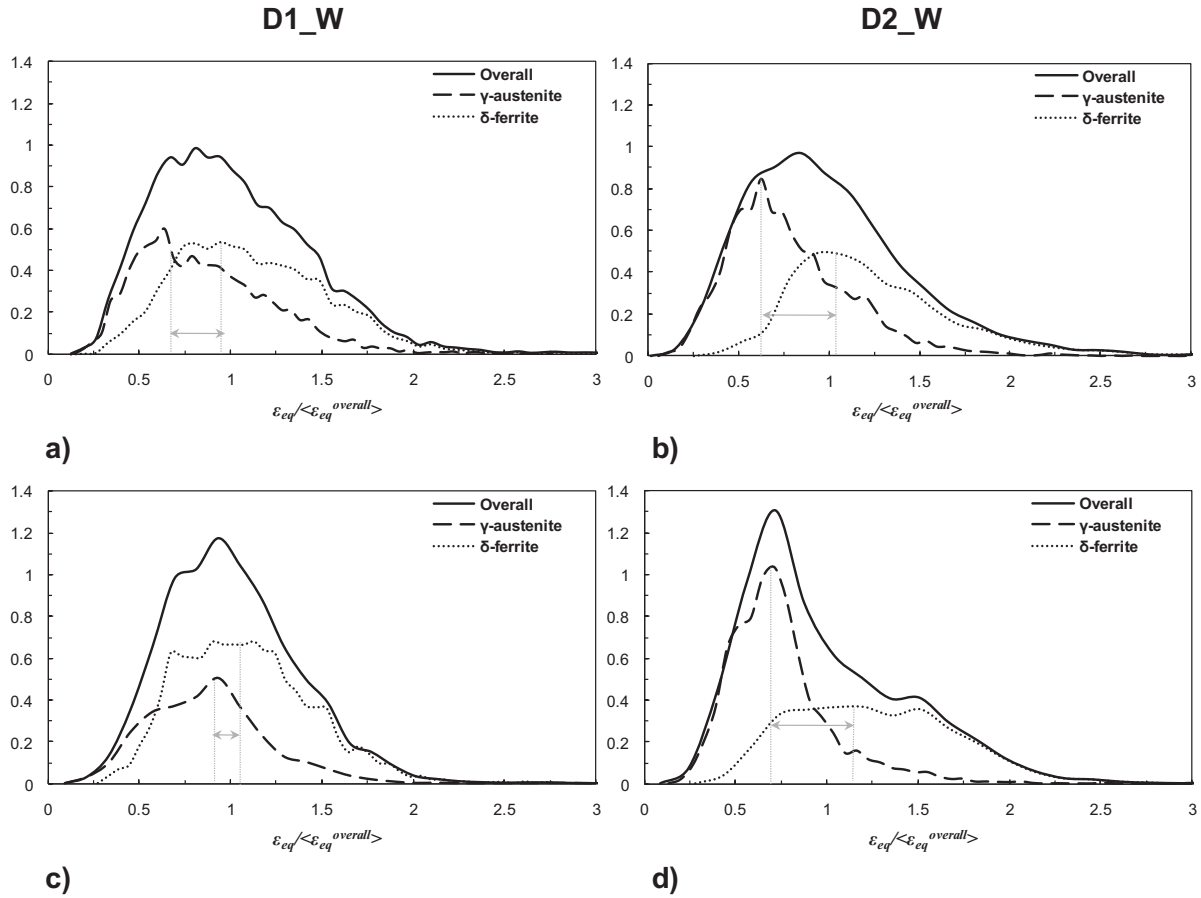


Figure IV.28. Strain distribution functions relative to the volume fraction of phase; D1_W microstructure: a) map 1 and c) map 2; D2_W microstructure: b) map 1; d) map 2.

❖ **Cumulative deformation distribution functions**

The cumulative deformation distribution functions normalized by the volume fraction are deduced from the strain distribution functions by integration, see Figure IV.29.

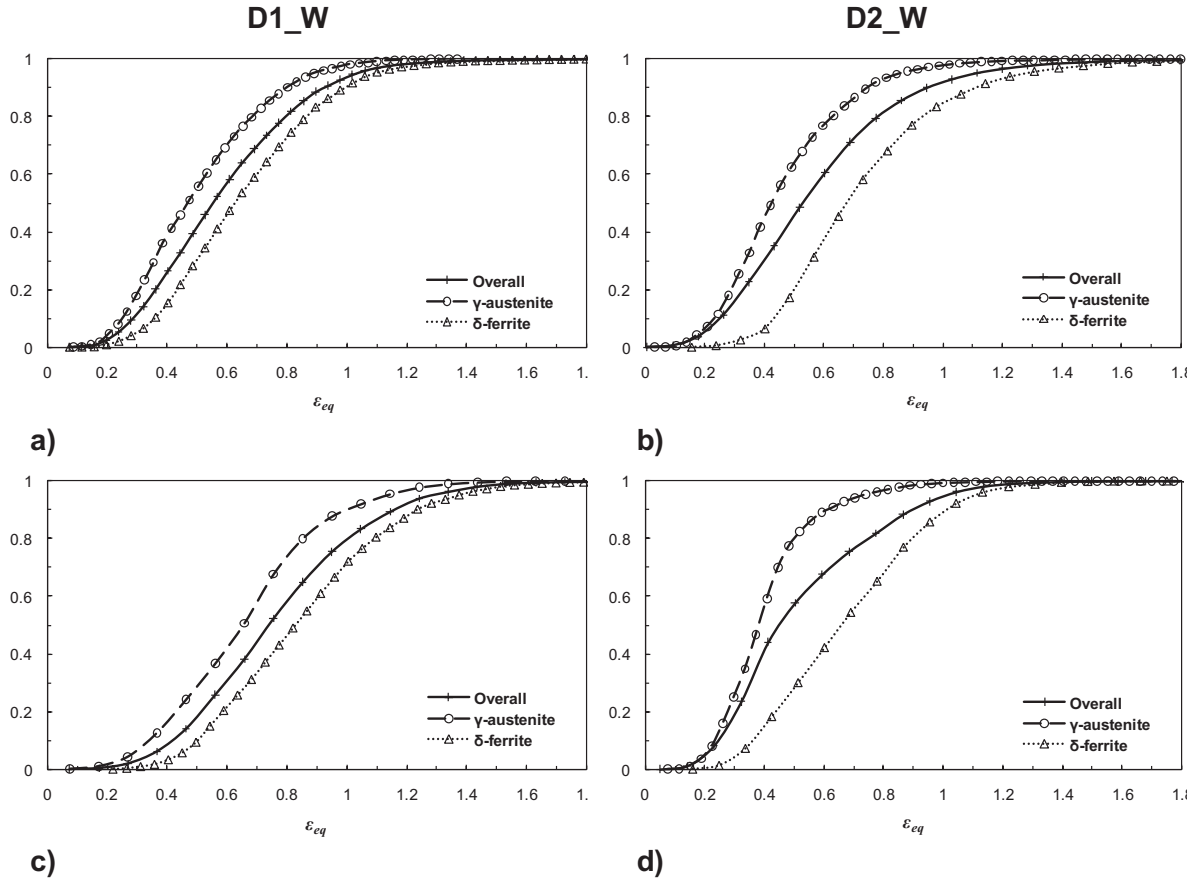
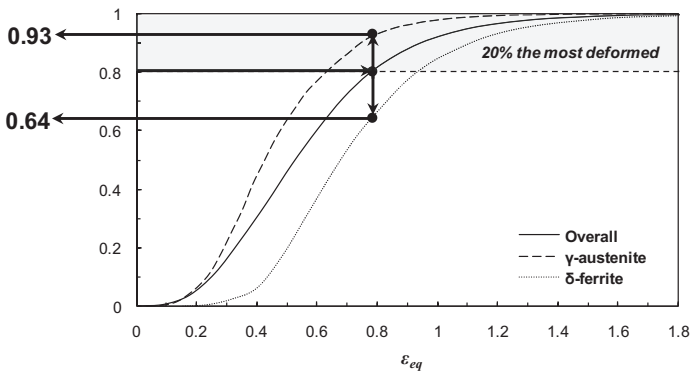


Figure IV.29. Strain cumulative distribution functions normalized by the volume fraction of phase; D1_W microstructure: a) map 1 and c) map 2; c) D2_W microstructure: b) map 1 and d) map 2.

These cumulative deformation distribution functions allow estimating the ferrite and austenite contents involved in the X% the most deformed. In Figure IV.30, an example is given to illustrate the method that permits to estimate graphically the ferrite and austenite contents in the 20% the more deformed of the considered material.



$$\frac{\%\gamma_{totale} - 0.93(\%\gamma_{totale})}{0.20} = \frac{\%\gamma_{totale}(1-0.93)}{0.20} = 19\%$$

$$\frac{\%\delta_{totale} - 0.64(\%\delta_{totale})}{0.20} = \frac{\%\delta_{totale}(1-0.64)}{0.20} = 81\%$$

Figure IV.30. Illustration of the method to estimate graphically the ferrite and austenite contents in the X% the more deformed of the material.

Analyzing the strain cumulative distribution functions as indicated in Figure IV.30 allows estimating the ferrite content involved in the X% the most deformed with X = 1, 5, 10, 15, 20, 25 and 30%. The results are given in Table IV.7 and confirm that the regions the more strained consist essentially of ferrite.

X% the more strained			1%	5%	10%	15%	20%	25%	30%
$\%\delta$	**D1_W**	Map 1	90 ± 1	86 ± 1	82 ± 1	81 ± 1	78 ± 1	76 ± 1	83 ± 1
		Map 2	100 ± 1	88 ± 1	89 ± 1	86 ± 1	85 ± 1	85 ± 1	83 ± 1
	D2_W	Map 1	90 ± 1	89 ± 1	87±1	85 ± 1	81 ± 1	78 ± 1	75 ± 1
		Map 2	90 ± 1	98 ± 1	95 ± 1	92 ± 1	90 ± 1	88 ± 1	85 ± 1

Table IV.7. Ferrite content ($\%\delta$) in the areas the more deformed in both D1_W and D2_W microstructures.

The strain maps provide qualitative information about the mechanisms involved in the high temperature deformation of duplex stainless steels. Nevertheless, it is difficult to compare the two investigated grades with only spatial information. Additional quantitative characterizations are therefore necessary to discriminate both microstructures.

IV.5.2 Discussion

The results presented in section IV.5.1 give a relatively good overview of the mechanisms involved in the high temperature deformation of duplex steels, however, a few points require discussion in more details. The discussions are conveyed in the form of questions/answers.

IV.5.2.1 What is the origin of the difference between D2_W and D1_W in terms of strain partitioning?

IV.5.2.1.1 Question

The results clearly demonstrate that the strain partitioning contrast between ferrite and austenite is smaller in the D1_W microstructure compared to the D2_W microstructure. Naturally, the question is to determine the origin of this difference.

IV.5.2.1.2 Answer

It could also be interesting to compare the D1_W austenite with the D2_W austenite and the D1_W ferrite with the D2_W ferrite. Such comparisons require normalizing the average deformation per phase by the overall strain in the region of interest as shown in Table IV.8.

		$< \varepsilon_{eq}^{\gamma} > / \varepsilon_{eq}^{overall}$	$< \varepsilon_{eq}^{\delta} > / \varepsilon_{eq}^{overall}$
D1_W	Map 1	0.87	1.12
	Map 2	0.89	1.08
	Average	0.88	1.10
D2_W	Map 1	0.80	1.22
	Map 2	0.78	1.24
	Average	0.79	1.23

Table IV.8. Normalization of the average deformation per phase by the overall strain in the region of interest for both D1_W and D2_W microstructures.

After the normalization step, the purpose is to compare the phase behaviour in both microstructures. One solution is to calculate the ratios indicated by eq IV-10 and eq IV-11. The results are given in Table IV.9.

$$\frac{\left(< \varepsilon_{eq}^{\gamma} > / \varepsilon_{eq}^{overall}\right)_{D1_W}}{\left(< \varepsilon_{eq}^{\gamma} > / \varepsilon_{eq}^{overall}\right)_{D2_W}} \qquad \textbf{eq IV-10}$$

$$\frac{\left(< \varepsilon_{eq}^{\delta} > / \varepsilon_{eq}^{overall}\right)_{D1_W}}{\left(< \varepsilon_{eq}^{\delta} > / \varepsilon_{eq}^{overall}\right)_{D2_W}} \qquad \textbf{eq IV-11}$$

$\frac{\left(< \varepsilon_{eq}^{\gamma} > / \varepsilon_{eq}^{overall}\right)_{D1_W}}{\left(< \varepsilon_{eq}^{\gamma} > / \varepsilon_{eq}^{overall}\right)_{D2_W}}$	$\frac{\left(< \varepsilon_{eq}^{\delta} > / \varepsilon_{eq}^{overall}\right)_{D1_W}}{\left(< \varepsilon_{eq}^{\delta} > / \varepsilon_{eq}^{overall}\right)_{D2_W}}$
1.11	0.89

Table IV.9. Comparison between the austenite and the ferrite in both investigated grades.

In other words, the values of the ratios calculated with eq IV-10 and eq IV-11 demonstrates that on the one hand the D1 austenite deforms more than the D2 austenite (about 11% more), and on the other hand the D1 ferrite strains less than the D2 ferrite (about 11% less).

Two mechanisms can be responsible for the change of rheology of a phase. A phase can be strengthened (i) by precipitation or (ii) reinforced by solute strengthening. Through this work, TEM observations have never shown any precipitates which could explain the strengthening of a phase. In addition, in the literature, there is not any reference which reports the existence of an hardening precipitation at high temperature. Figure IV.31 shows illustrations of the solute strengthening effect of various elements on the ferrite of low-alloyed steels (Figure IV.31.a) and on the austenitic stainless steels (Figure IV.31) at room temperature. Here, the situation involves high temperatures. As a consequence precautions must be taken when the results of Figure IV.31 are used to analyze high temperature behaviour.

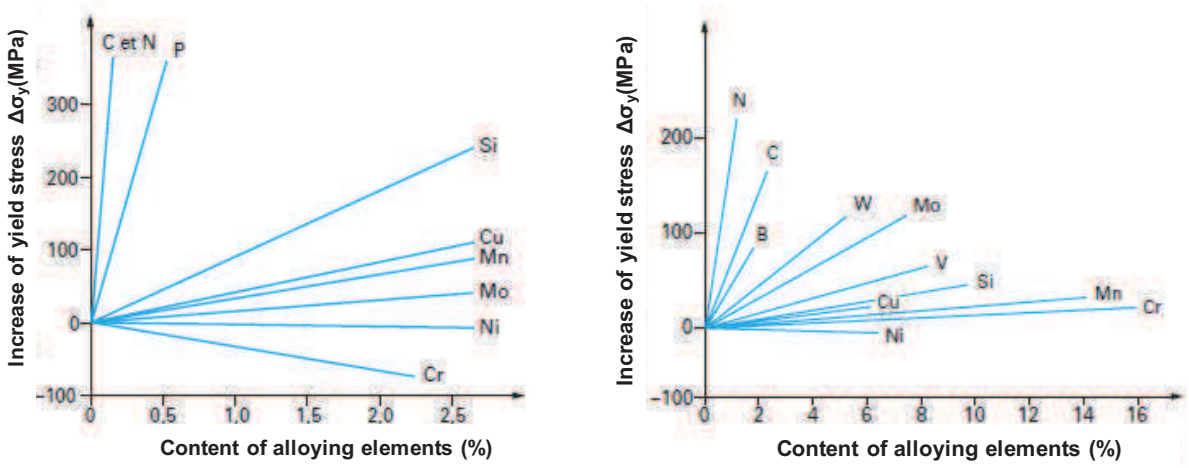


Figure IV.31. Influence of alloying content on the yield stress of a) ferrite and b) austenitic stainless steel at room temperature.

The difference in term of rheology contrast between ferrite and austenite at high temperature in the alloy D1 compared to that of the D2 alloy is attributed to a solute strengthening effect. Therefore, a particular attention has to be paid to the chemical composition of both alloys D1 and D2 in order to identify which are the elements that could be responsible for the solute strengthening effect of ferrite or austenite.

Chemical composition differences between D1 and D2 mainly exist in terms of Ni, Mo, and Mn contents. However, only some of them are known to have a strong solute strengthening effect. Ni and Mn are elements that do not exhibit a strong solute strengthening effect, as a consequence they are not considered. On the contrary, Mo is well-known to harden austenitic stainless steels as well as ferritic stainless steels at high temperature. The element partitioning phenomenon makes the problem more complicated because additionally to its solute strengthening effect, Mo dissolves preferentially in the ferrite phase compared to the austenite, see Table IV.10. As Mo is a strong ferrite stabilizer, it could be possible that the solute strengthening effect is higher in the ferrite than in the austenite.

		%Cr	%Ni	%Mn	%Mo
D1_W	δ	26.00	3.80	1.74	4.15
	γ	21.61	7.11	2.10	2.42
D2_W	δ	25.49	2.01	2.81	1.32
	γ	21.00	3.44	3.16	0.73

Table IV.10. Illustration of the element partitioning between ferrite and austenite in both alloys D1 and D2; the chemical compositions were determined by micro-probe analysis.

In D2 alloy, as the Mo content is very low about 1%, the rheology of the ferritic phase is critical for the duplex hot workability due to a flow stress significantly lower than that of the austenitic phase in the temperature range effective during the hot rolling process. On the contrary, in the alloy D1, the content of Mo is three times higher than in the alloy D2, about 3%. Consequently, the flow stress of the ferritic phase of the alloy D1 is significantly higher than the flow stress of the ferritic phase of the alloy D2 and thereby the flow stress differential between ferrite and austenite is reduced. Figure IV.32 summarizes the described situation.

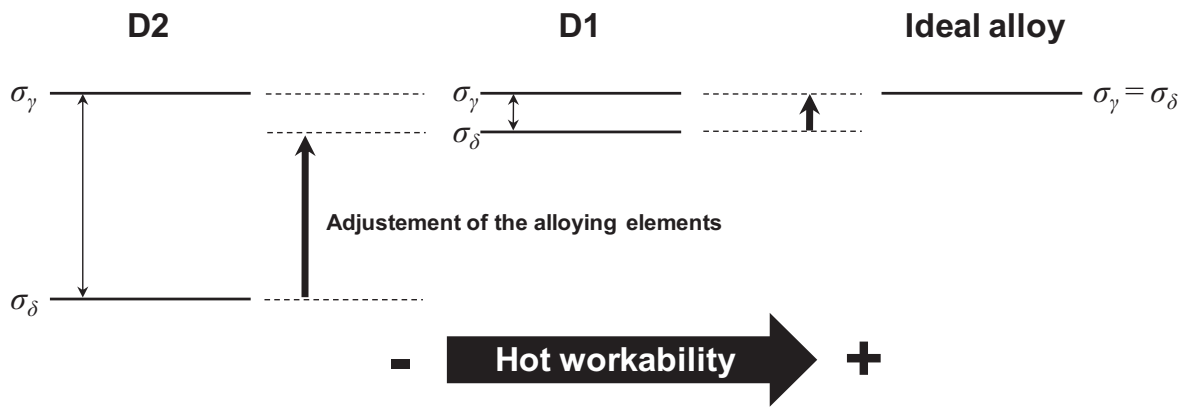


Figure IV.32. Schematic illustration of the effect of flow stress differential between ferrite and austenite on the hot workability.

IV.5.2.2 Why is the overall strain different from the macroscopic strain?

IV.5.2.2.1 Question

The second question that arises from the results is the difference between the overall strain (that is to say the average strain over the analyzed domain) and the macroscopic applied strain, see Table IV.8. How can we account for this difference?

		ε_{eq}^{macro}	$<\varepsilon_{eq}^{overall}>$
D1_W	Map 1	0.391	0.603
	Map 2		0.809
D2_W	Map 1	0.388	0.619
	Map 2		0.572

Table IV.11. Differences between the applied macroscopic strain and the overall strain measured over the analyzed fields in both D1_W and D2_W microstructures.

IV.5.2.2.2 Answer

❖ **Back to the literature**

Although the mechanics of the plane strain compression test appears rather simple, the material deforms inhomogeneously, the details depending upon external parameters such as the quality of tool lubrication and the material deformation characteristics themselves. Up to recently and the paper published by Loveday et al. [127], there was no standard for carrying out plane strain compression tests. Mirza et al. [130, 131] wrote a series of papers in an effort to show how parameters such as material type, specimen geometry (h_0 and b_0 in Figure IV.13.a), strain rate, and friction affect the macroscopic deformation behaviour. Mirza et al. [130, 131] used extensive finite element modeling to simulate the plane strain compression test. Two-dimensional models were adopted to reproduce hot compression of 316L-austenitic stainless steel and aluminium and a heterogeneous strain field was observed. Figure IV.33 shows this heterogeneity of strain, strain rate and temperature on one half of the deformed sample (the other half deforms symmetrically). It was also shown that the heterogeneity of deformation is affected by initial geometry of the specimen but is independent of the type of material and strain rate. In this scenario, it is essential to validate experimentally the local values of strain obtained through finite elements modeling.

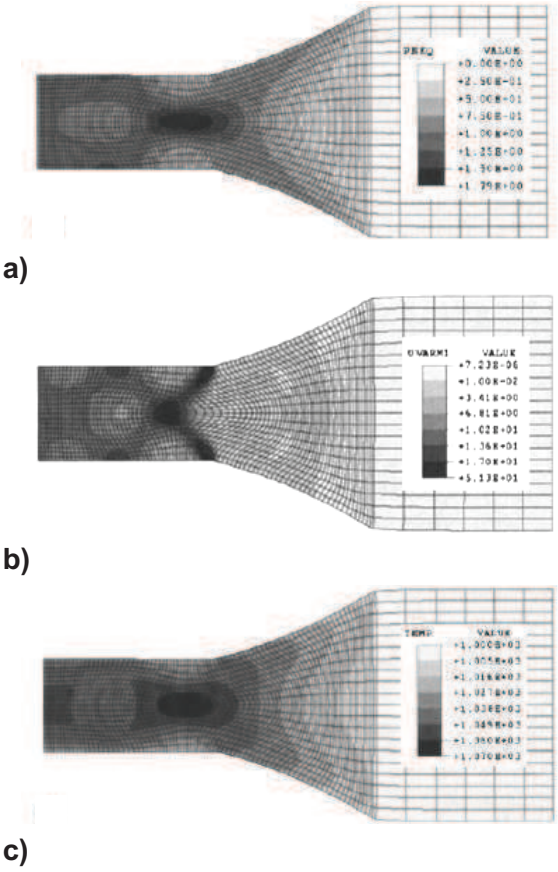


Figure IV.33. Finite elements predictions of given parameters at nominal equivalent strain of 1 for frictionless deformation of a 316L-austenitic stainless steel specimen with h_0 = 10 mm, $\dot{\varepsilon}$ = 10s^{-1} and T=1000°C; a) equivalent strain; b) equivalent strain rate; c) temperature distributions [130].

In order to investigate this aspect for aluminium, Beynon [132] used engraved grids laid on the centre plane of the specimen which had been previously cut along the centre plane itself. After the grid was engraved, the specimen was assembled again using two bolts. The samples were then compressed at 300°C and subsequently opened up in order to observe the deformed grid, see Figure IV.34.a. As a result of this work, Beynon confirmed that the strain distribution is not homogeneous, see Figure IV.34.b which shows a contour plot of the equivalent strain obtained from the grid analysis after deformation.

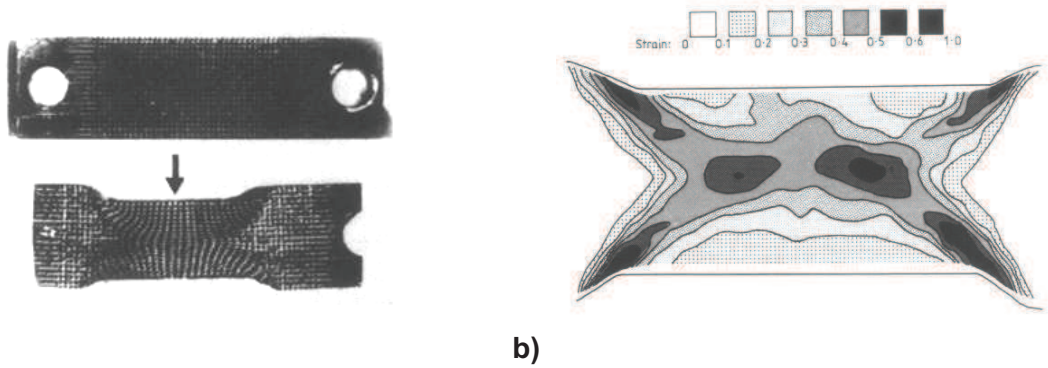


Figure IV.34. Investigation of the strain heterogeneity during plane strain compression test with the engraved grid technique, nominal strain = 0.33 and w/h_0 = 2; a) engraved grid before and after deformation; b) average equivalent strain distribution [132].

More recently Boldetti et al. [125] have reported new results on aluminum using a similar method. Figure IV.35.a shows a comparison between finite element simulations and experimental contour plots of the three components of the logarithmic plastic strain. The comparison in Figure IV.35.a has been obtained by considering a model with no misalignment of the tools during the test. In fact, as misalignment is common in a compression test, the same analysis was done in the case where an offset of about 1mm was measured between the tools and the results shown in Figure IV.35.b demonstrate a very good match between numerical and experimental plots.

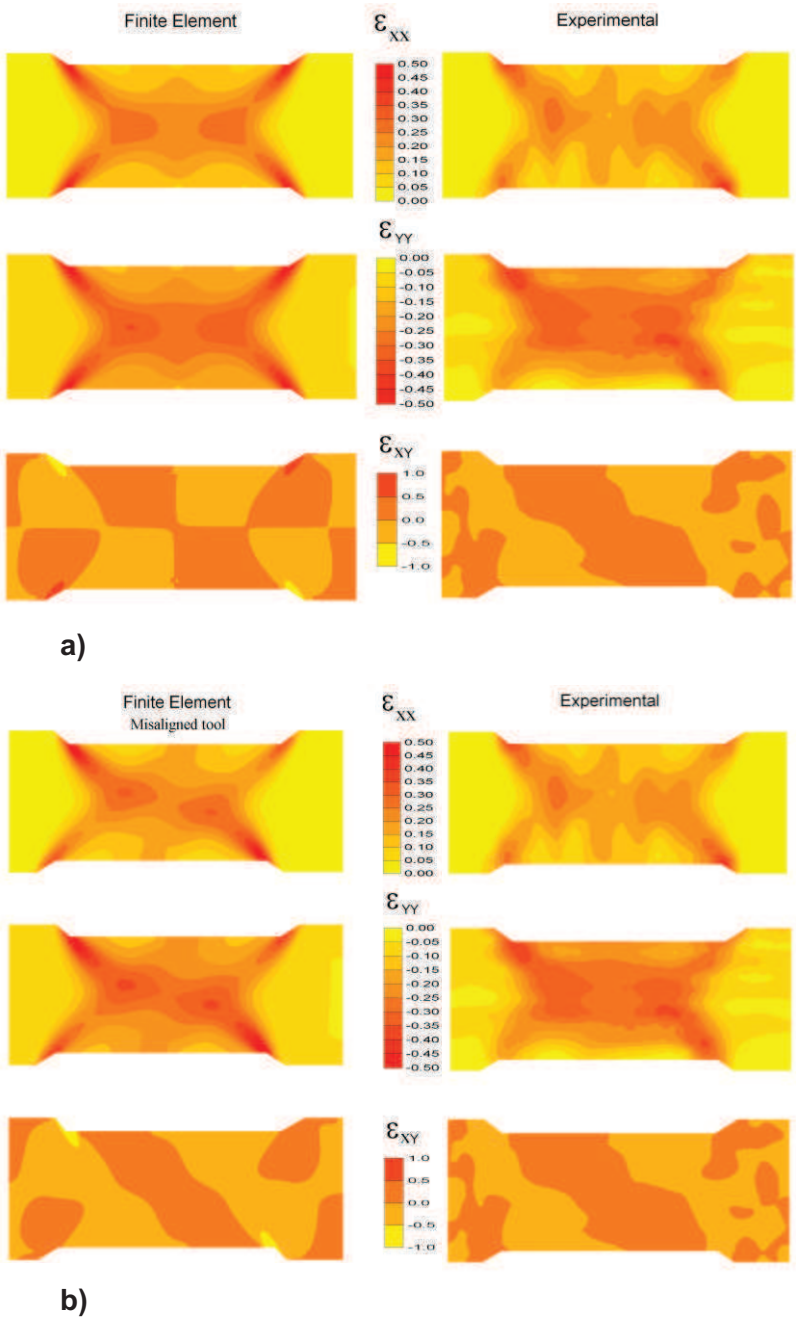


Figure IV.35. Numerical (left) and experimental (right) contour plots of the components of the logarithmic plastic strain; a) numerical values were obtained assuming perfect alignment between tools; b) results obtained considering a misalignment of 1mm between tools [125].

❖ **Additional proof**

Results about the strain heterogeneity in plane strain compression have been briefly reviewed. Literature data are completed by the results of this work. For example, the D1_W_{iii} specimen was macroscopically deformed to an equivalent strain of 0.391 and two regions located in different areas in the centre plane of the specimen were analyzed in terms of strain distribution. The overall strain measured over each region was different: 0.603 in the map 1 and 0.809 in the map 2. This difference can be attributed to the macroscopic strain heterogeneity. Indeed, as the areas where the strain is mapped are relatively small (500x500µm), the overall strain depend strongly on the location of the region of interest in the centre plane of the specimen. Larger areas have to be analyzed so that the overall strain matches with the applied macroscopic strain.

IV.5.3 Conclusions

- ❖ The modified microgrid method was successfully applied to two different duplex stainless steels providing the strain maps corresponding to both grades.
- ❖ The results showed that the D2 alloy is more affected by strain partitioning compared to the alloy D1.
- ❖ The austenite of the alloy D1 deforms more than the austenite of the alloy D2 whereas the ferrite of the alloy D1 strains less than the ferrite of the D2 alloy. This dual effect is a credible explanation of the difference of strain partitioning between the two investigated grades.
- ❖ The dispersion of the results, i.e. the differences between the results obtained from one sample, can be attributed to the macroscopic strain localization.
- ❖ The phase rheology depends strongly on the chemical composition, in particular on the strengthening effect of element such as Mo.

IV.6 Factors potentially impacting strain localization

As many results were obtained from the D1 grade, it has been decided to focus on this alloy in order to study the influence of various factors which could potentially impact the strain partitioning in duplex stainless steel. As some experiments have been carried out successfully at 850°C and 950°C, the influence of the temperature can be also discussed. In the previous chapter a particular attention has been paid to generate model microstructures: equiaxed or Widmanstätten. These results are used to investigate the influence of the phase morphology on the strain partitioning at a given temperature.

IV.6.1 Influence of the temperature

IV.6.1.1 Equiaxed morphology

IV.6.1.1.1 Macroscopic stress strain curves

D1 specimens with an equiaxed morphology (D1_E) were deformed at $1s^{-1}$ up to a reduction of 20% at two different temperatures, 850°C or 950°C.

The macroscopic equivalent stress strain curves are presented in Figure IV.36. The flow stress curves show a typical shape with a plastic regime which can be divided into two parts. The first one is the work-hardening stage and during this stage the flow stress increases when increasing the strain. Then, there is the steady state stage; it means that after a critical value of the strain, the flow stress saturates.

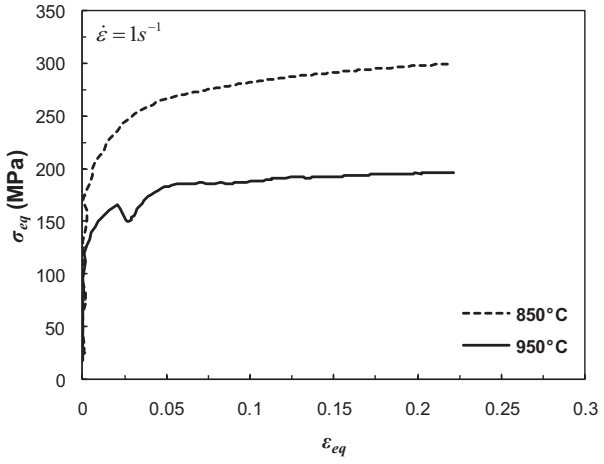


Figure IV.36. Comparison between the macroscopic equivalent stress strain curves of the equiaxed morphology obtained under plane strain compression at $1s^{-1}$ and different temperatures: T = 850°C and 950°C up to a reduction of 20%.

Considering the strength levels summarized in Table IV.12 as well as observing the stress strain curves, the material at 950°C deforms plastically much more easily than at 850°C.

T (°C)		sample	$\dot{\varepsilon}$ (s^{-1})	σ_0 (MPa)	$\sigma_{steady\ state}$ (MPa)
850°C	D1_E	B	1	175	300
950°C	D1_E	A	1	120	195

Table IV.12. Summary of the plane strain compression experimental conditions and typical stress values for the equiaxed morphology at T = 850°C and 950°C.

IV.6.1.1.2 Strain maps

The equivalent strain maps of the equiaxed morphology obtained at 850 and 950°C, are shown in Figure IV.37.a and Figure IV.37.b, respectively. In each plane strain compression specimen, only one strain map is plotted even if several were determined. This choice was made to be as clear as possible in the discussion.

The strain map observations lead to the same conclusions as before, i.e.:

- deformation is heterogeneously distributed;
- deformation is accommodated more by the ferrite;
- the most deformed regions are always located close to the interphase boundaries and as a consequence, locally the strain incompatibility between the austenite and the ferrite is huge;
- the development of a few shear bands is clearly visible.

However, the effect of an increase of the temperature can hardly be determined by qualitative observation of the strain maps, hence, a quantitative analysis is needed.

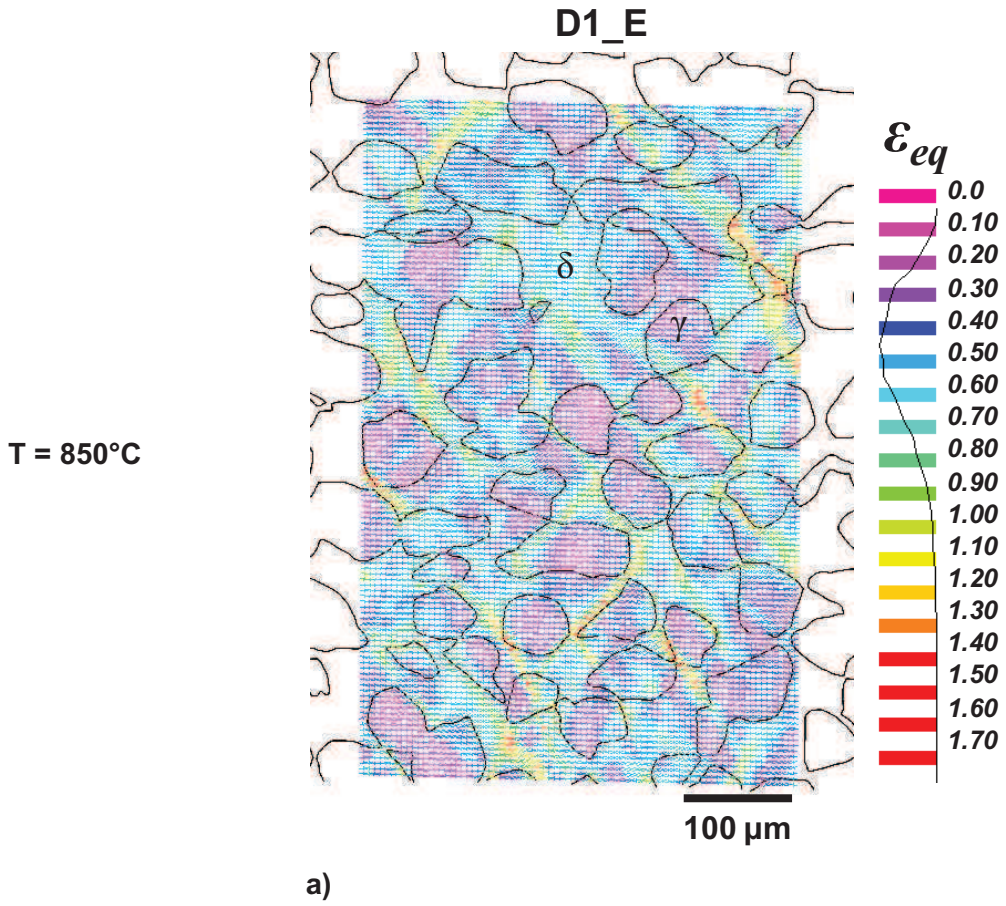


Figure IV.37. Equivalent strain distribution maps of the equiaxed morphology: D1_E at T = 850 and 950°C for a 20% macroscopic thickness reduction; a) strain map at T = 850°C; b) strain map at T = 950°C. The equivalent strain map is superimposed with the undeformed microstructure to clearly present where in the microstructure the strains are distributed. The loading direction corresponds to the vertical axis.

IV.6.1.1.3 Average deformation per phase

The average strains per phase for the equiaxed morphology are calculated at 850°C as well as at 950°C. The results are summarized in Table IV.13. Computing the average strain per phase in each strain map constitutes another way to look at the strain distribution. Although the spatial distribution effect is lost, it allows quantifying the data. The results demonstrate that the ferrite is always more deformed than the austenite whatever the temperature.

D1_E		$< \varepsilon_{11} >$	$< \varepsilon_{22} >$	$< \varepsilon_{12} >$	$< \varepsilon_{33} >$	$< \varepsilon_{eq} >$
Overall	T = 850°C	-0.467	0.397	-0.063	0.070	**0.509**
	T = 950°C	-0.402	0.342	-0.029	0.060	**0.435**
Austenite γ	T = 850°C	-0.404 ± 0.017	0.339 ± 0.013	-0.053 ± 0.004	0.066 ± 0.004	**0.438**
	T = 950°C	-0.337 ± 0.028	0.269 ± 0.029	-0.022 ± 0.004	0.069 ± 0.001	**0.357**
Ferrite δ	T = 850°C	-0.530 ± 0.002	0.449 ± 0.005	-0.072 ± 0.001	0.081 ± 0.003	**0.577**
	T = 950°C	-0.463 ± 0.014	0.402 ± 0.009	-0.035 ± 0.002	0.062 ± 0.006	**0.505**

Table IV.13. Average logarithmic deformation per phase in the equiaxed morphology: D1_E at T = 850°C and 950°C.

As the overall strain on the analyzed areas is different at 850°C and 950°C, it is not possible to compare the values of the average strain per phase obtained at the two different temperatures. Nevertheless, it is possible to compute the results at 850°C and at 950°C by analyzing the ratio between the average strain in the ferrite over the average strain in the austenite, and get rid of the difference in the overall strain. The results in Table IV.14 reveal that the strain partitioning contrast is a little bit larger at 950°C compared to that at 850°C.

D1_E	$< \varepsilon_{eq}^{overall} >$	$< \varepsilon_{eq}^{\delta} > / < \varepsilon_{eq}^{\gamma} >$
T = 850°C	0.509	1.32
T = 950°C	0.435	1.41

Table IV.14. Calculation of the ratio between the average deformation in the ferrite over the average deformation in the austenite for the equiaxed morphology at T = 850 and 950°C.

IV.6.1.1.4 Strain distribution functions

The strain distribution functions plotted in Figure IV.38 constitute an additional proof of the heterogeneity of the strain field. For low strain values, the austenite strain distribution function and the overall strain distribution function coincide confirming that the less deformed areas are in the austenite. For large strain values, the ferrite strain distribution function and the overall strain distribution function coincide showing that the most deformed regions involve ferrite.

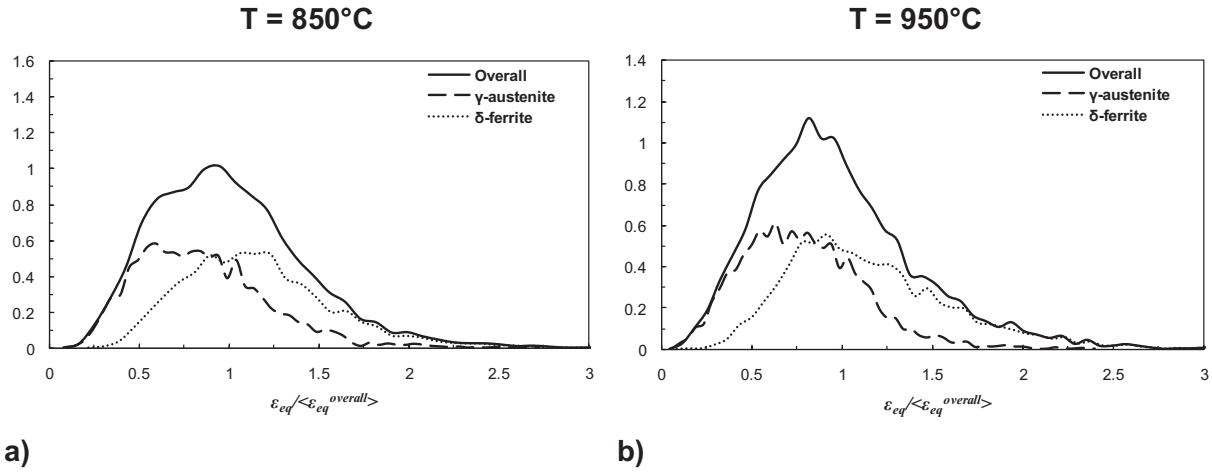


Figure IV.38. Strain distribution functions relative to the volume fraction of phase for the equiaxed morphology: D1_E. a) D1_E, T = 850°C. b) D1_E, T = 950°C.

The effect of temperature is also difficult to quantify. Nevertheless, considering the extreme right part of the ferrite strain distribution functions, it seems that the densities are higher for the largest values of strain at 950°C compared to at 850°C. This last comment is well-justified by quantifying the ferrite content in the most deformed regions, see Table IV.15.

X% the more strained			1%	5%	10%	15%	20%	25%	30%
D1_E	$\%\,\delta$	T = 850°C	90 ± 1	84 ± 1	79 ± 1	77 ± 1	77 ± 1	75 ± 1	73 ± 1
		T = 950°C	100 ± 1	92 ± 1	91 ± 1	86 ± 1	85 ± 1	82 ± 1	78 ± 1

Table IV.15. Ferrite content ($\%\delta$) in the areas the more deformed in the microstructure with an equiaxed morphology at T = 850°C and T = 950°C.

IV.6.1.2 Widmanstätten morphology

The influence of the temperature has been studied for the Widmanstätten morphology, using exactly the same procedure as for the equiaxed morphology.

IV.6.1.2.1 Macroscopic stress strain curves

D1 specimens showing a Widmanstätten morphology (D1_W) were deformed at $1s^{-1}$ up to a reduction of 20% at two different temperatures, 850°C or 950°C. The macroscopic equivalent stress strain curves are presented in Figure IV.39. Typical values of stress are summarized in Table IV.16.

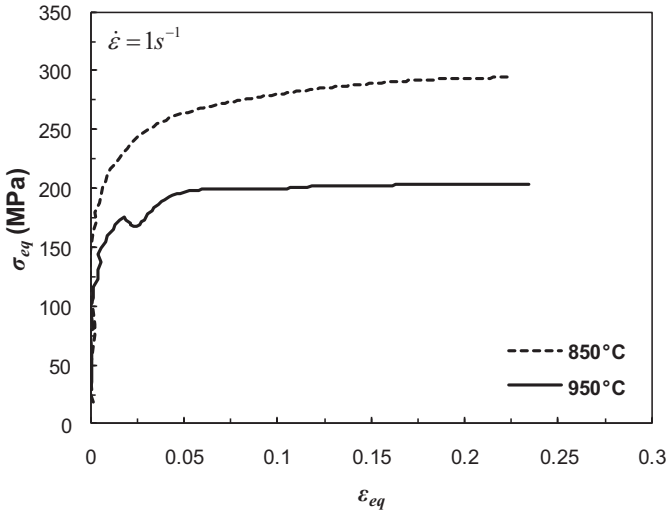


Figure IV.39. Comparison between the macroscopic equivalent stress strain curves of the Widmanstätten morphology obtained under plane strain compression at $1s^{-1}$ and different temperatures: T = 850°C and 950°C up to a reduction of 20%.

T (°C)		sample	$\dot{\varepsilon}$ (s^{-1})	σ_0 (MPa)	$\sigma_{steady\ state}$ (MPa)
850°C	D1_W	ii	1	175	295
950°C	D1_W	iiii	1	120	205

Table IV.16. Summary of the plane strain compression experimental conditions and typical stress values for the Widmanstätten morphology at T = 850°C and 950°C.

IV.6.1.2.2 Strain maps

The equivalent strain maps of the Widmanstätten morphology obtained at 850 and 950°C, are shown in Figure IV.40.a Figure IV.40.b respectively. In the strain map D1_W at 950°C (Figure IV.40.b), it is difficult to recognize the austenite laths. Indeed, in the region of interest, the laths were cut along their section and not along their length as in the strain map of D1_W at 850°C (Figure IV.39.a).

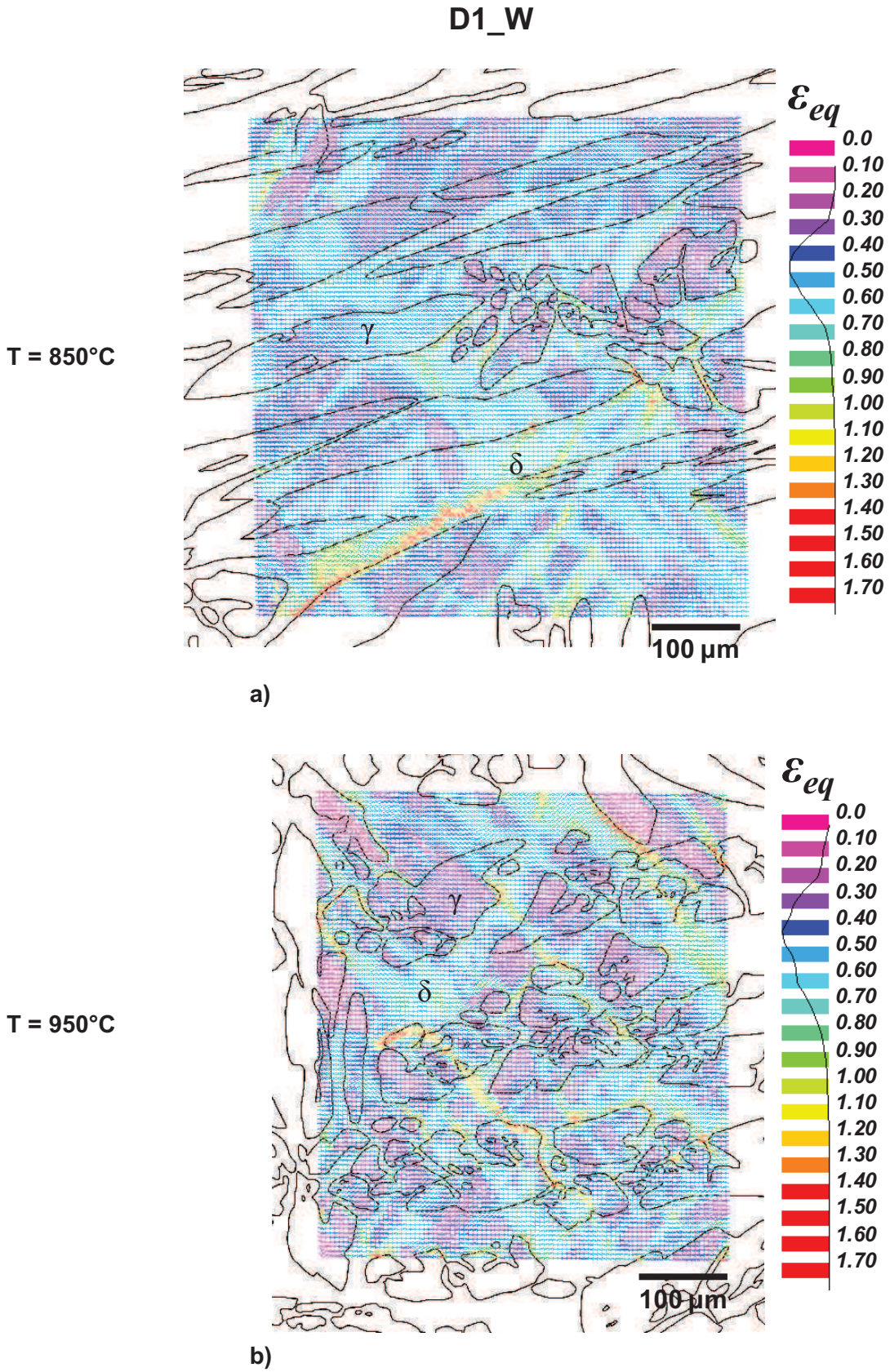


Figure IV.40. Equivalent strain distribution maps of the Widmanstätten morphology: D1_W at T = 850 and 950°C; a) strain map at T = 850°C; b) strain map at T = 950°C. The equivalent strain map is superimposed with the undeformed microstructure to clearly present where in the microstructure the strains are distributed. The loading direction corresponds to the vertical axis.

IV.6.1.2.3 Average deformation per phase

The average deformations per phase were computed and the results are presented in Table IV.17. As the overall strain in the regions of interest are identical: about 0.49 at 850°C and 950°C, the average strain per phase can be directly compared. At 950°C, the austenite is less deformed compared to at 850°C. On the contrary the ferrite deforms more at 950°C than at 850°C. In addition, the index that quantifies the strain partitioning allows demonstrating that a 100°C-temperature increasing leads to an increase of the strain partitioning contrast, see Table IV.18.

D1_W		$<\varepsilon_{11}>$	$<\varepsilon_{22}>$	$<\varepsilon_{12}>$	$<\varepsilon_{33}>$	$<\varepsilon_{eq}>$
Overall	T = 850°C	-0.441	0.400	-0.045	0.041	**0.490**
	T = 950°C	-0.432	0.402	-0.069	0.030	**0.489**
Austenite γ	T = 850°C	-0.387 ± 0.015	0.360 ± 0.012	-0.086 ± 0.013	0.027 ± 0.003	**0.444**
	T = 950°C	-0.381 ± 0.029	0.350 ± 0.026	-0.022 ± 0.014	0.031 ± 0.004	**0.423**
Ferrite δ	T = 850°C	-0.480 ± 0.001	0.426 ± 0.001	-0.014 ± 0.001	0.054 ± 0.001	**0.526**
	T = 950°C	-0.471 ± 0.008	0.437 ± 0.003	-0.110 ± 0.004	0.034 ± 0.005	**0.541**

Table IV.17. Average logarithmic deformation per phase in the Widmanstätten morphology: D1_W at T = 850°C and 950°C.

D1_W	$<\varepsilon_{eq}^{overall}>$	$<\varepsilon_{eq}^{\delta}>/<\varepsilon_{eq}^{\gamma}>$
T = 850°C	0.490	1.18
T = 950°C	0.489	1.28

Table IV.18. Calculation of the ratio between the average deformation in the ferrite over the average deformation in the austenite for the Widmanstätten morphology at T = 850 and 950°C.

IV.6.1.2.4 Strain distribution functions

The macroscopic densities (black curves) reveal that the deformation is more heterogeneous at 850°C than at 950°C. This difference is also obvious considering the strain distribution per phase for both morphologies. Indeed, at 850°C the peak in the strain distribution function of the austenite is very close to the peak of the strain distribution function of the ferrite, whereas at 950°C the peaks relative to each phase are well-distinct. This effect is probably related to the orientation of the austenite laths which can more or less impact the deformation of the softer phase and limit the development of the shear bands.

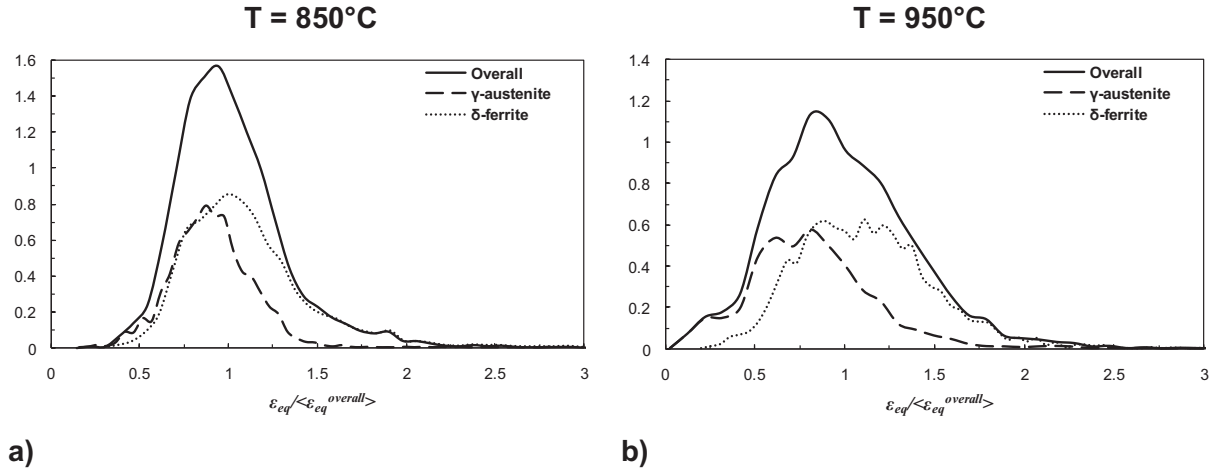


Figure IV.41. Strain distribution functions relative to the volume fraction of phase for the Widmanstätten morphology: D1_W. a) D1_W, T = 850°C. b) D1_W, T = 950°C.

X% the more strained			1%	5%	10%	15%	20%	25%	30%
D1_W	$\%\,\delta$	T = 850°C	94 ± 1	98 ± 1	93 ± 1	91 ± 1	86 ± 1	83 ± 1	80 ± 1
		T = 950°C	76 ± 1	87 ± 1	87 ± 1	87 ± 1	86 ± 1	83 ± 1	80 ± 1

Table IV.19. Ferrite content ($\%\delta$) in the areas the more deformed in the microstructure with a Widmanstätten morphology at T = 850°C and T = 950°C.

IV.6.1.3 Conclusion

By analyzing in details the effect of a 100°C-temperature increase on the strain partitioning, it can be concluded that the temperature impacts the strain localization. The ratio between the average strain in the ferrite over the average strain in the austenite increases when the temperature rises from 850°C up to 950°C. In others words, the contrast in rheology between ferrite and austenite rises when the temperature increases.

IV.6.2 Influence of the phase morphology

Although the results obtained on both morphologies give similar trends regarding the strain heterogeneity, two differences can be discussed.

- Firstly, the development of shear bands seems to depend strongly on the distribution of the austenite phase in the ferrite matrix. In other words, the equiaxed morphology would be more favorable to the development of the shear bands than the Widmanstätten one, and consequently the ferrite matrix would easily accommodate the strain. In the microstructure with Widmanstätten morphology, the development of shear bands depends strongly on the orientation of the austenite lath compared with the loading direction.

- Secondly, an additional deformation mechanism seems to be activated in the equiaxed morphology: sliding at the interphase boundaries, see Figure IV.42. The microgrid pattern turns out to be very useful to determine such a deformation mechanism. Sliding at the interphase boundaries is frequently observed in the microstructure showing an equiaxed morphology whereas it is very rare to see this mechanism when the austenite presents a Widmanstätten morphology. These observations are in agreement with literature data since they confirm the results published by Pinol-Juez et al. [12, 95]. The authors have shown that the activation of sliding at the interphase boundaries depends on the nature of the interface. In the equiaxed morphology, the interfaces are incoherent; consequently they are more able to slide. On the contrary, in the Widmanstätten morphology as the δ/γ interphase boundaries are related by a Kurdjumov-Sachs orientation relationship, the interfaces are semi-coherent and the ability of the interface to slide is suppressed.

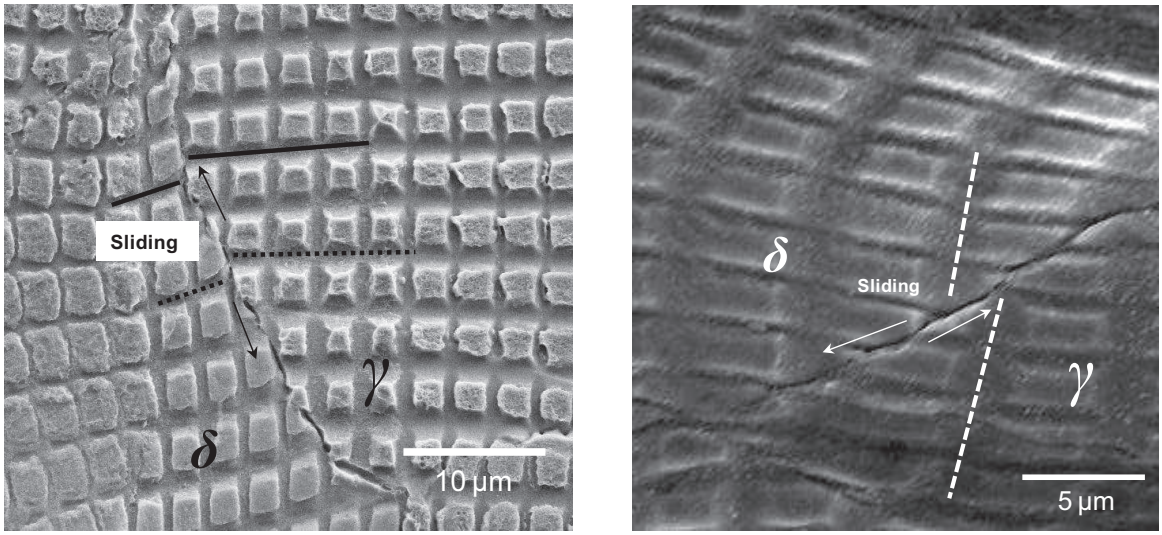


Figure IV.42. Illustration at different magnifications and different locations of the δ/γ sliding mechanism occurring along the incoherent interface boundaries in the equiaxed microstructure.

All the results obtained for the strain partitioning index are summarized in Table IV.20. To highlight a possible influence of the phase morphology, the strain partitioning index relative to each morphology has to be compared for a given temperature. Whatever the morphology, the strain partitioning tends to increase when the austenite presents an equiaxed morphology in comparison with a Widmanstätten austenite. This difference is attributed to an additional deformation mechanism: the sliding at the δ/γ interfaces.

		$< \varepsilon_{eq}^{overall} >$	$< \varepsilon_{eq}^{\delta} > / < \varepsilon_{eq}^{\gamma} >$
T = 850°C	D1_E	0.509	1.32
	D1_W	0.490	1.18
T = 950°C	D1_E	0.435	1.41
	D1_W	0.489	1.28

Table IV.20. Summary of the results of the strain partitioning index for both morphologies at T = 850°C and T = 950°C.

IV.6.3 Conclusions

- In the temperature range 850-950°C, increasing the temperature tends to increase the strain partitioning.

- At a given temperature, the strain partitioning depends significantly on the distribution of the austenite: orientation of the austenite laths or morphology.

IV.7 Limits of the technique

Technical and conceptual limitations of the microgrid technique were found during the present investigation, but could not be addressed due to time constraints. These different limitations of the microgrid technique are discussed in this section.

IV.7.1 A time consuming technique

Although the modified microgrid method is very well-adapted at high temperature, this technique is time consuming, see Table IV.21. The time required to obtain a result on one insert depends significantly on the time necessary to match the homologous points (grid intersections) between the deformed and the undeformed configurations. Indeed, most of the time, the initial satisfying grey level contrast is affected by the temperature and the deformation. As a consequence the automatic matching of the grid intersections cannot be used and only a manual matching which takes a lot of time (5h) provides a result.

Procedure	Aims	Equipment	Time needed	Success rate	Place
Heat treatments	To generate model microstructures	Furnace	1day	100%	SIMaP (Grenoble)
Specimen machining	To have modified plane strain compression specimens	Machining	4h	100%	SIMaP (Grenoble)
Polishing of insert	To obtain a flat and good quality surface	Polishing wheels	1h	100%	SIMaP (Grenoble)
Electro-etching	To reveal the austenite ferrite microstructure	DC Power Source	15min	90%	SIMaP (Grenoble)
Resin depositing and polymerizing	To process the microgrid	Rotating stage Furnace	45min	100%	LMS (Paris)
Resin irradiating	To process the microgrid	SEM	15min	80%	LMS (Paris)
Microgrid engraving	To process the microgrid	DC Power Source	5min	40%	LMS (Paris)
High-resolution picture	To obtain picture in the undeformed conditions	SEM	30min	100%	LMS (Paris)
Insert-sample assembling	To embed the insert in the work piece	TIG welding device	1h	100%	University of Sheffield
Compression test	To carry out the plane strain compression with the specified conditions	Thermo-mechanical compression machine	2h	90%	University of Sheffield
Microgrid extraction	To see the microgrid after deformation	Crosscut saw Polishing wheels	1h	90%	SIMaP (Grenoble)
High-resolution picture	To obtain picture in the deformed conditions	SEM	30min	100%	LMS (Paris)
Analysis of results	To measure and map the deformation	CorrelManuV software	6h	90%	SIMaP (Grenoble)
		TOTAL	**≈ 40h**		

Table IV.21. Summary of the required equipment and estimation of the time needed to perform and analyze a test with the modified microgrid technique.

IV.7.2 Effect of sliding at the δ/γ boundaries and consequence on the strain calculation

Since the local strains forming the strain distributions are computed from the displacement of the microgrid intersections, when an interphase boundary crosses a grid square, it opens the possibility of inaccurate estimations of the strains around the boundary. In some locations, the shear deformation at the vicinity of interphase boundaries can be relaxed if sliding takes place at such boundaries, as shown in Figure IV.43.a. However, if we look only at the positions of the grid intersections after deformation (black dots in Figure IV.43.b), it will be interpreted by the calculations as a shear strain higher than the actual one (Figure IV.43.c).

δ/γ interphase boundary sliding was mainly observed in the deformed microgrids of the specimens presenting an equiaxed austenite. The extent of the sliding varied from one boundary to another, and did not seem to have a direct relation with geometrical factors such as the length and shape of the boundaries. It could change from one place to another along the same boundary, possibly due to the interaction among grains/phases which varies the constraint at different places along the boundary. It is considered that high strain values located at the interphase boundaries must be carefully analyzed, especially in microstructures presenting an equiaxed austenite and which exhibit a high tendency to interphase boundaries sliding. One solution consists in comparing the strain maps with the deformed microstructure in order to find out if sliding has not occurred at the interphase boundaries, and confirm that they are genuine heavily deformed locations.

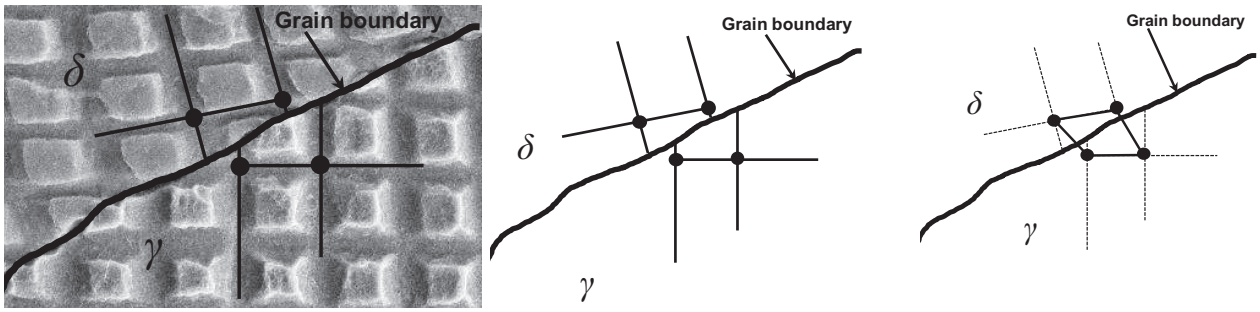


Figure IV.43. a) SEM micrograph and b) schematic of sliding at a δ/γ interphase boundary; and c) shear deformation as interpreted by the strain calculation method, which only takes into account the four corners of each microgrid square.

IV.7.3 A 2-dimensional measurement

Regardless, this method provides only an estimation of the true deformation through a two-dimensional measurement of the strain fields. The 2-dimensional estimation of the strain can be insufficient in some situations. As a consequence, the question of the out-of-plane displacement must be discussed.

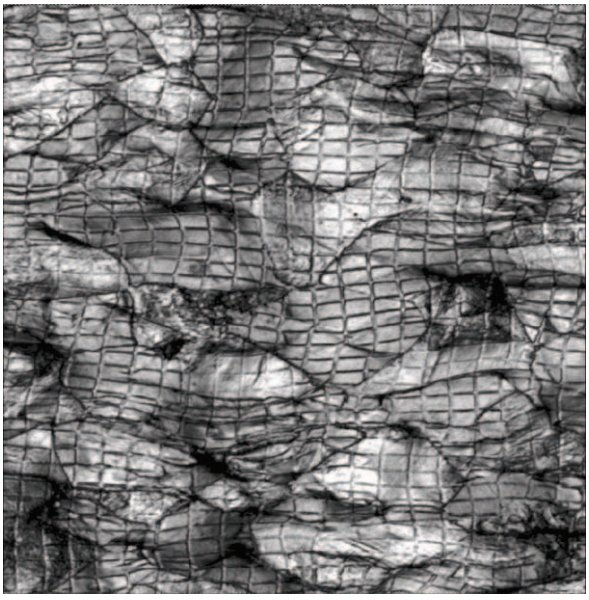
The microgrids were engraved on free surfaces but they were restrained by the tight contact against the flat surface of another sample made of the same material as the microgrid sample (Figure IV.14). Evidence of good restraint was provided by the impression of the microgrid on the surface of the polished plate sample faced to the microgrid sample. However, the SEM micrographs of the deformed microgrids revealed the occurrence of out-of-plane displacement at some locations (see examples in

Figure IV.25, Figure IV.26 and in Appendix C). In the present investigation, the out-of-plane strain was estimated using the isochoric assumption (no volume variation). In most cases, as the out-of-plane strain component is insignificant compared to the in plane strain components, this method seems relatively justified.

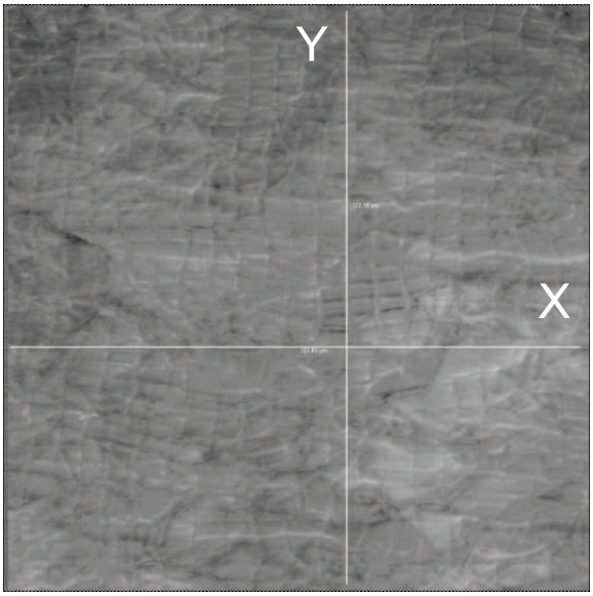
Several authors have attempted to provide an estimation of the out-of-plane displacement.

Soppa et al. [133] compared the strain distributions measured by the microgrid method in an Ag/Ni(57%)-particulate composite taking or not into account the out-of-plane displacement. The out-of-plane displacement was measured on a sample deformed at 8.6% under uniaxial compression at room temperature by atomic force microscopy. The authors found that the discrepancies between the two strain distributions were so small, that the corrections could be neglected, at least for the testing conditions used.

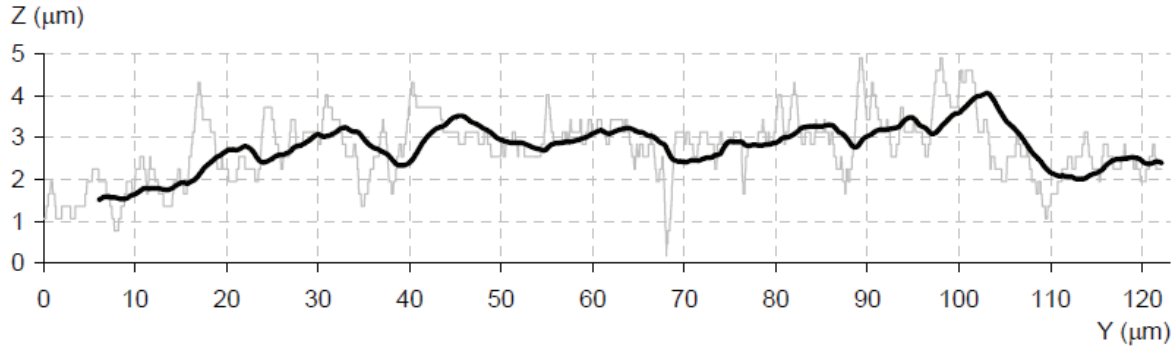
Hernandez-Castillo et al. [50] has measured at the surface of some deformed microgrid samples the out-of-plane displacement with a laser scanning confocal microscope. Figure IV.44.a and Figure IV.44.b show an example of an optical micrograph and the corresponding topological image, of a small area from a deformed microgrid of a laboratory duplex steel sample. Height profiles corresponding to the vertical and horizontal lines in Figure IV.44.b were plotted in order to quantify out-of-plane displacement. Some enhanced local out-of-plane displacement was observed, see Figure IV.44.c and Figure IV.44.d. However, the authors concluded that the displacements were such that they would not result in significantly different strain values.



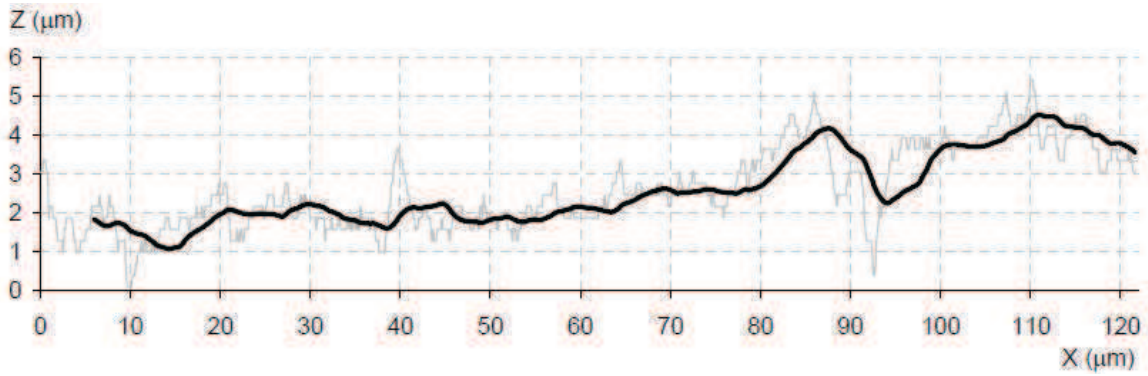
a)



b)



c)



d)

Figure IV.44. a) Optical micrograph of a small area (125x125µm) from a deformed microgrid on a laboratory duplex steel sample; b) grey scale topological image of the same area in a); c) and d) height profiles of the vertical and horizontal lines in b), respectively. The thinner and thicker lines in c) and d) correspond to the original profiles and their smoothed versions respectively.

IV.7.4 Limitations due to experimental conditions

The temperature range of the industrial hot rolling process is between 1000 and 1280°C and the strain rate range is between 1-100s^{-1}. That is why a few microgrid experiments have been performed at a temperature of 1050°C and a strain rate of 10s^{-1}. These experimental conditions turned out to be so constraining that no satisfying results could be obtained. It was extremely difficult or impossible to extract the deformed microgrids from the plane strain compression specimen. Indeed, the two inserts were welded together by diffusion. Even when it was possible to separate the two inserts, the deformed microgrids were strongly damaged or not clearly visible as shown in Figure IV.45. It means that using the microgrids technique above 1000°C requires additional experimental developments.

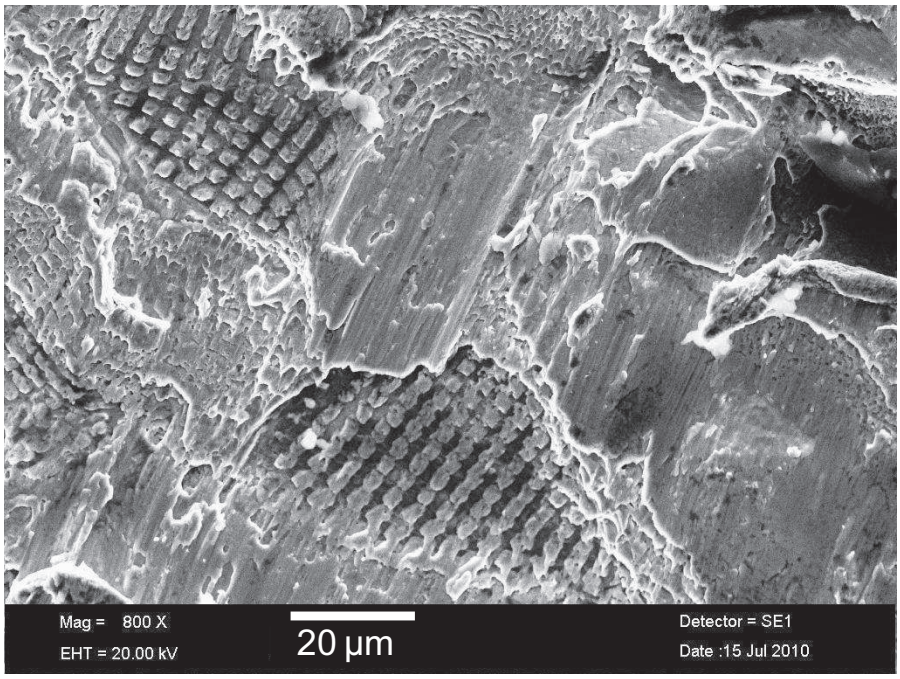


Figure IV.45. SEM micrograph showing the deformed microgrids after plane strain compression at 1050°C and 10s^{-1}.

IV.8 Perspective: derivation of per-phase flow properties

IV.8.1 Introduction

The published literature indicates that the accommodation of macroscopic deformation of DSS depends on the plastic characteristics of both phases [25, 29, 48] and the interface [9, 12, 95], as well as the morphology of the two phases [11]. The results of this work confirm and complete the published results. However, lack of accurate information of flow properties of individual phases makes it challenging to clearly understand the damage mechanisms taking place at the interface. As a consequence, deformation models should be developed based on the microstructures analyzed experimentally by the microgrid technique in order to determine the flow properties of the individual phase. This modelling effort is currently undertaken by co-workers: Sampath Kumar-Yerra et al. [134, 135] at the University of Louvain-la-Neuve in Belgium. The objective of this section is to briefly present the strategy used to derive the flow properties of the individual phases, and to give some results based on one example. The purpose is to show that this strategy allows a systematic approach to determine the contrast in terms of plastic properties between both phases. The finite element (FE) analysis has been used to study the macroscopic mechanical behaviour of DSS in rolling process and in hot plane strain compression [16, 125]. In this work, the technique is used to compute the flow properties of the individual phases. The adopted approach mainly relies on reproducing through FE modeling the experimentally determined micro-scale strain distribution in the two phases of a DSS sample subjected to hot plane strain compression test. Two levels of information can be extracted from the microgrid experiments: average strain per phase and strain maps showing complete strain distribution i.e., with information of the strain tensor at every microgrid intersection.

IV.8.2 Microstructure modelling

The principle involved in the modeling strategy is schematically shown in Figure IV.46. The various aspects of it are explained and illustrated with an example below. The chosen duplex stainless steel sample is the D2 alloy with a Widmanstätten morphology. This sample was deformed at 850°C and $1s^{-1}$ applying a 30% thickness reduction.

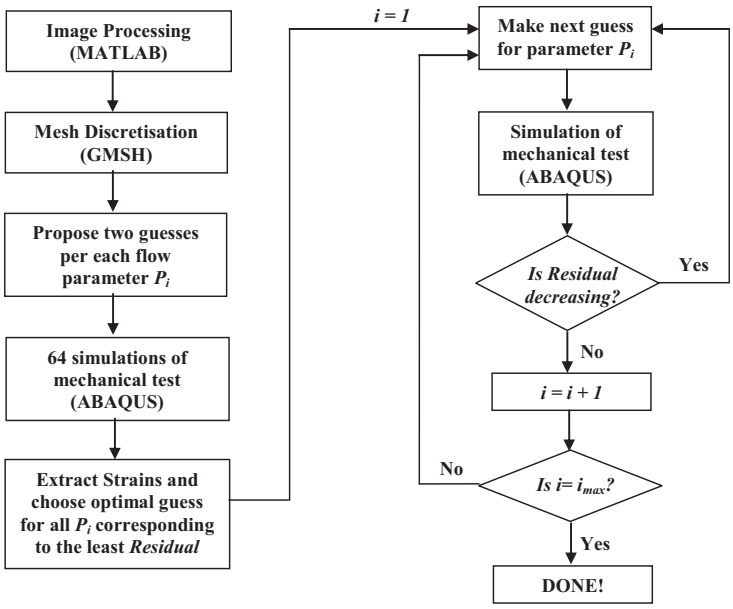


Figure IV.46. Schematic of the modelling strategy for identification of the phase properties.

The derivation of flow properties consists of four steps: (i) image processing of a SEM micrograph; (ii) discretization of the representative microstructure; (iii) simulating the experimental hot plane strain compression test; and (iiii) iteratively tuning the parameters describing the constitutive behaviour of individual phases in the FE model until a good agreement is found between the experimental and simulated strain distribution.

IV.8.2.1 Image processing of the SEM micrograph

A high-resolution SEM micrograph of the undeformed sample (for instance, see Figure IV.47.a), taken prior to testing the specimen is first chosen and subjected to the image processing in MATLAB [136], see Figure IV.47.b. Black and white images of high contrast are desirable for this procedure so that the two phases are clearly distinguishable. In the shown example, white colour represents ferrite and black colour represents austenite. The image analysis algorithm reads the grey value of each pixel of the micrograph, stores its coordinates, and computes the profile of the entire image, see Figure IV.47.c.

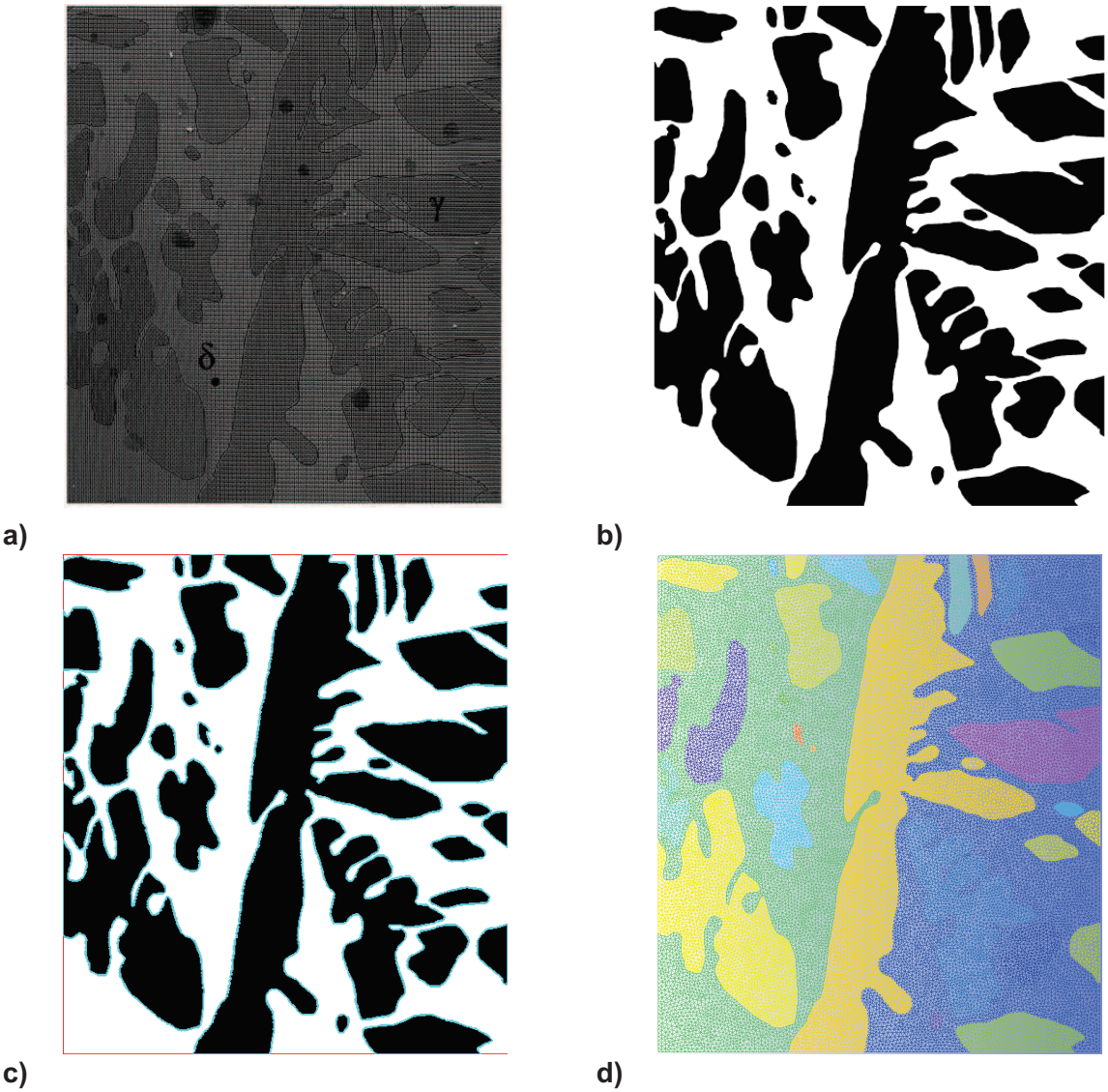


Figure IV.47. Illustration of the microstructure modelling using sample D2_W, map2; a) SEM micrograph of undeformed sample; b) micrograph after image processing in MATLAB [136] (black = austenite, white = ferrite); c) geometric profile (green boundary lines computed by image analysis algorithm; d) FE mesh, as discretized by GSMH [137].

IV.8.2.2 Discretization of the microstructure

The geometric profile of the microstructure that results from the image analysis algorithm is then input into GMSH [137], a 2D/3D mesh generator, which discretizes it into a finite element mesh, see Figure IV.47.d. In this example, about 32000 first-order triangular elements (element type: CPE3) are generated during mesh discretization. The volume fractions of austenite and ferrite in this example are found to be 52% and 48% respectively.

IV.8.2.3 Optimization of flow properties

The constitutive behaviour of the two phases is described using rate-independent Kocks-Mecking hardening law:

$$\sigma = \sigma_0 + \frac{\theta_0}{\beta}\left(1 - e^{-\beta\varepsilon_p}\right), \qquad \text{eq IV-12}$$

where σ_0 is the yield stress, θ_0 (in MPa) and β are parameters that describe the rate of hardening. The effects of strain rate and temperature are not considered in the constitutive law at this stage. Hence the objective now is to optimize six parameters $(\sigma_0^{\gamma}, \theta_0^{\gamma}, \beta^{\gamma}, \sigma_0^{\delta}, \theta_0^{\delta}, \beta^{\delta})$ i.e., 3 per phase. The optimization is then carried out in 6 steps, each step is described in details.

- ***Step1.***

As a starting point to have a first guess of phase properties, the parameters of Kocks-Mecking hardening law for the overall composite material are first identified based on the response of the hot plane strain compression test. These are determined by fitting the measured true stress – true strain curve using non-linear least square fitting procedure. A very good fit, with a regression coefficient as high as 0.97, is used in the subsequent analysis, see Figure IV.48.

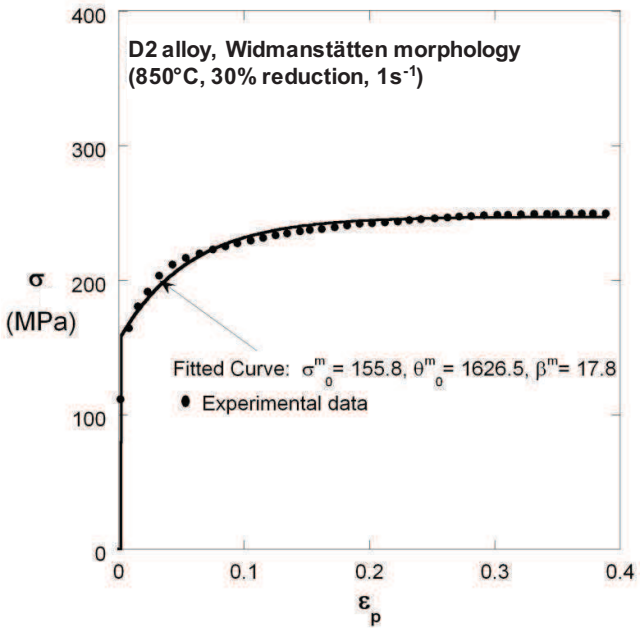


Figure IV.48. Macroscopic equivalent true stress-strain curve of D2 alloy presenting a Widmanstätten morphology measured during plane strain compression test at 850°C and $1s^{-1}$. Thick curve is the fit to Kocks-Mecking hardening law, see eq IV-12. The superscript 'm' means macroscopic.

The macroscopic flow properties are denoted as σ_0^m, θ_0^m, and β^m and their corresponding numerical values obtained via the non-linear least square fitting procedure are given in Table IV.22. The elastic modulus is estimated from the slope of the tangent drawn at 0.2% strain on the flow curve. This value is approximated as 70 GPa and the Poisson's ratio is taken as 0.3.

σ_0^m (MPa)	θ_0^m (MPa)	β^m
155.8	1626.5	17.8

Table IV.22. Numerical values for the three parameters of the Kocks-Mecking hardening law describing the macroscopic flow properties of the specimen D2_W deformed at 850°C; σ_0^m macroscopic yield stress, θ_0^m and β^m are parameters that describe the macroscopic rate of hardening.

- ***Step2.***

Using the macroscopic flow properties, now for each phase, two initial guesses for every flow parameter are considered such that a mismatch of 20%-50%, as anticipated from the literature, is maintained between the flow parameters of the two phases, see Table IV.23.

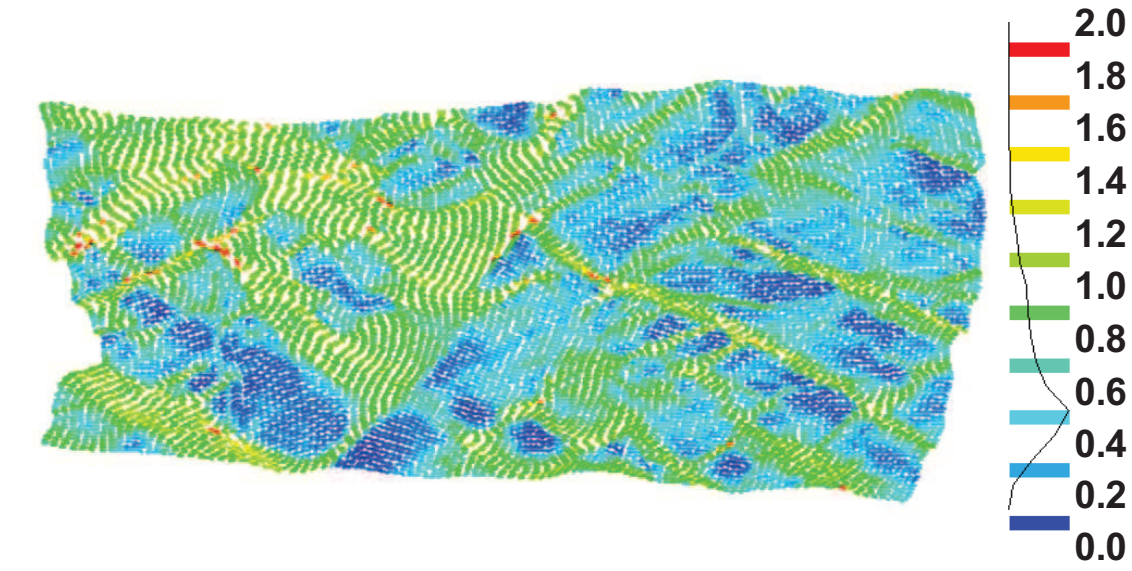
$\sigma_0^\gamma = 1.1\sigma_0^m,\ 1.2\sigma_0^m$	$\theta_0^\gamma = 1.1\theta_0^m,\ 1.2\theta_0^m$	$\beta^\gamma = 1.1\beta^m,\quad 1.2\beta^m$
$\sigma_0^\delta = 0.8\sigma_0^m,\ 0.9\sigma_0^m$	$\theta_0^\delta = 0.9\theta_0^m,\ 0.8\theta_0^m$	$\beta^\delta = 0.9\beta^m,\quad 0.8\beta^m$

Table IV.23. Initial guesses for every flow parameter.

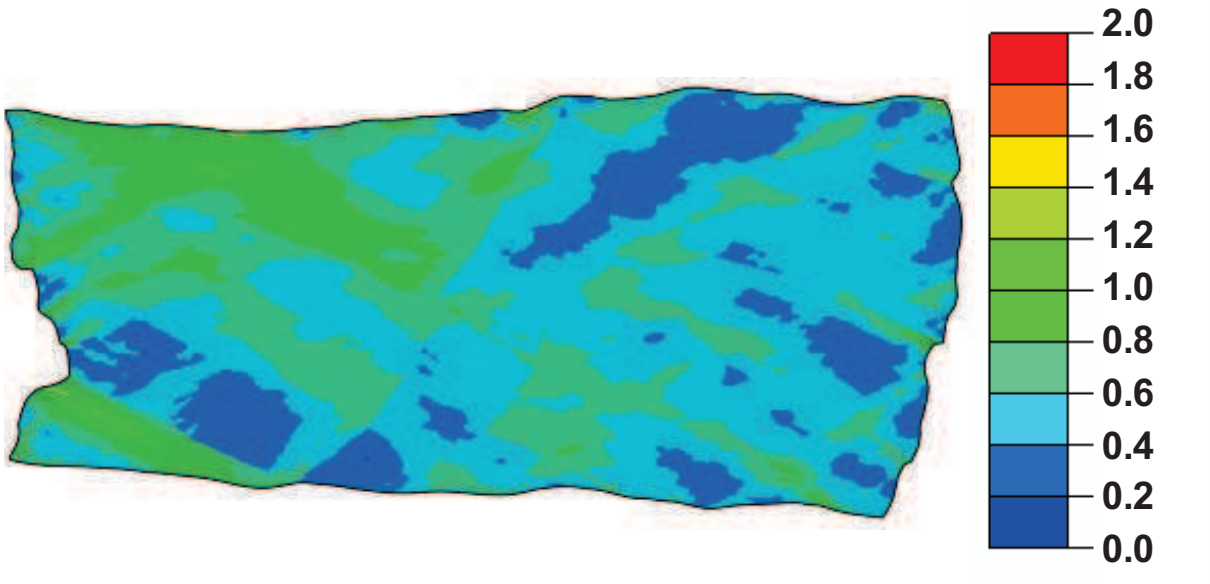
The elastic properties of both phases are considered the same as that of the macroscopic material.

- ***Step3.***

A two-dimensional FE simulation of the plane strain compression-test is performed in Abaqus/Standard that uses implicit-integration scheme [138] choosing the first of the above 64 combinations of the flow parameters for the two phases. As mentioned in the previous section, it was difficult to achieve truly plane strain deformation conditions in the experiments. It is also clear from Figure IV.49.a that the observed shear strains are quite significant. In order to closely reproduce the experimental conditions, the displacements observed along the four edges of each micrograph are imposed in the finite element analysis. Many points are considered along each edge in order to capture the local strain fields with sufficient accuracy. Furthermore, to overcome numerical singularities and also to improve the rate of convergence in FE analyses, the displacement profile on these edges is slightly smoothened in highly distorted regions along the edges.



a)



b)

Figure IV.49. Equivalent strain distribution; a) experimental; b) computed by FE model for the best solution. The displacement profile on the edges is in good agreement with the experimental. Clearly, the strain localization is more in ferrite than in austenite. The compression is applied vertically.

The computation time per simulation is typically observed as 6min in general. At the end of the simulation, the following *Residual*, R, is computed:

$$R = W\left(\bar{\varepsilon}_{ij}^{\gamma,\exp} - \bar{\varepsilon}_{ij}^{\gamma,\mathrm{mod}}\right)^2 + W\left(\bar{\varepsilon}_{ij}^{\delta,\exp} - \bar{\varepsilon}_{ij}^{\delta,\mathrm{mod}}\right)^2 + W\left(\grave{\varepsilon}_{ij}^{\gamma,\exp} - \grave{\varepsilon}_{ij}^{\gamma,\mathrm{mod}}\right)^2 + W\left(\grave{\varepsilon}_{ij}^{\delta,\exp} - \grave{\varepsilon}_{ij}^{\delta,\mathrm{mod}}\right)^2 + \sum\left(\sigma^{m,\exp} - \sigma^{m,\mathrm{mod}}\right)^2 \quad \text{eq IV-13}$$

where indices $i,j = 1,2$; exp denotes experimental and mod denotes model and W is a weight factor equal to 1000 in this procedure introduced in order to make all the terms in the Residual comparable. All strain measures used in eq IV-13 are logarithmic. $\bar{\varepsilon}_{ij}$ denotes average strain components. In FE analysis for a given phase, these are computed by volume-averaging scheme:

$$\bar{\varepsilon}_{ij} = \frac{\sum_{k=1}^{K} \varepsilon_{ij}^{k} v^{k}}{\sum_{k=1}^{K} v^{k}}, \quad \text{eq IV-14}$$

where v^k is the volume of an element k in the FE mesh. K denotes total number of finite elements in the given phase. $\grave{\varepsilon}_{ij}$ denotes the spread or dispersion in the strain components and is calculated as:

$$\grave{\varepsilon}_{ij} = \sqrt{\frac{\sum_{k=1}^{K}\left(\varepsilon_{ij}^{k} - \bar{\varepsilon}_{ij}\right)^2}{K-1}}. \quad \text{eq IV-15}$$

$\sigma^{m,exp}$ and $\sigma^{m,mod}$ respectively denote the experimental and simulated macroscopic stress. The latter is computed by volume-averaging of the Von Mises equivalent stress:

$$\sigma^{m,mod} = \frac{\sum_{k=1}^{K} \sigma_{vm}^{k} v^{k}}{\sum_{k=1}^{K} v^{k}}, \quad \text{eq IV-16}$$

where σ_{vm}^{k} is the von Mises equivalent stress in an element k. K denotes the total number of finite elements (of both phases) in FE mesh. The experimental macroscopic stress at a given strain is computed using eq IV-12 and the Kocks-Mecking law parameters given in Table IV.22. The last term in the *Residual* is calculated by computing the difference between $\sigma^{m,exp}$ and $\sigma^{m,mod}$ at 8 points along the curve.

- ***Step4.***

The simulation of the mechanical test is conducted another 63 times, each time with one of the 64 combinations of flow parameters and the *Residual* is computed at the end of every simulation. The set of parameters that yields the least *Residual* of all is chosen as the starting point for the subsequent analyses. Figure IV.50.a shows the plot of *Residual* for the 64 simulations.

- ***Step5.***

Starting with the optimal starting point found above, a *line search* procedure is then carried. It involves iterative minimisation of the *Residual* by tuning one flow parameter at a time with a predefined step in the direction of descent. When *Residual* is no longer decreasing further for that parameter, the direction of descent for the next flow parameter is found and the tuning of it is continued. The procedure is terminated when all parameters are considered for the optimization. The iteration at which *Residual* is the least is considered as the *optimal* solution for the final step.

- ***Step6.***

To ensure the stability of the solution, the line search procedure is repeated one more time starting with the optimal solution found in Step 5 but with a different ordering of the optimization of the flow parameters. The evolution of *Residual* during *line search* procedure is shown in Figure IV.50.b. It is clear that the *Residual* does not decrease significantly further assuring the uniqueness of the solution. The iteration that yields the least *Residual* by the end of this last run is taken as the *best* solution.

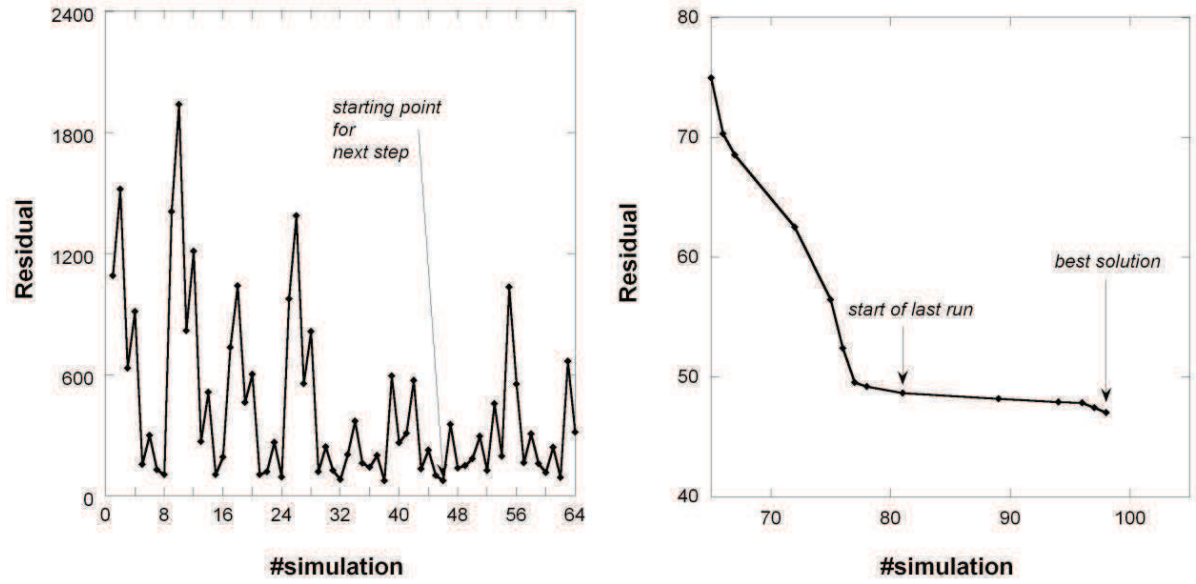


Figure IV.50. Evolution of the residual as a function of simulation number a) during the set of 64 simulations and b) during the line search procedure. The last run assures that the residual does not decrease further. It is observed in general that the best solution is achieved within 100 simulations.

The simulated strain distribution for the best solution is shown in Figure IV.49.b. The displacement profile on the edges of the micrograph is very well reproduced. Like in experiments, the simulation also shows that the strain localization is predominant in ferrite, see Figure IV.49 and Figure IV.51.

More quantitative prediction of strain partitioning is given in Figure IV.51. The comparison between experimental and simulated average strain components is shown in Figure IV.51.a, while the comparison of dispersion in strain components is shown in Figure IV.51.b. It is clear from Figure IV.49 and Figure IV.51 that the strain partitioning computed by FE model is in quite good agreement with that of the experiment. The best Kocks-Mecking flow properties for the two phases are given in Table IV.24.

σ_0^{γ} (MPa)	θ_0^{γ} (MPa)	β^{γ}	σ_0^{δ} (MPa)	θ_0^{δ} (MPa)	β^{δ}
187.0	1789.2.0	20.16	136.2	1301.2	15.52

Table IV.24. Numerical values of the best Kocks-Mecking parameters for the two phases.

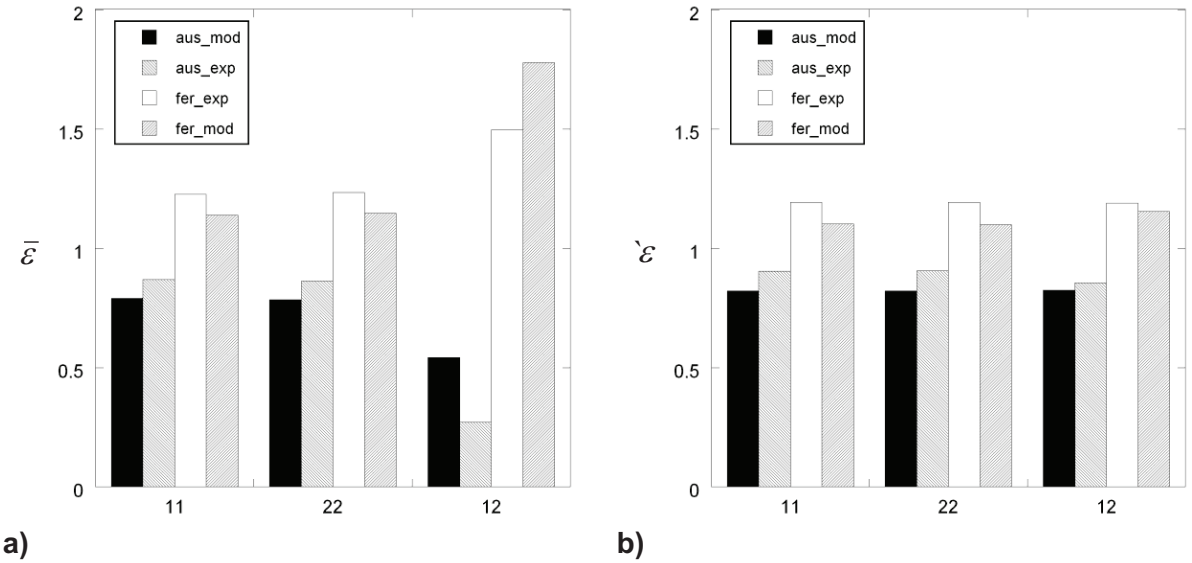


Figure IV.51. Comparison of experimental (denoted as *exp*) and finite element predictions (denoted as *mod*); a) average strain per phase; b) dispersion for strain components 11, 22 and 12. The strains and dispersions are expressed relative to the respective totals in the map. *aus* stands for austenite, and *fer* stands for ferrite.

The yield stress of austenite is found to be at least 1.3 times the yield stress of ferrite. Figure IV.52 compares the flow curves of the two phases with that of macroscopic material. The remarkable overlap of the experimental and simulated macroscopic flow curves comforts us in the belief that we have found as the best possible solution. The degree of mismatch in the flow parameters of the two phases clearly emphasizes the difference in rheological behaviour of the two phases. It can be inferred that the strategy presented here is able to identify the phase properties quite well and indeed helps in understanding the strain partitioning in duplex stainless steels.

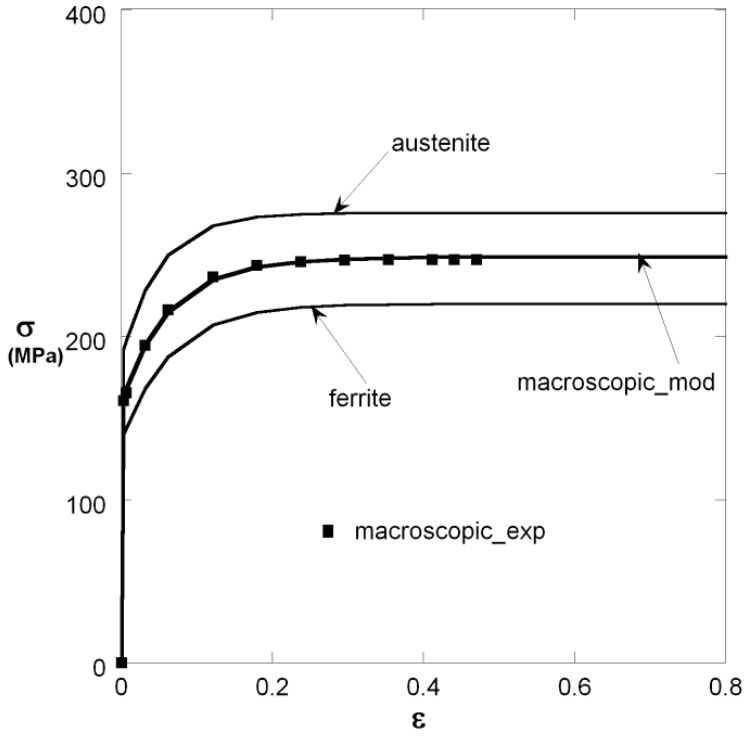


Figure IV.52. Flow curves for the macroscopic material and the two phases. The measured data is indicated by solid squares. The simulated macroscopic stress-strain curve is rather well in agreement with the experimental one.

IV.9 Conclusions

- The modified microgrid technique compared to the classical microgrid method, presents the advantage to be applicable at high temperature.

- The modified microgrid technique was successfully used to determine the high temperature micro-scale strain distribution in duplex stainless steels.

- The characteristics of the deformation mechanisms and partitioning in duplex stainless steels have been determined. The most deformed zones are very often located in the vicinity of the interface between ferrite and austenite and almost always on the ferrite side. The development of shear bands and the possible sliding at the δ/γ interphase boundaries are also mechanisms involved in the deformation of duplex steels.

- The level of strain partitioning seems to play a crucial role in the edge cracking phenomenon and it was identified as a key factor to improve the hot workability of duplex stainless steels.

- The strain incompatibility between ferrite and austenite is higher in the D2 alloy than in the D1 alloy. This difference was attributed to a difference in chemical elements such as Mo or N. Indeed these two elements have a strong solute strengthening effect. Addition of different amounts of Molybdenum or Nitrogen can change the rheology of the phases, and as a result, change also the strain partitioning and the edge cracking resistance.

- Increasing the temperature from 850°C to 950°C increases the strain partitioning between ferrite and austenite.

- The geometric features of the austenite: orientation of the Widmanstätten laths or change in morphology can affect strain localization.

- The coupled experimental-numerical strategy developed in collaboration with colleagues from the University of Louvain-la-Neuve in Belgium will permit a systematic approach to determine the plastic properties of the individual phases.

Chapter V. Conclusions and perspectives

Chapter V. Conclusions and perspectives

Generally, duplex stainless steels exhibit a poor hot workability which results in the occurrence of edge-cracks during the hot rolling processing of flat products. The immediate consequence of the poor hot workability of duplex steels is a dramatic increase of the manufacturing costs because additional operations like grinding or scraping are often required. Two different duplex grades were investigated: D1 and D2. The first one, D1, was known to show a reasonable level of hot workability (edge crack length does not exceed 5mm) whereas D2 is affected by 50mm-long edge-cracks. Both grades constitute good examples to address hot workability issues such as the edge-cracking phenomenon.
Starting from a concrete industrial problem, subjacent scientific issues were identified through this work. Thus, fundamentals aspects about the origin of the edge-cracking problem were addressed and industrial recommendations were formulated.

The literature data about the hot working of duplex steels is very rich. In the literature review (Chapter II), all the factors affecting the hot workability of duplex stainless steels were summarized, and two missing pieces of the “puzzle” to understand completely the hot workability of duplex steels were identified.

First of all, the lack of a method that quantifies properly the high temperature resistance to crack propagation was pointed out as a key parameter to better understand the edge-cracking issue. Secondly, although several authors have suggested the occurrence of strain partitioning between ferrite and austenite in duplex steels, there was clearly a lack of quantitative data about the high temperature micro-scale strain distribution. As a consequence, experimental developments were done to provide quantitative information about high temperature strain partitioning between ferrite and austenite.

These two identified missing pieces of the duplex steels hot workability puzzle were discussed in depth in chapter III and IV, respectively. After having summarized the chapters describing the results obtained throughout these investigations, we give a few recommendations in order to design a “better microstructure”. Finally, as perspectives, several tasks are suggested to complement the work.

V.1 Summary of the chapters III and IV

An overview of the results of this work is given. The main results from chapters III and IV are summarized separately.

V.1.1 Chapter III

The interest in using the essential work of fracture (EWF) concept as a reliable and discriminating tool for quantifying the high temperature tearing resistance and to generate a physically relevant fracture index to guide the optimization of microstructures towards successful forming operations has been demonstrated. Before listing the main results of chapter III, we call that two duplex grades were investigated: D1 and D2, D1 showing a relatively good hot workability compared to D2.

- ✓ In the as-cast conditions, D1 was two times more resistant to hot tearing than D2 at 1050°C. The effect of temperature was also pointed out: the higher temperature in the 1000-1250°C range, the better hot workability. However, the as-cast microstructures exhibit a high degree of heterogeneity. The direct consequence of these heterogeneities was a significant dispersion of the results that induced inaccurate results.

- ✓ To improve the accuracy of the results and to investigate the influence of other parameters (phase morphology, inclusion content…), model microstructures were required. Proper control of the $\delta \rightarrow \gamma$ phase transformation mechanisms allowed the generation of a variety of microstructures with different phase morphologies. By controlling temperature, duration of annealing sequences and cooling rate, alloys with a desired phase proportion, and desired size and shape of the microstructural constituents were produced.

- ✓ The EWF applied to model microstructures confirmed that D1 was two times more resistant to hot tearing than D2 and the accuracy of the results were significantly improved. It was suggested that this difference was probably related to a higher mismatch of the plastic properties of the two phases in D2 when comparing with D1. This assumption was checked and discussed in depth in chapter IV.

- ✓ At constant volume fraction, the austenite morphology impacts significantly the high temperature fracture resistance: for a given alloy, to break a sample showing an equiaxed austenite required two times more energy than to break a sample presenting a Widmanstätten austenite.

- ✓ The inclusions content has to be very well-controlled because high densities of inclusions lead to a significant decrease of hot tearing resistance.

V.1.2 Chapter IV

The modified microgrid technique was successfully applied to duplex stainless steels. This technique provided quantitative data about the high temperature micro-scale strain distribution. The main results are summarized below.

- ✓ The modified microgrid technique has the powerful combination of allowing direct observation and measurement of micro-scale deformation together with the capability to be performed at high temperature.

- ✓ This technique revealed some deformation features. The most deformed regions are very often located in the vicinity of the interphase boundaries, especially on the ferrite side. The development of shear bands and the possible sliding at the interphases boundaries are also mechanisms involved in the deformation of duplex stainless steels at high temperature.

- ✓ The results showed that the D2 alloy exhibits a higher strain partitioning contrast between ferrite and austenite compared to the alloy D1.

- ✓ The phase rheology depends strongly on the chemical composition, in particular on the strengthening effect of element such as N or Mo.

- ✓ Increasing the temperature from 850°C to 950°C results in increasing the strain partitioning contrast.

- ✓ At a given temperature, the strain partitioning depends significantly on the distribution of the austenite: orientation of the austenite laths compared with the loading direction or changes in austenite morphology.

- ✓ The model developed in collaboration with colleagues from the University of Louvain-la-Neuve in Belgium will permit a systematic approach to determine the plastic properties of the individual phases.

V.2 Recommendations for an optimized microstructure

The results provided by the present work lead to formulating several recommendations to design a duplex microstructure highly resistant to edge-cracking. Only some of the recommendations can be industrially applied, that is why the recommendations are divided into two different categories. The first category involves the recommendations which can be relatively easily applied industrially; this category is called “realistic recommendations”. The second category gives the solutions which cannot be changed on the industrial process: “unrealistic recommendations”. For example generate an equiaxed morphology before the hot rolling process constitutes an unrealistic solution to improve the hot workability of duplex steels. The main recommendations are summarized in Table I.1.

Realistic recommendations	Unrealistic recommendations
• A well-controlled temperature of the material during the hot rolling operations, especially for the edge parts.	• Generation of an equiaxed austenite morphology.
• A high quality refining stage to maintain the sulphur and the oxygen contents as low as possible.	• Generation of very fine Widmanstätten austenite.
• Addition of alloying elements in order to reduce as much as possible the rheological contrast between ferrite and austenite.	

Table V.1. Summary of the recommendations for a perfect microstructure, i.e. a high-resistant edge-crack microstructure.

V.3 Perspectives

Technical and conceptual limitations were found during the present investigation, but could not be addressed due to time constraints. Therefore, some future tasks are suggested to complement the work presented in this report.

V.3.1 Essential work of fracture concept

Some perspectives for the EWF concept are given below.

- ✓ The Cotterell test turns out to be an interesting tool to mechanically characterize materials exhibiting some defects. Indeed, performing tensile tests on specimens with defects do not give quantitative data due to a strong dispersion of the results: the tensile specimen breaks where the more critical defect is located. In other words, the initial defects of the specimen govern the final fracture. When the EWF is applied, DENT specimens are used, that permits to localize the deformation and the fracture along the ligament. The DENT specimen is broken taking into account the plasticity in the total specific work of fracture.

- ✓ The essential work of fracture concept applied at high temperature with different specimen thicknesses would allow determining the high-temperature toughness of the materials.

- ✓ The high temperature Cotterell test opens the path to systematically investigate the influence of temperature on the mechanical properties controlling ductile fracture.

- ✓ Modelling effort developing a micromechanical approach of the high temperature ductile fracture in order to relate microstructure and damage could be very interesting. The purpose would be to predict quantitatively the hot ductility of the different model microstructures. Such task is one of the objectives that my co-workers Sampath Kumar-Yerra et al. [134, 135] are pursuing at the University of Louvain-la-Neuve in Belgium. It is currently under progress, making use of the experimental findings of this PhD.

V.3.2 Modified microgrid technique

The microgrid technique offers numerous perspectives. In this section a short overview of these perspectives is given.

- ✓ In order to continue exploring the deformation of microgrid at high temperature under harsh conditions applying larger deformation and increasing the testing temperature, new experimental developments are required.

- ✓ The strain distribution should be determined over large areas within the microgrids, in order to study the macroscopic strain distribution patterns, and to possibly carry out a statistically more relevant analysis over a large number of grains. For instance, in the Widmanstätten morphology, the primary ferrite grain size is very large, about several millimeters but in this work only areas about 500x500µm were analyzed. In addition, as the strain map was plotted on one or two primary ferrite grain, the effect of grain orientation which can play a crucial role was not taken into account.

- ✓ The strengthening effect of Molybdenum and Nitrogen should be accurately quantified in order to confirm the results of this work. For example, hot mechanical tests could be performed using different alloys with the same composition except for different Molybdenum or Nitrogen content.

- ✓ A three dimensional characterization would provide more accurate and realistic determination of the strain components. For instance, pictures obtained via X-ray tomography combined with three dimensional digital image correlation would permit an estimation of the complete strain tensor.

- ✓ The microstructure should be analyzed by electron back-scattered diffraction (EBSD) before microgrid engraving, deformation, and strain calculation procedures, in order to allow the study of the relationship between the original crystallographic orientation and the subsequent deformation.

- ✓ The application of this microgrid technique opens new paths in the investigation of multiphase microstructures deformed at high temperature, such as duplex stainless steels, low-alloy C-Mn steels or α-β titanium alloys during the hot rolling processes.

Bibliography

Bibliography

[1] www.infomine.com. 2011.

[2] **Soulignac P**. “Les aciers austéno-ferritiques”. Ecole sur les aciers inoxydables. Aix-les-Bains, 2000.

[3] **Portevin PA**. “Facteurs de forgeabilité et influence des éléments d’alliages”. Colloque sur la déformation plastique des métaux, 1971.

[4] **Ahlblom B, Sandström R**. “Hot workability of stainless steels : influence of deformation parameters, microstructural components and restoration processes”. *International Metals Reviews* 1982:1.

[5] **Gutierrez I, Iza-Mendia A**. “Chapter 1. Process: Hot Workability”. In: Alvarez-Armas I, Degallaix-Moreuil S, editors. Duplex Stainless Steels. 2009. p.1.

[6] **Herrera C, Ponge D, Raabe D**. “Characterization of the microstructure, crystallographic texture and segregation of an as-cast duplex stainless steel slab”. *Steel Research International* 2008;79:482.

[7] **Monlevade EF, Falleiros IGS**. “Orientation relationships associated with austenite formation from ferrite in a coarse-grained duplex stainless steel”. Hume-Rothery Symposium on Structure and Diffusional Growth Mechanisms of Irrational Interphase Boundaries. Charlotte, NC, 2004. p.939.

[8] **Menezes JWA, Abreu H, Kundu S, Bhadeshia H, Kelly PM**. “Crystallography of Widmanstatten austenite in duplex stainless steel weld metal”. *Science and Technology of Welding and Joining* 2009;14:4.

[9] **Iza-Mendia A, Pinol-Juez A, Gutierrez I, Urcola JJ**. “Study of the role of the interface coherence on the hot deformation behaviour of duplex stainless steels”. In: Fuentes M, MartinezEsnaola JM, Daniel AM, editors. 1st International Conference on Ceramic and Metal Matrix Composites (CMMC 96). San Sebastian, Spain, 1996. p.1033.

[10] **Bugat S, Besson J, Gourgues AF, N'Guyen F, Pineau A**. “Microstructure and damage initiation in duplex stainless steels”. *Materials Science and Engineering A-Structural Materials Properties Microstructure and Processing* 2001;317:32.

[11] **Pinol-Juez A, Iza-Mendia A, Gutierrez I, Urcola JJ**. “Influence of phase morphology and deformation mode on the behaviour during hot working of a two-ductile phase composite”. In: Fuentes M, MartinezEsnaola JM, Daniel AM, editors. 1st International Conference on Ceramic and Metal Matrix Composites (CMMC 96). San Sebastian, Spain, 1996. p.1025.

[12] **Pinol-Juez A, Iza-Mendia A, Gutierrez I**. “Delta/gamma interface boundary sliding as a mechanism for strain accommodation during hot deformation in a duplex stainless steel”. *Metallurgical and Materials Transactions A-Physical Metallurgy and Materials Science* 2000;31:1671.

[13] **Pinol-Juez A, Iza-Mendia A, Gutierrez I**. “Hot workability of a duplex stainless steel related to the interface sliding under different strain paths”. Thermomechanical Processing: Mechanics, Microstructure & Control. p.398.

[14] **Pinna C, Beynon JH, Sellars CM, Bornert M**. “Experimental investigation and micromechanical modeling of the hot deformation of duplex stainless steels”. Conference on mathematical modelling in metal processing and manufacturing. Ottawa, Ontario, Canadian Institute of Mining, 2000.

[15] **Lan YJ, Pinna C**. “A finite element model of the heterogeneous deformation of austenite and ferrite in a duplex stainless steel under hot plane strain compression”. *Advances in Heterogeneous Material Mechanics* 2008 2008:312.

[16] **Reparaz MT, Martinez-Esnaola JM, Urcola JJ**. “Numerical simulation of plane strain compression tests of a bimetallic composite”. In: Fuentes M, MartinezEsnaola JM, Daniel AM, editors. Cmmc 96 - Proceedings of the First International Conference on Ceramic and Metal Matrix Composites, Pts 1 and 2, vol. 127-. 1997. p.1215.

[17] **Rupin N**. “Déformation à chaud de métaux biphasés : modélisations théoriques et confrontations expérimentales”. PhD thesis. Laboratoire de Mécanique des Solides. Ecole Polytechnique, 2007.

[18] **Boldetti C**. “Multi-scale measurement and modelling of large deformation of structural metals during thermomechanical processing”. PhD thesis. Department of Mechanical Engineering. The University of Sheffield, 2006.

[19] **Hernandez-Castillo LE**. “Determination of micro-scale strain distribution in hot-worked steel microstructures”. PhD thesis. Department of Mechanical Engineering. The University of Sheffield, 2005.

[20] **Iza-Mendia A, Gutierrez I**. “Factors affecting the hot workability of duplex stainless steels”. Duplex Stainless Steels 2007. Grado Italy, 2007.

[21] **Cizek P, Wynne BP**. “A mechanism of ferrite softening in a duplex stainless steel deformed in hot torsion”. *Materials Science and Engineering A-Structural Materials Properties Microstructure and Processing* 1997;230:88.

[22] **Cizek P, Wynne BP, Rainforth WM**. “EBSD investigation of the microstructure and texture characteristics of hot deformed duplex stainless steel”. *Journal of Microscopy-Oxford* 2006;222:85.

[23] **Dehghan-Manshadi A, Hodgson PD**. “Effect of delta-ferrite co-existence on hot deformation and recrystallization of austenite”. *Journal of Materials Science* 2008;43:6272.

[24] **Dehghan-Manshadi A, Barnett MR, Hodgson PD**. “Microstructural evolution during hot deformation of duplex stainless steel”. Conference on High Temperature Fatigue - Infuences of Environment Creep. London, ENGLAND, 2006. p.1478.

[25] **Iza-Mendia A, Pinol-Juez A, Urcola JJ, Gutierrez I**. “Microstructural and mechanical behaviour of a duplex stainless steel under hot working conditions”. *Metallurgical and Materials Transactions A-Physical Metallurgy and Materials Science* 1998;29:2975.

[26] **Botella J, Martos JL, Sanchez R**. “Optimizing the hot deformabiblity of 2205 duplex stainless steel by thermal/mechanical simulation”. Stainless Steels '96. Dusseldorf, 1996. p.116.

[27] **Cabrera JM, Mateo A, Llanes L, Prado JM, Anglada M**. “Hot deformation of duplex stainless steels”. International Conference on Advanced Materials Processing Technologies. Madrid, Spain, 2001. p.321.

[28] **Duprez L, De Cooman BC, Akdut N**. “Flow stress and ductility of duplex stainless steel during high-temperature torsion deformation”. *Metallurgical and Materials Transactions A-Physical Metallurgy and Materials Science* 2002;33:1931.

[29] **Evangelista E, McQueen HJ, Niewczas M, Cabibbo M**. “Hot workability of 2304 and 2205 duplex stainless steels”. *Canadian Metallurgical Quarterly* 2004;43:339.

[30] **Carsi M, Jimenez JA, Rieiro I, Ruano OA**. “Conformado a altas temperaturas, y simulacion por torsion, de un acero superduplex”. Barcelona, 2001. p.105.

[31] **Jimenez JA, Carsi M, Ruano OA, Penalba F**. “Characterization of a delta/gamma duplex stainless steel”. *Journal of Materials Science* 2000;35:907.

[32] **Jimenez JA, Carreno F, Ruano OA, Carsi M**. “High temperature mechanical behaviour of delta-gamma stainless steel”. *Materials Science and Technology* 1999;15:127.

[33] **Balancin O, Hoffmann WAM, Jonas JJ**. “Influence of microstructure on the flow behaviour of duplex stainless steels at high temperatures”. *Metallurgical and Materials Transactions A-Physical Metallurgy and Materials Science* 2000;31:1353.

[34] **Roberti R, Faccoli M, Veronesi C**. “Hot deformation behaviour of 2205 duplex stainless steel”. Duplex Stainless Steels. Grado, Italy, 2007.

[35] **Farnoush H, Momeni A, Dehghani K, Mohandesi JA, Keshmiri H**. “Hot deformation characteristics of 2205 duplex stainless steel based on the behaviour of constituent phases”. *Materials & Design* 2010;31:220.

[36] **Momeni A, Dehghani K**. “Hot working behaviour of 2205 austenite-ferrite duplex stainless steel characterized by constitutive equations and processing maps”. *Materials Science and Engineering A-Structural Materials Properties Microstructure and Processing* 2011;528:1448.

[37] **Han Y, Zou DN, Chen ZY, Fan GW, Zhang W**. “Investigation on hot deformation behaviour of 00Cr23Ni4N duplex stainless steel under medium-high strain rates”. *Materials Characterization* 2011;62:198.

[38] **Spigarelli S, El Mehtedi M, Ricci P, Mapelli C**. “Constitutive equations for prediction of the flow behaviour of duplex stainless steels”. *Materials Science and Engineering A-Structural Materials Properties Microstructure and Processing* 2010;527:4218.

[39] **Paul A, Martos JL, Sanchez R**. “Behaviour of 2205 under hot working conditions”. Processing, Materials Innovation Stainless Steel. Florence, Italy, 1993. p.297.

[40] **Sellars CM, Sah JP, Beynon J, Foster SR**. “Plane Strain Compression Testing at elevated Temperature”. 1976.

[41] **McQueen HJ, Ryan ND**. “Constitutive analysis in hot working”. *Materials Science and Engineering A-Structural Materials Properties Microstructure and Processing* 2002;322:43.

[42] **Rupin N**. “Déformation à chaud de métaux biphasés : modélisations théoriques et confrontations expérimentales”. PhD thesis. Laboratoire de Mécanique des Solides. Ecole Polytechnique, 2007. p.245.

[43] **Tendo M, Tadokoro Y, Suetsugu K, Nakazawa T**. “Effects of nitrogen, niobium and molybdenum on strengthening of austenitic stainless steel produced by thermo-mechanical control process”. *Isij International* 2001;41:262.

[44] **Sandstrom R, Bergqvist H**. “Temperature-dependence of tensile properties and strenghtening of nitrogen alloyed austenitic stainless steel”. *Scandinavian Journal of Metallurgy* 1977;6:156.

[45] **Verlinden B, Cuypers K, Aernoudt E**. “Influence of nitrogen content, ferrite/austenite ratio and grain size on the hot strength of duplex stainless steel”. In: Charles J, Bernhardson S, editors. Duplex Stainless Steels, vol. 2, 1991. p.711.

[46] **Duprez L, De Cooman BC, Akdut N**. “Deformation behaviour of duplex stainless steel during industrial hot rolling”. *Steel Research International* 2002;73:531.

[47] **Al-Jouni FE, Sellars CM**. “Hot deformation of two-phase stainless steels”. In: Sorensen B, Hansen N, Horsewell A, Leffers T, Lilholt H, editors. International Symposium on Metallurgy and Materials Science. Roskilde, Denemark: Riso National Laboratory, 1983. p.131.

[48] **Duprez L, De Cooman BC, Akdut N**. “High-temperature stress and strain partitioning in duplex stainless steel”. *Zeitschrift Fur Metallkunde* 2002;93:236.

[49] **Unckel H**. *Journal of the Institute of Metals* 1937;61.

[50] **Hernandez-Castillo LE, Beynon JH, Pinna C, van der Zwaag S**. “Micro-scale strain distribution in hot-worked duplex stainless steel”. *Steel Research International* 2005;76:137.

[51] **Vernusse P**. “Comportement mécanique d'un matériau microhétérogène. Application à la déformation à chaud d'aciers à deux phases ductiles”. PhD thesis. Laboratoire Claude Goux. Ecole des Mines de Saint-Etienne, 1993.

[52] **Muller TLF**. “The deformation of duplex alloys”. PhD thesis. Department of Materials science. The University of Sheffield, 1967.

[53] **Furuhara T, Mizuno Y, Maki T**. “Microstructure development and superplasticity in (alpha+gamma) microduplex alloys with different matrix phases”. *Materials Transactions* 1999;40:815.

[54] **Furuhara T, Maki T**. “Grain boundary engineering for superplasticity in steels”. *Journal of Materials Science* 2005;40:919.

[55] **Maki T, Furuhara T, Tsuzaki K**. “Microstructure development by thermomechanical processing in duplex stainless steel”. *Isij International* 2001;41:571.

[56] **Maehara Y, Ohmori Y**. “Microstructural change during superplastic deformation of a delta-ferrite austenite duplex stainless-steel”. *Metallurgical Transactions A-Physical Metallurgy and Materials Science* 1987;18:663.

[57] **Maehara Y**. “High strain rate superplasticity of a 25 wt pct Cr-7 wt pct Ni-3 wt pct Mo-0.14 wt pct N-duplex stainless-steel”. *Metallurgical Transactions A-Physical Metallurgy and Materials Science* 1991;22:1083.

[58] **Maehara Y**. “Effect of microstructure on hot deformation in duplex stainless-steels”. *Scripta Metallurgica et Materialia* 1992;26:1701.

[59] **Liou HY, Pan YT, Hsieh RL, Tsai WT**. “Effects of alloying elements on the mechanical properties and corrosion behaviours of 2205 duplex stainless steels”. *Journal of Materials Engineering and Performance* 2001;10:231.

[60] **Komi JI, Karjalainen LP**. “Effect of restoration on hot ductility of high alloy and duplex stainless steels”. *Materials Science and Technology* 2002;18:563.

[61] **Lin G, Zhang ZX, Song HW, Tong J, Zhou CD**. “Investigation of the Hot Plasticity of Duplex Stainless Steel”. *Journal of Iron and Steel Research International* 2008;15:83.

[62] **Song H, Zhang W, Yang Y, Jiang L**. “Effect of the Chemical Composition and Hot Rolling Techniques on Hot Ducvtility of Duplex Stainless Steel 2205”. DuplexWorld2010. Beaune, France, 2010.

[63] **Tsuge S**. “Effects of impurity and MicroAlloying Elements on Hot Workability of Duplex Stainless Steels”. International Conference on Stainless steel, vol. 2. Chiba, 1991. p.799.

[64] **Fourmentin R**. “Effect of the oxygen/sulfur on the hot workability of the DX 2205 Duplex grade (Part I)”. NT n°2236: ArcelorMittal, 2009.

[65] **Calliari I, Straffelini G, Ramous E**. “Investigation of secondary phase effect on 2205 DSS fracture toughness”. *Materials Science and Technology* 2010;26:81.

[66] **Nilsson JO, Kangas P, Karlsson T, Wilson A**. “Mechanical properties, microstructural stability and kinetics of sigma-phase formation in 29Cr-6Ni-2Mo-0.38N superduplex stainless steel”. *Metallurgical and Materials Transactions A-Physical Metallurgy and Materials Science* 2000;31:35.

[67] **Ibrahim OH, Ibrahim IS, Khalifa TAF**. “Effect of Aging on the Toughness of Austenitic and Duplex Stainless Steel Weldments”. *Journal of Materials Science & Technology* 2010;26:810.

[68] **Keshmiri H, Momeni A, Dehghani K, Ebrahimi GR, Heidari G**. “Effect of Aging Time and Temperature on Mechanical Properties and Microstructural Evolution of 2205 Ferritic-Austenitic Stainless Steel”. *Journal of Materials Science & Technology* 2009;25:597.

[69] **Sieurin H, Sandstrom R**. “Sigma phase precipitation in duplex stainless steel 2205”. *Materials Science and Engineering A-Structural Materials Properties Microstructure and Processing* 2007;444:271.

[70] **Cotterell B, Reddel JK**. “Essential work of plane stress ductile fracture”. *International Journal of Fracture* 1977;13:267.

[71] **Broberg KB**. “Stable crack growth”. *Journal of the Mechanics and Physics of Solids* 1975;23:215.

[72] **Pardoen T, Marchal Y, Delannay F**. “Essential work of fracture compared to fracture mechanics - towards a thickness independent plane stress toughness”. *Engineering Fracture Mechanics* 2002;69:617.

[73] **Marchal Y, Walhin JF, Delannay F**. “Statistical procedure for improving the precision of the measurement of the essential work of fracture of thin sheets”. *International Journal of Fracture* 1997;87:189.

[74] **Marchal Y, Delannay F**. “Influence of test parameters on the measurement of the essential work of fracture of zinc sheets”. *International Journal of Fracture* 1996;80:295.

[75] **Knockaert R, Doghri I, Marchal Y, Pardoen T, Delannay F**. “Experimental and numerical investigation of fracture in double-edge notched steel plates”. *International Journal of Fracture* 1996;81:383.

[76] **Pardoen T, Hachez F, Marchioni B, Blyth PH, Atkins AG**. “Mode I fracture of sheet metal”. *Journal of the Mechanics and Physics of Solids* 2004;52:423.

[77] **Cotterell B, Pardoen T, Atkins AG**. “Measuring toughness and the cohesive stress-displacement relationship by the essential work of fracture concept”. Conference on Prospects in Fracture in honor of the 65th Birthday of JG Williams, vol. 72. London, ENGLAND, 2003. p.827.

[78] **Marchal Y, Oldenhove B, Daoust D, Legras R, Delannay F**. “Characterization of the fracture toughness of rubber-toughened polypropylene thin plates”. *Polymer Engineering and Science* 1998;38:2063.

[79] **Mai YW, Cotterell B**. “On the essential work of ductile fracture in polymers”. *International Journal of Fracture* 1986;32:105.

[80] **Mai YW, Pilko KM**. “Essential work of plane stress ductile fracture of a strain-aged steel”. *Journal of Materials Science* 1979;14:386.

[81] **Mai YW, Powell P**. “Essential work of fracture and J-integral measurements for ductile polymers”. *Journal of Polymer Science Part B-Polymer Physics* 1991;29:785.

[82] **Garnier G, Chehab B, Yrieix B, Brechet Y, Flandin L**. “On the essential work of fracture in polymer-metal multilayers”. *Journal of Materials Science* 2009;44:5537.

[83] **Barany T, Czigany T, Karger-Kocsis J**. “Application of the essential work of fracture (EWF) concept for polymers, related blends and composites: A review”. *Progress in Polymer Science* 2010;35:1257.

[84] **Arkhireyeva A, Hashemi S**. “Influence of temperature on plane stress ductile fracture of poly(ethylene terephthalate) film”. *Plastics Rubber and Composites* 2001;30:125.

[85] **Arkhireyeva A, Hashemi S**. “Effect of temperature on work of fracture parameters in poly(ether-ether ketone) (PEEK) film”. *Engineering Fracture Mechanics* 2004;71:789.

[86] **Arkhireyeva A, Hashemi S**. “Combined effect of temperature and thickness on work of fracture parameters of unplasticized PVC film”. *Polymer Engineering and Science* 2002;42:504.

[87] **Zhang H, Zhang Z, Yang JL, Friedrich K**. “Temperature dependence of crack initiation fracture toughness of various nanoparticles filled polyamide 66”. *Polymer* 2006;47:679.

[88] **Hashemi S**. “Temperature and deformation rate dependence of the work of fracture in polycarbonate (PC) film”. *Journal of Materials Science* 2000;35:5851.

[89] **Hashemi S**. “Temperature dependence of work of Fracture parameters in polybutylene terephthalate (PBT)”. *Polymer Engineering and Science* 2000;40:1435.

[90] **Hashemi S, Arkhireyeva A**. “Influence of temperature on work of fracture parameters in semi-crystalline polyester films”. *Journal of Macromolecular Science-Physics* 2002;B41:863.

[91] **Hashemi S, Xu Y**. “Thermal effects on fracture of biaxial-oriented poly(ethylene terephthalate) (BOPET) film”. *Journal of Materials Science* 2007;42:6197.

[92] **Chehab B, Brechet Y, Glez JC, Jacques PJ, Mithieux JD, Veron M, Pardoen T.** “Characterization of the high temperature tearing resistance using the essential work of fracture - Application to dual phase ferritic stainless steels”. *Scripta Materialia* 2006;55:999.

[93] **Chéhab B**. “Etude de la forgeabilité d'un acier inoxydable ferritique biphasé à chaud”. Laboratoire SIMaP. PhD thesis. Laboratoire SIMAP. Institut National Polytechnique de Grenoble, 2007.

[94] **Dernoncourt P**. “Faisabilité des éprouvettes Cotterell sur la Gleeble 3500 de ArcelorMittal Stainless Europe en réduisant la consommation de métal”. Centre de Recherche d'Isbergues, 2009.

[95] **Pinol-Juez A, Iza-Mendia A, Gutierrez I**. “Hot workability of a duplex stainless steel related to the interface sliding under different strain paths”. In: Palmiere EJ, editor. Thermomechanical Processing: Mechanics, Microstructure & Control. Sheffield, 2003. p.398.

[96] **Raabe D, Sachtleber M, Zhao Z, Roters F, Zaefferer S**. “Micromechanical and macromechanical effects in grain scale polycrystal plasticity experimentation and simulation”. *Acta Materialia* 2001;49:3433.

[97] **Hernandez-Castillo LE**. “Determination of micro-scale strain distribution in hot-worked steel microstructures”. PhD thesis. Department of Engineering Materials. The University of Sheffield, 2005. p.207.

[98] **Allais L, Bornert M, Bretheau T, Caldemaison D**. “Experimental characterization of the local strain field in a heterogeneous elastoplastic material”. *Acta Metallurgica et Materialia* 1994;42:3865.

[99] **Ososkov Y, Wilkinson DS, Jain M, Simpson T**. “In-situ measurement of local strain partitioning in a commercial dual-phase steel”. *International Journal of Materials Research* 2007;98:664.

[100] **Hatanaka K, Fujimitsu T, Inoue H**. “A measurement of 3-dimensional strains around a creep-crack tip”. *Experimental Mechanics* 1992;32:211.

[101] **Goldrein HT, Palmer SJP, Huntley JM**. “Automated fine grid technique for measurement of large strain deformation maps”. *Optics and Lasers in Engineering* 1995;23:305.

[102] **Berka L, Sova M, Fischer G**. “Residual stress evaluation by microscopic strain measurement”. *Experimental Techniques* 1998;22:22.

[103] **Soula A, Renollet Y, Boivin D, Pouchou JL, Locq D, Caron P, Brechet Y**. “Analysis of high-temperature creep deformation in a polycrystalline nickel-base superalloy”. 11th International Conference of Creep and Fracture of Engineering Materials and Structures. Bad Berneck, GERMANY, 2008. p.301.

[104] **Heripre E, Dexet M, Crepin J, Gelebart L, Roos A, Bornert M, Caldemaison D**. “Coupling between experimental measurements and polycrystal finite element calculations for micromechanical study of metallic materials”. *International Journal of Plasticity* 2007;23:1512.

[105] **Franke EA, Wenzel DJ, Davidson DL**. “Measurement of microdisplacements by machine vision photogrammerty (DISMAP)”. *Review of Scientific Instruments* 1991;62:1270.

[106] **Chao YJ, Luo PF, Kalthoff JF**. “An experimental study of the deformation fields around a propagating crack tip”. *Experimental Mechanics* 1998;38:79.

[107] **Lee C, Chao YJ, Sutton MA, Peters WH, Ranson WF**. “Determination of plastic strains at notches by image processing methods”. *Experimental Mechanics* 1989;29:214.

[108] **Han G, Sutton MA, Chao YJ**. “A study of stationary crack tip deformation fields in thin sheets by computer vision”. *Experimental Mechanics* 1994;34:125.

[109] **Dawicke DS, Sutton MA**. “CTOA and crack tunneling measurements in thin sheet 2024-T3 aluminium alloy”. *Experimental Mechanics* 1994;34:357.

[110] **McNeill SR, Peters WH, Sutton MA**. “Estimation of stress intensity factor by digital image correlation”. *Engineering Fracture Mechanics* 1987;28:101.

[111] **Lyons JS, Liu J, Sutton MA**. “High-temperature deformation measurements using digital-image correlation”. *Experimental Mechanics* 1996;36:64.

[112] **Liu J, Sutton M, Lyons J, Deng XM**. “Experimental investigation of near crack tip creep deformation in alloy 800 at 650 degrees C”. *International Journal of Fracture* 1998;91:233.

[113] **Grant BMB, Stone HJ, Withers PJ, Preuss M**. “High-temperature strain field measurement using digital image correlation”. *Journal of Strain Analysis for Engineering Design* 2009;44:263.

[114] **Bastawros A, McManuis R**. “Case study. Use of digital image analysis software to measure non-uniform deformation in cellular aluminum alloys”. *Experimental Techniques* 1998;22:35.

[115] **Zhang D, Zhang X, Cheng G**. “Compression strain measurement by digital speckle correlation”. *Experimental Mechanics* 1999;39:62.

[116] **Wang Y, Cuitino AM**. “Full-field measurements of heterogeneous deformation patterns on polymeric foams using digital image correlation”. *International Journal of Solids and Structures* 2002;39:3777.

[117] **Buffiere JY, Maire E, Adrien J, Masse JP, Boller E**. “In Situ Experiments with X ray Tomography: an Attractive Tool for Experimental Mechanics”. *Experimental Mechanics* 2010;50:289.

[118] **Leclerc H, Perie JN, Roux S, Hild F**. “Voxel-Scale Digital Volume Correlation”. *Experimental Mechanics* 2011;51:479.

[119] **Vendroux G, Knauss WG**. “Submicron deformation field measurements: Part 1. Developing a digital scanning tunneling microscope”. *Experimental Mechanics* 1998;38:18.

[120] **Vendroux G, Knauss WG**. “Submicron deformation field measurements: Part 2. Improved digital image correlation”. *Experimental Mechanics* 1998;38:86.

[121] **Vendroux G, Schmidt N, Knauss WG**. “Submicron deformation field measurements: Part 3. Demonstration of deformation determinations”. *Experimental Mechanics* 1998;38:154.

[122] **Schroeter DM, McDowell DL**. “Measurement of deformation fields in polycrystalline OFHC copper”. *International Journal of Plasticity* 2003;19:1355.

[123] **Carbonneau X, Thollet G, Olagnon C, Fantozzi G**. “Development of high temperature extensometric microgrids”. *Journal of Materials Science Letters* 1997;16:1101.

[124] **Soula A**. “Etude de la déformation intergranulaire au cours du fluage à haute température d’un superalliage pour disque de turbine”. ONERA. Grenoble: Institut Polytechnique de Grenoble, 2008. p.199.

[125] **Boldetti C**. “Multi-scale measurement and modelling of large deformation of structural metals during thermomechanical processing”. PhD thesis. Department of Mechanical Engineering. The University of Sheffield, 2006. p.203.

[126] **Pinna C, Lan Y**. “Local strain measurement in hot deformed microstructures. In: DaFonseca JQ, editor. 5th International Conference on Advances in Experimental Mechanics”. Manchester, England, 2007. p.167.

[127] **Loveday MS, Mahon GJ, Roebuck B, Lacey AJ, Palmiere EJ, Sellars CM, Van der Winden MR**. “Measurement of flow stress in hot plane strain compression tests”. *Materials at High Temperatures* 2006;23:85.

[128] **Bornert M**. “Morphologie microstructurale et comportement mécanique; caractérisations expérimentales, approche par bornes et estimations autocohérentes généralisées”. PhD thesis. Laboratoire de Mécanique des Solides. Ecole Polytechnique, 1996. p.407.

[129] **Doumalin P**. “Microextensométrie locale par corrélation d'images numériques”. PhD thesis. Laboratoire de Mécanique des Solides. Ecole Polytechnique, 2000. p.260.

[130] **Mirza MS, Sellars CM**. “Modelling the hot plane strain compression test Part 2 - Effect of friction and specimen geometry on spread”. *Materials Science and Technology* 2001;17:1142.

[131] **Mirza MS, Sellars CM**. “Modelling the hot plane strain compression test Part I - Effect of specimen geometry, strain rate, and friction on deformation”. *Materials Science and Technology* 2001;17:1133.

[132] **Beynon JH, Sellars CM**. “Strain distribution patterns during plane strain compression”. *Journal of Testing and Evaluation* 1985;13:28.

[133] **Soppa E, Doumalin P, Binkele P, Wiesendanger T, Bornert M, Schmauder S**. “Experimental and numerical characterisation of in-plane deformation in two-phase materials”. *Computational Materials Science* 2001;21:261.

[134] **Yerra SK, Martin G, Willemet M, Veron M, Bréchet Y, Fourmentin R, Mithieux JD, Delannay L, Pardoen T**. “A numerical study on damage nucleation of duplex stainless steel”. In: Charles J, editor. DuplexWorld2010. 13-15 october 2010, Beaune, France, 2010.

[135] **Yerra SK, Martin G, Veron M, Bréchet Y, Fourmentin R, Mithieux JD, Delannay L, Pardoen T**. “Damage nucleation and growth in dual-phase materials”. CFRAC 2011, International conference on computational modelling of fracture and failure of materials. 6-8 june 2011, Barcelona, Spain, 2011.

[136] MATLAB. vol. The Mathworks, 2008.

[137] **Geuzaine C, Remacle JF**. “Gmsh: A 3-D finite element mesh generator with built-in pre- and post-processing facilities”. *International Journal for Numerical Methods in Engineering* 2009;79:1309.

[138] ABAQUS/Standard FE Software. vol. Dassault Systèmes, 2009.

Appendices

Appendix A: Post processing-analysis of the raw data of the plane strain compression tests

A.1 Specimens measurements

The undeformed and deformed specimens were measured as described in Figure A. 1.

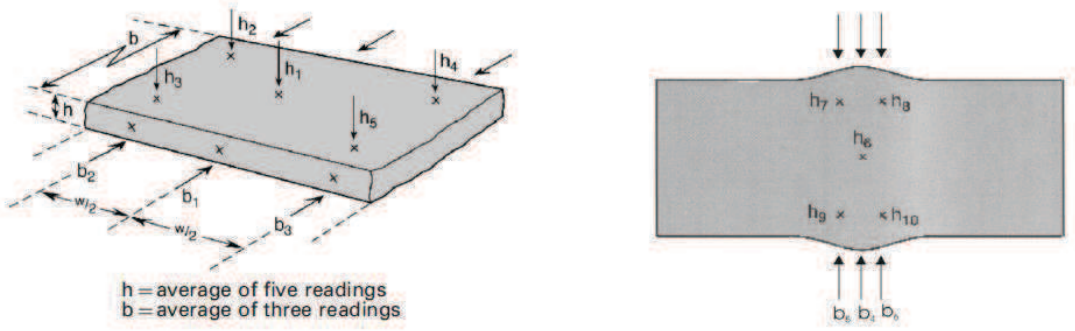


Figure A. 1. Schematic diagram of a testpiece; a) before and b) after testing, and approximate dimensional measurement positions.

For the thickness, the measurements were averaged over five readings. In the breadth direction the average was weighted towards the central measurement, with this being counted twice during the calculation. The cold final measurements were then used to calculate the hot final measurements of the specimen using eq A.1:

$$h_h = h_f + \alpha h_f (T - T_0) \qquad \textbf{eq A.1}$$

where h_h is the hot thickness, h_f is the deformed cold thickness, α is the thermal expansion coefficient, T the deformation temperature and T_0 is room temperature.

A.2 Breadth spread, origin and machine compliance corrections

It was impractical to use a specimen geometry for which the tool width was not a significant factor of the specimen breadth. This led to lateral spread of the specimen and uncertainty in the contact area when the stress was applied. An ‘instantaneous’ breadth was empirically defined following the test, to take into account the changing contact area between the tools and the specimen.

A satisfactory empirical relationship, which defined a 'spread coefficient' C_b from the specimen dimensions before and after the test can be defined, see eq A.2.

$$C_b = \frac{(b_f / b_0) - 1}{1 - (h_f / h_0)^{0.5}} \qquad \textbf{eq A.2}$$

where b_f and h_f are the average breadth and height post deformation, with b_0 and h_0 the equivalent dimensions pre deformation.

The breadth b, at an intermediate time, can therefore be estimated from:

$$b = b_0\left[1 + C_b - C_b(h/h_0)^{0.5}\right]. \qquad \textbf{eq A.3}$$

The first origin correction, shown by the red line in Figure A.2 was applied for errors that arise from the maximum displacement recorded by the displacement transducers on the ram. This was done by measuring the mean thickness of the specimen after the deformation. The value was then corrected for the thermal expansion of the specimen, which was always accounted for when determining the initial hot thickness from cold measurements.

The second origin correction was applied to the raw data for errors in the zero position. This is shown in Figure A.2 where the red data has been corrected from the black line. The illustrated data was taken from one of the test discussed in this work. The aim of this was to correct for slight drift in the machine and align the slope which arises from machine compliance with the origin, as shown in Figure A.2. From the initial and final hot thickness, the maximum displacement of the upper tool $\delta^{\max}_{measured}$ was derived. This figure was then compared to the maximum value recorded by the displacement transducer $\delta^{\max}_{nominal}$. Any discrepancy between the values was corrected for by shifting the load displacement curve in such a way that the maximum actuator displacement was equal to the maximum measured displacement.

Thus:

$$\delta'_{corr} = \delta_{nominal} - (\delta^{\max}_{nominal} - \delta^{\max}_{measured}) \qquad \textbf{eq A.4}$$

$$\delta'_{corr} = \delta_{nominal} - \delta_{\sigma_c} \qquad \textbf{eq A.5}$$

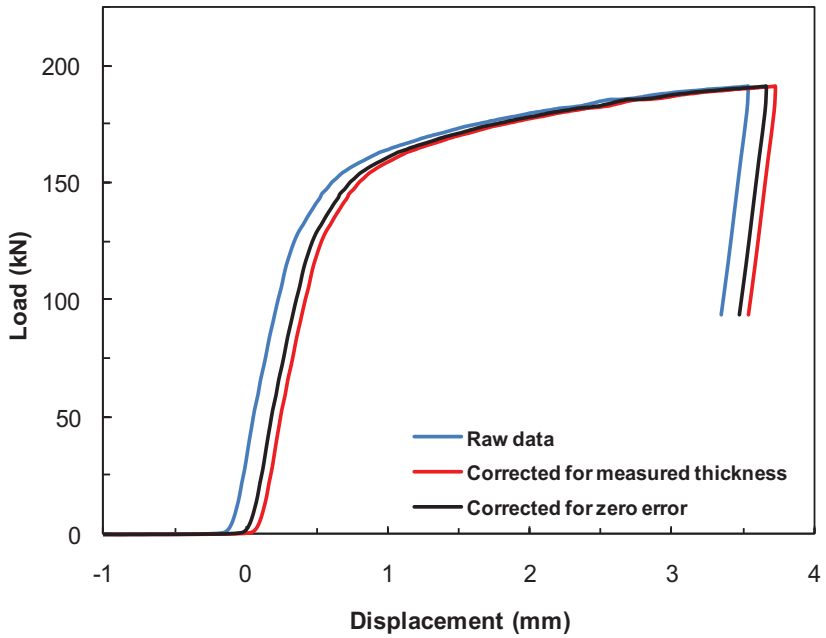


Figure A.2. Origin corrections, taken from a single deformation carried out at 850°C and $1s^{-1}$.

The TMC machine has a machine stiffness of approximately 410 $kNmm^{-1}$ which implies that at maximum load, the machine frame and tooling will deform elastically by more than 1mm. The machine compliance (slope of the load/displacement curve) was measured for each test. The technique was used to correct the displacement data at the beginning of the deformation. This is shown in Figure A.3, with the twice corrected data from Figure A.2. This method produced a corrected data set of load and displacement values. When combined with the temperature, time and velocity data, the equivalent stress and strain and strain rate could be determined.

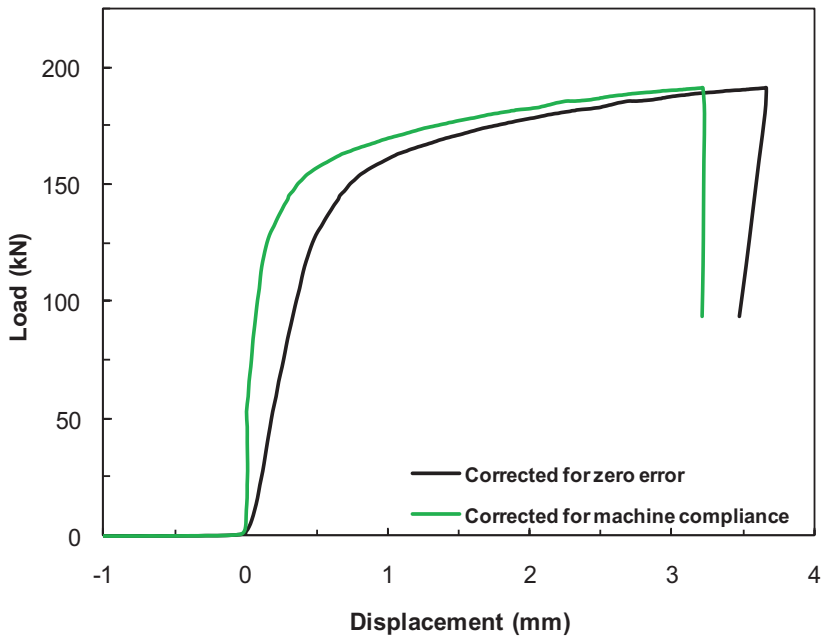


Figure A.3. Machine compliance corrections.

A.3 Calculation of pressure and equivalent strain ε_{eq}

To determine the flow stress of the material, the load exerted by the ram L was converted into an average pressure p using the instantaneous breadth b and the platen width w, such that

$$p = \frac{L}{wb} \qquad \textbf{eq A.6}$$

eq A.7 presented the equation for equivalent tensile strain ε_{eq} and eq A.8 was for the ideal plane strain conditions, i.e. ε_3 = 0 and ε_1 = -ε_2.

$$\varepsilon_{eq} = \frac{\sqrt{2}}{3}[(\varepsilon_1 - \varepsilon_2)^2 + (\varepsilon_2 - \varepsilon_1)^2 + (\varepsilon_3 - \varepsilon_1)^2]^{1/2} \qquad \textbf{eq A.7}$$

$$\varepsilon_{eq} = \frac{2}{\sqrt{3}} \ln\left(\frac{h_f}{h_0}\right) \qquad \textbf{eq A.8}$$

However accounting for the lateral spread, $\varepsilon_3 = \ln(b/b_0)$, $\varepsilon_1 = \ln(h/h_0)$ and therefore ε_2 = -ε_1-ε_3. Then by substitution, ε_{eq} is given through eq A.9.

$$\varepsilon_{eq} = \frac{2}{\sqrt{3}}[\varepsilon_1^2 + \varepsilon_1\varepsilon_3 + \varepsilon_3^2]^{1/2} \qquad \textbf{eq A.9}$$

From eq A.9, ε_{eq} may be determined from the instantaneous width and thickness measurements. As shown, ε_1 is related to ε_3 by eq A.3 and a factor f can be defined as:

$$\varepsilon_{eq} = -f\varepsilon_1 \qquad \textbf{eq A.10}$$

For example, in the limit of zero spread, then $f = 2/\sqrt{3} = 1.155$. However, as there is a clear lateral spread for all these tests, the equivalent strain was determined using eq A.9, then f may be determined from eq A.11.

$$f = -\frac{\varepsilon_{eq}}{\varepsilon_1} \qquad \textbf{eq A.11}$$

With f determined this factor was then used to determine the equivalent stress and strain rate for the deformation.

A.4 Determination of equivalent flow stress σ_{eq}

The equivalent flow stress σ_{eq} was calculated from the maximum shear stress k. This was deduced from the instantaneous pressure using the method described in Ref. [127] where the friction conditions were determined to be either predominantly sliding, sticking or a combination of the two. Sliding friction assumed that contact stress at the tool/specimen interface was equal to the material flow stress in

pure shear. An intermediate situation during deformation existed when the sticking friction conditions were found in the central region and sliding friction conditions occurred towards the outer edges. The position, z_0 where the friction conditions changed was found by from eq A.12, see Ref. [127] for more details.

$$z_0 = \left(\frac{h}{2\mu}\right)\ln\left(\frac{1}{2\mu}\right) \qquad \textbf{eq A.12}$$

where h is the instantaneous thickness and μ is the friction coefficient. The methods reported by the good practice guide [127] summarized the conditions for friction found during a PSC test. These are shown through eq A.13-eq A.15.

- If $2z_0 > w$ (sliding friction)

$$\frac{p}{2k} = \frac{1}{bw}\left[\frac{2h^2}{\mu^2} + \frac{(b-w)h}{\mu}\right]\left[\exp\left(\frac{\mu w}{h}\right) - 1\right] - \frac{2h}{\mu b} \qquad \textbf{eq A.13}$$

- If $w > 2z_0 > 0$ (partial sticking friction)

$$\frac{p}{2k} = \frac{h}{\mu w}\left(\frac{1}{2\mu} - 1\right) + \frac{(w/2) - z_0}{\mu w} + \frac{\left[(w/2) - z_0\right]^2}{hw} + \frac{1}{\mu b}\left(\frac{2z_0^2}{w} - z_0 - \frac{2hz_0}{\mu w} + \frac{h}{2\mu} - h + \frac{h^2}{w\mu^2} - \frac{2h^2}{\mu w}\right) + \frac{1}{hb}\left(z_0^2 - \frac{4z_0^3}{3w} - \frac{w^2}{12}\right) \qquad \textbf{eq A.14}$$

- If $0 > z_0$ (sticking friction)

$$\frac{p}{2k} = 1 + \frac{w}{4h} - \frac{w^2}{12hb} \qquad \textbf{eq A.15}$$

These correction factors were applied to the test data through a computer programme, with z_0 calibrated at each data point throughout the deformation for the instantaneous thickness. This value was used to determine the appropriate friction conditions. The values of instantaneous thickness and breadth were then used according to the equations above and the shear stress, k was determined from the recorded values of p. The equivalent flow stress was then calculated from:

$$\sigma_{eq} = \frac{2k}{f} \qquad \textbf{eq A.16}$$

where f is the correction factor discussed previously.

Appendix B: Strain computations

The calculations presented in this section can also be found in Refs. [98] and [128]. The objective is to understand how the strains are computed in the software *CorrelManuV*.

B.1 Definition of the local strain

Let $\underline{X}$ be the position in a reference orthonormal coordinate system of a material point in the initial configuration of a three dimensional continuous medium and $\underline{x}$ its position in the same reference system in the current configuration. The gradient of the mechanical transformation at $\underline{X}$ is then:

$$\overline{\overline{F}} = \frac{\partial \underline{x}}{\partial \underline{X}}, \qquad \textbf{eq B.1}$$

where $\underline{X} = \begin{vmatrix} X \\ Y \\ Z \end{vmatrix}$ et $\underline{x} = \begin{vmatrix} x \\ y \\ z \end{vmatrix}$.

The Green-Lagrange strain tensor $\overline{\overline{\varepsilon_{GL}}}$ is defined as:

$$\overline{\overline{\varepsilon_{GL}}} = \frac{1}{2} \cdot (\overline{\overline{F}}^{t} \cdot \overline{\overline{F}} - \overline{\overline{I}}), \qquad \textbf{eq B.2}$$

where $\overline{\overline{I}}$ is the unit tensor and ^{t} denotes the transposition. $\overline{\overline{\varepsilon_{GL}}}$ depends non-linearly on $\overline{\overline{F}}$, but for small strains it may be approximated by its linearized counterpart:

$$\overline{\overline{\varepsilon_{lin}}} = \frac{1}{2} \cdot (\overline{\overline{F}}^{t} + \overline{\overline{F}}) - \overline{\overline{I}}. \qquad \textbf{eq B.3}$$

B.2 Average strain over a domain

Let Ω be a given regular domain of the initial configuration, which might be multiply connected. Let $\partial\Omega$ be its regular edge, with outer normal $\underline{n}$, and V_Ω its volume. The average transformation gradient over Ω is given by:

$$\overline{\overline{\langle F \rangle_\Omega}} = \frac{1}{V_\Omega} \cdot \int_\Omega \overline{\overline{F}} dV_\Omega. \qquad \textbf{eq B.4}$$

This volume integral may be transformed into a surface integral according to Green's formula:

$$\overline{\overline{\langle F \rangle}}_{\Omega} = \frac{1}{V_{\Omega}} \cdot \int_{\partial\Omega} \underline{x} \otimes \underline{n} \; da . \qquad \text{eq B.5}$$

The global Green-Lagrange strain tensor over Ω is:

$$\overline{\overline{\varepsilon_{GL\,\Omega}}} = \frac{1}{2} \cdot \left(\overline{\overline{\langle F \rangle}}_{\Omega}^{t} \cdot \overline{\overline{\langle F \rangle}}_{\Omega} - \overline{\overline{I}} \right). \qquad \text{eq B.6}$$

When Ω is a domain representative of the microstructure, $\overline{\overline{\varepsilon_{GL\,\Omega}}}$ is the macroscopic Green-Lagrange strain tensor. When Ω is the domain occupied by a given phase in such a representative domain, then $\overline{\overline{\varepsilon_{GL\,\Omega}}}$ is the average Green-Lagrange strain over this phase.

B.3 Computation of local strains

The relations described previously cannot be used to compute the local strains due to the following reasons:

- The coordinates are given in pixels along the orthogonal directions X and Y of the micrograph on the analyzer which has an hexagonal frame with a principal direction parallel to the horizontal direction of the micrograph (considered as the X-direction): this is not an orthonormal coordinate system.
- The magnification of the SEM may vary and the micrograph may be slightly distorted.
- The displacement is only known in a discrete way through the grid intersections, so that its local derivatives cannot be computed exactly.
- It is a two-dimensional measurement, only two coordinates are available, the Z-coordinate, orthogonal to the observation plane, cannot be measured directly.

In order to deal with these limitations, several corrections or assumptions have to be made.

- ✓ The pixel coordinates are changed into orthonormal coordinates by correcting the Y-coordinate with a constant factor, which is experimentally determined by comparing the length of a given detail on a micrograph, measured in pixels along direction X, and the length of the same detail after a 90° rotation, measured in pixels along direction X.
- ✓ The magnification of the SEM after deformation must be the same as before or a whole number multiple for all the micrographs. The distortions of the micrographs are neglected.

- ✓ The local transformation gradient at a given grid intersection p is computed as the average of the true local gradient over a small volume Ω_p around the grid intersection. The chosen volume is a cylinder with its axis orthogonal to the surface of the sample, height e arbitrarily small, and a polygonal upper surface Σ_p whose vertices are neighbours of the considered grid intersection (see Figure B.1). Let $\partial\Sigma_p$ be the boundary of Σ_p, $S_{\Sigma p}$ its area and $\underline{n}_{\Sigma p}$ its normal. Σ_{p-} is the lower surface of the cylinder.

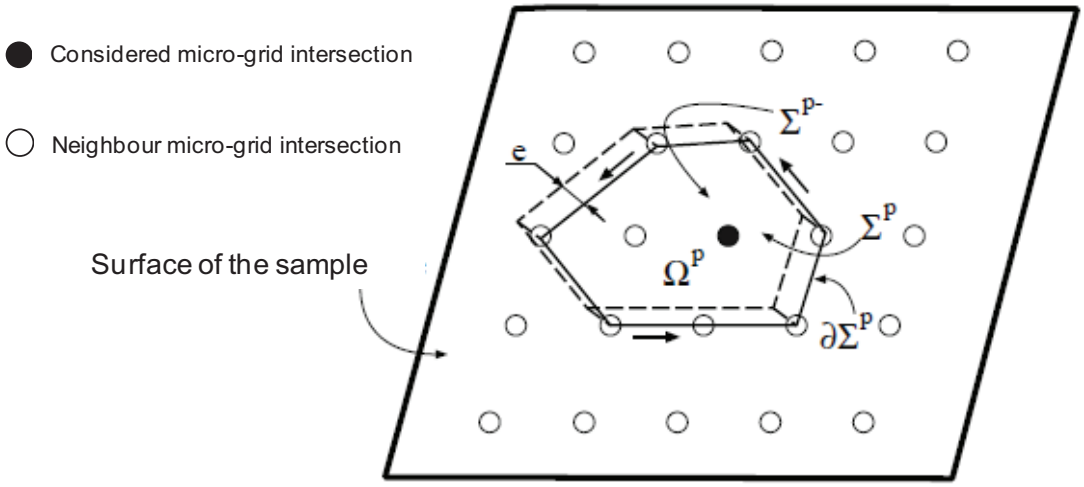


Figure B.1. Averaging volume for local strain computation [98].

Then, eq B.5 gives:

$$\overline{\overline{F}}_p = \left\langle \overline{\overline{F}} \right\rangle_{\Omega p} = \frac{1}{V_{\Omega p}} \cdot \int_{\partial\Omega p} \underline{x} \otimes \underline{n} \; ds \,, \qquad \textbf{eq B.7}$$

$$\overline{\overline{F}}_p = \frac{1}{S_{\Sigma p}} \cdot \left[\int_{\partial\Sigma p} \frac{\int_e \underline{x} de}{e} \otimes \underline{n} dl + \frac{\int_{\Sigma p} \underline{x} ds - \int_{\Sigma p-} \underline{x} ds}{e} \otimes \underline{n}_{\Sigma p} \right]. \qquad \textbf{eq B.8}$$

With e tending to 0, one gets then:

$$\overline{\overline{F}}_p = \frac{1}{S_{\Sigma p}} \cdot \left[\int_{\partial\Sigma p} \underline{x} \otimes \underline{n} dl + \frac{\partial \int_{\Sigma p} \underline{x} ds}{\partial \underline{n}_{\Sigma p}} \otimes \underline{n}_{\Sigma p} \right], \qquad \textbf{eq B.9}$$

since $\underline{x}$ is continuous.

Now, we assume that the surface of the unstrained sample is perpendicular to the observation axis Z. The components of $\overline{\overline{F}}_p$ in the Cartesian coordinate system XYZ are then:

$$F_p^{ij} = \frac{1}{S_{\Sigma p}} \cdot \left[\int_{\partial \Sigma p} x_i n_j dl + \frac{\partial \int_{\Sigma p} x_i ds}{\partial Z} (e_Z)_j \right], \qquad \text{eq B.10}$$

where e_Z is the unit vector along direction Z. $\partial \int_{\Sigma p} x_i ds / \partial Z$ would need a non-available three-dimensional information to be computed. Nevertheless the second part of expression vanishes for components F_p^{ij} with $j \neq Z$, since $(e_Z)_j$ vanishes. x_Z is not available either, so the components F_p^{Zj} cannot be computed. Finally, one gets the two-dimensional counterpart of equation for the in-plane components F_p^{ij} with $i \neq Z$ and $j \neq Z$ of the transformation gradient:

$$\overline{\overline{F}}_p = \frac{1}{S_{\Sigma p}} \cdot \int_{\partial \Sigma p} \underline{x} \otimes \underline{n} dl, \qquad \text{eq B.11}$$

$\underline{n}dl$ is constant on a segment of $\partial \Sigma_p$ and $\underline{x}$ is assumed to vary linearly from one extremal point of the segment to the other. Let N be the number of grid intersection on $\partial \Sigma_p$, $\underline{x}^q$ the coordinates of the q^{th} one, $\underline{n}^q$ the outer normal to the segment between grid intersection q and grid intersection $q+1$, dl^q the length of this segment. Equation can be rewritten as:

$$\overline{\overline{F}}_p = \frac{1}{2S_{\Sigma p}} \cdot \sum_{q=1}^{N} \left[\underline{x}^q + \underline{x}^{q+1} \right] \otimes \underline{n}^q dl^q, \qquad \text{eq B.12}$$

where superscript $^{q+1}$ is assumed equivalent to superscript ^{1}. Since the segments $\partial \Sigma_p$ have been assumed to belong to the XY plane, so does n^q. In fact, if the vertices of Σ_p are numbered counter-clockwise, the array of components of $\underline{n}^q dl^q$ is:

$$[\underline{n}^q dl^q] = \begin{bmatrix} Y^{q+1} - Y^q \\ -X^{q+1} + X \\ 0 \end{bmatrix}. \qquad \text{eq B.13}$$

Finally, one gets:

$$F_{XX} = \frac{1}{2S_{\Sigma p}} \cdot \sum_{q=1}^{N} (\underline{x}^q + \underline{x}^{q+1})(Y^{q+1} - Y^q) \ , \qquad \textbf{eq B.14}$$

$$F_{XY} = \frac{1}{2S_{\Sigma p}} \cdot \sum_{q=1}^{N} -(\underline{x}^q + \underline{x}^{q+1})(X^{q+1} - X^q) \ , \qquad \textbf{eq B.15}$$

$$F_{YX} = \frac{1}{2S_{\Sigma p}} \cdot \sum_{q=1}^{N} (\underline{y}^q + \underline{y}^{q+1})(Y^{q+1} - Y^q) \ , \qquad \textbf{eq B.16}$$

$$F_{YY} = \frac{1}{2S_{\Sigma p}} \cdot \sum_{q=1}^{N} -(\underline{y}^q + \underline{y}^{q+1})(X^{q+1} - X^q) \ . \qquad \textbf{eq B.17}$$

The area $S_{\Sigma p}$ of the polygon may be computed as:

$$S_{\Sigma p} = \frac{1}{2} \cdot \sum_{q=1}^{N} \begin{vmatrix} X^n & X^{n+1} \\ Y^n & Y^{n+1} \end{vmatrix} . \qquad \textbf{eq B.18}$$

There are several possible choices for Σ_p, see Figure B.2. “Scheme a” has the smallest possible averaging surface, but it is not centered on the considered grid intersection. “Scheme b” has the smallest centered averaging surface. “Schemes c and d” have larger averaging surfaces, so that they may smooth out local strain heterogeneities but their accuracy is better. Note that when the considered grid intersection is close to the edge of the region of interest, these schemes must be truncated to the available neighbor grid intersections.

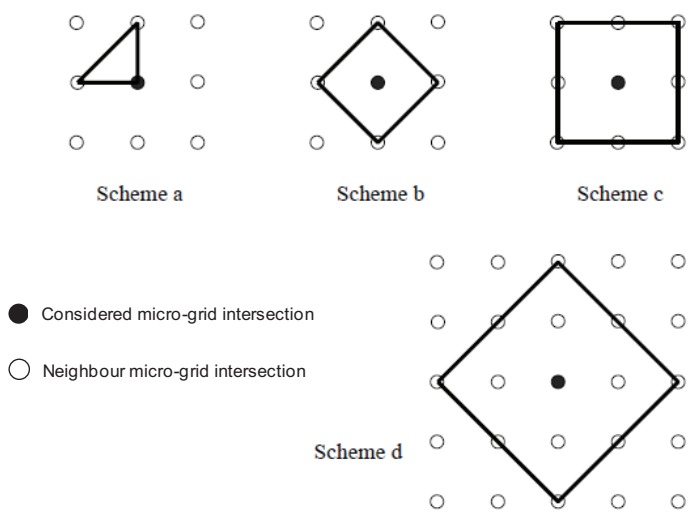


Figure B.2. Several possible integration schemes [98].

The knowledge of the in-plane components of $\overline{\overline{F}}_p$ allows computing the same components of the linearized strain tensor $\overline{\overline{\varepsilon}}_{lin\ p}$, according to eq B.3, without any approximation. However, the computation of the same components of the Green-Lagrange tensor needs the value of components F_{ZX} and F_{ZY} of $\overline{\overline{F}}_p$ which are unknown. So one has to assume these may be neglected. This assumption is satisfied if the surface of the deformed specimen is still plane and parallel to the surface before deformation; in particular, out-of-plane rotations are forbidden. This condition is locally not ensured because of the triaxiality of the strain state. Thus, the local Green-Lagrange tensor can only be computed in an approximate way.

It is also possible to calculate an equivalent strain, which is a measure of the distortions, but it requires the value of the unknown third out-of-plane value of the tensors.

Finally, one may decompose the strain gradient into rigid-body rotation tensor $\overline{\overline{R}}$ and symmetric stretch tensor $\overline{\overline{U}}$ as followed:

$$\overline{\overline{F}} = \overline{\overline{R}} \cdot \overline{\overline{U}}. \qquad \textbf{eq B.19}$$

$\overline{\overline{R}}$ gives the in-plane rotation angle of the transformation. The principal axes of the symmetric stretch tensor $\overline{\overline{U}}$ are those of $\overline{\overline{F}}$. Let λ_i be the eigenvalues of $\overline{\overline{U}}$; they permit to compute the principal stretches in any other deformation scale. The logarithmic deformation tensor has for instance the same principal axes as $\overline{\overline{U}}$, and its eigenvalues are $\ln(\lambda_i)$.

B.4 Computation of average strains

The procedure used to compute local gradients as averages over a small domain around a considered grid intersection can be used to calculate an average gradient over any polygonal domain. eq B.14-18 are still valid. In particular, the overall gradient is obtained when Σ is the entire representative domain.

The average gradient over a given phase may also be computed: $\partial\Sigma$ is then a polygonal line separating the grid intersections from a phase from the gird intersections of the other. The problem is that a such line is not exactly the interface between the phases and thus the obtained average is not exactly the average over the considered phase. In order to quantify the error related to this effect, two different separating polygonal lines are constructed: the first one has vertices that belong to the considered phase and will be called “without interface”; the second one’s vertices do not belong to the considered phase, except for grid intersections which are at the edge of the image and it will be referred as “with interface”. The sides of these polygonal lines belong to the octagonal graph associated to the square network of the grid intersections. Figure B. 3 shows an example of such lines.

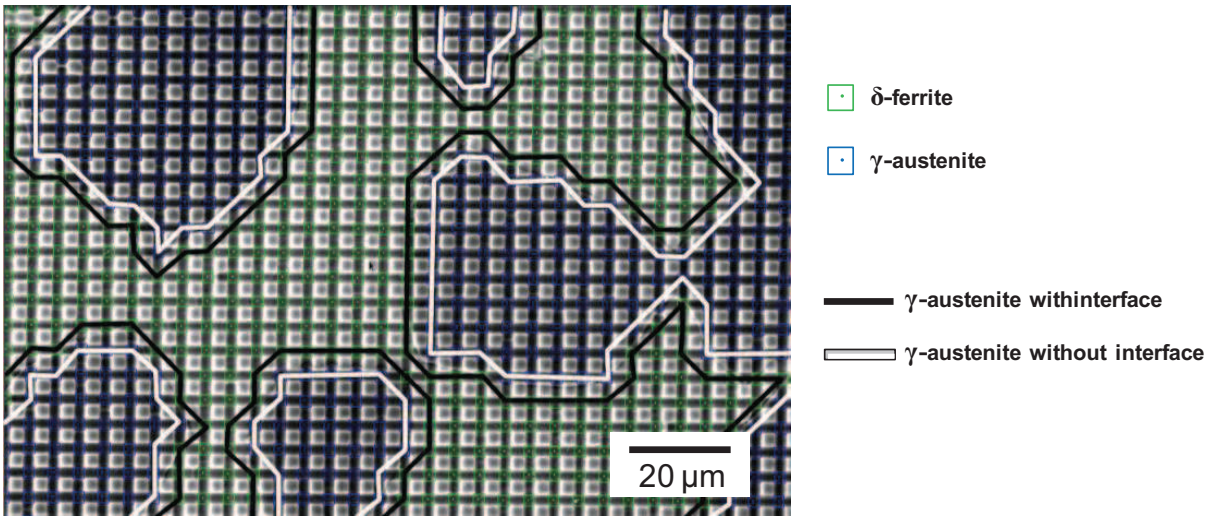


Figure B. 3. Integration scheme for the average gradient over a phase; two different polygonal lines are constructed: one called “without interface” and the other referred as “with interface”.

The average gradient components allow to compute the in-plane components of the average strain tensors $\overline{\overline{\varepsilon_{GL}}}$ and $\overline{\overline{\varepsilon_{lin}}}$. For $\overline{\overline{\varepsilon_{GL}}}$, one has still to assume that the unknown components vanish. However, for isotropy reasons, the average rotation of the phases should equal the global rotation of the specimen and the principal direction of the strain tensors should be parallel. If there is no global out-of-plane rotation, the average ZX and ZY components actually vanish and there is no approximation. When the Y direction is slightly shifted from the actual tensile direction, the XY component does not vanish; in such a case one has just to diagonalize the in-plane tensors to get the actual principal values. Average equivalent strains or strain tensors in any deformation scale can of course be computed as described previously without approximation.

Appendix C: Illustration of the microgrids

In the report, there are not a lot of SEM micrographs illustrating the microgrids. As a consequence it has been decided to show more micrographs of the microgrids before and after deformation.

C.1 Undeformed configuration

Figure C. 1-Figure C. 8 show large areas with engraved microgrids on both alloys D1 and D2 with different microstructures: Widmanstätten or equiaxed in their undeformed configuration.



Figure C. 1. High resolution SEM micrograph of the D1_W microstructure (map1) in the undeformed configuration; sample iii. The compression will be applied vertically.



Figure C. 2. High resolution SEM micrograph of the D1_W microstructure (map2) in the undeformed configuration; sample iii. The compression will be applied vertically.

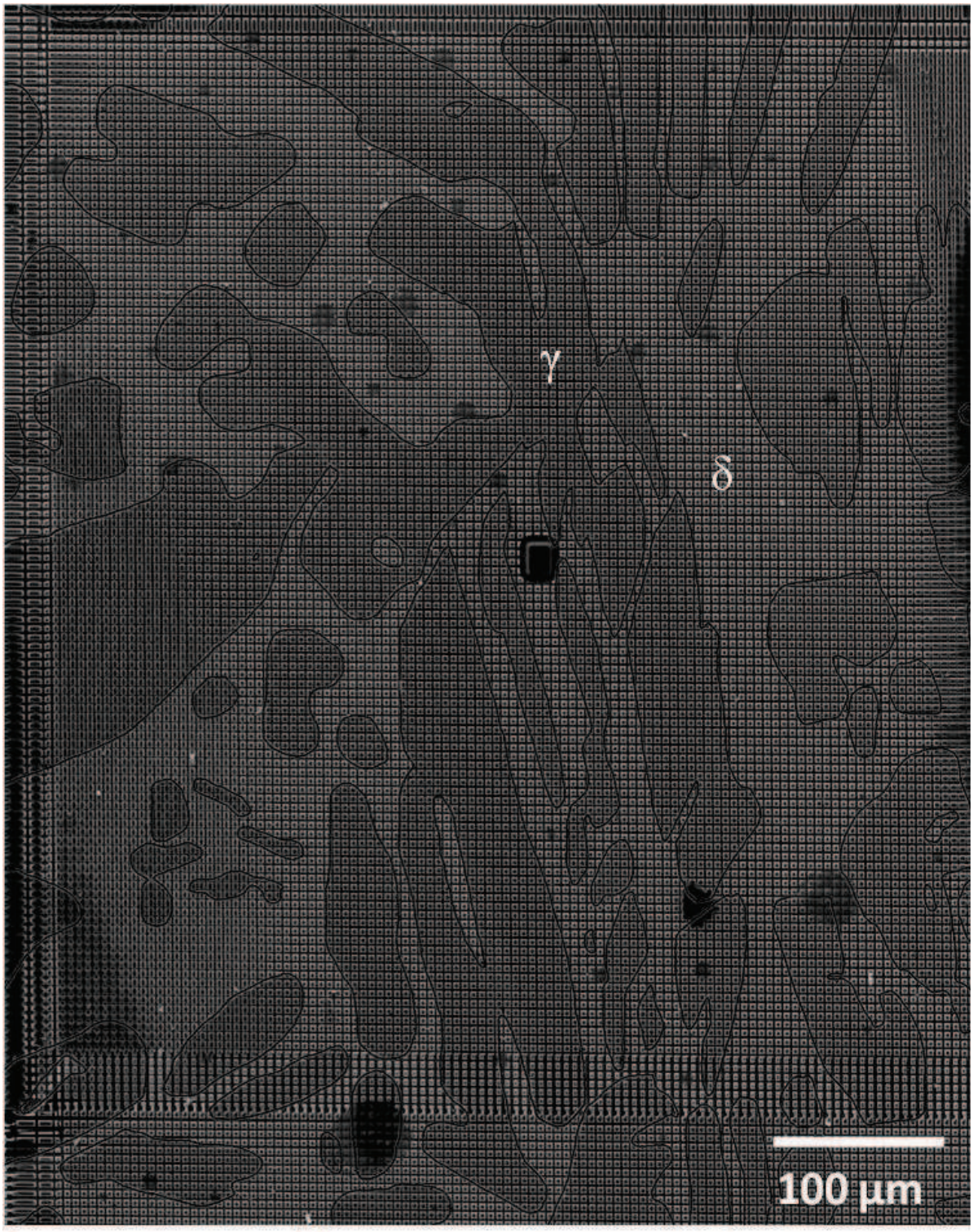


Figure C. 3. High resolution SEM micrograph of the D2_W microstructure (map1) in the undeformed configuration; sample III. The compression will be applied vertically.

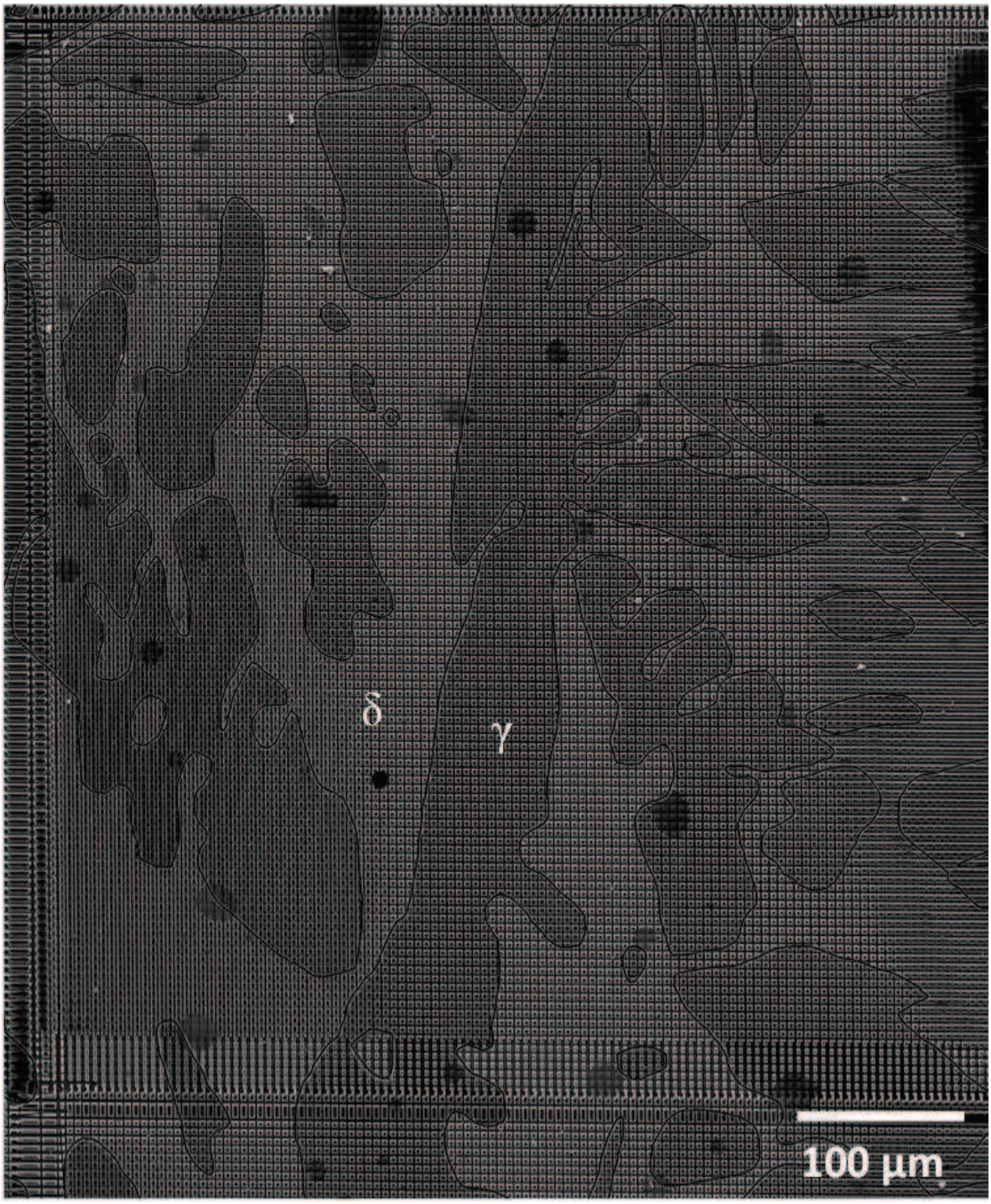


Figure C. 4. High resolution SEM micrograph of the D2_W microstructure (map2) in the undeformed configuration; sample III. The compression will be applied vertically.

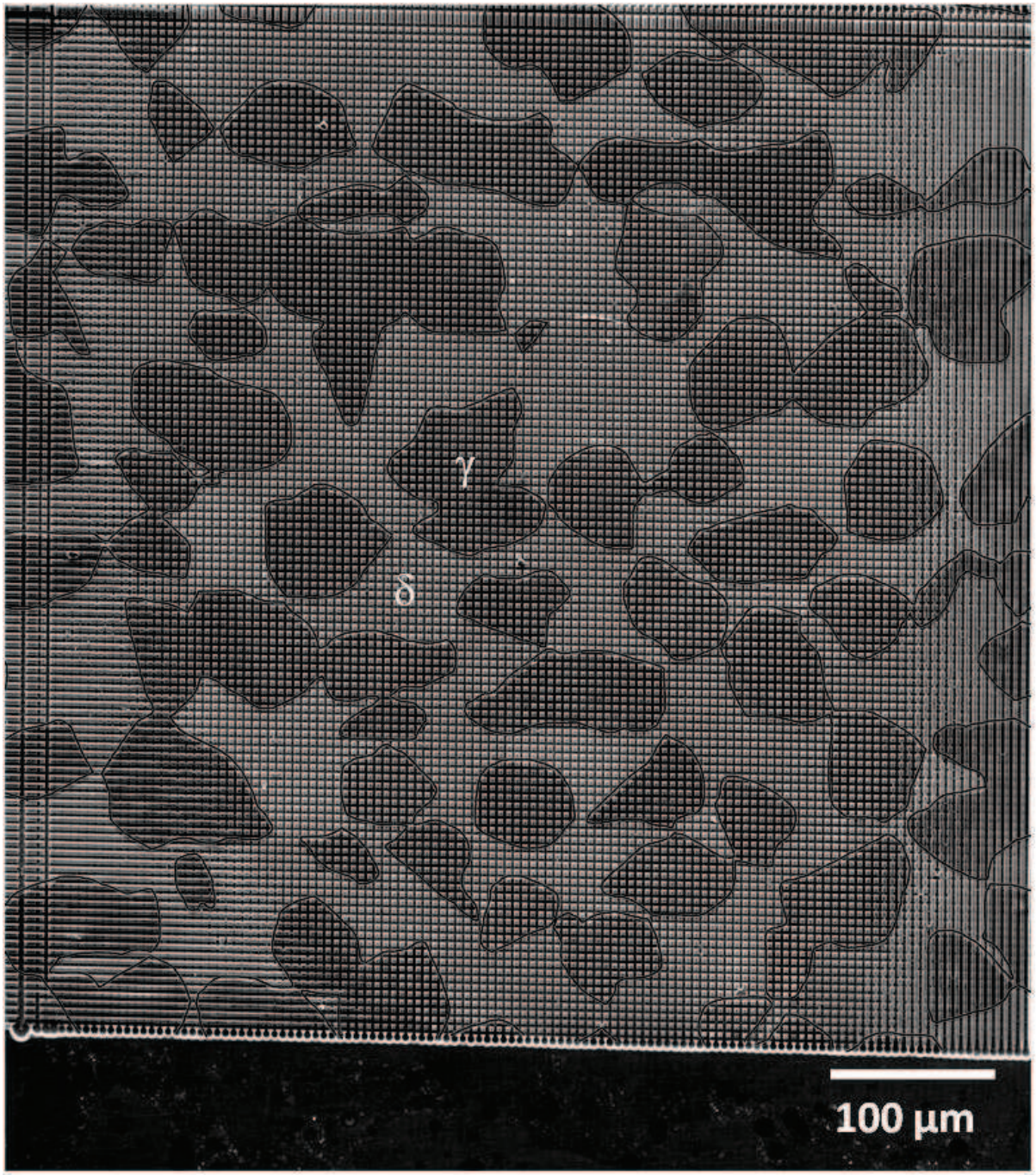


Figure C. 5. High resolution SEM micrograph of the D1_E microstructure in the undeformed configuration; sample B. The compression will be applied vertically.

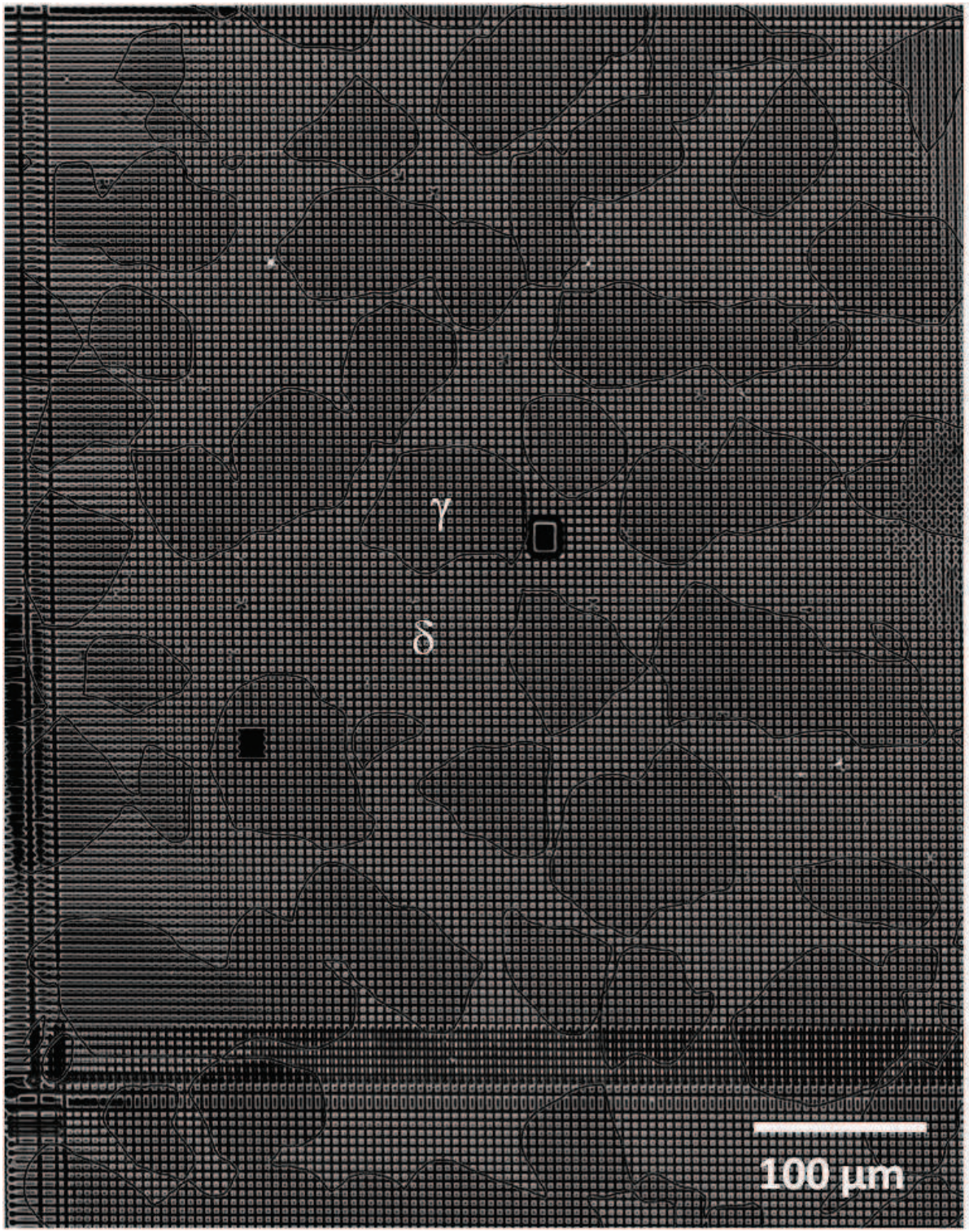


Figure C. 6. High resolution SEM micrograph of the D1_E microstructure in the undeformed configuration; sample A. The compression will be applied vertically.

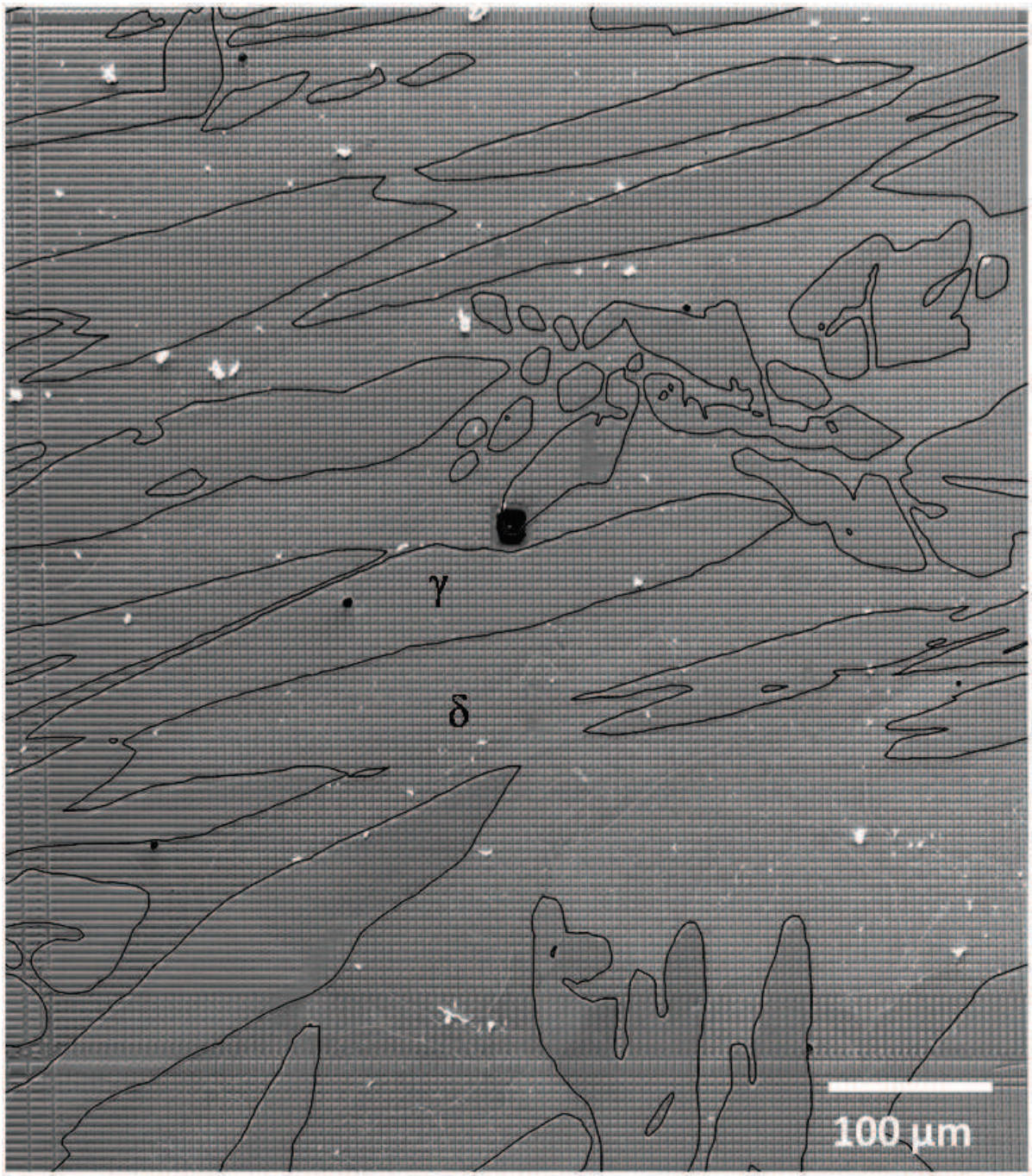


Figure C. 7. High resolution SEM micrograph of the D1_W microstructure in the undeformed configuration; sample ii. The compression will be applied vertically.

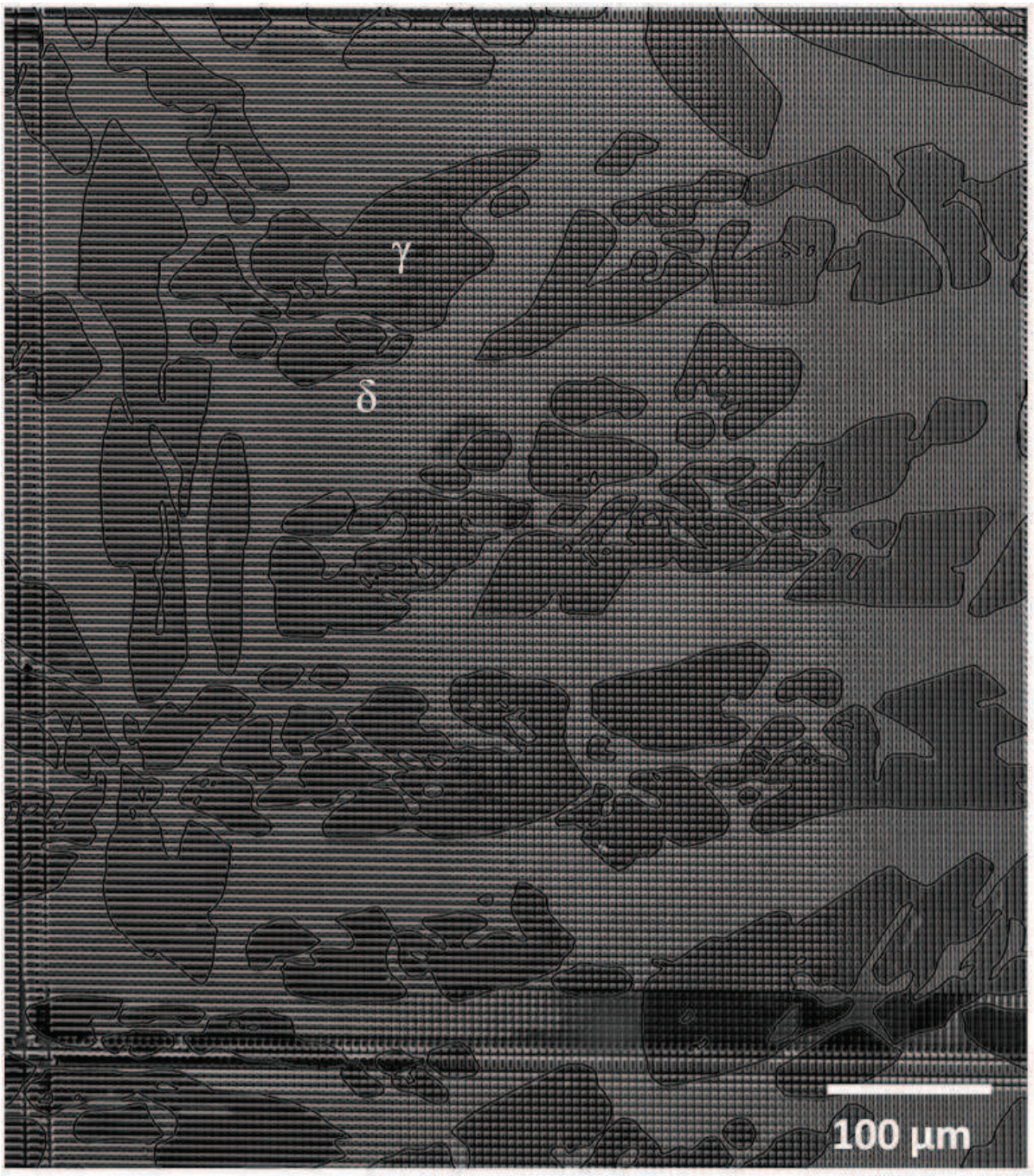


Figure C. 8. High resolution SEM micrograph of the D1_W microstructure in the undeformed configuration; sample iiii. The compression will be applied vertically.

C.2 Deformed configuration

In this section, several SEM micrographs illustrating microgrids after high temperature deformation from different samples are given. Small areas (see examples in Figure C. 9-Figure C. 12) as well as large areas (see examples in Figure C. 13-Figure **C. 15**) are shown in order to see the deformed microgrids at different scales.

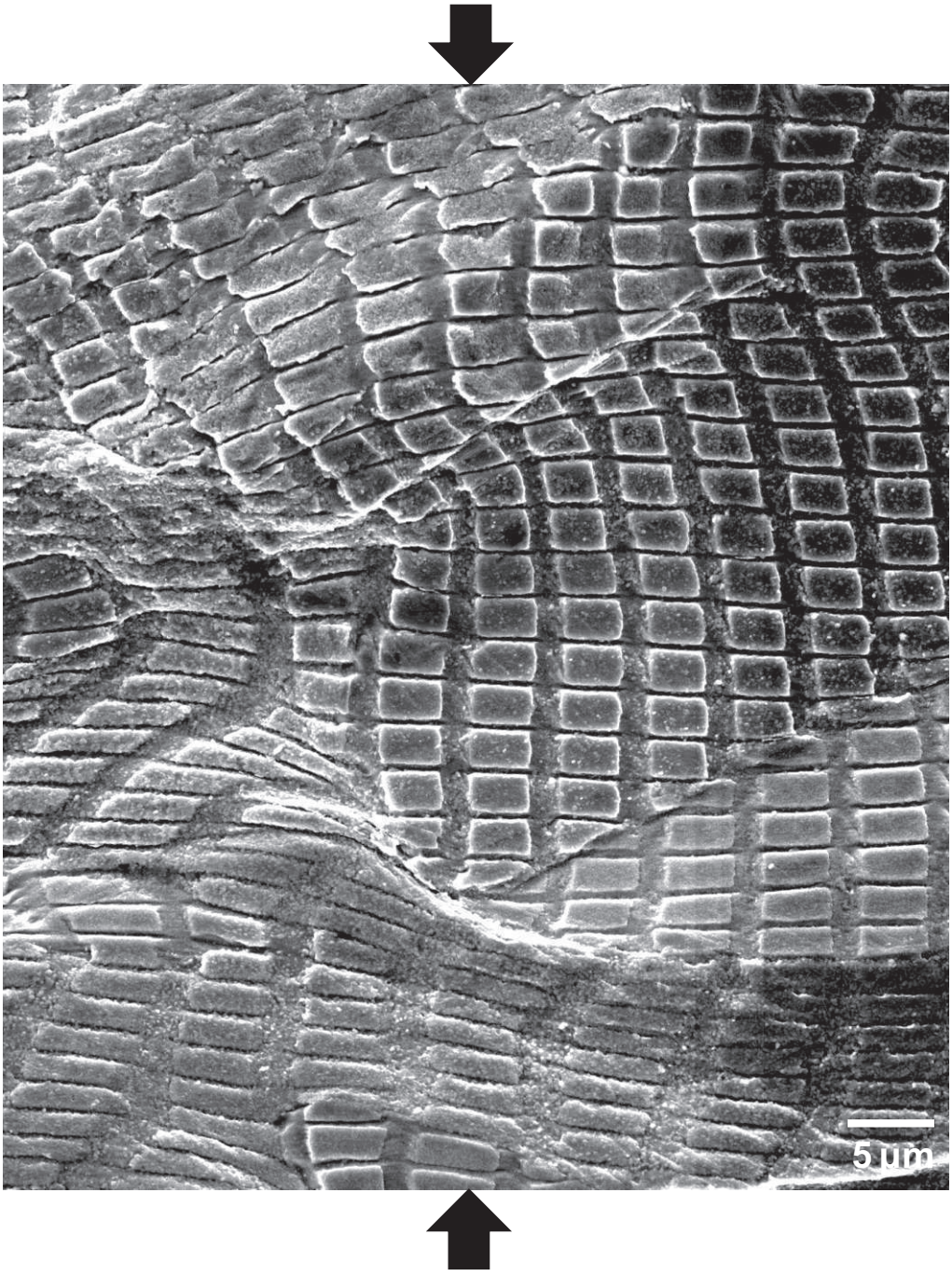


Figure C. 9. Small area from the deformed microgrid on sample III, D2_W microstructure, map1. The arrows indicate the loading direction.

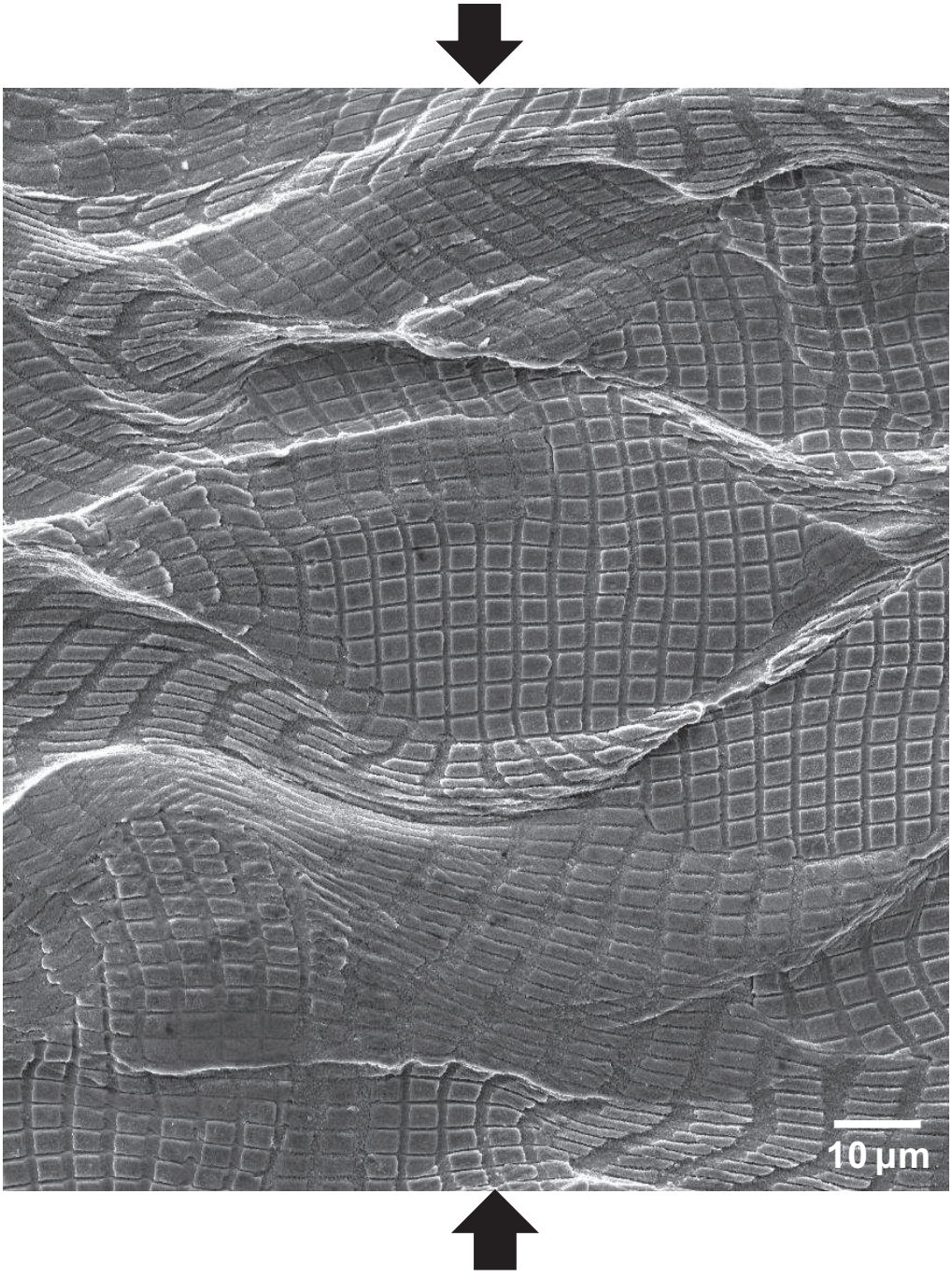


Figure C. 10. Small area from the deformed microgrid on sample III, D2_W microstructure, map1. The arrows indicate the loading direction.

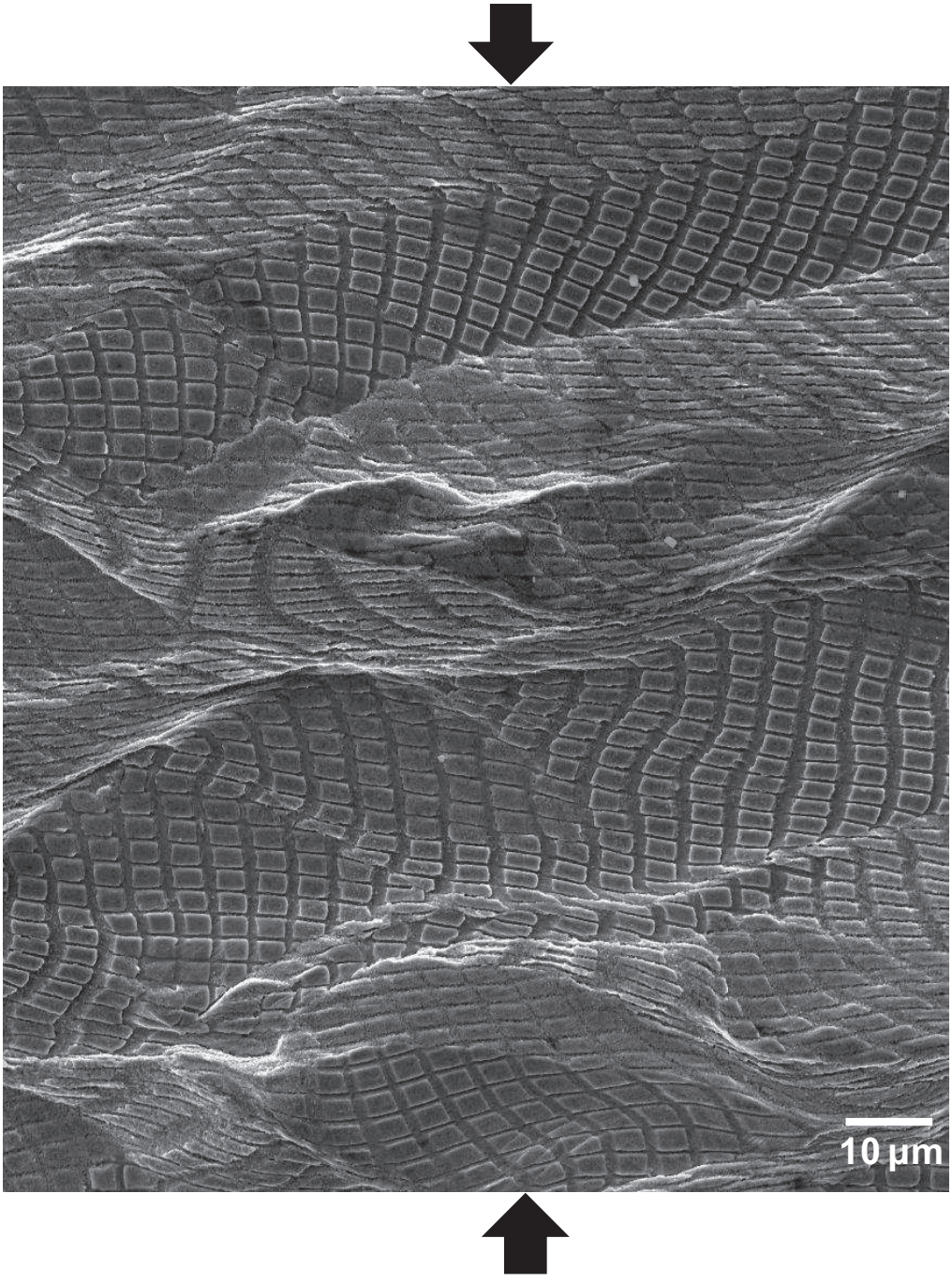


Figure C. 11. Small area from the deformed microgrid on sample III, D2_W microstructure, map2. The arrows indicate the loading direction.

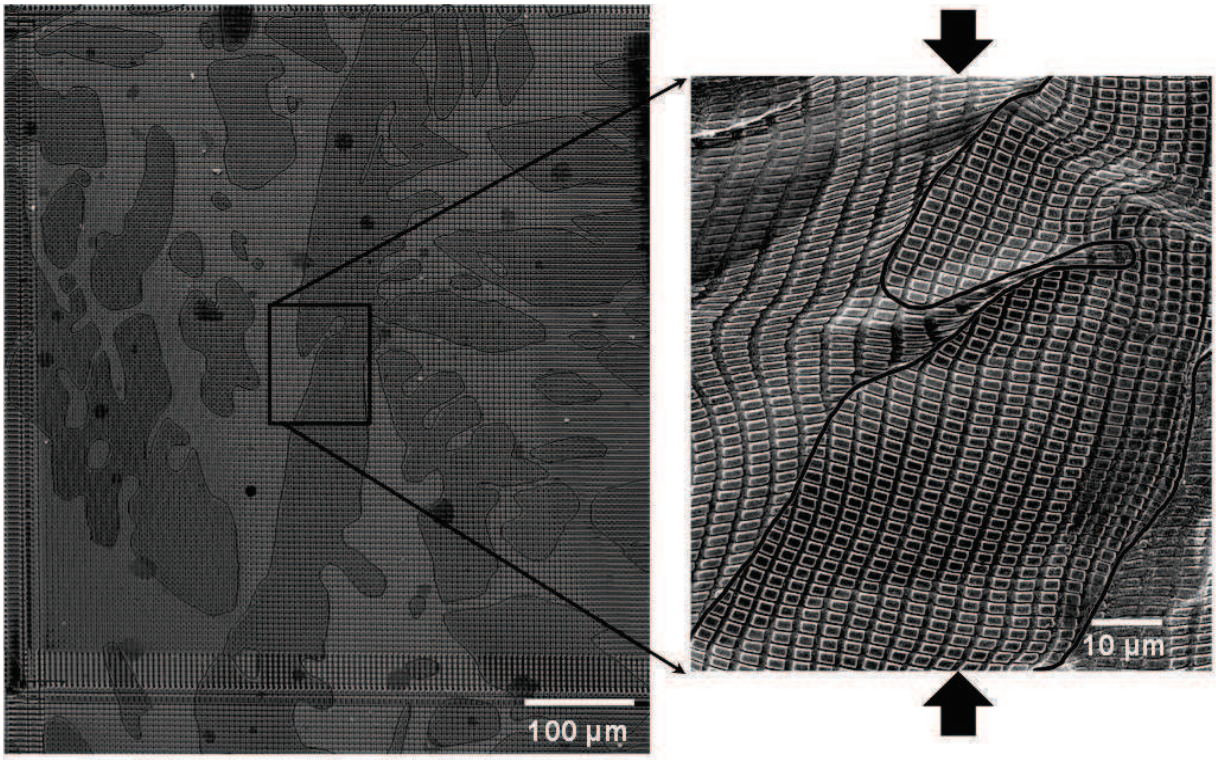


Figure C. 12. Undeformed state of the map2 of the D2_W microstructure and zoom of a part of the corresponding deformed microgrid. The arrows indicate the loading direction.

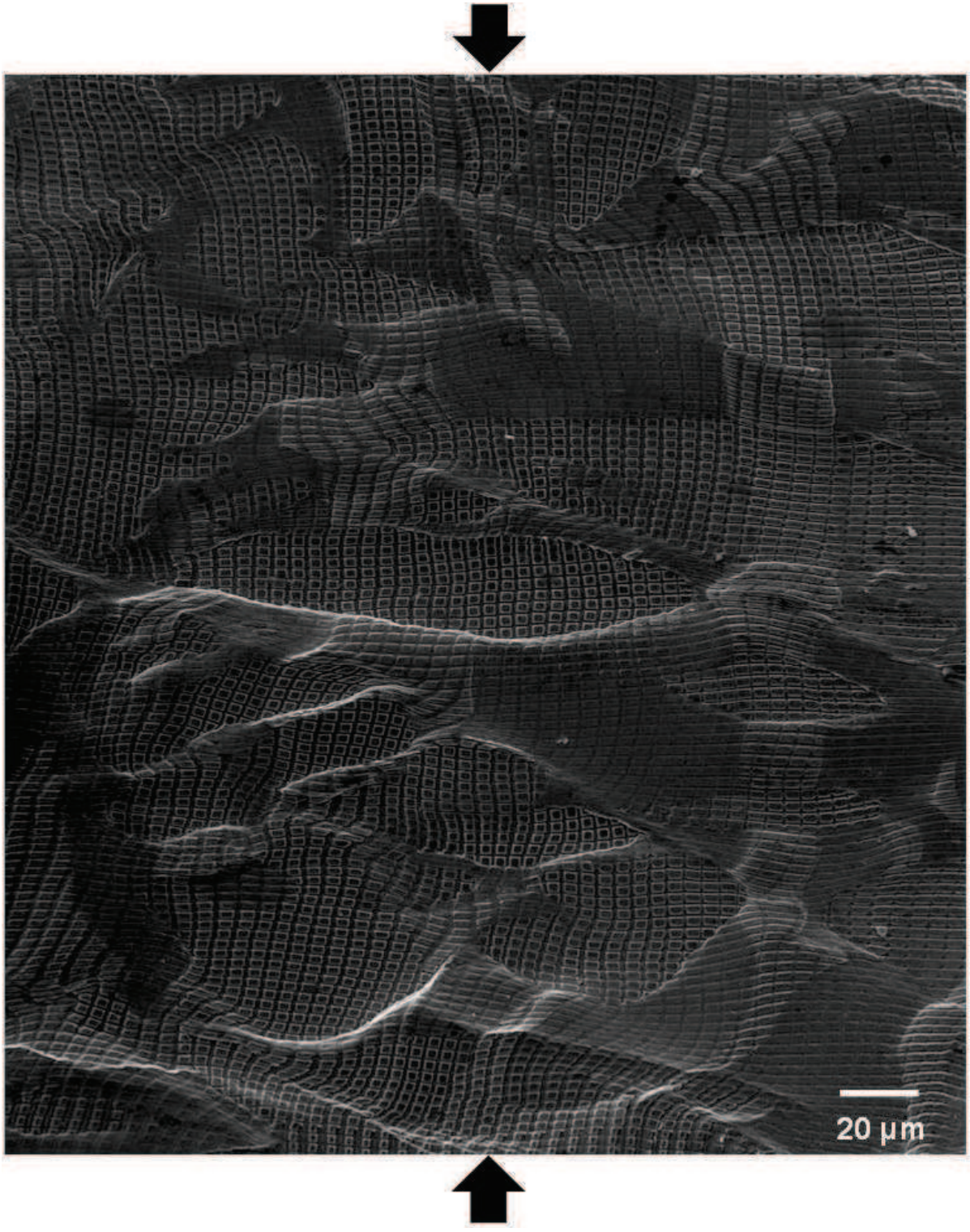


Figure C. 13. Large part of the deformed microgrid from sample III, D2_W microstructure. The arrows indicate the loading direction.

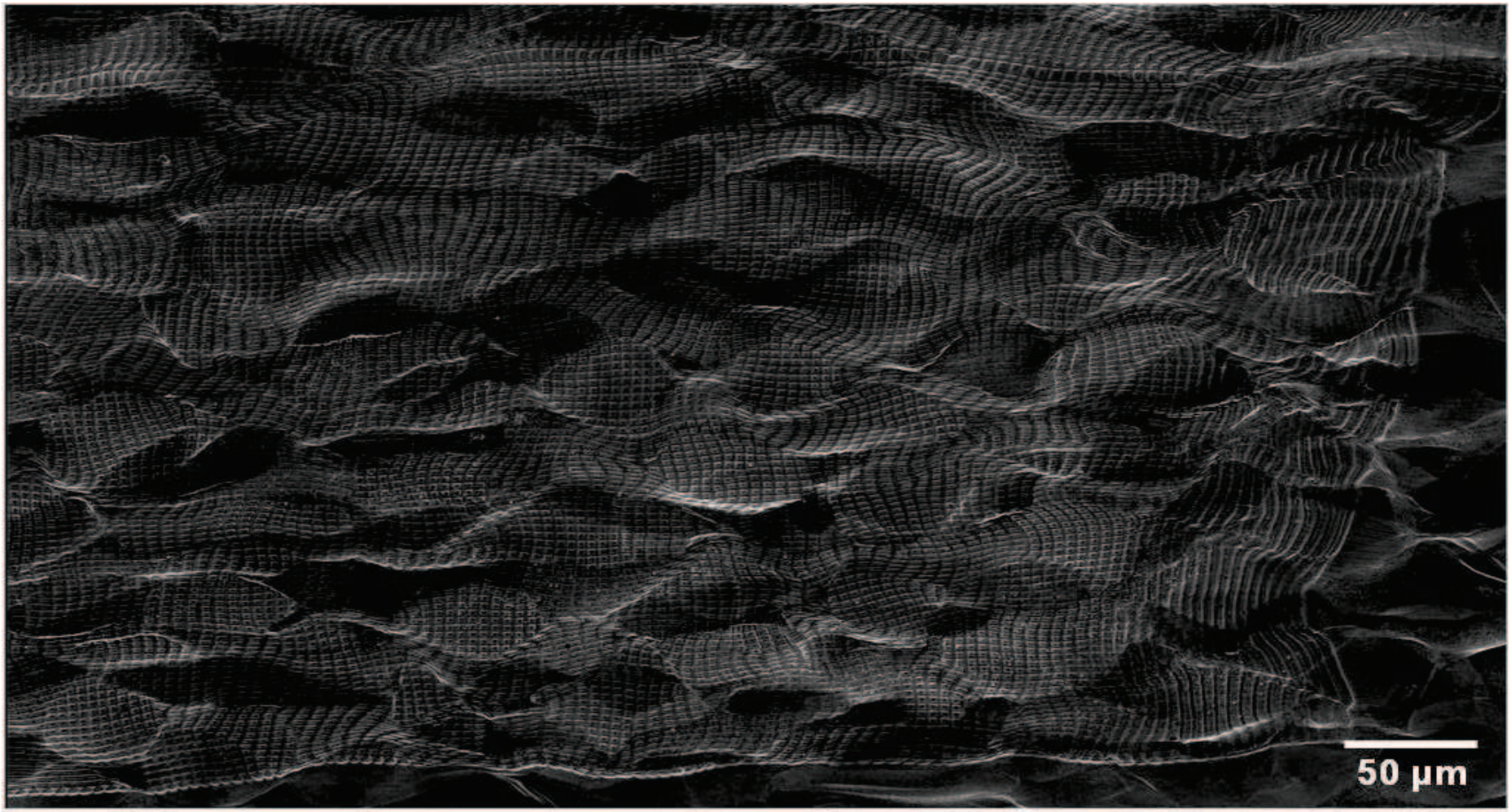


Figure C. 14. Microgrid of the D1_E microstructure from sample B after plane strain compression at 850°C.

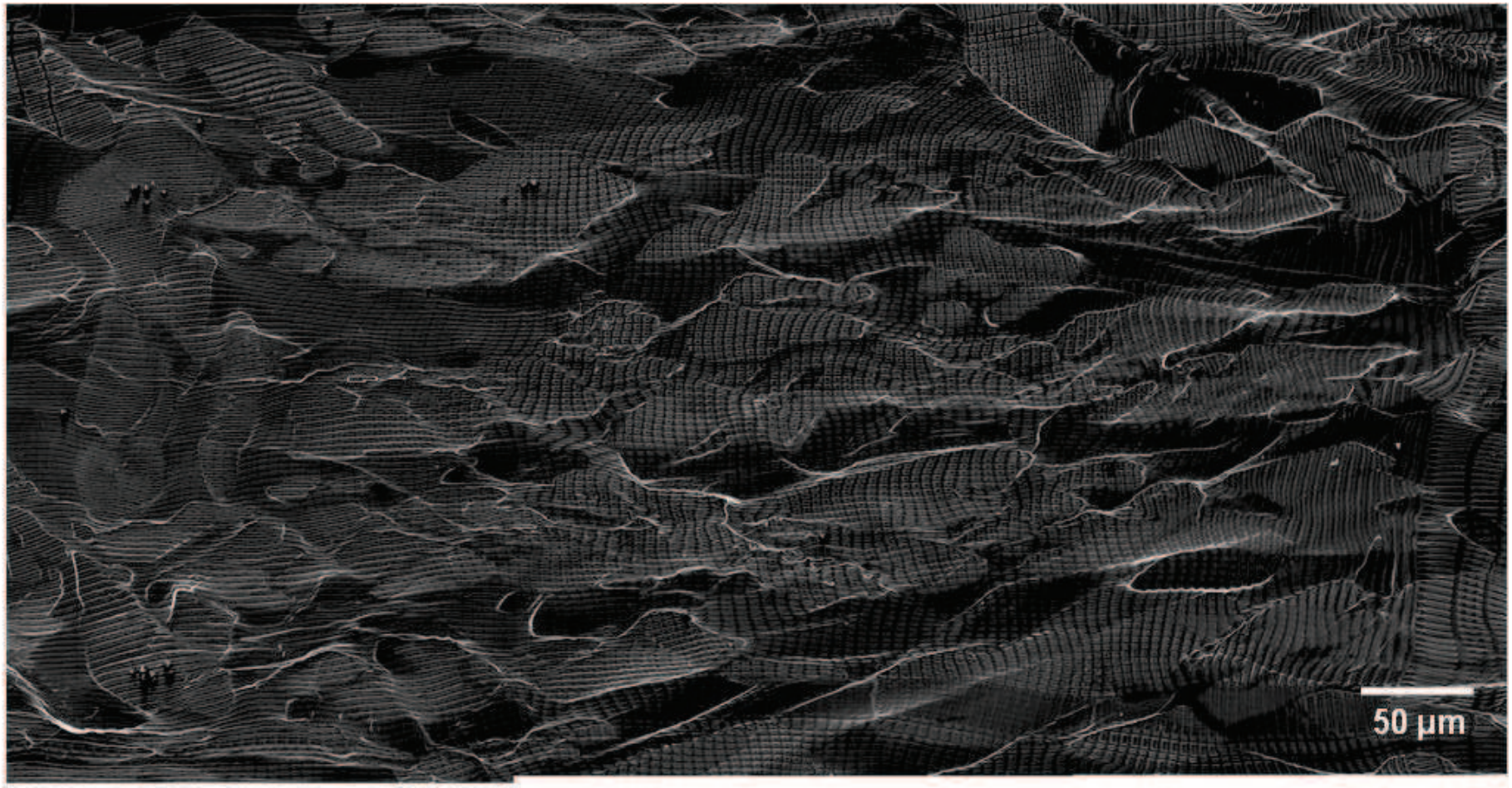


Figure C. 15. Microgrid of the D1_W microstructure from sample iiii after plane strain compression at 950°C.

Résumé étendu

Chapitre I. Introduction : Motivations scientifiques et industrielles. p11-20

Contexte

Nous proposons tout d'abord de décrire le contexte dans lequel s'inscrit ce travail. Les aciers inoxydables se distinguent de leurs cousins les aciers « carbone » par une teneur en chrome supérieure à 11% qui leur confère d'excellentes propriétés de résistance à la corrosion. Parmi les aciers inoxydables, il est possible de distinguer différentes familles :

- les aciers inoxydables ferritiques (≈0% Ni) ;
- les aciers inoxydables austéno-ferritiques ou dits « duplex » (≈5% Ni) ;
- les aciers inoxydables austénitiques (≈10% Ni). Les aciers austénitiques standards, à savoir le 304L et le 316L représentent à eux deux plus de 65% de part de marché.

Les aciers inoxydables austéno-ferritiques présentent par rapport aux nuances austénitiques standards de nombreux avantages :

(1) un coût matière première moins élevé en relation directe avec la quantité de nickel : entre 8-10 %Ni pour les austénitiques contre 2-5 %Ni pour les duplex, élément qui a vu son prix énormément fluctuer et augmenter au cours de ces dernières années ;

(2) une bonne tenue à la corrosion, au moins aussi bonne que les nuances austénitiques 304L et 316L;

(3) des caractéristiques mécaniques élevées, meilleures que les nuances austénitiques standards.

L'ensemble de ces caractéristiques rendent les aciers inoxydables austéno-ferritiques compétitifs vis-à-vis des nuances austénitiques standards et se posent en candidats sérieux pour, à court terme, remplacer les nuances 304L et 316L dans un certain nombre d'applications. Néanmoins, la situation n'est pas aussi idéale car les coûts de production de tôles en aciers inoxydables austéno-ferritiques demeurent, à ce jour, très élevés notamment à cause des problèmes de forgeabilité qui surviennent lors du procédé de laminage à chaud. Cette forgeabilité médiocre rend la fabrication de tôles particulièrement critique. En effet, le phénomène de criques de rive se produit fréquemment, il consiste en une fissuration des bords des tôles, voir illustrations Fig 1. Par conséquent, il est souvent nécessaire d'ajouter une étape au procédé qui consiste à venir cisailler les parties endommagées des tôles. Une telle opération a bien entendu un coût non négligeable, ceci explique en partie pourquoi les aciers inoxydables austéno-ferritiques peinent à se développer et à gagner des parts de marché malgré leurs nombreux atouts.



a) **b)**

Fig 1. Illustrations du phénomène de criques de rives.

D'un point de vue industriel, s'intéresser à la forgeabilité des aciers inoxydables austéno-ferritiques doit permettre de répondre à des questions d'ordre plus général comme l'endommagement des matériaux ductiles biphasés. L'objectif est d'abord de développer de nouveaux outils afin de mieux appréhender les relations entre le procédé, la microstructure et les propriétés mécaniques. *In fine*, le but est de formuler quelques recommandations concernant le procédé (élaboration, affinage, réchauffage, laminage à chaud), ou la composition chimique des nuances (fractions volumiques des phases et rhéologies des phases) afin d'éliminer ou au moins de limiter la formation de criques de rive.

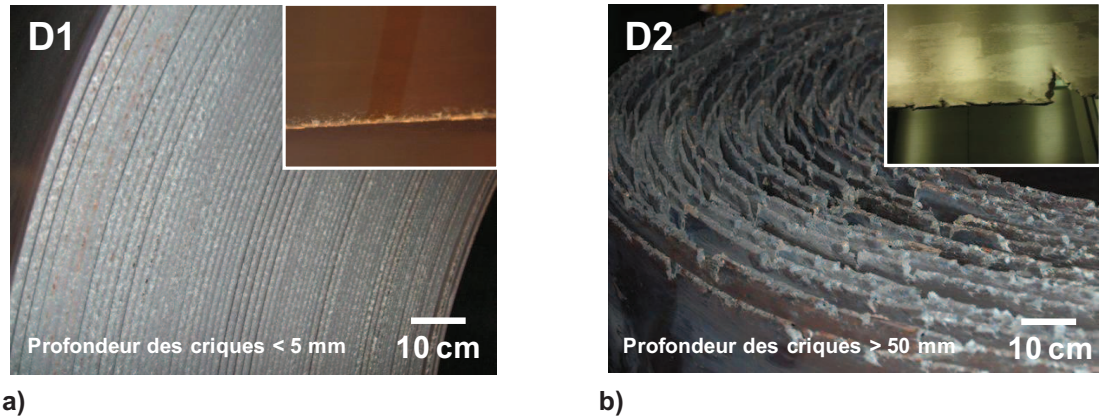
Matériaux et microstructures

Après avoir exposé le contexte de cette étude, les matériaux et les microstructures sont brièvement présentés. Nous nous sommes intéressés à deux nuances différentes d'acier inoxydable austéno-ferritiques qui diffèrent par leur composition chimique, notamment en Ni et Mo (Tableau 1) : l'acier que nous appellerons D1 et qui correspond à l'acier commercial EN. 1.4462 ; et l'acier que nous dénommerons D2 qui est issue d'essais industriels.

	%Cr	%Ni	%Mo	%Mn	%Si	%Cu	%C	%N
D1	22.90	5.59	3.11	1.75	0.55	0.19	0.02	0.17
D2	21.96	2.99	0.91	2.88	0.39	0.67	0.03	0.18

Tableau 1. Composition chimique en pds% des deux nuances d'aciers duplex étudiées.

Notre choix s'est porté sur ces deux aciers car ils présentent une sensibilité très différente vis-à-vis du phénomène de criques de rive. En effet, l'acier D1 est considéré comme un cas « quasi-idéal » car il n'est pas systématiquement affecté par les criques de rives et lorsqu'il l'est, les criques se propagent seulement sur des distances inférieures à 5 mm, voir Fig 2a. *A contrario*, l'acier D2 représente le cas critique puisque les criques peuvent affecter les tôles sur des distances pouvant atteindre plusieurs centimètres, voir Fig 2b. La comparaison de ces deux aciers doit permettre de mettre en évidence certains paramètres clés impliqués dans le phénomène de criques de rive.



a) b)

Fig 2. Bobines à l'issue des étapes de laminage à chaud montrant différents degrés de sensibilité aux criques de rives ; a) bobine de l'acier D1 avec des criques dont la profondeur ne dépasse pas 5 mm ; b) bobine de l'acier D2 sur laquelle les criques peuvent atteindre plusieurs centimètres.

Nous présentons ensuite des observations micrographiques effectuées à l'issue de chaque étape du procédé d'élaboration de produits plats en acier duplex, voir Fig 3: microstructures typiques des brames brutes de solidification et microstructures typiques pendant le laminage à chaud ; dans la partie centrale des tôles et aussi proche des rives, régions au niveau desquelles les premiers signes d'endommagement apparaissent.

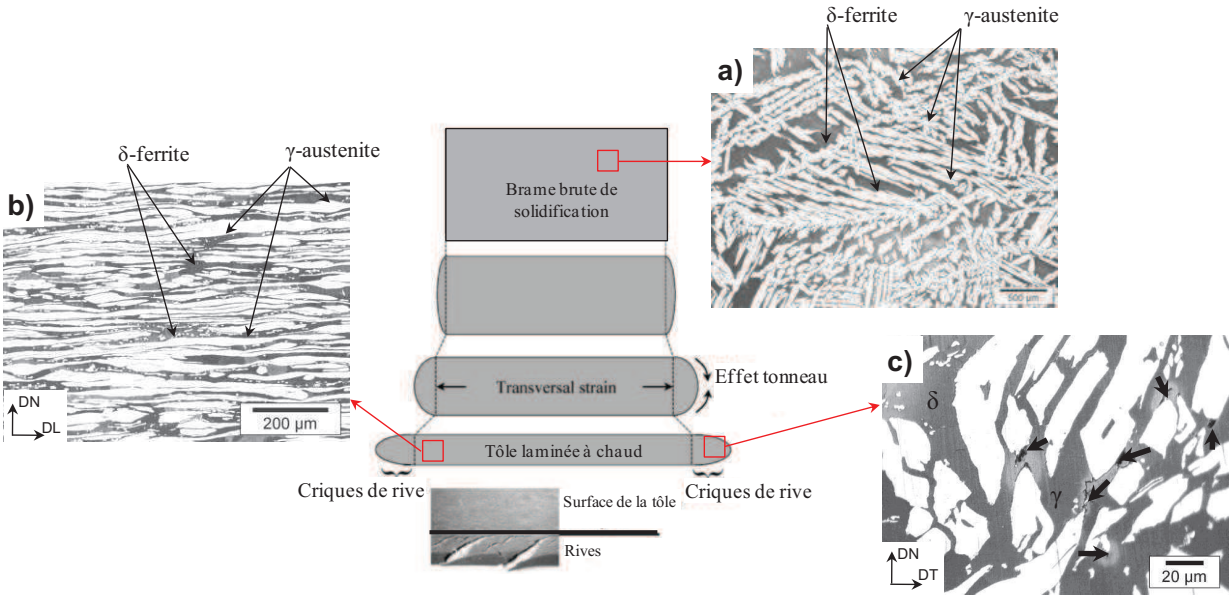


Fig 3. Illustration avec l'acier D2 des microstructures présentes aux différentes étapes du procédé de laminage à chaud industriel ; a) microstructure typique de la brame brute de coulée ; b) microstructure typique au centre de la tôle laminée à chaud avec un alignement des îlots d'austénite dans la direction de laminage ; c) microstructure de la tôle laminée proche des rives (zone endommagée) les cavités sont pointées par des flèches.

Stratégie adoptée

Nous proposons d'expliciter la stratégie qui a été adoptée pour répondre à la problématique des criques de rive. En premier lieu, nous avons effectué une large revue bibliographique, pour cibler l'ensemble des facteurs affectant la forgeabilité des aciers inoxydables austéno-ferritiques. Cet état de l'art sur la déformation à chaud des aciers duplex est exposé dans le Chapitre II. Cette revue de la littérature doit permettre d'identifier des « zones d'ombres » c'est-à-dire les points qui nécessitent des compléments ou des approfondissements. Nous avons notamment relevé deux « zones d'ombres ».

(1) Si dans la littérature il existe différents essais pour évaluer l'aptitude à la mise en forme à chaud, les techniques existantes ne permettent en aucun cas de discriminer le comportement des différentes nuances ou microstructures vis à vis du phénomène de criques de rive. Nous suggérons d'utiliser le concept de travail essentiel de rupture et de l'adapter à haute température pour discriminer les différents alliages en termes de sensibilité à la crique, cela fait l'objet du Chapitre III.

(2) Par ailleurs, il est souvent mentionné que la mauvaise forgeabilité de ces aciers provient de la différence de comportement mécanique entre la ferrite et l'austénite lors des traitements thermomécaniques. Néanmoins, il y a peu de preuves qualitatives, et aucune données quantitatives au sujet de la partition des déformations entre la ferrite et l'austénite dans des conditions représentatives des opérations de mise en forme à chaud. Nous avons ainsi adapté une technique de microgrille dans le but d'apporter de nouvelles informations à propos de la distribution des déformations à l'échelle de la microstructure, les résultats et les discussions qui en découlent sont présentés au Chapitre IV.

Les outils présentés et utilisés dans les chapitres III et IV pour comparer l'acier D1 à l'acier D2 permettent de donner quelques remèdes pour supprimer ou au moins réduire la formation de criques de rive (Chapitre V).

Chapitre II. Etat de l'art sur la déformation à chaud des aciers inoxydables austéno-ferritiques. p21-44

L'objectif de ce chapitre est d'établir l'état de l'art touchant au formage à chaud des aciers inoxydables austéno-ferritiques. Il se décline en trois grandes parties : la première traite des évolutions microstructurales observées lors des traitements thermomécaniques, la seconde se focalise sur le comportement mécanique des aciers inoxydables austéno-ferritiques lors de la mise en forme à chaud et enfin la troisième s'intéresse plus particulièrement aux aspects « endommagement ».

Evolution microstructurale au cours du formage à chaud

La première partie de ce chapitre retrace l'évolution des microstructures à partir de l'état brut de solidification jusqu'au stade de tôle laminée. Les différents micro-mécanismes impliqués dans l'évolution des microstructures sous l'effet des traitements thermomécaniques sont recensés : glissement au niveau des joints d'interphase δ/γ, rotation des grains d'austénite, développement de bandes de cisaillement etc. Certains de ces phénomènes sont illustrés à la Fig 4. L'importance du caractère incohérent ou cohérent des joints d'interphase δ/γ est également soulignée. Du point de vue de la déformation plastique, les deux phases montrent un comportement très différent : la phase ferritique s'adoucit via le phénomène dit de « recristallisation dynamique continue » pendant que l'austénite s'écrouit, les traces de recristallisation dynamique étant plutôt rares.

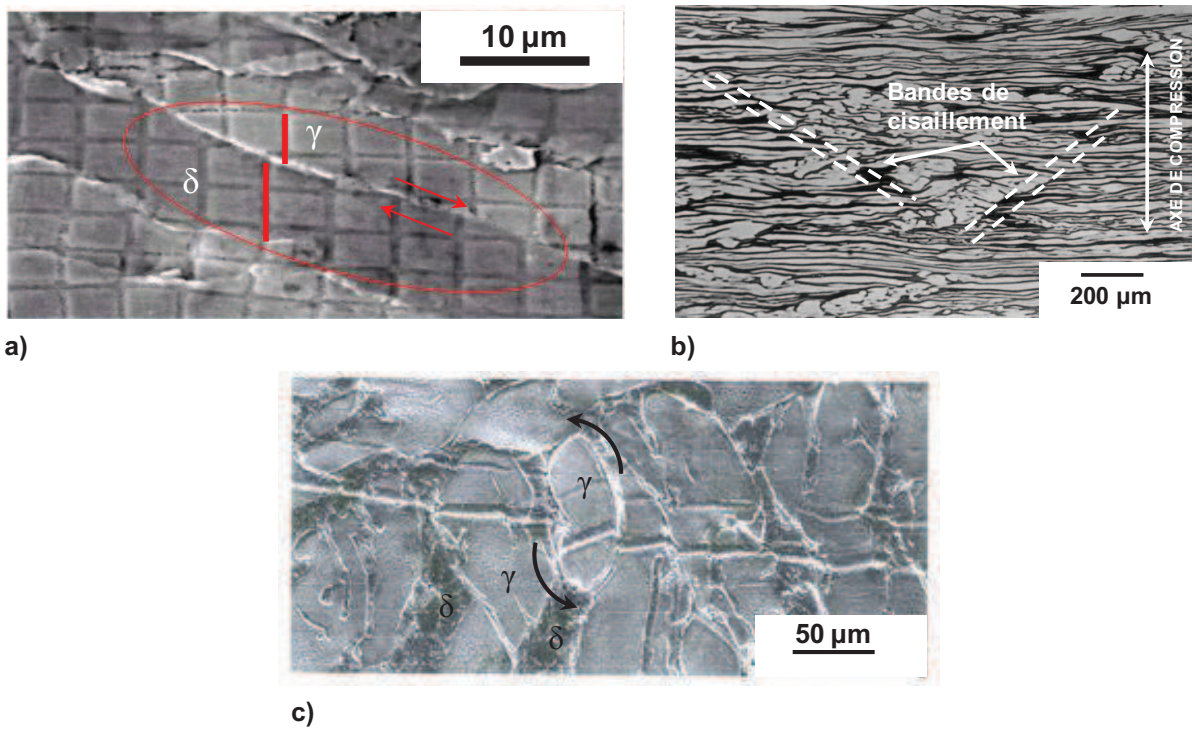


Fig 4. Illustrations de plusieurs micro-mécanismes affectant la déformation à chaud des aciers inoxydables austéno-ferritiques ; a) glissement aux joints d'interphase [14]; b) développement de bandes de cisaillement [16]; c) rotation de grains austénitiques [25].

Comportement mécanique lors du formage à chaud

La seconde partie de ce chapitre traite du comportement mécanique des aciers inoxydables austéno-ferritiques lors des opérations de mise en forme à chaud. Le comportement viscoplastique de plusieurs alliages est présenté ainsi que l'influence de la composition chimique, en particulier l'effet de la proportion des phases sur la loi de comportement à diverses vitesses de déformation. Il est souligné que la distribution des déformations semble hétérogène à l'échelle de la microstructure, cela motivera une part importante de la recherche, voir Chapitre IV notamment. L'influence de la morphologie des phases est aussi discutée tout comme l'influence du mode de chargement sur la loi de comportement mesurée, avec des différences notables entre les résultats de compression en état de déformation plane et les résultats obtenus en torsion.

Endommagement lors des étapes de mise en forme à chaud

Ce chapitre bibliographique se termine en passant en revue l'endommagement durant le laminage à chaud. Le paramètre conventionnellement utilisé pour caractériser la susceptibilité à l'endommagement est la déformation à rupture. La proportion des phases semble jouer un rôle prépondérant, puisque une fraction volumique de ferrite comprise entre 10 et 50% conduit à un minimum de ductilité, voir Fig 5.

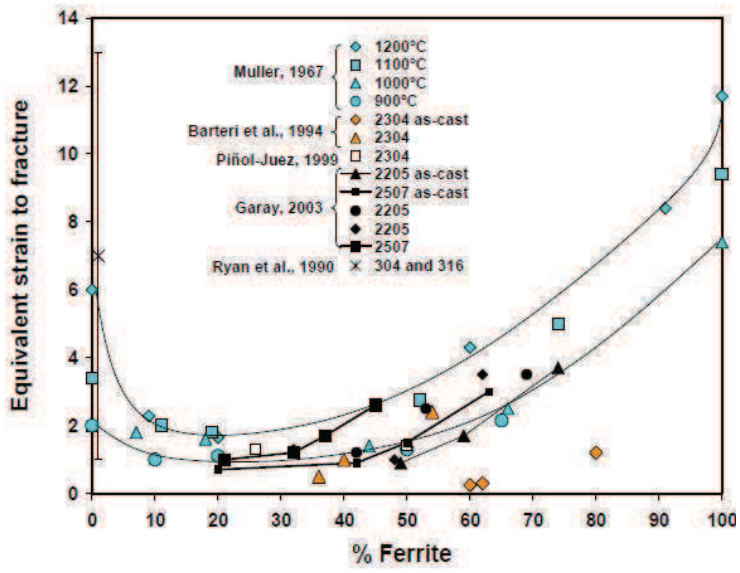


Fig 5. Influence de la fraction volumique de ferrite sur la deformation équivalente à rupture de différents aciers duplex [20].

Entre deux alliages ou deux microstructures présentant des proportions de phases voisines et dans la gamme 10-50% de ferrite, il semble très délicat de pouvoir discriminer leur comportement vis-à-vis de l'endommagement en utilisant comme critère la déformation à rupture. Il apparaît ainsi nécessaire de développer un nouvel essai permettant de discriminer ces microstructures. L'influence de la teneur en N est également pointée du doigt, puisque plus la teneur en azote est élevée, plus le risque de former des criques est important. Les températures plus élevées tendent par contre à les réduire voir même les supprimer. Les zones critiques sur lesquelles nous devons nous focaliser semblent être les interfaces δ/γ, car c'est ici que les déformations semblent se localiser et c'est aussi au voisinage de ces zones que les premières cavités germent.

Conclusion

Lorsque nous avons décris la stratégie proposée pour répondre à la problématique des criques de rives, nous avons précisé les deux points que nous avions identifiés comme étant cruciaux pour bien comprendre l'origine de la formation des criques. Ce travail de synthèse bibliographique a permis de mettre en avant ces deux points que nous rappelons rapidement ici.

(1) Si la littérature fait état de l'existence de plusieurs techniques pour déterminer la forgeabilité des matériaux métalliques, les essais disponibles ne permettent pas de discriminer le comportement des différentes microstructures en terme de résistance à la propagation de fissure, mécanisme qui gouverne pourtant la formation des criques. Il est donc nécessaire de développer un nouvel essai qui serait discriminant en termes de sensibilité aux criques, c'est l'objet du chapitre III.

(2) A ce jour, s'il est souvent mentionné que la mauvaise forgeabilité de ces aciers provient au moins partiellement de la différence de comportement mécanique entre la ferrite et l'austénite lors des traitements thermomécaniques, aucune preuve irréfutable et aucune donnée quantitative ne sont disponibles dans la littérature au sujet de la partition des déformations entre la ferrite et l'austénite. Nous avons ainsi utilisé une technique de micro-grille modifiée dans le but de fournir des informations qualitatives et quantitatives à propos de la distribution des déformations à l'échelle de la microstructure, le chapitre IV se focalise sur ces aspects.

Chapitre III. Résistance au déchirement ductile à haute température. p45-96

Présentation du concept de travail essentiel de rupture (ou méthode EWF)

La revue bibliographique a mis en évidence que les essais de forgeabilité standards ne permettaient pas de discriminer le comportement des différents aciers austéno-ferritiques vis à vis de l'endommagement. Par exemple, nous ne voyons pas de différence entre les aciers D1 et D2 sur les courbes de forgeabilité, voir Fig 6. De plus, dans la gamme de température qui correspond au laminage à chaud industriel (1000-1250°C), nous nous trouvons au-delà du critère de forgeabilité, nous ne devrions donc pas rencontrer de problèmes de ductilité lors de la mise en forme. Les observations montrent pourtant la formation de criques, ceci conforte l'idée que les essais standards ne conviennent pas dans le cas présent.

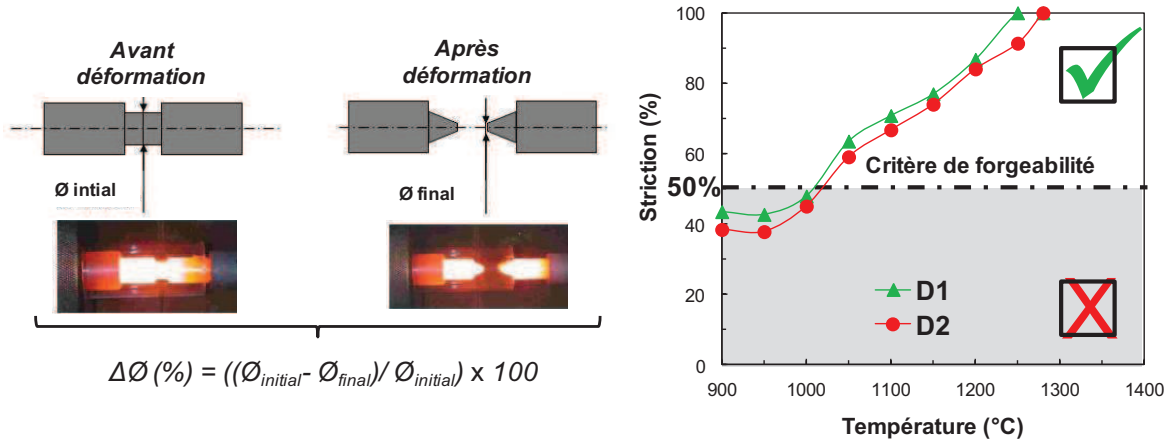


Fig 6. Principe de l'essai de forgeabilité standard et résultat d'un tel essai sur nos deux alliages D1 et D2.

Nous avons alors utilisé le concept du travail essentiel de rupture (Essential Work of Fracture : EWF) afin de caractériser la résistance à la propagation de fissure. Ce chapitre s'ouvre sur la présentation du concept de travail essentiel de rupture et sur la méthode expérimentale de mesure au moyen d'éprouvettes planes de traction avec entailles doubles. L'énergie totale pour rompre une éprouvette pré-entaillée peut se diviser en deux contributions, une contribution « plastique » qui permet de déformer plastiquement notre matériau et une contribution « endommagement » qui sert à faire germer, croitre et coalescer des cavités conduisant à la rupture totale de l'éprouvette, voir Fig 7.

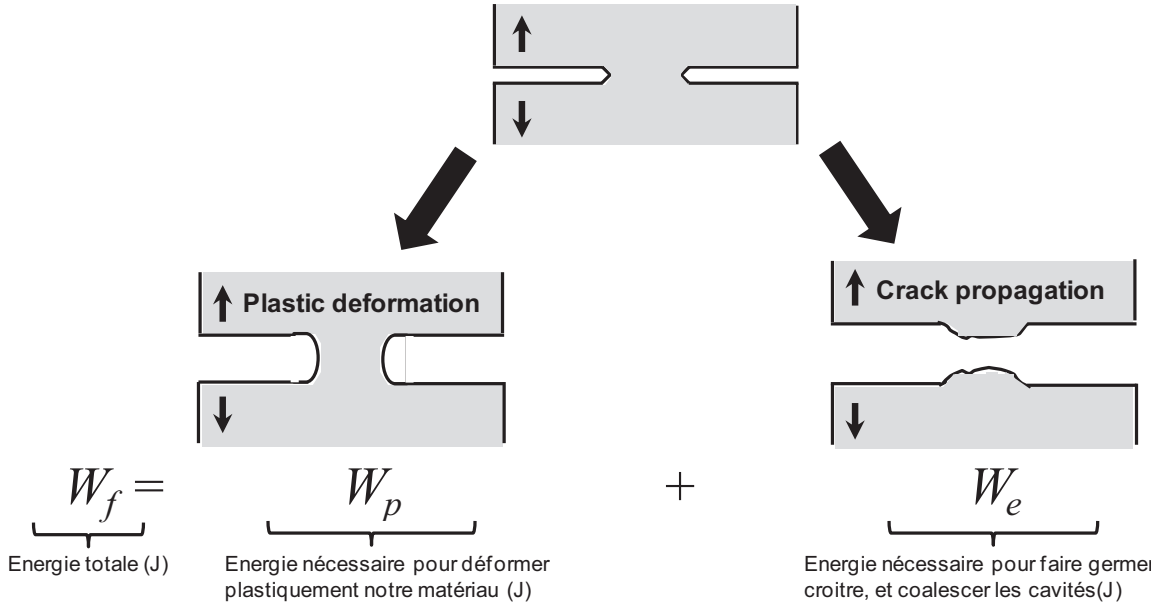
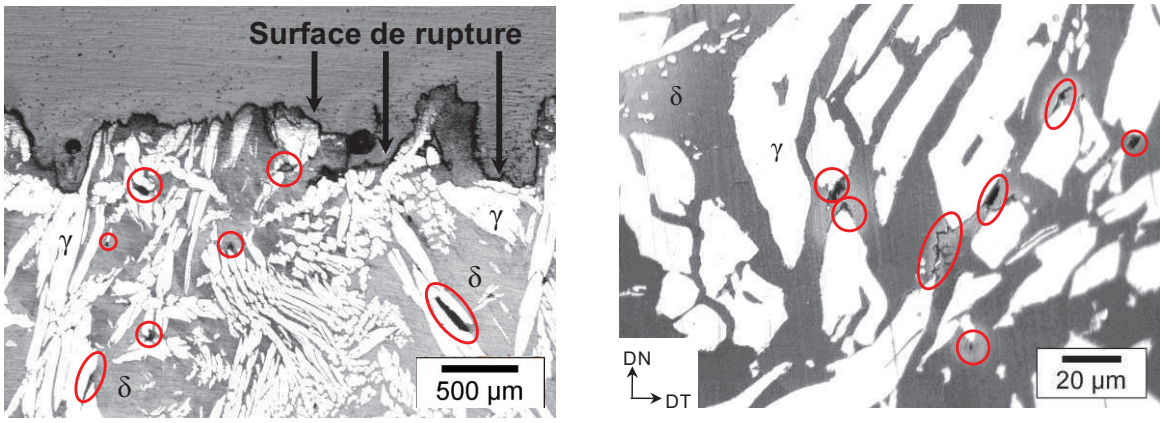


Fig 7. Principe du concept de travail essential de rupture

Ce qui nous intéresse, c'est de déterminer la contribution « endommagement » afin de quantifier la résistance à la propagation de fissures. Cette contribution porte le nom de travail essentiel de rupture. Le travail essentiel de rupture fournit un critère énergétique qui quantifie la résistance au déchirement ductile. Les détails concernant la détermination du travail essentiel de rupture sont donnés dans le manuscrit (p45-47). Si cette méthode a été largement utilisée à température ambiante pour déterminer la ténacité de tôles minces métalliques ou de films polymères, de nombreuses adaptations, également décrites dans ce manuscrit (p49-50), ont été nécessaires pour pouvoir appliquer cette technique à haute température.

Application du concept de travail essentiel de rupture aux matériaux bruts de coulée

Le concept de travail essentiel de rupture a été d'abord appliqué à haute température aux aciers D1 et D2, en prélevant des éprouvettes pré-entaillées directement dans les brames brutes de solidification. Les résultats ont montré que cette méthode est un outil discriminant pour caractériser la résistance au déchirement ductile à haute température des aciers inoxydables austéno-ferritiques. Les essais menés à 1050°C ont montré que l'acier D1 était deux fois plus résistant à la propagation de fissure à haute température que l'acier D2 (le travail essentiel de rupture de l'acier D1 étant deux fois plus grand que celui de l'acier D2). A 1200°C, la nuance D1 reste plus ductile que la nuance D2 mais la différence au niveau des travaux essentiels de rupture n'est pas significative. Des observations fractographiques ont également été réalisées pour compléter l'étude. Des observations micrographiques effectuées proche des surfaces de rupture des éprouvettes pré-entaillées et proche des rives ont révélé que les cavités germaient systématiquement au niveau des interfaces δ/γ et que les fissures ne se propageaient jamais dans la phase austénitique, voir Fig 8.



a) **b)**

Fig 8. Micrographies optiques qui montrent que les cavités germent par décohésion partielle au niveau des interfaces δ/γ et que les fissures ne se propagent jamais dans la phase austénitique; a) micrographie proche de la rupture d'une éprouvette pré-entaillée ; b) micrographie proche des rives, c'est-à-dire des zones endommagées sur une tôle industrielle. Les sites d'endommagement sont entourés en rouge.

Toutes nos observations et caractérisations nous ont conduis à proposer un mécanisme de rupture qui s'opère par germination, croissance puis coalescence des cavités, conduisant à la rupture complète de l'éprouvette. Ce mécanisme s'applique aussi bien pour D1 que pour D2. Des essais de microdureté ont mis en évidence les mécanismes d'adoucissement impliqués dans chacune des deux phases, et suggèrent une partition des déformations entre la ferrite et l'austénite à haute température avec un effet plus significatif pour l'acier D2, cela sera étudié en détails dans le chapitre IV. Cependant, il faut noter que les résultats étaient entachés d'une forte dispersion. Cette dispersion a été attribuée aux gradients de microstructure observés dans l'épaisseur des brames brutes de solidification (variation de la proportion des phases et de la taille des lattes d'austénite en fonction de la position dans l'épaisseur des brames). Ce dernier commentaire suggère que des résultats plus précis sont probablement accessibles à condition de tester des microstructures plus homogènes. Nous avons alors fabriqué des microstructures modèles et appliqué la même technique.

Génération de microstructures modèles

Dans cette partie, nous nous sommes attachés à fabriquer des microstructures modèles, plus homogènes que celles présentes dans les brames brutes de coulée, et dans lesquelles nous contrôlions très bien :

(i) la morphologie de l'austénite (équiaxe 'E' ou Widmanstätten 'W'),
(ii) la fraction volumique des phases ;
(iii) les tailles caractéristiques des microstructures (taille des lattes d'austénite de Widmanstätten ou taille des grains équiaxes d'austénite).

Cela nécessite de suivre des chemins thermiques appropriés, deux exemples sont donnés à la Fig 9 ainsi que les microstructures qui en résultent.

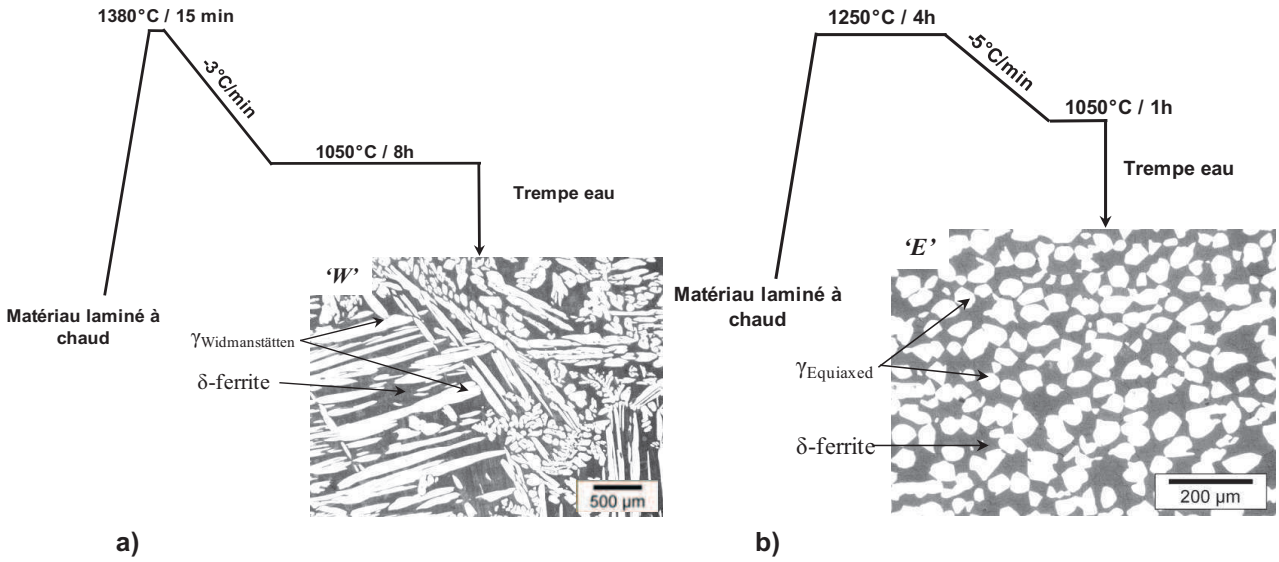


Fig 9. Chemins thermiques permettant de générer des microstructures modèles, exemple avec l'acier D2; a) chemin thermique pour fabriquer une morphologie d'austénite de Widmanstätten; b) chemin thermique pour générer une austénite équiaxe.

Le but est d'avoir, à notre disposition, un ensemble de microstructures modèles à tester à l'aide du concept de travail essentiel de rupture pour mettre en évidence l'influence de certains paramètres tel que la morphologie de la phase austénitique.

Application du concept de travail essentiel de rupture aux microstructures modèles

Nous avons testé l'ensemble de ces différentes microstructures modèles à l'aide du concept de travail essentiel de rupture à 1050°C.

Nous avons d'abord comparé les microstructures modèles des aciers D1 et D2 présentant une morphologie d'austénite de Widmanstätten : D1_W et D2_W. Les résultats ont montré qu'à 1050°C, la microstructure D1_W était deux fois plus résistante au déchirement ductile que la microstructure D2_W. Cela est bien en accord avec ce que nous avions trouvé lorsque nous avions analysé les microstructures des brames brutes de solidification, le facteur deux entre l'acier D1 et D2 est respecté. Nous insisterons ici sur le fait que la précision des résultats, en utilisant des microstructures modèles, s'est considérablement améliorée du fait d'une réduction significative de la dispersion par rapport à celle constatée lors de la caractérisation des microstructures brutes de solidification.

Afin d'étudier la morphologie des phases, nous avons ensuite comparé deux morphologies d'austénite différentes pour l'alliage D2 : une morphologie dite de Widmanstätten D2_W et une autre équiaxe D2_E. Ces microstructures contiennent la même fraction volumique d'austénite ce qui permet de s'affranchir de l'effet proportion des phases. Les résultats ont montré que la morphologie des phases a une influence significative sur la résistance à la propagation de fissure à haute température : en effet, il faut dépenser deux fois plus d'énergie pour rompre une éprouvette présentant une austénite équiaxe que pour rompre une éprouvette présentant une morphologie d'austénite de Widmanstätten.

Pour finir, nous avons étudié l'influence de la propreté inclusionnaire sur la résistance au déchirement ductile. Pour se faire, nous avons introduis un troisième alliage, l'acier D1bis. Cet acier D1bis possède la même composition chimique en élément majeurs que l'acier D1 (même nuance industrielle) avec néanmoins une quantité d'inclusions bien supérieure à celle mesurée dans D1 (environ 10

fois plus). Il s'avère que la propreté inclusionnaire est un paramètre clé. Il est en effet nécessaire de bien la contrôler dans le but de limiter la propagation des criques : l'acier D1 est quatre fois plus résistant que l'acier D1bis. Des caractérisations plus fines de l'état inclusionnaire ont aussi montré que les inclusions les plus critiques étaient celles qui se situaient au voisinage des joints d'interphase δ/γ, régions d'ores et déjà identifiées comme critiques car c'est au niveau de ces zones que germent les premières cavités.

L'ensemble de ces résultats ont été interprétés à l'aide de modèles micromécaniques simples dans le soucis d'établir le mieux possible les liens entre la microstructure et les propriétés d'endommagement.

Conclusion

Le concept de travail essentiel de rupture s'avère un outil très discriminant en termes de sensibilité à la crique pour les différentes microstructures d'alliages austéno-ferritiques étudiées. Il demeure néanmoins une interrogation sur l'origine de la différence en termes de résistance au déchirement ductile entre les microstructures D1_W et D2_W. Sur la base des résultats du concept de travail essentiel de rupture appliqué à D1_W et à D2_W, et de la littérature, nous avons émis l'hypothèse que la différence de comportement entre les deux aciers proviendrait d'un plus grand contraste de comportement mécanique entre ferrite et austénite dans le cas D2_W que dans le cas D1_W. Ce dernier commentaire justifie pourquoi nous nous sommes intéressés aux mesures de partition des déformations à haute température entre ferrite et austénite dans chacun des matériaux étudiés.

Chapitre IV. Distribution des déformations entre ferrite et austénite à haute température. p97-160

Introduction : les techniques disponibles pour mesurer les champs de déformation

Ce chapitre commence par une description des différentes techniques disponibles pour mesurer des champs de déformation. Ces techniques sont classées en deux grandes catégories : les techniques de grilles et les techniques de corrélation en mettant en avant respectivement, leurs avantages et leurs inconvénients. De nombreuses références sont données afin d'illustrer chacune des deux techniques à travers divers exemples. Ensuite, le champ de recherche est restreint aux techniques qu'il est possible d'utiliser pour mesurer les déformations à l'échelle de la microstructure dans des conditions sévères : haute température et grandes déformations. Parmi les techniques ayant données des résultats, nous avons sélectionnée une méthode de micro-grille développée récemment à l'université de Sheffield que nous avons adaptée et développée par rapport à notre problématique.

Méthode des micro-grilles modifiée

La technique permettant de fabriquer des micro-grilles résistante à haute température est ensuite décrite en détails, voir Fig 10. Il s'agit d'utiliser le procédé de micro-lithographie. Ce procédé nous vient directement de la micro-électronique, cependant, à la place de déposer notre matériau constituant la grille, classiquement de l'or qui ne résiste pas aux températures visées, nous avons effectué une gravure à l'aide d'une attaque électrochimique, Fig 10e. Nous avons ainsi obtenu des micro-grilles gravées à la surface de nos échantillons, la microstructure biphasée sous-jacente étant visible.

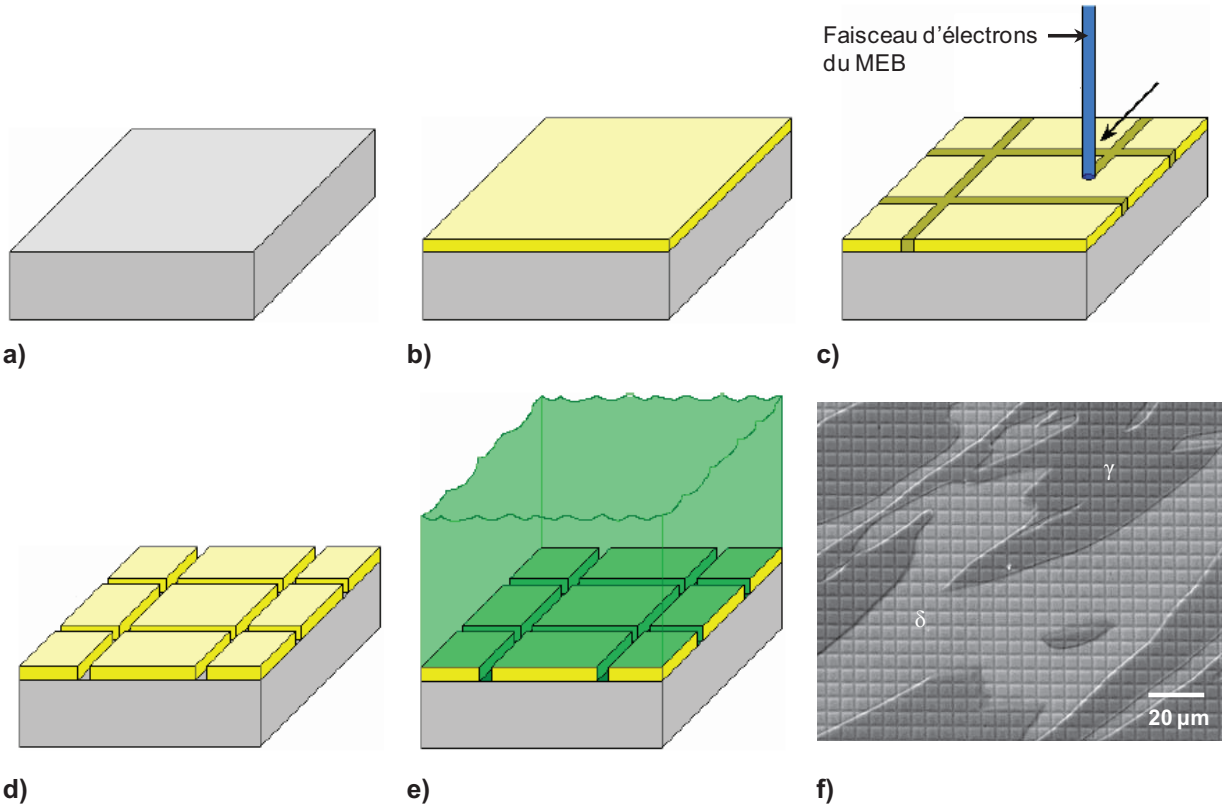


Fig 10. Les différentes étapes de la fabrication de micro-grilles résistantes aux hautes températures ; a) polissage et attaque préalable pour révéler la microstructure biphasée ; b) dépôt d'une résine électro-sensible à la surface de l'échantillon ; c) irradiation de la résine avec le faisceau d'électrons du MEB ; d) dissolution avec un solvant spécifique des chaînes de polymère irradiées ; e) gravure par attaque électrochimique des micro-grilles ; f) dissolution de la résine restante, des micro-grilles avec un pas de 5 µm gravées à la surface de l'échantillon sont obtenues.

Modification de l'échantillon de compression plane

Nous sommes capables maintenant de fabriquer des micro-grilles résistantes aux hautes températures, nous devons ensuite imaginer un système qui va nous permettre de solliciter notre micro-grille dans des conditions représentatives de celles qui existent lors du procédé industriel de laminage à chaud. Nous avons, pour se faire, opter pour l'essai de compression plane, essai qui se rapproche le plus du laminage. L'astuce consiste à usiner un trou au centre d'une éprouvette de compression plane, puis à y insérer l'échantillon sur lequel est gravé la micro-grille. Finalement, une étape de soudure permet de ne former plus qu'un seul échantillon. Il faut tout de même veiller à ce que la soudure n'affecte pas thermiquement la microstructure au niveau de la micro-grille. Toutes ces étapes sont résumées à la Fig 11.

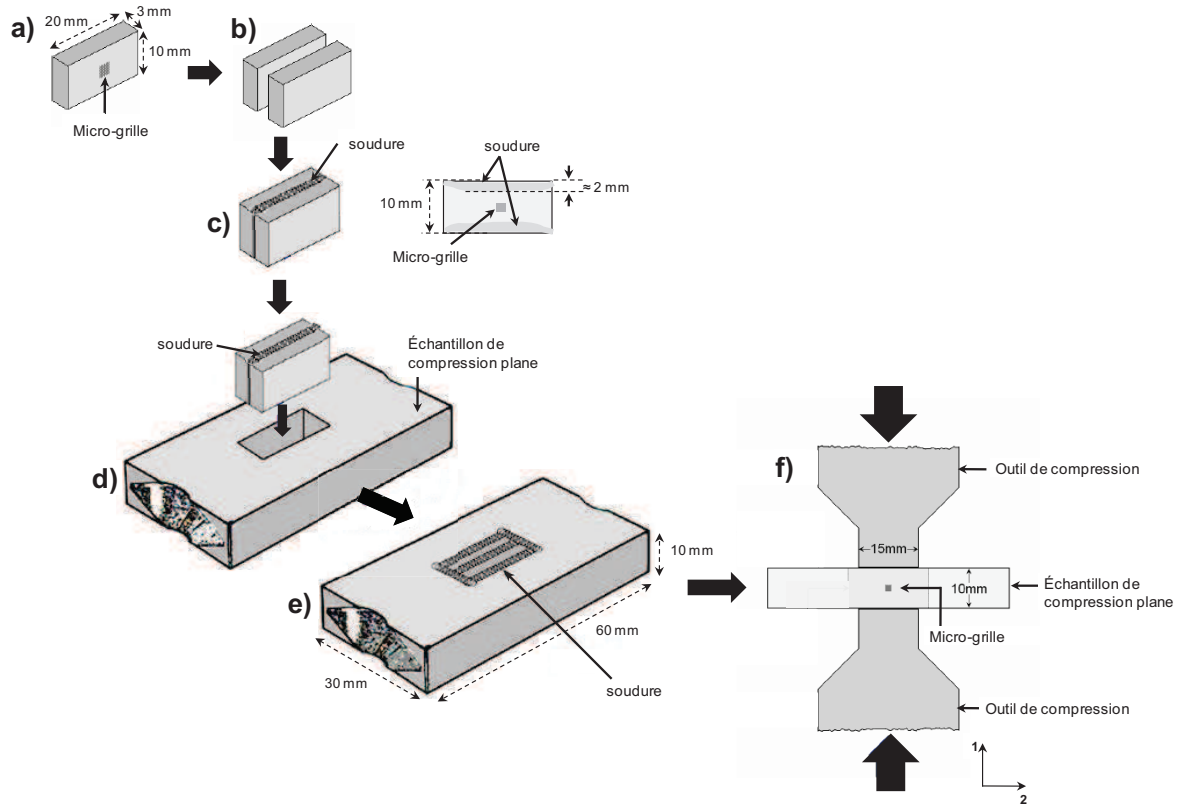


Fig 11. Modification de l'échantillon de compression plane; a) échantillon sur lequel est gravé la micro-grille ; b) mise en regard de l'échantillon sur lequel est gravé la micro-grille d'un insert métallique poli présentant strictement les mêmes dimensions ; c) soudure des deux inserts ; d) & e) assemblage des inserts et de l'échantillon de compression plane par soudure ; f) sollicitation mécanique en compression plane avec vue schématique de la localisation de la micro-grille par rapport aux deux outils de compression.

Conditions expérimentales

Dans ces travaux, nous avons effectué diverses expérimentations sur les microstructures modèles des alliages D1 et D2, à différentes températures : 850, 950 et 1050°C et à des vitesses de déformation de 1 et $10s^{-1}$. Si les essais menés à 1050°C et $10s^{-1}$ n'ont rien donné, les essais pratiqués à 850 et 950°C et à $1s^{-1}$ ont donné des résultats intéressants.

Calcul des déformations

Nous disposons d'images MEB des mêmes régions avant et après déformation, cela nous permet en repérant les points homologues, c'est-à-dire les intersections de micro-grilles appartenant aux mêmes points physiques avant et après déformation, de remonter au champ de déplacement et ensuite au champ de déformation, voir Fig 12.

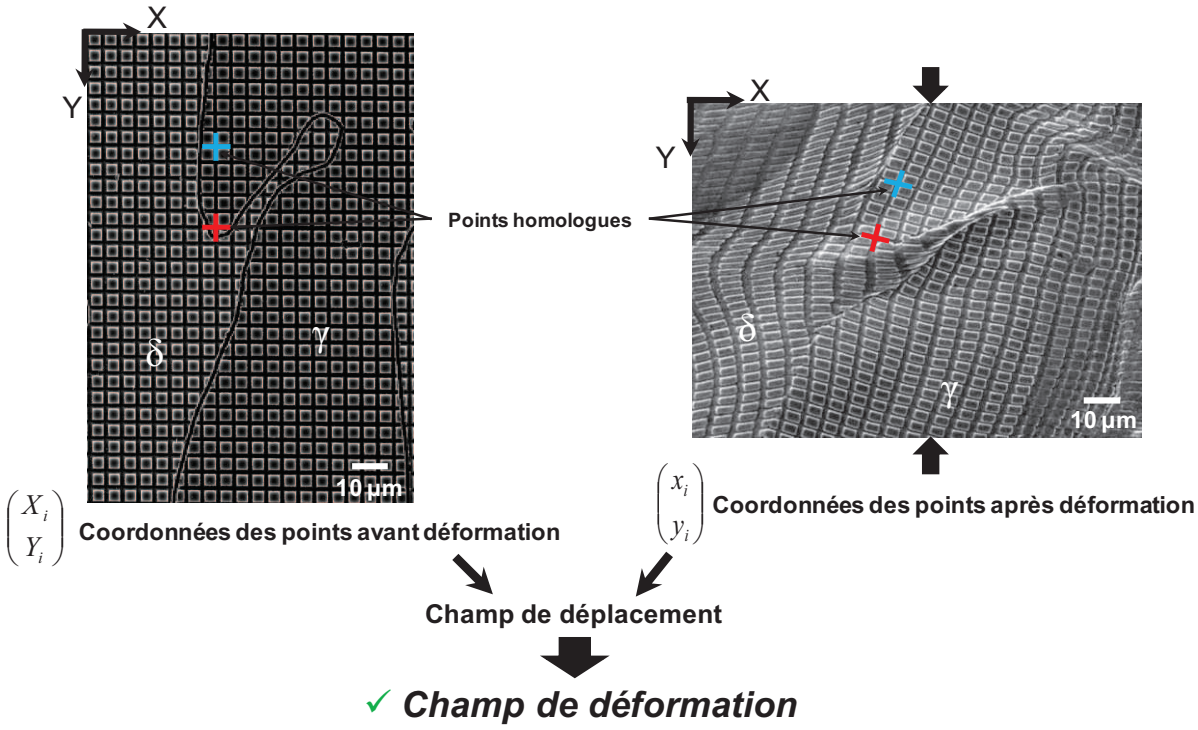


Fig 12. Principe de determination des champs de déformation.

Résultats

L'application de cette technique des micro-grilles a permis de mettre en évidence les micro-mécanismes impliqués dans la déformation à chaud des aciers inoxydables austéno-ferritiques : hétérogénéité des déformations, localisation des déformations au niveau des interfaces δ/γ, signature d'une déformation hors plan, développement de bandes de cisaillement (voir une illustration Fig 13)… Elle fournit aussi des données quantitatives au sujet de la partition des déformations à l'échelle de la microstructure : déformations moyennes par phase, fonction de distribution de la déformation, pourcentage de ferrite dans les régions les plus déformées (voir manuscrit pour plus de détails)…

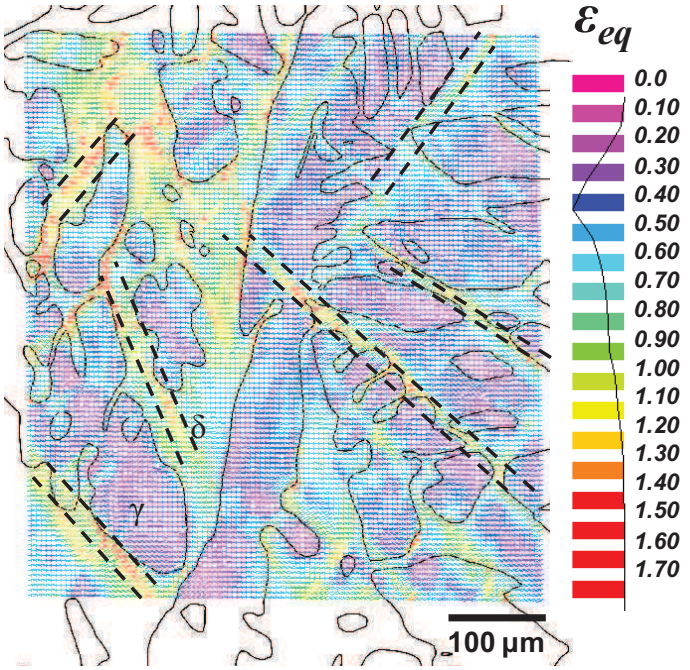


Fig 13. Exemple d'un champ de déformation obtenu avec l'acier D2 et dans lequel l'austénite présente une morphologie dite de Widmanstätten après une réduction de 30% à 850°C et $1s^{-1}$. Les traits en pointillés mettent en lumière le développement des bandes de cisaillement.

La comparaison entre D1_W et D2_W dans les mêmes conditions expérimentales (850°C, réduction = 30% et vitesse de déformation de $1s^{-1}$), a révélé que les déformations se répartissent de manière plus hétérogène dans le matériau D2 que dans le matériau D1. La ferrite se déforme environ 30% fois plus que l'austénite dans l'acier D1 alors que dans l'acier D2, la ferrite se déforme 60% fois plus que l'austénite.

La dispersion des résultats, c'est-à-dire les différences entre les champs de déformation déterminés dans un même échantillon s'explique par une localisation macroscopique des déformations dans l'échantillon de compression plane.

La rhéologie des phases semble dépendante de la composition chimique, notamment du pouvoir de durcissement en solution solide d'élément tel que le Molybdène.

D'autres facteurs ont également été identifiés dans les sens ou ils peuvent modifier la distribution des déformations : il a en particulier été étudié l'influence de la température et de la morphologie des phases sur la partition des déformations dans notre acier D1.

Limites de la technique des micro-grilles modifiée

Dans cette partie sont mises en évidence les nombreuses limitations de cette technique. Nous insistons sur les principales. La technique est très coûteuse en termes de temps, il faut compter environ 50h de travail pour déterminer un seul champ de déformation. La mesure des déformations s'effectue en deux dimensions, il n'y a donc pas de prise en compte de l'aspect tridimensionnel du problème. Enfin, nous pouvons également rappeler que cette technique n'est pas viable au dessus de 1050°C, voir Fig 14 qui montre l'état d'une micro-grille après déformation à 1050°C et $10s^{-1}$.

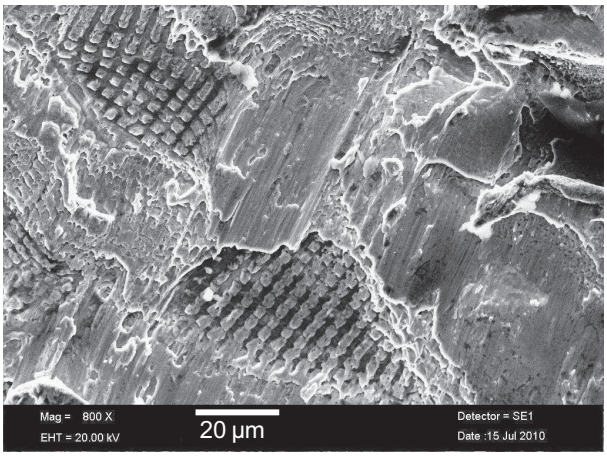


Fig 14. Image MEB qui montre l'état des micro-grilles après déformation à 1050°C et 10s-1, les micro-grilles s'avèrent inexploitables pour déterminer des champs de déformation.

Utilisation des données expérimentales dans un modèle pour déterminer les rhéologies de la ferrite et de l'austénite au sein de notre matériau biphasé

Ce travail a été le fruit d'une collaboration avec des partenaires de l'université Catholique de Louvain en Belgique. L'objectif est de décrire brièvement la stratégie utilisée pour déterminer les lois de comportement de la ferrite et de l'austénite au sein de nos alliages austéno-ferritiques et de donner des résultats issus d'un exemple. Le but est de montrer que cette stratégie permet une approche systématique pour déterminer le contraste de propriétés plastiques entre les deux phases. Une analyse par éléments finis a été utilisée pour étudier le comportement mécanique macroscopique des aciers inoxydables austéno-ferritiques lors d'un essai de compression plane. Nous avons tout d'abord modélisé la loi de comportement macroscopique de notre acier par une loi de Kocks-Mecking. Ceci nous fourni un jeu de paramètres pour notre loi de comportement macroscopique. Nous savons par ailleurs que la matrice ferritique s'apparente à la phase molle et que l'austénite correspond plutôt à la phase dure. Nous avons donc entré un jeu de paramètres initiaux pour chacune des deux phases de manière à ce que nous ayons bien une phase (austénite) plus dure que l'autre (ferrite). Ensuite, la technique adoptée consiste à reproduire par un modèle d'éléments finis les champs de déformation déterminés expérimentalement. Pour se faire, nous procédons par itération, c'est-à-dire que nous modifions le jeu de paramètres de la loi de comportement de chacune des phases jusqu'à minimisation de l'écart entre le champ de déformation expérimental et le champ de déformation simulé (méthode inverse). Lorsque le minimum est atteint, nous retenons le jeu de paramètres de notre loi de comportement pour chacune des phases ce qui permet de remonter à la rhéologie de la ferrite et de l'austénite au sein du matériau biphasé à haute température. Quelques résultats obtenus via cette approche sont présentés à la Fig 15 et montrent une bonne adéquation entre ce que nous avons mesuré expérimentalement et ce que nous avons déterminé par notre méthode inverse.

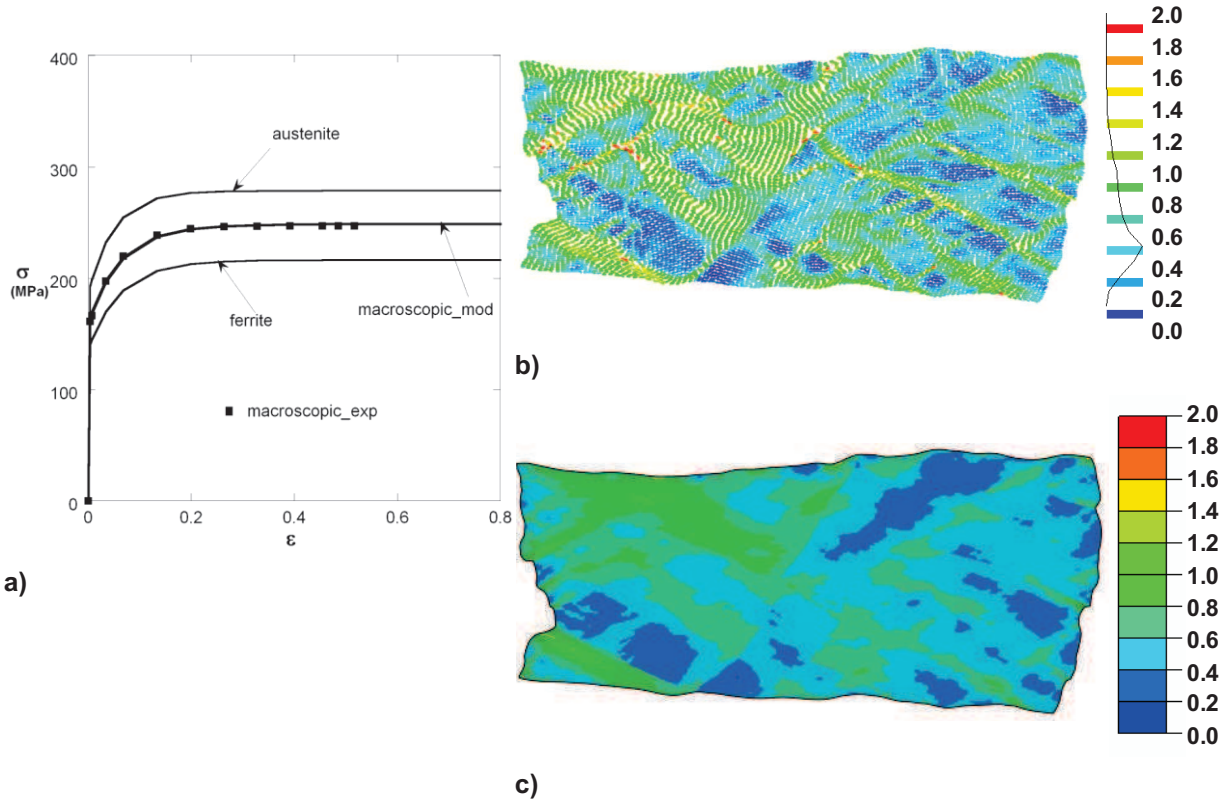


Fig 15. Quelques résultats obtenus sur l'acier D2 avec la stratégie développée en collaboration avec l'Université catholique de Louvain (échantillon déformé à 850°C et $1s^{-1}$); a) courbe contrainte-déformation macroscopique de l'acier D2 et rhéologies de la ferrite et de l'austénite déterminées via l'approche développée ; b) champ de déformation expérimental ; c) champ de déformation simulé.

Conclusions

La technique des micro-grilles modifiée présente l'avantage par rapport à la méthode des micro-grilles classique d'être applicable à haute température. Cette technique a été utilisée avec succès pour déterminer des champs de déformation à haute température (≥850°C) dans les aciers inoxydables austéno-ferritiques. Des caractéristiques intéressantes de la déformation à chaud de ces alliages ont été identifiées : régions les plus déformées situés très souvent au voisinage des interfaces δ/γ et presque toujours du côté ferritique (Fig 13), développement de bandes de cisaillement, et aussi possible glissement au niveau des joints d'interphase δ/γ. Le niveau de partition des déformations semble jouer un rôle considérable dans le phénomène de criques de rive et a été identifié comme un paramètre clé pour améliorer la forgeabilité des aciers inoxydables austéno-ferritiques. L'incompatibilité des déformations entre la ferrite et l'austénite est plus importante dans l'alliage D2 que dans l'alliage D1. Cette différence a été attribuée à des différences de compositions chimiques en éléments tels que Mo ou N, éléments notoirement connus pour avoir un fort pouvoir de durcissement en solution solide. Des additions d'éléments comme Mo ou N peuvent changer le comportement mécanique des phases, et donc par conséquent modifier la distribution des déformations à l'échelle de la microstructure. Une augmentation de 100°C pour passer de 850°C à 950°C augmente la partition des déformations entre la ferrite et l'austénite. La distribution de la phase austénitique dans la matrice

ferritique : l'orientation des lattes d'austénite ou un changement de morphologie peut aussi jouer sur la localisation des déformations. Enfin, la stratégie développée en collaboration avec des chercheurs de l'Université Catholique de Louvain en Belgique permettra une approche systématique pour déterminer les lois de comportement de la ferrite et de l'austénite au sein de nos microstructures biphasées.

Chapitre V. Conclusions et perspectives. p161-166

Le dernier chapitre reprend les principales conclusions de ces travaux et propose un certain nombre de recommandations pour supprimer ou du moins réduire le phénomène de criques de rive. Il est possible de classer ces recommandations en deux catégories :

- les recommandations « procédé »;
- les recommandations « métallurgiques ».

Les recommandations « procédé » sont celles qui peuvent être obtenues en jouant sur l'élaboration et la fabrication des tôles. Elles sont au nombre de trois :

(1) Il faudra bien contrôler la température au niveau de rives car nous avons bien vu qu'une diminution de la température, ne serait-ce que d'une centaine de degrés, conduit à chute brutale de la forgeabilité;

(2) Il est également nécessaire de bien veiller lors des étapes d'affinage de maintenir le soufre et l'oxygène le plus bas possible afin d'obtenir une propreté inclusionnaire satisfaisante;

(3) Il semble enfin que favoriser des tailles de lattes d'austénite de Widmanstätten fines en jouant sur les vitesses de refroidissement soit bénéfique du point de vue de la propagation des criques.

La recommandation métallurgique consiste à ajuster les éléments d'alliages, notamment en jouant sur Mo et N, de manière à réduire au maximum le contraste de comportement mécanique entre la ferrite et l'austénite lors des opérations de mise en forme à chaud.

Le manuscrit se termine en évoquant brièvement certaines perspectives qu'il serait possible de donner à un tel travail. La principale serait à étudier dans les détails les effets liés à la plasticité cristalline, c'est-à-dire l'influence de l'orientation des grains de ferrite ou des lattes d'austénite de Widmanstätten sur la localisation des déformations.